Spectral variability in cool main-sequence stars due to small-scale magnetic features

Charlotte Norris
Astrophysics Group

Department of Physics
Imperial College London

Thesis submitted for the Degree of
Doctor of Philosophy in Physics
to
Imperial College London

· 2018 ·

Declaration and Copyright

I declare that the work contained within this thesis is my own, except where reference is given to others' work.

The copyright of this thesis rests with the author. Unless otherwise indicated, its contents are licensed under a Creative Commons Attribution-Non Commercial 4.0 International Licence (CC BY-NC).

Under this licence, you may copy and redistribute the material in any medium or format. You may also create and distribute modified versions of the work. This is on the condition that: you credit the author and do not use it, or any derivative works, for a commercial purpose.

When reusing or sharing this work, ensure you make the licence terms clear to others by naming the licence and linking to the licence text. Where a work has been adapted, you should indicate that the work has been changed and describe those changes.

Please seek permission from the copyright holder for uses of this work that are not included in this licence or permitted under UK Copyright Law.

Charlotte Norris

December 2018

Publications

- "Spectral variability of photospheric radiation due to faculae. I. The Sun and Sun-like stars"
  Norris, C. M., Beeck, B., Unruh, Y. C., Solanki, S. K., Krivova, N. A., Yeo, K. L., 2017, A&A, 605, A45

- "Solar Irradiance Variability is Caused by the Magnetic Activity on the Solar Surface"
  Yeo, K. L., Solanki, S. K., Norris, C. M., Beeck, B., Unruh, Y. C., Krivova, N. A., 2017, PRL, 119

Abstract

Stellar variability on timescales of days and longer is attributed to magnetic surface features, such as dark spots and bright faculae. The spectral variability of these features introduces noise and systematics to planetary transit spectroscopy by affecting the shape and depth of observed transit curves. To ensure that the correct planetary parameters are obtained from these observations, accurate facular contrasts and limb darkening must be accounted for in their extraction. Facular contrasts have been observed only in a few wavelength bands on the Sun and cannot be resolved on other stars. Therefore, for full spectral coverage, spectra must be derived from atmospheric models. Until now, only 1D atmospheric models have been widely available. These 1D models do not fully reproduce the observed centre-to-limb variations of faculae, as they neglect the 3D geometry of the faculae.

In this thesis, I derive the first spectral contrasts from the UV (149.5 nm) to the infrared (160 000 nm) for small-scale magnetic features as a function of limb distance and magnetic activity using 3D magneto-convection simulations for multiple cool main-sequence spectral types (F3V-M2V). I find that facular contrasts have a complex relationship with magnetic field strength, limb distance, wavelength and spectral type.

The spectral facular contrasts are used to provide centre-to-limb variation coefficients for multiple exoplanetary mission filters. In addition to the magnetic centre-to-limb variations, field-free limb darkening coefficients across the spectral types are derived. Crucially, our calculations provide a direct link between facular contrast and magnetic field that has allowed reconstruction of total solar irradiance without the need for a free parameter.

Contents

List of Tables **9**

List of Figures **10**

Acknowledgements **13**

1 Introduction **14**
1.1 Overview . . . 14
1.2 Stellar spectra . . . 15
1.2.1 Absorption continua . . . 17
1.2.2 Spectral lines . . . 18
1.2.3 Spectral lines as continua . . . 20
1.2.4 Limb effects . . . 21
1.3 Causes of stellar variability . . . 21
1.3.1 Magnetic features . . . 23
1.3.2 Radiation from magnetic features . . . 26
1.4 Observations of variability . . . 29
1.4.1 Solar variability . . . 29
1.4.2 Mount Wilson sample . . . 31
1.4.3 *Kepler* . . . 33
1.4.4 Planetary observations . . . 36
1.4.5 Other observational methods . . . 39
1.5 Understanding the observations . . . 40

2 Simulating observations **44**
2.1 MURaM simulations and snapshots . . . 44
2.2 Line of sight algorithm . . . 50
2.3 ATLAS9 . . . 52

3 Field-free centre-to-limb variations 54
3.1 Field-free solar centre-to-limb variations 55
3.2 3D vs. 1D field-free centre-to-limb variations 57
3.3 Field-free centre-to-limb coefficients for exoplanetary missions 61

4 Magnetic regions on G2V stars 70
4.1 Radiation from magnetic regions on G2V stars 70
4.2 Contrasts of magnetic regions on G2V stars 79

5 Magnetic regions on F, K and early M stars 86
5.1 Stellar spectral type and disc centre snapshots 86
5.1.1 Images 86
5.1.2 Histograms 92
5.2 Stellar spectral type and limb dependence 98
5.3 Contrast spectra of magnetic regions on F, K and early M stars . . . 105
5.4 Centre-to-limb contrast variations for F, K and early M stars 111
5.5 Contrasts of magnetic regions for exoplanetary missions 113

6 Small-scale magnetic structures 120
6.1 Applications to total solar irradiance 120
6.2 Effect of pixel size on bolometric intensity vs. magnetic field 125
6.3 Effect of activity on bolometric intensity vs. magnetic field 127
6.4 Effect of spectral type on bolometric intensity vs. magnetic field . . . 129
6.5 Effect of wavelength on intensity vs. magnetic field 131
6.6 Summary 134

7 Conclusion 135
7.1 Summary of thesis achievements 135
7.2 Future work 138

Bibliography 141

A Abbreviations 152

B *Spitzer* IRAC centre-to-limb coeff. tables 153

C Additional figures 158

D Yeo et al. 2017 167

E Permissions **192**

List of Tables

2.1 Spectral types and simulation parameters. 45

3.1 *Kepler* field-free centre-to-limb variation coefficients 67
3.2 CoRoT field-free centre-to-limb variation coefficients 67
3.3 TESS field-free centre-to-limb variation coefficients 67
3.4 *Spitzer* IRAC1 field-free centre-to-limb variation coefficients 68
3.5 *Spitzer* IRAC2 field-free centre-to-limb variation coefficients 68
3.6 *Spitzer* IRAC3 field-free centre-to-limb variation coefficients 69
3.7 *Spitzer* IRAC4 field-free centre-to-limb variation coefficients 69

5.1 Bolometric intensities and standard deviations for F-K stars. 108
5.2 Bolometric intensities and standard deviations for M stars. 109
5.3 *Kepler* centre-to-limb variation coefficients 117
5.4 CoRoT centre-to-limb variation coefficients 118
5.5 TESS centre-to-limb variation coefficients 119

B.1 *Spitzer* IRAC1 centre-to-limb variation coefficients 154
B.2 *Spitzer* IRAC2 centre-to-limb variation coefficients 155
B.3 *Spitzer* IRAC3 centre-to-limb variation coefficients 156
B.4 *Spitzer* IRAC4 centre-to-limb variation coefficients 157

List of Figures

1.1 Temperature as a function of atmospheric height 15
1.2 Spectra for a 1D atmosphere compared to the Planck function 17
1.3 Magnetic flux concentration schematic 25
1.4 Ca II K emission reversal 28
1.5 TSI observations with monthly sunspot number 1979-2016 29
1.6 PMOD TSI composite 1979-2016 30
1.7 Ca II H & K flux variability 32
1.8 Kepler light curves for periodic and non-periodic G dwarves 34
1.9 Simulated facular occulting transit curve with incorrect fit. 38
1.10 Predicted fractional errors of planetary radius when ignoring facular and spot occultations. 39

2.1 Temperature as a function of optical depth 47
2.2 Vertical magnetic field in a G2V $\langle B_z \rangle = 300$ G snapshot 49
2.3 Temperatures and vertical velocities in G2V field-free and $\langle B_z \rangle = 300$ G snapshots 51

3.1 Filter responses as a function of wavelength 55
3.2 Emergent intensities for a G2V field-free snapshot at various limb angles 56
3.3 MURaM field-free G2V limb darkening vs. measured solar values. . . 57
3.4 3D MURaM field-free limb darkening vs. previously published 1D models 58
3.5 3D MURaM field-free limb darkening vs. 1D MURaM field-free limb darkening 59
3.6 Fits to MURaM field-free limb darkening 63
3.7 MURaM field-free limb darkening for F3V-M2V stars in visible filters. 64
3.8 MURaM field-free limb darkening for F3V-M2V stars in *Spitzer* IRAC filters. 65

4.1 Emergent intensities for a G2V field-free and $\langle B_z \rangle = 100$ G snapshot 72

4.2 Emergent intensities for a G2V $\langle B_z \rangle$ = 300 G and $\langle B_z \rangle$ = 500 G snapshot 73
4.3 Histograms of intensity for G2V field-free and $\langle B_z \rangle = 300$ G snapshots. 75
4.4 Histograms of intensity for G2V field-free, $\langle B_z \rangle = 100$ G, 300 G and 500 G snapshots. 77
4.5 Mean G2V centre-to-limb contrast variations for all calculated $\langle B_z \rangle$s . 81
4.6 Mean G2V contrast spectra for all calculated $\langle B_z \rangle$s 82
4.7 Mean G2V contrast centre-to-limb variation (CLV) for all calculated $\langle B_z \rangle$s vs. Yeo et al. 2013 85

5.1 Disc-centre intensities for F3V field-free, $\langle B_z \rangle = 100$ G & 500 G snapshots 88
5.2 Disc-centre intensities for K0V field-free, $\langle B_z \rangle = 100$ G & 500 G snapshots 89
5.3 Disc-centre intensities for M0V field-free, $\langle B_z \rangle = 100$ G & 500 G snapshots 90
5.4 Disc-centre intensities for M2V field-free, $\langle B_z \rangle = 100$ G & 500 G snapshots 91
5.5 2D histograms of disc-centre intensity for F3V snapshots. 93
5.6 2D histograms of disc-centre intensity for K0V snapshots. 94
5.7 2D histograms of disc-centre intensity for M0V snapshots. 95
5.8 2D histograms of disc-centre intensity for M2V snapshots. 96
5.9 Histograms of intensity for F3V snapshots at disc-centre and $\mu = 0.5$. 99
5.10 Histograms of intensity for K0V snapshots at disc-centre and $\mu = 0.5$. 100
5.11 Histograms of intensity for M0V snapshots at disc-centre and $\mu = 0.5$. 101
5.12 Histograms of intensity for M2V snapshots at disc-centre and $\mu = 0.5$. 102
5.13 Mean contrast spectra for all MURaM spectral types with $\langle B_z \rangle = 100\,G$. 106
5.14 Mean contrast spectra for all MURaM spectral types with $\langle B_z \rangle = 500\,G$. 107
5.15 Mean centre-to-limb contrast variation for all MURaM spectral types in given wavelength bins. 112
5.16 Mean centre-to-limb contrast variation for all MURaM spectral types in visible filters. 115
5.17 Mean centre-to-limb contrast variation for all MURaM spectral types in *Spitzer* filters. 116

6.1 G2V bolometric intensity vs. magnetic field strength for HMI pixels . 122
6.2 G2V 300 G bolometric intensity vs. magnetic field 123
6.3 G2V 300 G bolometric intensity image with magnetic field contours . 125

6.4 Bolometric intensity vs. magnetic field across activities 127
6.5 100 G bolometric intensity vs. magnetic field for G2V to early M stars 130
6.6 G2V 100 G bolometric intensity vs. magnetic field across wavelength 132

C.1 Emergent intensities for a G2V $\langle B_z \rangle$ = 200 G and $\langle B_z \rangle$ = 400 G snapshot 159
C.2 Histograms of normalised intensity for G2V field-free and $\langle B_z \rangle$ = 300 G snapshots. 160
C.3 2D normalised histograms of disc-centre intensity for F3V snapshots. 161
C.4 2D normalised histograms of disc-centre intensity for K0V snapshots. 162
C.5 2D normalised histograms of disc-centre intensity for M0V snapshots. 163
C.6 2D normalised histograms of disc-centre intensity for M2V snapshots. 164
C.7 Same as Fig. 6.4, for averaged pixel size 165
C.8 500 G bolometric intensity vs. magnetic field for G2V to early M stars 165
C.9 M0V 100 G bolometric intensity vs. magnetic field across wavelengths 166

Acknowledgements

Firstly, I'd like to thank my supervisor, Dr Yvonne Unruh, for taking me on after two years out from Astrophysics and academia. I have learnt a lot from her and am grateful for the opportunity, expertise and guidance. Additionally, thank you for being ever-patient, particularly during writing, and for putting up with all my preemptive panics!

The Astrophysics group at Imperial have been welcoming and helpful and, in addition to this, they almost always supply me with tea(bags). Throughout my PhD I have shared office space with a number of them: Ciaran, Claude, Josh, Rhys and others more temporarily. I'd like to thank them for providing distractions when I need them (and sometimes when I don't) and for always being willing to go on an expedition for pick 'n' mix.

In addition to my local group, I have had support from the members of the Max Planck Institute for Solar-system research, and would like to thank them all for their help and insights.

My constant rants and complaints would go almost unheard without Alix, Lauren, Leo and Viktoria, who have provided constant reassurance that at some point I'll get through this (mostly) unscathed. On that note, thanks goes to Stewart and Laurie for encouraging me, or tricking me, into doing the thing in the first place!

For providing me with somewhere to live while writing up and for all their proof reading, at a time when additional stress in the house could really be done without, I'd like to thank Ethan's family.

Support and encouragement and a true belief that they would love me and be happy whatever I choose to do – fail or succeed – as long as it makes me happy, as always, comes from my family - parents, siblings(&-in-laws), niblings and the emergency-backup variety. I am always grateful to them.

And finally, I'd like to thank Ethan for his constant love, support, and general doses of silliness, and for dealing with my bi-weekly crises of confidence. I hope now I'll get to actually spend a little more time with you!

Chapter 1

Introduction

1.1 Overview

The Sun has been the subject of many studies since the days that we, as a species, began to wonder how we came to be. We now know that it is the main input of energy into our home, the Earth, providing much of what we need to survive. Even though it has existed for about 4.6 billion years, and allowed life to persist for over 3 billion years, the energy it provides us with is by no means constant. This variability in both total and spectral energy has and will continue to affect our climate. More recently, it has become important to understand variability for increasing the longevity of space-based instrumentation and space-visiting humans. While our proximity gives us a privileged view of the Sun, it is just one of the many similar, albeit much further away, objects that we see in the night sky.

This chapter is intended as an introduction to solar and stellar variability and its causes. It begins with an explanation of the formation of spectra observed from stars. It then discusses the known causes of stellar variability leading to the justification for small-scale magnetic features (faculae) being the main focus of the work in this thesis. Comments are then made on the existing observations of the variability of the Sun and stars and how this variability may affect the detection and characterisation of exoplanets. The final section of the chapter introduces the use of modelling for the investigation of variability caused by small-scale magnetic features.

Throughout this text I use the terms "late-type" and "solar-type". For the purpose of this thesis "late-type" stars are defined as main-sequence stars (luminosity class V) with an outer convective zone. This includes stellar spectral types from early M through to late F, with masses ranging from approximately 0.35 to 1.3 solar masses ($M_{\odot}$), and spanning effective temperatures of 2500 to 7500 K. While early G type stars are included in "late-type" stars, "solar-type" refers specifically to early

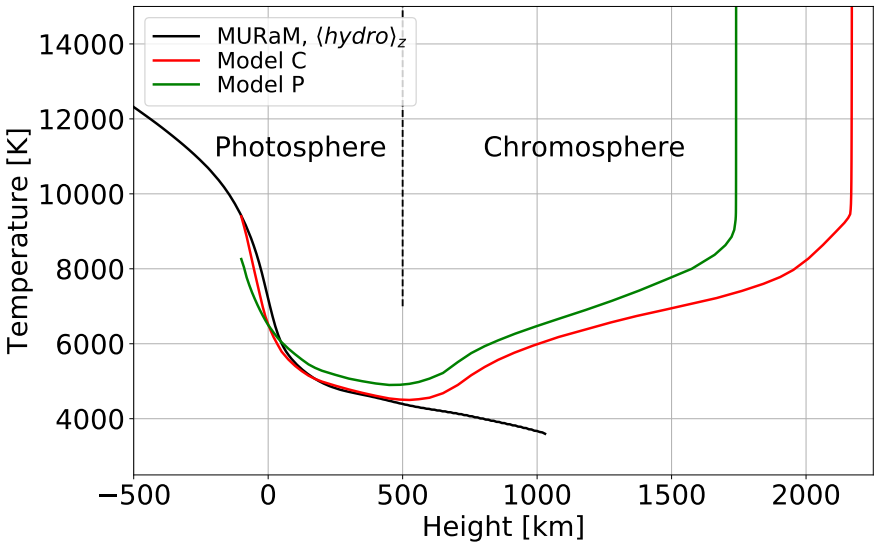


Figure 1.1: Temperature as a function of atmospheric height for different solar atmospheres. The black solid line shows the mean of the hydrodynamic MURaM snapshot atmospheres, shifted in height so that zero height corresponds to $\log(\tau_{500}) = 0$, where τ_{500} is the optical depth at 500 nm. Two 1-dimensional models from Fontenla et al. (1993) are shown: FAL C (labelled model C in red), for the quiet Sun, and FAL P (labelled model P, in green), for a plage region. The approximate height of transition between the photosphere and chromosphere is shown by a vertical black dashed line.

G types.

1.2 Stellar spectra

The light that reaches us from a star is the result of the underlying blackbody emission of a star and the emission and absorption of photons in the upper layers of the stellar atmosphere. As such, observed stellar spectra depend on the structure of these upper layers. To illustrate a typical atmospheric structure, Figure 1.1 shows the temperature changes with atmospheric height of model solar atmospheres for the photosphere and chromosphere. A height of zero corresponds to the approximate point where optical depth (explained below) is one. The solid black line shows the mean atmosphere of all pixels in all snapshots from the three-dimensional hydrodynamic MURaM simulation of spectral type G2V, described in Chap. 2. This model extends only to the lower chromosphere. The red and green lines show 1D "FAL" models of the Sun, presented in Fontenla et al. (1993) and named for its authors, for the quiet Sun (FAL C, labelled model C) and a bright plage region (FAL P, labelled model P), respectively. The "bright plage" atmosphere refers to being bright in

the visible, which means it corresponds to a facular region (Domingo et al., 2009). 1D atmospheric models including the FAL P plage atmosphere will be discussed in Sect. 1.3.2.

Most of the visible light seen in a stellar spectrum originates in the photosphere, where the temperature, pressure and density decrease with height. At about 500 km there is a temperature minimum. While pressure and density continue to decrease with height, the temperature begins to increase: this is the start of the chromosphere. In the deep photospheric layers very few photons are able to escape as the optical depth to the surface is high. The photons are absorbed close to where they are emitted and when re-emitted will radiate in any direction, meaning that almost as many photons are heading into the layer as heading out. This leads to near thermodynamic equilibrium. Therefore, the radiation from these layers can be described by the laws of a blackbody. Looking at higher and higher layers in the atmosphere, this approximation is less and less valid, as more and more photons are able to escape and departure from thermodynamic equilibrium occurs (Gray, 1992).

A comparison of a typical disc-centre solar spectrum (shown by a black line), synthesised from the Kurucz' quiet-Sun model atmosphere (Kurucz, 1992a,b,c) using ATLAS9 (Kurucz, 1992a; Castelli & Kurucz, 1994) and a Planck function of the same effective temperature, i.e., assuming the Sun to be a blackbody (green line), is shown in Figure 1.2 (see Sect. 2.3 for discussion of the red line). The differences in energy distribution across wavelength between the Planck function and the synthesised spectrum show that as photons travel through the atmosphere, their energy is redistributed in wavelength and can no longer be assumed to be Planckian.

As it travels through the atmosphere, the radiation will be absorbed in bound-to-free and free-to-free electron transitions (both of which produce absorption continua), as well as bound-to-bound electron transitions (which produce spectral lines). The overall shape of the emission is governed by the line of sight through the stellar atmosphere and the wavelength, λ, or, equivalently, the frequency, ν, of the radiation. Over a path length, L, through a star's atmosphere radiation will be affected by both scattering and absorption of photons (which is accounted for by the mass absorption coefficient at a given frequency, κ_ν). In spectral modelling κ_ν is typically split into a continuum and a line part. The radiation is also affected by the mass density, ρ, and the depth into the atmosphere, dz. These combined effects are given by the optical depth at a given frequency, τ_ν, which is calculated by

$$\tau_\nu = \int_0^L \kappa_\nu \rho \, dz. \tag{1.1}$$

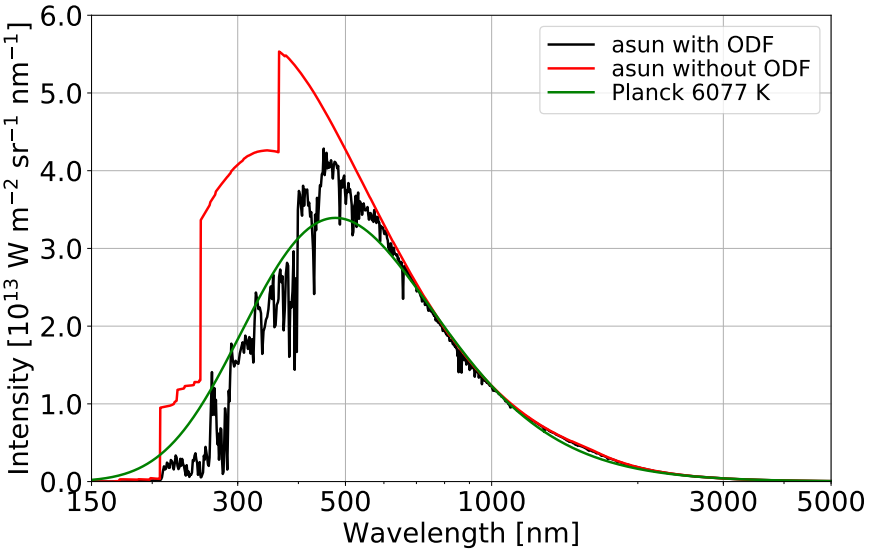


Figure 1.2: The disc centre spectrum produced by ATLAS9 for the Kurucz' quiet-Sun model atmosphere (labelled asun, in black, Kurucz, 1992a,b,c), compared with the Planck function (green) at the disc centre effective temperature, 6077 K, of the Kurucz' quiet-Sun model. The red line shows the resultant spectrum if no opacity distribution function (ODF) is included in the calculation.

This leads to the simplest example of the radiative transfer equation

$$dI_\nu = -I_\nu \, d\tau_\nu, \tag{1.2}$$

which has the solution

$$I_\nu = I_\nu^0 \exp(-\tau_\nu), \tag{1.3}$$

where I_ν is the specific intensity, which in cgs units is given in erg $s^{-1}cm^{-2}sr^{-1}Hz^{-1}$, and I_ν^0 is the specific intensity before traversing L (Gray, 1992).

Subsections 1.2.1-1.2.3 contain discussions of species with the largest optical depth contributions in late-type stellar atmospheres. Effects of the environment (including pressure, velocity and magnetic field), in terms of continua and spectral lines will also be included. The final subsection, 1.2.4, then explains why the spectrum observed varies across the stellar disc.

1.2.1 Absorption continua

Hydrogen is responsible for most of the continuum opacity in stellar atmospheres. For neutral hydrogen, the bound-free electron transition can occur from any electron level to the continuum. This means that several absorption edges are seen, where the

photons of this wavelength are no longer energetic enough to free an electron from the specified orbit. The first few edges appear at 91.2 (Lyman), 364.7 (Balmer), 820.6 (Paschen), 1458.8 (Brackett) and 2279.0 nm (Pfund). The absorption cross-section then falls off as ν^{-3} with increasing frequency for each (Mihalas, 1978). Neutral hydrogen is a dominant continuum absorber in B, A and F type stars.

The negative hydrogen ion becomes more important than neutral hydrogen for continuum absorption in cool stars, such as G, K and M type stars. This set of cool stars includes the Sun, which is of type G2V. Hydrogen is capable of holding a second electron due to the polarised nature of the proton-electron pair. This is a fairly unstable bond, therefore, to neutralise this ion, only an energy of 0.754 eV is required. This corresponds to a wavelength of 1644.4 nm. The negative hydrogen ion therefore absorbs photons with wavelengths shorter than this. Its absorption cross-section varies with wavelength and has a peak at 850 nm. The abundance of H^- is dependent on the abundance of (electron donating) metals in the star. As such, metallicity is an important factor when considering H^- opacities (Mihalas, 1978).

Free-free transitions can occur for both neutral and negative hydrogen. When a free electron interacts with a proton, its unbound orbit is altered. A photon may be absorbed in this process, and the electron energy is increased by the photon energy. A slow electron velocity means that a photon is more likely to pass and be absorbed (Gray, 1992). For negative hydrogen, the free-free transition cross-section increases with wavelength, with a similar cross-section as the bound-free transition at about 1.5 μm. Combining both free-free and bound-free absorptions, negative hydrogen has an opacity minimum at approximately 1.6 μm (Mihalas, 1978). Therefore often the deepest can be seen into the atmosphere of a star at this wavelength.

1.2.2 Spectral lines

Spectral lines are produced when photons of a given wavelength are absorbed resulting in a transition of an electron from one bound orbit in an atom, or ion, to another of higher energy. The energy, or wavelength, of the photon required depends on the energy levels in the absorbing atom. As a consequence of Heisenberg's uncertainty principle, each electron energy level has an uncertainty. As such, the energy of the transition between two levels will vary. This leads to natural broadening of the spectral line. The energies of absorbed photons have a Lorentzian distribution, with a width referred to as the 'natural width' (Gray, 1992).

The width of spectral lines will be affected according to the environment. Fac-

tors include pressure, temperature, bulk gas motions and magnetic fields in the atmosphere. Colliding particles will perturb the energy levels, depending on the separation of the particles. This, like the natural width, gives a Lorentzian distribution to the photon energies absorbed. Therefore, as more collisions are likely to occur at higher pressures, or densities, more broadening will occur under these conditions.

Movement of an absorbing particle along the line of sight will Doppler shift the wavelengths absorbed. This velocity can be in the form of thermal motions causing a Gaussian broadening of the line due to the distribution of line-of-sight velocities at a given temperature. This effect is called thermal broadening. Combining these Lorentzian and Gaussian components produces a Voigt profile for each of the spectral lines (Posener, 1959).

Doppler shifting velocities can also be in the form of bulk gas motions. For example, as stars rotate, one side of the stellar disc will be moving away from the observer along the line of sight (LOS) (red-shifted) and the other will be moving towards the observer along the line of sight (blue-shifted), with the highest LOS velocities being furthest from the rotational axis. Broadening of the disc-integrated spectral line will occur due to this spread of velocities, and therefore the spread of photon energies absorbed.

Additionally, asymmetries are introduced to the disc-integrated spectral line profile by Doppler shifts caused by the convective motions in the atmosphere. These motions and their effects are further discussed in Section 1.3.

Suprathermal line broadening is referred to as turbulence, although it has little to do with aerodynamic turbulence. For convenience, when modelling stellar spectra, it is dealt with by two approximations: microturbulence for turbulent elements that are small compared to unit optical depth, and macroturbulence for turbulent elements that are large compared to unit optical depth.

The microturbulence approximation must be used in the case where line opacities are calculated without accounting for the actual line-of-sight velocities of particles in the atmosphere, e.g., when using pretabulated opacities, as described in Sect. 1.5. Neglecting to treat the velocity broadening of lines can reduce the total line absorption in the case of a saturated line, and reduce important line opacity effects, such as line blanketing (discussed in Sect 1.2.3), by reducing the width and, hence, the overlapping of spectral lines. Microturbulence allows for the consideration of when the line of sight passes through many cells of motion in the photosphere. As the velocities and therefore their effects on spectral lines are typically relatively small, it is difficult to measure the shape of their distribution. Therefore, it is often

assumed to be an isotropic Gaussian centred on the microturbulent dispersion velocity, ξ. Microturbulence can then be introduced in radiative transfer by increasing the thermal velocity in the atomic absorption coefficient by ξ. This increases the width of the Gaussian component of the line (Gray, 1992).

Macroturbulence bypasses radiative transfer. If a single macroturbulent element was observed, only a simple Doppler shift for the entire line would be seen, with no broadening. However, when looking at the disc-integrated spectrum, as is the case for a stellar disc, these various shifts will superimpose to form a broadened line. Both approximations only consider the Doppler shifts introduced by the velocities, and ignore the temperature and pressure changes caused by the motions (Gray, 1992).

1.2.3 Spectral lines as continua

When many spectral lines overlap, they produce what appears as continua. Some of the radiation emitted from deeper layers than the atmospheric depth at which the absorption occurs will be blocked from escaping the star at these wavelengths. The presence of multiple dark spectral lines in a photometric band is called the blocking effect, as it directly affects the measured flux. Due to this blocked flux, temperatures will rise in lower atmospheric layers (backwarming or line blanketing) and decrease in higher layers, creating a higher temperature gradient (Milne, 1928). Radiation is then received from higher, cooler layers, and thus less energy is emitted. The transport of energy is restricted by lines, where it would normally occur, and the blocked flux must emerge elsewhere in the spectrum to conserve the total flux. The higher temperature gradient produced by the line blanketing leads to this blocked flux emerging from the blanketed, deeper, hotter layers at longer wavelengths (Mihalas, 1978).

In the Sun, thousands of millions of spectral lines of predominantly neutral and singly ionised metals block the flux in UV wavelengths forcing it to be emitted at longer wavelengths (i.e., the infrared). This effect can be seen in Fig. 1.2, where the synthesised solar spectrum (black line) has a lower intensity than that of the Planck function (green line) in the UV, but exceeds it around 1.6 μm. Therefore, the composition of the atmosphere, and any factors affecting the width of these lines, e.g., the metallicity of the star, are very important in determining the spectrum that we expect to see when observing late-type stars.

1.2.4 Limb effects

The radiation observed in a stellar spectrum not only varies with wavelength but also across the stellar disc due to the line of sight. As the viewing angle is increased (i.e., towards the limb), the length of the path, dz, along the line of sight in each layer of the atmosphere is increased. Therefore, a shallower layer of the atmosphere is observed than at disc centre. In the photosphere, deeper layers tend to be hotter. As such, when viewing in visible light, i.e., observing the photosphere, cooler layers are observed towards the limb than at disc centre. On the Sun, at optical wavelengths, this leads to limb darkening in the quiet flux. This was measured and parameterised by Neckel & Labs (1994) between 303 nm and 1099 nm. However, when moving into the UV the centre-to-limb variation becomes flat, and at extreme UV and X-ray wavelengths there is limb brightening (Goldberg et al., 1968; Withbroe, 1970). This effect is demonstrated in Solar Dynamics Observatory (SDO) images of the Sun in Llama & Shkolnik (2015). Viewing effects across the disc are also important for magnetic regions. These are described in Section 1.3. The distance from centre to limb is generally referred to in terms of $\mu = \cos\theta$, where θ is the angle between surface normal and the line of sight. This means that $\mu = 1.0$ is at disc centre and $\mu = 0.0$ is at the limb.

1.3 Causes of stellar variability

Stars are not constant in their emission of radiation. Wilson (1978) measured chromospheric variations in Ca II H & K lines for a sample of stars of F5V to M2V types. Many of these stars were found to vary in H-K flux in the short term, and several showed complete or almost complete cycles of cyclic variation. Cyclic variations, analogous to the solar cycle, were also found in photometric Strömgren uvby bands by Radick et al. (1983b,a). Radick et al. (1983b) used a subset of the stars in Wilson (1978) and found that continuum variability accompanies chromospheric variability, with chromospheric activity often being in anti-phase with continuum brightness. Many have continued to measure these variations (Lockwood et al., 2007; Radick et al., 2018), along with variations in stellar spectra (see Sects 1.4.2 and 1.4.3 for more details on observations of stellar variability). Similar irradiance and spectral variations occur on the Sun (Willson & Hudson, 1991, see Sect. 1.4.1 for more information on solar variability) where we are able to directly observe some of the phenomena that cause them. As we are unable to resolve the surface features on other cool main-sequence stars, we must rely on disc-integrated data as our source

of information for stellar surface variation.

The surface of a star is constantly evolving due to motions in the atmosphere. Granulation is observed on the Sun and is produced by convection in the stellar atmosphere creating upwellings of hot plasma (granules) and intergranular lanes where this material, after cooling, sinks downwards again. On the Sun, these granules have typical sizes of 500 km to 1.5 Mm and a lifetime of minutes (Wiegelmann et al., 2014). Radiation is blueshifted as it rises towards the observer in the granules and redshifted in the intergranular lanes as the material then falls back inwards. Granules are brighter and cover more of the stellar surface than the intergranular lanes, producing a net blueshift in the spectral lines. However, with the additional redshift effect of the intergranular lanes, the spectral lines produced are asymmetric with a 'C'-shaped line bisector (Voigt, 1956, 1959; Dravins et al., 1981; Cegla et al., 2015). For a review of solar surface convection see Nordlund et al. (2009).

Acoustic or pressure waves (p-mode oscillations) generated by motions in the star produce fluctuations in the atmosphere, and therefore in the fluxes seen, on timescales of less than a day. Each solar p-mode is trapped inside a specific region of the solar interior. The frequency of the wave is sensitive to the properties of that region, such as the temperature and the mean molecular weight of the material. Therefore, these fluctuations can be used to probe the interior of the Sun. This technique is called helioseismology for the Sun (see, e.g., Broomhall et al., 2014), and can also be used for other stars (called asteroseismology, see, e.g. Gilliland et al., 2010).

Motions of the electrically conducting fluid of which a star is made induces magnetic field within the star. For cool main-sequence stars of spectral type M2V to F3V (i.e., those with a rigidly rotating radiative core and a differentially rotating convective envelope), the dynamo mechanism often considered is an $\alpha\Omega$ dynamo. Differential rotation in the lower convection zone converts rotational kinetic energy to magnetic energy. Magnetic field lines are wound tightly around the core in an axisymmetric toroidal field. This winding converts poloidal field to toroidal field – this is the Ω effect. The concentrated areas of magnetic field are lower density than the surrounding atmosphere due to magnetic pressure. This causes them to be buoyant and rise to the surface. Large-scale motions in the convective envelope twist these field lines, converting toroidal field elements into poloidal field. This is known as the α effect. Thus, the combined effect is known as an $\alpha\Omega$ dynamo. For reviews on solar and stellar dynamos see Charbonneau (2010) and Brun & Browning (2017).

The dynamo of a star maintains the magnetic field and leads to the activity

cycles observed on the surface (see Sects 1.4.1 to 1.4.3 for more details on observations). As magnetic field emerges at the surface, the pressure balance between the emerging field and the surrounding atmosphere determines whether the field remains where it emerges or if the convective motions in the atmosphere will sweep the field into the intergranular lanes, where regions of high magnetic field form, producing dark and bright patches that evolve on timescales of hours to days. Not only does rotation cause rotational broadening in lines, it also changes the part of the star's surface that is observed. Therefore, different features are brought into and out of view. As the features move across the stellar disc the angle at which they are observed and therefore the radiation received from them will vary. This rotational modulation occurs on timescale of hours to days (Solanki & Unruh, 2013; Shapiro et al., 2017). Over 95% of the variability of the Sun on timescales longer than a day can be attributed to magnetic activity (Krivova et al., 2003; Yeo et al., 2017). It is expected that similar results will be found on other cool stars. Therefore, the radiation from magnetic features must be investigated in order to determine the magnitude of the contribution of magnetic activity to variability on other stars. The remaining subsections of Section 1.3 will focus on what is currently known about photospheric magnetic features and their radiation.

1.3.1 Magnetic features

Magnetic features reveal themselves as either dark or bright areas on the stellar surface (spots and faculae respectively when observing in visible wavelengths). As these are not currently resolvable on main-sequence stellar surfaces (see, e.g., Roettenbacher et al., 2014, 2017, for methods for resolving large spots on giant stars), we must learn about them from what we can observe on the solar surface. The evolution of a star's magnetic field and the plasma in its atmosphere are intrinsically linked. Thus, they must be considered together when simulating the evolution of magnetic features. For a review on solar surface magneto-convection see Stein (2012). Also, see Sections 1.5 and 2.1 for more in depth descriptions of stellar atmosphere simulation relevant to this thesis.

Sunspots and faculae are generally attributed to magnetic flux tubes (Fan, 2009). These tubes contain high magnetic field on the order of a kG. The magnetic field suppresses convective heat transport inside the tubes, cooling them. Within the tubes, plasma is evacuated in an enhanced downdraft (Parker, 1978), which causes a decrease in the gas pressure compared to the surrounding area. The field in the tube then becomes compressed until it reaches a strength to balance the surrounding gas

pressure. The evacuation of the tube decreases the opacity, increasing the depth at which $\tau = 1$ occurs and allowing deeper layers to be visible. The walls of the feature at this increased depth are hot due to temperature increasing with depth in the quiet atmosphere outside the flux tube. These hot walls radiate into the cooled flux tube. If the flux tube has a small diameter the radiative heating can compensate for the cooling, hence the observed layers within the tube become hotter than the observed layers of the quiet Sun, therefore brighter in the optical. Such small-scale flux tubes are called faculae. When the diameter is such that the heating is not sufficient to compensate, dark pores are seen (Spruit, 1976).

Sunspots are high magnetic field regions thought to be created by the coming together of many small flux tubes of the same polarity producing a large feature that is dark in the visible. They consist generally of an umbra (a central region with vertical or nearly vertical magnetic field of strengths between 2 and 4 kG), and a penumbra (the surrounding region consisting of a filamentary structure with a weaker more horizontal magnetic field of strength of about 1 kG – Title et al., 1993; Lites et al., 1993; Schad, 2014). Sunspots typically have diameters of 3 Mm to 60 Mm (Bray & Loughhead, 1964) and survive for hours to months. Faculae, in comparison, have a range of sizes with a spatially averaged field strength between 100 G and 500 G (Title et al., 1992). For more information on sunspots see Solanki (2003) and references therein.

The flux observed from these features will be affected by the angle at which the tubes are viewed, particularly for faculae. At disc centre in visible light, many faculae are only slightly brighter than the surrounding photosphere, although this varies with wavelength. Figure 1.3, taken from Keller et al. (2004), shows a schematic of a magnetic flux concentration between two granules. The schematic shows an observer viewing the feature at an angle (i.e., the feature is positioned towards the limb of the star). The grey rectangle shows the section of the observers view that contains observable features caused by the magnetic flux concentration, with the light grey portion showing bright areas (in visible light), and the dark grey showing dark areas. Dotted lines indicate the regions where 80 % of the continuum brightness comes from. Towards the limb, instead of seeing directly down into the feature (approximately along the field lines), radiation from the walls of the feature will become visible. These walls are formed by the surrounding granules. The low opacity of the magnetic feature allows deeper layers of the granular edges to be seen. Most of the continuum radiation, when looking through the low opacity feature to the granular wall, is formed in a thin region at the interface between the magnetic flux concentration and the granular wall. Due to the positive temperature gradient with

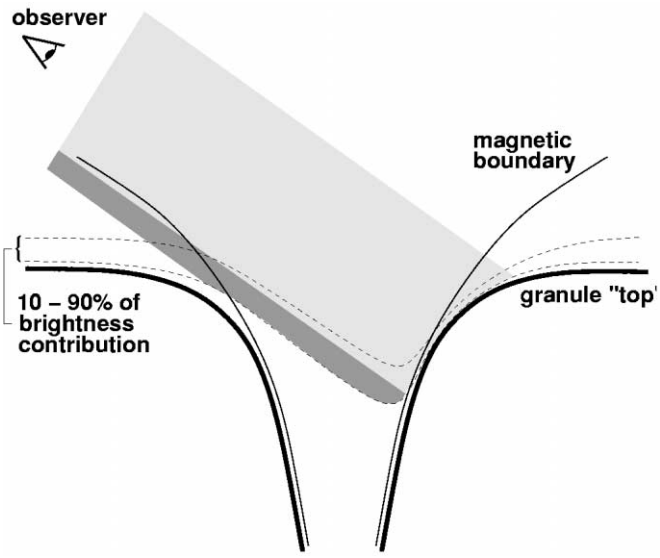


Figure 1.3: Schematic of a magnetic flux concentration between two granules. Dashed lines show where 80% of the of the continuum radiation is formed. The schematic shows an observer, viewing the magnetic region at an angle with the grey areas indicating where a dark lane is seen (dark grey) and where a bright region is seen (light grey). *Figure from "On the Origin of Solar Faculae", Keller et al. (2004). ©AAS. Reproduced with permission.*

depth in this part of the atmosphere, these deeper layers are hotter than those seen looking directly at the granule top. Therefore, towards the limb, more of the hot wall will be visible, increasing the flux. It is therefore possible for certain diameters of flux tubes to be dark at disc centre for a given wavelength, and still bright when the hot walls are revealed towards the limb (Keller et al., 2004).

Further towards the limb, the cool gas above the adjacent granules and in the magnetic flux tube can begin to dominate the radiation that emerges, leading to dark lanes by the faculae (Keller et al., 2004). This is demonstrated in Fig. 1.3 where the dark grey rectangle indicates where the dark lane would be observed. Thus, it is important to model faculae in 3D, so that the effect of the hot wall and surrounding atmosphere can be included correctly and accurate contrasts can be obtained. Overall, the brightness of these features depends on wavelength, magnetic field strength, their diameter and their limb distance (Fligge & Solanki, 2000).

On the Sun, it has been shown that bright faculae, although low in contrast, counteract the suppression of flux by sunspots. In fact, faculae actually cause the Sun to be brighter in the more active parts of the solar cycle, due to their greater number, covering fraction and longer lifetimes (Fligge et al., 1998). This effect is shown by Fig. 1.5 in Sect. 1.4.1. For a review on the magnetic field in the solar atmosphere see Wiegelmann et al. (2014) and references therein.

1.3.2 Radiation from magnetic features

The radiation from magnetic features is often given in terms of a contrast with respect to the quiet star. This contrast is calculated as

$$\text{contrast} = \frac{I_f - I_q}{I_q}, \tag{1.4}$$

where I_f and I_q are the feature and quiet-star intensity, respectively.

Ortiz et al. (2002) and Yeo et al. (2013) measured the contrast as a function of viewing angle and magnetic field (B) of photospheric faculae on the solar disc from the Michelson Doppler interferometer (MDI) on board the Solar and heliospheric observatory (SOHO) and the Helioseismic and magnetic imager (HMI) on board the Solar dynamics observatory (SDO), respectively. Both binned their data according to $\langle B_l \rangle / \mu$, where $\langle B_l \rangle$ is the unsigned longitudinal magnetogram signal. The division by limb distance, μ, is done to account for the foreshortening effects, as the line-of-sight magnetic field goes to zero at the limb even when a substantial field is present. Within $\langle B_l \rangle / \mu$ bins it was found that intensity contrast increased from disc centre towards the limb until a turnover point, where the contrast begins to decrease. Data from Yeo et al. (2013) shows that the contrast at disc centre decreases with increasing $\langle B_l \rangle / \mu$, becoming negative at higher $\langle B_l \rangle / \mu$ values, i.e., larger than 200G. The increase in contrast towards the limb also becomes steeper at high magnetic fields, with very low magnetic fields having almost flat contrast curves with respect to μ. Other measurements of facular contrasts include Frazier (1971); Auffret & Muller (1990); Topka et al. (1992, 1997); Taylor et al. (1998); Kobel et al. (2011) and Kobel et al. (2012). All these measurements are usually restricted to one or a few wavelengths.

Due to the difficulty in measuring facular contrasts with full spectral coverage, models must be employed to account for them in variability studies. Facular contrasts are typically derived from semi-empirical, plane-parallel, 1D atmosphere models such as those developed by Vernazza et al. (1981); Lemaire et al. (1981); Fontenla et al. (1993, 1999); Fontenla et al. (2002) and Fontenla et al. (2006). Examples of a 1D facular and a 1D quiet Sun model are shown in Fig. 1.1 as model P and C (also known as FAL P and C), respectively. For the facular model, an increase in temperature compared to the quiet Sun is introduced in the upper photosphere and the chromosphere to allow the resulting spectrum to be brighter in the visible.

Although wavelengths of faculae are not resolved, studies that have measured contrasts in multiple filters have shown that solar facular contrasts vary with wavelength. The relationship found appears to be an inverse wavelength dependence

(Chapman & McGuire, 1977). This was successfully reproduced by Unruh et al. (1999), via a modelled facular contrast with respect to the quiet Sun, based on a modified 1D facular model, FAL P, by Fontenla et al. (1993).

For 1D model atmospheres an approximation of plane-parallel geometry is used. This means that optical depth is artificially adjusted to account for the longer path length traversed when viewing faculae at the limb. This method captures the overall disc-integrated properties of faculae reasonably well, but is unable to reproduce observed limb-dependent contrasts. For example, facular contrasts produced by Unruh et al. (1999) show that contrast increases towards the limb. However, they do not demonstrate a point of turnover as seen in solar data in Yeo et al. (2013). The steep increase of the modelled contrast towards the limb, instead of a turnover point occurring, is largely an artefact of the plane-parallel geometry approximation (Unruh et al., 1999). Unruh et al. (1999) found that facular contrast colour dependencies also vary with position on the disc. Towards the limb, these colour dependencies become steeper in the blue and show less variation over small wavelength ranges. The damped variation is due to spectral lines showing lower contrasts relative to the continuum at small μ. Foukal et al. (1990) found that faculae in the infrared ($\lambda = 1.6\ \mu m$) are dark compared to the photosphere near the disc centre, but still appear bright at the limb.

Due to their large size compared to faculae, spots can often be resolved into umbral and penumbral regions on the Sun, and thus their contrasts are more easily measured. However, spectral resolution is still low for measurements of these features. Therefore, to achieve the required spectral resolution, contrasts derived from 1D models are often used for spots, often simply using two cooler (compared to the quiet Sun) radiative equilibrium atmospheres, one for umbral and one for penumbral areas (see, e.g., Krivova et al., 2003). In reconstructions of the total solar irradiance (TSI, see Sect. 1.4.1 for definition), these 1D models are found to be sufficient as they reproduce the observed sunspot darkening.

As well as spots and faculae, bright magnetic regions called plages exist high above the Sun's surface. Plages emit UV and EUV from the upper photosphere, chromosphere and transition region (Lean, 1997). Moving from optical to EUV wavelengths, in the area around which a dark spot or faculae are seen in the visible, a plage may be seen as an extended bright region, as they correlate spatially with faculae and are considered to be their chromospheric extensions (Lean, 1987).

In the Sun, chromospheric emissions are known to be well correlated with surface magnetic fields (Noyes et al., 1984). The H and K absorption lines from singly ionised calcium are the strongest spectral features observable from the ground. Figure 1.4

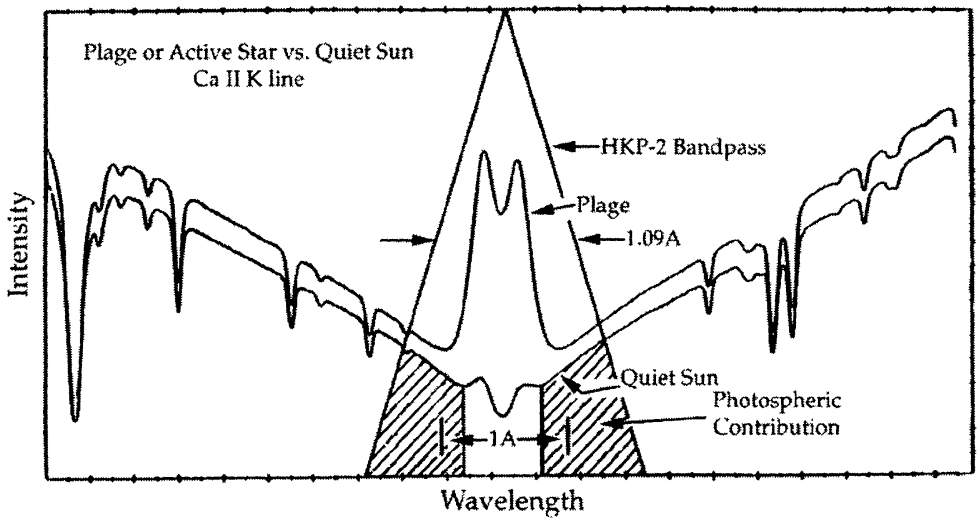


Figure 1.4: The Calcium II K emission core for a quiet Sun and a plage, or active stellar, region. *Figure from "Ca II H and K measurements made at Mount Wilson Observatory, 1966-1983", Duncan et al. (1991). ©AAS. Reproduced with permission.*

shows the Ca II K line for a quiet Sun and a plage, or active stellar, region. When magnetic field is introduced, the emission at these wavelengths is strengthened, leading to emission reversal. Emission reversal in Ca II H & K line cores is formed high in the chromosphere, and reflects the local plasma conditions (Hall, 2008). Chromospheric activity produces a stronger and more easily detectable signal than photometric variability (Wilson, 1978; Lockwood et al., 2007). For example, in the Sun, Ca II line core emission reversal varies by 20 % over a cycle whereas the smoothed total irradiance varies by less than 0.1 %. Plages are the dominant evidence of magnetic activity in data taken in the emission core of the Ca II K line at 3933.7 nm (Lean, 1987). For these reasons, two indices have been derived from measurements of Ca II H & K lines. The instrumental S-index is the ratio of the emission flux in 0.1 nm bands centred on the Ca II H and K cores and 0.2 nm continuum bands bracketing the emission cores (Lockwood et al., 2007). This can be transformed into a dimensionless ratio, R'_{HK}, called the chromospheric activity index (or the Ca II H & K emission index), which is the ratio of chromospheric emission and bolometric luminosity and is a measure of the magnetic activity at a single point in time. The S-index is used for displaying observed time series, and R'_{HK} is used to compare different stars as the spectral type has been factored into the calculation.

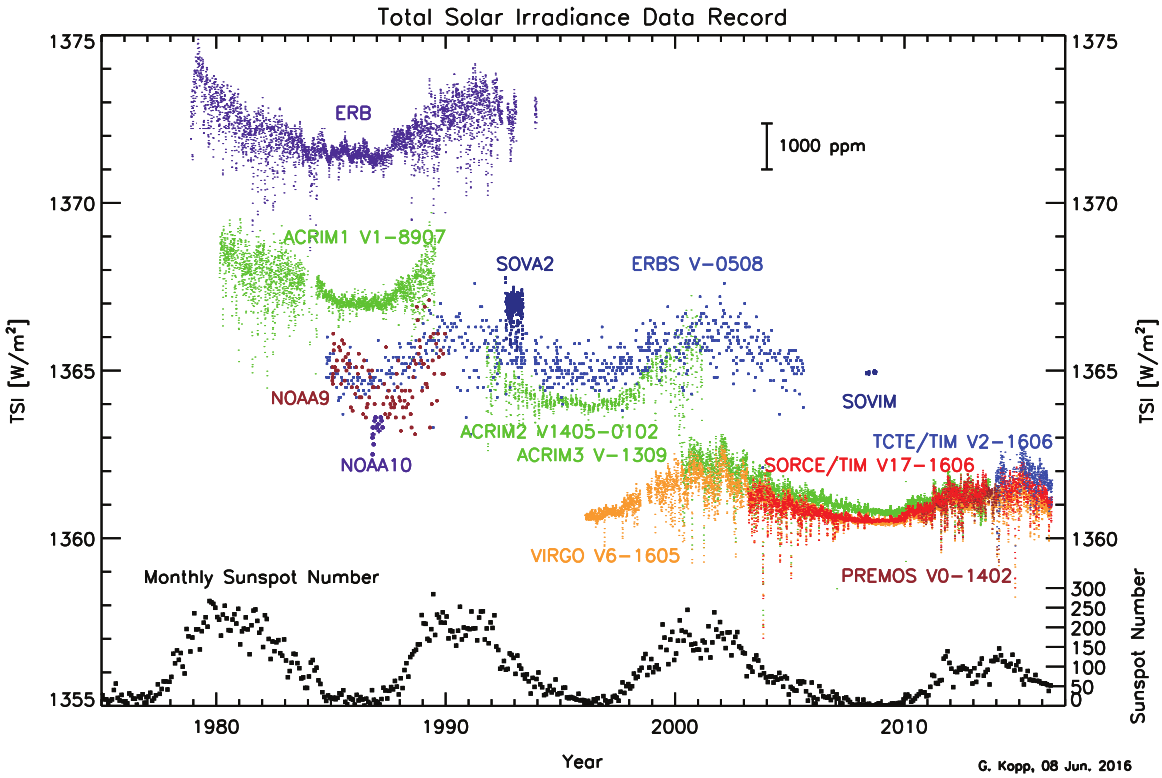


Figure 1.5: Observations of the total solar irradiance since 1978 by various satellites, shown by different coloured points with satellites labelled. The Monthly sunspot number is show with black points. *Figure from "Magnitudes and timescales of total solar irradiance variability", Kopp (2016). Reproduced with permission.*

1.4 Observations of variability

Variability is observed for the Sun and other stars. For stars, the radiant flux is observed. This is the energy passing through a unit area in a unit time at the Earth, and is therefore dependent on the distance of the star from Earth. For the Sun, the quantity measured is irradiance. Irradiance is the power per unit area observed at 1 AU (i.e., at the Earth). For the Sun, we are only able to observe the photons emitted from the solar hemisphere in the direction of the Earth. The following section describes observations of variability for both the Sun and other stars, and discusses ways used to link this variability data to physical phenomena occurring on the stellar or solar surface.

1.4.1 Solar variability

Solar variability can be measured both in terms of total irradiance and spectral irradiance. Total solar irradiance is the spectrally-integrated power from the entire

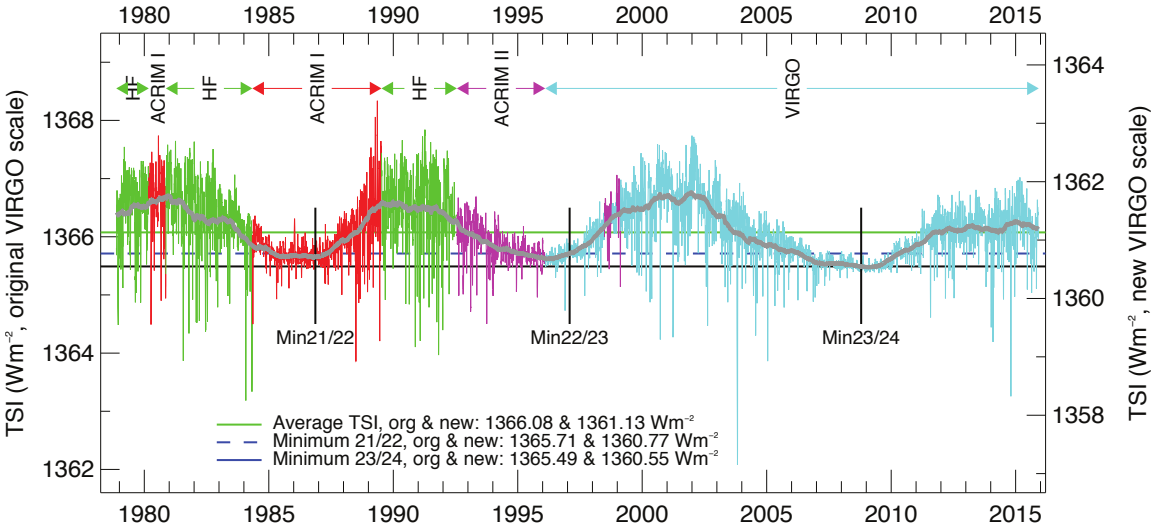


Figure 1.6: The Physikalisch-Meteorologisches Observatorium Davos (PMOD) composite of the total solar irradiance observed by various satellites since 1978. *Figure from "Magnitudes and timescales of total solar irradiance variability", Kopp (2016). Reproduced with permission.*

disc of the Sun measured at the Earth (above the atmosphere) per unit area. Solar spectral irradiance is this quantity at a given wavelength. Due to our excellent view of the Sun and ability to measure these parameters, the Sun is the star that we have the greatest measurement record of variability. Figure 1.5 shows the total solar irradiance (TSI) measured with direct observations of the Sun almost continually since 1978 by various satellites, signified by different colored points. The monthly sunspot number is also shown with black dots. On solar cycle timescales, peaks in the monthly sunspot number can be seen to coincide with times of increased TSI, showing that bright faculae are dominant on these timescales. These TSI measurements can be combined into a composite time series, an example of which is shown in Figure 1.6. These can be used to monitor the 11 year solar cycle and other variability (Fröhlich, 2006). The TSI has been observed to vary on many timescales (Willson et al., 1981; Fröhlich & Lean, 2004; Fröhlich, 2009; Kopp, 2016), as seen in Figs. 1.5 and 1.6. Peak-to-peak variations over the solar cycle timescale are found at the 0.1 % level, with 27 -day solar rotational variation found at the 0.2 % level. This variation in total irradiance is the summation of variation over many wavelengths, each with different levels of variability.

Although measurements of SSI are much less continuous than TSI, over a solar cycle variations have been measured in different spectral regions. For example, several percent variation is found around 200-250 nm, with even higher variation at shorter wavelengths, leading to up to 60 % of the solar variability being accounted

for below 400 nm (Floyd et al., 2003; Krivova et al., 2006). See Ermolli et al. (2013) for an overview of SSI observing satellites.

Other observed properties, such as the group sunspot number (SSN), are used as proxies for solar activity to extend the TSI measurement record back to 1610. This can be useful to extract any long term trends in the solar irradiance (Hoyt & Schatten, 1998; Dasi-Espuig et al., 2016).

1.4.2 Mount Wilson sample

(Wilson, 1978) observed 91 main-sequence stars for a period of 9-11 years at the Mount Wilson Observatory using the cores of the Ca II H & K lines as a measure of chromospheric activity. The stars were of spectral types F5V to M2V. Many of the stars observed showed fluctuations in seasonal observations, indicating changes on short timescales. About 20 stars were either found to have completed a cycle of H-K flux variation or were expected to be found to be cyclic if observations were continued. The observed cycles appeared to be analogous to those of the Sun. This was the discovery of cyclic magnetic activity variations in stars from early-F to early-M main-sequence stars.

This "HK program" was continued at the Mount Wilson Observatory with the number of stars and the frequency of observations increased (see Baliunas et al., 1995, 1998). Figure 1.7, taken from Baliunas et al. (1998), shows nightly measurements of the S-index (small dots), detailed in Section 1.3.2, for three stars, each with different categories of variability. 30-day averages of the S-index are also shown (large dots). HD 206860 (top) shows variability with no clear cyclic pattern, HD 4628 (middle) shows cyclic variability on timescales similar to those of the Sun, and HD 143761 (bottom) shows no significant variability.

In parallel to the chromospheric observations, photospheric (b & y band) variability was monitored at the Lowell Observatory (Lockwood et al., 1997) and the Fairborn Observatory (Henry, 1999). Lockwood et al. (2007) compared this chromospheric (Ca II) and photospheric (b & y band) variability data over a period of 13-20 years to investigate patterns of variation in stars. The stars observed were mainly of the main sequence of types F5 to K7, with colour indices (B-V) between 0.42 and 1.4. They obtained the chromospheric activity index, $\log(R'_{HK})$, and the S-index from Mount Wilson observatory data. Both indices are detailed in Section 1.3.2.

It was seen that stars with larger photometric variability also show larger chromospheric activity. Young stars' photometric behaviour is apparently spot dominated (negative correlation with chromospheric variations) and old stars' photo-

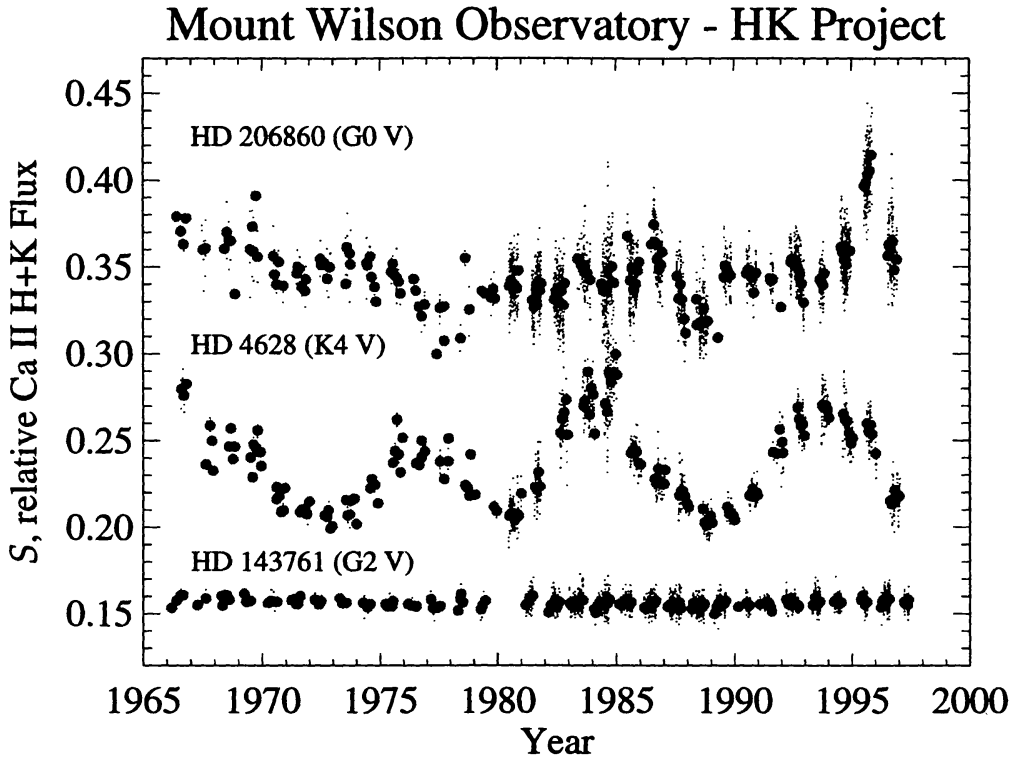


Figure 1.7: The Calcium II H & K S-index for three example stars from the Mount Wilson sample. The small dots show nightly measurements, the large dots show 30-day averages. Taken from Baliunas et al. (1998).

metric behaviour is faculae dominated (positive correlations with chromospheric activity), as seen with the Sun.

Additionally, they found that the relationship between chromospheric and photospheric variability depends on the overall chromospheric activity, finding that stars with low activity levels ($\log(R'_{HK}) < -4.7$) tend to have faculae dominated variation and stars with high activity level ($\log(R'_{HK}) > -4.7$) tend to have spot dominated variation. However, stars with lower $\log(R'_{HK})$ than the Sun appear to be scattered considerably. Lockwood et al. (2007) attribute this mainly to the poorly known level of photometric activity rather than an astrophysically meaningful effect (see also Shapiro et al., 2014).

Radick et al. (2018) compare stellar chromospheric Ca II H & K and photometric b, y variability data for an extended period of time (1992-2016), and confirm the results found in Lockwood et al. (2007). Additionally, these data are compared with equivalent solar observations. In comparing the Sun to other "Sun-like" stars with its stellar age and spectral class, they conclude that the Sun has a comparatively smooth and regular activity cycle, and its photometric brightness variation relative to its chromospheric activity level and variation is unusually low. This observation could indicate that the facular and spot contributions are unusually well balanced on the Sun (Radick et al., 2018).

1.4.3 *Kepler*

NASA's *Kepler* mission was launched in 2009 and aims to determine the frequency of Earth-sized and larger planets in the habitable zones of over 150 000 Sun-like stars. In order to do this it uses the transit method of planet detection, which requires high precision and rapid cadence photometry (see Sect. 1.4.4 for more detail on planetary detection methods). Due to this almost continuous monitoring, *Kepler* also provides an opportunity to learn about the stars themselves and stellar variability can be monitored to greater precision than ever before (Walkowicz & Basri, 2013). Stellar magnetic activity is primarily seen through starspot modulation. Therefore, the photometric curves must be analysed for any periodic behaviour which could be on the scale of the stellar rotation (Basri et al., 2011). Figure 1.8 shows a selection of *Kepler* observations for variable main-sequence G-type stars presented in Basri et al. (2011). The top panels of the figure show periodic variability and the bottom panels show non-periodic variability.

Basri et al. (2010) studied light curves covering approximately 33.5 days from *Kepler* Quarter 1 observations in order to compare variability due to magnetic ac-

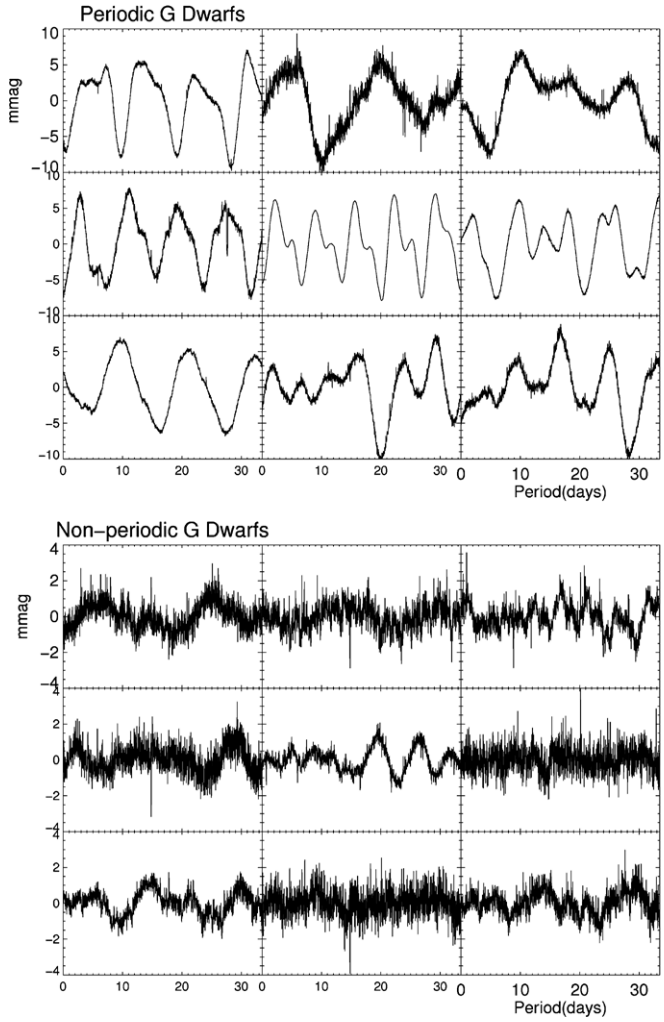


Figure 1.8: First quarter *Kepler* observations of variable main-sequence G-type stars. Periodic variability is shown in the top nine panels, non-periodic variability is shown in the bottom nine panels. Note the different y-scales. *Figure from "Photometric Variability in Kepler Target Stars. II. An Overview of Amplitude, Periodicity, and Rotation in First Quarter Data", Basri et al. (2011). ©AAS. Reproduced with permission.*

tivity of main-sequence stars in the solar-neighbourhood with that of our own Sun. To quantify solar variability, they used the photometric variability range, or half-amplitude, that has also been employed in later *Kepler* studies. It is calculated by converting lightcurves to differential photometry by dividing out the median flux and subtracting unity and taking the absolute deviations from zero. The study found that a large number of stars (nearly half of the sample) are more active than the Sun, as expected. When separated by spectral type, the fractions of stars more variable than the Sun (the active fractions) found are lower for late-F to early-G stars (about a third), and increase with decreasing effective temperature (about half for late-G and K and almost 90 % for cooler stars).

McQuillan et al. (2012) performed a similar investigation with the *Kepler* Quarter 1 data and found a similar trend of increasing active fraction with decreasing effective temperature. However, when combining all of the spectral types, they found that 60 % of the stars were more variable that the Sun. They note that the active fraction is a sensitive function of the active solar value taken, for which Basri et al. (2010) and McQuillan et al. (2012) use different levels. Basri et al. (2013) revisited this data, and found agreement with their original results from Basri et al. (2010). They attribute the differences between McQuillan et al. (2012) and Basri et al. (2013) to how they choose the active level that characterises the Sun and the difference in definition of G dwarfs. They also find that the results would be closer to agreement if both studies used the same magnitude limit for inclusion in the sample of stars.

Walkowicz & Basri (2013) used the photometric variability range detailed by Basri et al. (2010) as a measure of variability in *Kepler* Quarter 9 data of approximately 950 *Kepler* Object of Interest (KOI) host stars and compared with the Rossby number. The Rossby number is the ratio of the stellar rotation period to the time-scale of convective overturn, and is a measure of whether the fluid dynamics of the system are dominated by rotation. The spread in the solar variability range values shows that an individual star's variability range can be dependent on the surface distribution of features at the time of observation and may change over time. For example, a single feature being modulated by rotation will have higher variability range than multiple evenly distributed features; even though the star is quite magnetically active, it will appear to have low photometric variability. This means that optical photometric variability is an ambiguous measure of overall activity. However, measurements of chromospheric activity (e.g. Ca II H & K emission) could break this degeneracy and allow information of the distribution of magnetic features to be inferred (Walkowicz & Basri, 2013).

1.4.4 Planetary observations

The variability of stars is not only important for our understanding of stellar physics, but it also affects our ability to understand the planets that orbit them. By studying planets orbiting stars other than our Sun, we are able to learn more about the mechanisms for the origins and evolution of our own solar system through observing other planetary systems at various stages. Due to their relative dimness when compared to their host star, planets are very difficult to directly image and remove the contamination from the host star's emission (Examples of the considerations needed can be found in Agol, 2007). Although methods for direct imaging are being improved and it is now possible for certain star-planet pairs, it is still difficult to get a significant sample of planets. This means that other methods of planet detection and characterisation are primarily used.

Examples of other planetary detection and characterisation methods include radial velocity (RV) and transit measurements. For the radial velocity method, the tiny fluctuations in a star's line of sight velocity due to the gravitational pull of the planet are measured via Doppler shifts in its spectrum. This allows the mass and orbital parameters of the planet to be obtained. The more massive a planet is, the larger, and more easily detectable, these stellar movements will be. For example, a Jupiter-sized planet at 1 AU will invoke a radial velocity semi-amplitude of approximately 28 m s^{-1} for its host star (Haywood, 2015), while an Earth-sized planet at the same distance, a RV of 0.09 m s^{-1} (Cegla et al., 2018).

The transit method, as used for *Kepler*, uses the fractional decrease in radiation received from the host star due to the planet passing in between the observer and its host star to infer its existence and various planetary and orbital parameters, including size. A larger planet produces a larger fractional decrease in radiation, making it easier to detect. Transits can also be used to obtain spectral information about the planetary atmosphere by extracting the transit depth at multiple wavelengths. Information about the planet is obtained not only from the depth of the transit, but the shape of the transit curve, allowing for extraction of parameters such as the impact parameter. The shape of the transit curve can be fitted using known, or simulated, information about the stellar radiation. Incorrectly parameterising the stellar radiation, for example the limb darkening, could lead to errors in the obtained planetary characteristics, such as the radius or the impact parameter (and therefore the inclination and absolute mass). For a full review on planetary detection methods see, e.g., Wright & Gaudi (2013).

When a planet transits the star during a radial velocity observation it blocks the line of sight radiation from the stellar photosphere, therefore the shape of the

disc-integrated RV line will be affected. This departure from the standard orbital RV effect, particularly that caused by the rotational velocities of the star, is called the Rossiter-Mclaughlin effect. This effect allows the alignment between the planets orbital plane and the stellar spin-axis to be obtained (Winn et al., 2010; Triaud, 2011).

Variability of the host star can affect the results obtained from these planetary detection and characterisation methods. For the radial velocity (RV) method, convection on the surface of the star causes an overall blueshift of radiation (Dravins et al., 1981). Magnetic regions can suppress convection, suppressing also this blueshift. Rotation of the star produces Doppler broadening of spectral lines. Dark magnetic regions dim the component of the rotational Doppler shift at its position. Together these effects will cause the shape of the disc-integrated RV line to be different from that of a quiet star, and therefore, if not included, may affect the parameters obtained for the planet (Lagrange et al., 2010; Meunier et al., 2010; Cegla et al., 2013, 2018).

The transit method obtains information about the planet based on the fractional starlight blocked by the planet. If an unocculted spot (facular region) is present on the surface, it will lower (raise) the expected photospheric flux and make the normalised transit deeper (shallower) than if the surface was homogeneous. Therefore, the presence of magnetic features on the stellar surface, in itself, will not change the shape of the transit curve, but can change the transit depth. The planet-star radius ratio will thus be overestimated in the case of spot dominated stars, or underestimated in the case of faculae dominated stars. However, if these features are occulted by the planet while in transit, they will change the shape of the transit light curve (Czesla et al., 2009). Faculae will produce a dip in the curve, while spots produce a bump. Figure 1.9, taken from Oshagh et al. (2014), shows the bottom of a resulting light curve when a plage (or faculae), with a filling factor of 0.25 %, is occulted during a simulated transit with red data points. If it is assumed that there is no activity feature present, it can lead to bad curve fits, as demonstrated by the green line in Fig. 1.9. This, in turn, leads to errors in the estimation of the planet-star radius ratio and any further parameters calculated (Oshagh et al., 2014).

While spots are accepted as having a significant effect on planetary transit curves, and are included in many recent transit calculations (Pont et al., 2013; Nascimbeni et al., 2013; Sing et al., 2011), the effects of faculae are still often ignored. Oshagh et al. (2014) used current estimates and measurements of solar facular and sunspot temperatures, and modelled both to emit as blackbodies, to simulate transit lightcurves, as in Fig. 1.9. These were used to investigate the impacts of stellar active

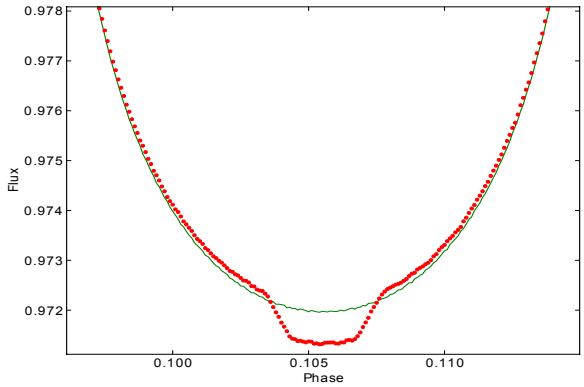


Figure 1.9: A zoomed view of the bottom of a simulated transit curve for a Jupiter sized planet occulting a facular region (filling factor 0.25 %) on an M dwarf (red dots). The green line shows a fit to the simulated transit curve ignoring the presence of magnetic features. Credit: Oshagh et al., A&A, 568, A99, 6pp., 2014, reproduced with permission © ESO.

regions being occulted by a planet on the transmission spectra of planets around a G dwarf (5780 K) and an M dwarf (3000 K). The spots were assumed to be 1500 K cooler than the photosphere and the faculae were 100 K hotter than the star for both spectral types (as implied by 1D facular models – though see caveats below).

Ignoring the presence of the magnetic features, the generated light curves were fitted and the relative errors in planetary radius, $\Delta R/R_p$, were obtained for various models. Fig. 1.10, taken from Oshagh et al. (2014), shows the results for a G dwarf. These models use different filling factors and planetary radii, with models 1-4 being with a spot and model 5-10 being with a facular region. The figure shows that errors become more significant towards the blue end of the spectrum, and that the radius can be miscalculated by up to 3 % in the case of faculae on G dwarfs. Similar results were found for the M dwarf, but with radius errors of up to 10 %. By measuring the depth of transits at various wavelengths, a transit spectrum for the planetary atmosphere can be obtained. This allows for characterisation of the atmosphere. Excesses in planetary radius in the blue, when found in real planetary transit data, will often be interpreted as Rayleigh scattering in the planet's atmosphere. Oshagh et al. (2014) show that it is, in principle, possible to reproduce this excess by assuming the planet is overlapping a stellar facular region.

Although facular contrasts on the Sun are known to increase towards the blue wavelengths (Chapman & McGuire, 1977), Solanki & Unruh (1998) showed that they are not effectively modelled by a simple temperature difference alone. Additionally, 3D models show that facular contrast spectra and limb darkening do not vary simply with spectral type (Beeck et al., 2015a). Therefore, to include their

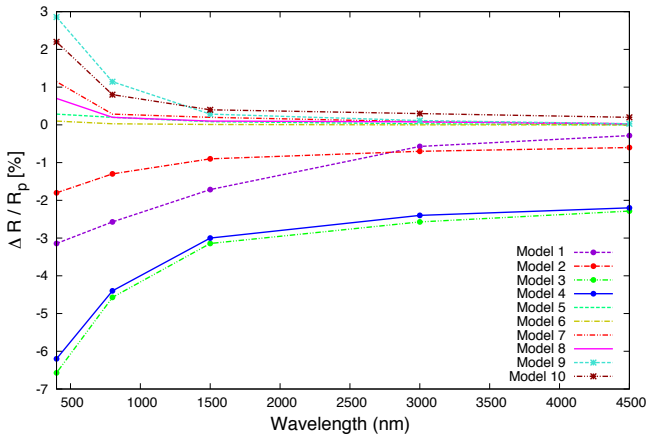


Figure 1.10: Predicted fractional errors of planetary radius obtained when ignoring the presence of occulted magnetic features in modelled transit curves for G dwarfs in multiple wavelengths. Models 1 to 4 are for spot occultations, models 5 to 10 are for occultations of facular regions with various filling factors and planet sizes. Credit: Oshagh et al., A&A, 568, A99, 6pp., 2014, reproduced with permission © ESO.

influence across the stellar disc correctly and, thus, improve results from planetary transit and radial velocity observations, 3D models must be employed for accurate stellar limb darkening and facular contrasts.

As a consequence of the measured planetary transit curve being affected by occulted dark or bright areas on the surface of stars (i.e., spots or facular regions), one can infer the positions, sizes and contrasts of these regions along a transit chord (e.g., Rabus et al., 2009; Kirk et al., 2016; Morris et al., 2017; Espinoza et al., 2018). This effect can also be taken advantage of in radial velocity observations (see, e.g., Collier Cameron et al., 2010; Cegla et al., 2016). This can allow mapping of the stellar surface and validation of models of active regions.

1.4.5 Other observational methods

Other methods of stellar observation allow information to be extracted about the magnetic activity of stars. For example, Doppler imaging utilises the rotational broadening of a stellar spectral line to track the movement of a spot across the disc of the star. When a spot of sufficient size is present, a dip in the broadened spectral line will appear where the light is dimmed. This dip will move from blue to red wavelengths as the spot crosses the stellar disc (Vogt & Penrod, 1983).

When a high resolution spectrum of a star is obtained, splitting of magnetically sensitive lines may be observed. This is due to the Zeeman splitting of atomic energy levels in the presence of a magnetic field. The extent of the splitting in the spectral

line depends on the strength of the magnetic field and the sensitivity of the line to magnetic field. For detection of a split, a large magnetic field of greater than 1-2kG is often required, as the splitting of lines below this strength tends to be smaller than the width of the spectral line (Robinson, 1980). However, at lower magnetic fields, a broadening of the line can be observed due to the overlapped Zeeman-split lines (see, e.g., Reiners & Basri, 2006, 2010). A Zeeman split spectral line will also show polarisation. Measuring this polarisation with Zeeman spectropolarimetry gives information on the orientation of the magnetic field.

The techniques of Zeeman Spectropolarimetry and Doppler imaging can be combined to map the topologies of a stellar magnetic field. The combined technique is called Zeeman-Doppler imaging (ZDI) (Semel, 1989). For reviews of these magnetic field detecting and mapping methods see Donati & Landstreet (2009) and Kochukhov (2016).

1.5 Understanding the observations

Studies such as the Mount Wilson follow-up (Lockwood et al., 2007), *Kepler* (Walkowicz & Basri, 2013), and solar studies (Willson et al., 1981), show that variability on timescales of days and longer result from interplay of spots and faculae. For the Sun, TSI and SSI variability on timescales of longer than a day can be reconstructed assuming the surface consists of only quiet Sun, spots (often split into penumbra and umbra) and faculae. An example of such a reconstruction is the semi-empirical model Spectral and Total Irradiance Reconstruction for the Satellite Era (SATIRE-S – Fligge & Solanki, 2000; Krivova et al., 2003; Yeo et al., 2014). In this method, the radiation from these features is summed according to observed full-disc magnetograms of the solar surface, separating the solar disc into the 3 or 4 types of pixel. For a review on solar surface magnetism and irradiance see Domingo et al. (2009). As faculae are often unresolved and measurements are generally restricted to one or a few wavelengths (as seen in Sect. 1.3.2), 1D atmospheric models are currently used to obtain the spectral contrasts for these features.

In addition to the issues of using plane-parallel geometry for the derivation of facular contrasts discussed in Sect. 1.3.2, 1D models do not provide a direct link to the magnetic field strength on which the facular brightness depends. Therefore, the SATIRE model (Yeo et al., 2014), for example, scales the contrast of faculae to the observed magnetic field between the noise threshold and the saturation limit, above which the brightness of faculae saturates and does not increase further. The saturation limit is a free parameter whose value is chosen by fitting the reconstructed

TSI to measured TSI values. By modelling facular regions in 3D, a direct link to the magnetic flux in the facular region can be established and potentially remove the need for a free parameter in solar variability models.

While the variability of (typically 'white-light') flux from other stars has been measured, and single wavelengths monitored, spectrally resolved information for stars is lacking. This situation may, however, be improved by the increase in transit spectroscopy measurements.

As we are unable to resolve the discs of distant stars at the present time, we cannot yet observe and measure each of the causes of the stellar variability directly, particularly those that are on small scales. In order to gain a greater understanding of the mechanisms for this variability and how they vary across spectral types, we must produce models of stellar atmospheres, where features and their properties are allowed to evolve. These models of different features can then be combined to produce expected observations. Where a model's output is close to observation, it may tell us something about the mechanisms for variability on those stars. This could, in turn, inform interpretation of planetary transit spectroscopy when removing the stellar light. This section outlines some of the available 3D magneto-convection codes and common spectral synthesis methods.

There are a few existing Magneto-convection modelling codes available. Three such models, namely CO^{5}BOLD (Freytag et al., 2002), MURaM (Vögler et al., 2005), and Stagger (Galsgaard & Nordlund, 1996) are described and their results compared, considering solar parameters, by Beeck et al. (2012).

All three codes compared in this paper consider a partially ionised medium split into layers. They use the coupled time-dependent equations of compressible radiative (magneto)hydrodynamics and radiative transfer in three-dimensions assuming local thermodynamic equilibrium (LTE) with a Planckian source function. For details of the equations used in the MURaM code, see Vögler et al. (2005). Each code treats a box in the stellar atmosphere with height containing the photosphere and the uppermost few Mm of the convection zone and horizontal extent (6-9 Mm) to contain about 15-40 granules. The horizontal boundaries are forced to be periodic, and the lower boundary allows free in and outflow of fluid (Beeck et al., 2012). The upper boundaries are treated differently in this study. For example, MURaM uses a closed top boundary (zero vertical velocity), while CO^{5}BOLD uses an open top boundary that allows transmission of waves.

Although various numerical methods and different grid sizes and resolutions were used to produce each of the models, it was found that their overall agreement in both mean (optical and geometrical) depth profiles of the basic quantities (e.g.

temperature, gas pressure and velocities) and spatial fluctuations of these quantities was good and suggests reliability in these types of tools for studying stellar atmospheres. There were slight differences in some quantities, that were probably caused by the differences in spatial resolution and in the opacity binning procedures. For example, the relative temperature difference between CO^{5}BOLD and MURAM is up to 2 % at some geometrical depths (Beeck et al., 2012). MURaM was selected to produce the simulations for this study. Further information on the MURaM simulations used for this work is detailed in Section 2.1.

To produce images of radiation emitted from these simulations at different wavelengths, synthetic spectra must be obtained for each pixel. For disc centre calculations each vertical line of depths can be considered as a 1D model atmosphere and a radiative transfer model used to obtain a spectrum. This approach is commonly referred to as 1.5D, as radiation passing from one pixel into neighbouring pixels is ignored. To obtain synthetic spectra for various limb angles, cuts can be taken diagonally through the box to produce new sets of 1D model atmospheres. Details of our viewing angle calculations are in Section 2.2

Multiple options are also available when considering radiative transfer codes. Calculations can be done under the assumption of local thermodynamic equilibrium (LTE), or fully treated using non-LTE (nLTE) methods. LTE methods are simpler calculations and thus can be performed faster. However, the LTE assumption begins to break down and yield inaccurate intensities in the UV. For these wavelengths, nLTE codes may be chosen to achieve more accurate results, but will take a significantly longer time to calculate.

As it would be computationally demanding to calculate the spectral energy distribution fully for a large range in wavelength, the treatment of line opacity must be simplified in radiative transfer codes. This can be done by opacity distribution functions (ODF) or opacity sampling (OS). The ODF method in ATLAS9 uses pretabulated line opacities for given abundances and microturbulent velocities. This means that single models will take only a short time to be calculated. ATLAS12 uses the OS method, which calculates each model from the input abundances and microturbulent velocities, this takes much longer than the ODF method (Castelli, 2005). For this reason, ATLAS9 is used for this study to calculate spectra as continuum intensities from UV to near infrared wavelengths are of interest, therefore a low resolution is sufficient. More details on the use of ATLAS9 are given in Section 2.3.

Afram et al. (2011) used ATLAS9 to perform spectral synthesis calculations at multiple limb angles on solar type MURaM simulation snapshots for field-free, $\langle B_z \rangle = 50$ G and $\langle B_z \rangle = 200$ G. They compared calculations of small-scale mag-

netic element contrasts with Hinode satellite observations of the Sun and found good agreement between them. These promising results have led to MURaM hydrodynamic and magnetic simulations being performed for multiple effective temperatures, $T_{\rm eff}$, and strengths of gravity, log g, in order to represent different main-sequence spectral types with different magnetic activities (Beeck et al., 2013). These simulations allow for a large-scale study of contrasts of small-scale magnetic features across stellar spectral type and of how they affect the variability of our Sun and other stars. This thesis is the presentation of the spectra calculated from this array of MURaM simulations, along with spectra from additional simulations for a higher resolution of magnetic field strength study of the Sun. Results obtained from this large variable space are also presented, as a sample of the wealth of information that can be extracted from the spectra produced.

This thesis contains six further chapters. The properties of the magneto-convection simulations used for this study are summarised in Chapter 2. This chapter also details the methods used to obtain the synthetic spectra that are the focus of this thesis. These spectra are presented in Chapters 3 to 6. Comparisons of limb darkening, for multiple spectral types, calculated using 1D and 3D modelling are made in Chapter 3. Limb darkening coefficients are provided here for commonly used limb darkening functions for *Kepler*, CoRoT, TESS and the four *Spitzer* IRAC bands. Chapter 4 is based on the work published in Norris et al. (2017) focusing on spectra produced for a simulation of spectral type G2V with $\langle B_z \rangle = 100$ G intervals. Chapter 5 discusses how the magnetic features and resultant limb-dependent spectra vary across spectral type. For the final research chapter, Chapter 6, the relationship between the magnetic field in small-scale features and their intensity is explored and the main results obtained by use of these spectra in Yeo et al. (2017) are described. Finally, the main outcomes of the work of this thesis are summarised in Chapter 7.

Chapter 2

Simulating observations

For accurate centre-to-limb variations in simulated observations, the 3D nature of the stellar surface, and the magnetic features that form there, must be captured. To achieve this, 3D simulations are employed. These simulations are then used to explore the radiation observed at different viewing angles. This chapter describes the codes and simulations used within this study. In Section 2.1 the set of simulations used are detailed. The algorithm for producing atmospheres for calculations of different viewing angles are described in Section 2.2. Finally, Section 2.3 describes the spectral synthesis code and details the parameters used to calculate observed radiation.

2.1 MURaM simulations and snapshots

Stellar atmospheres were simulated using the magnetohydrodynamics code, MURaM (Vögler et al., 2005). The simulations produce grids of temperature, pressure, density, magnetic field and velocity for a box in a stellar atmosphere with a depth containing the photosphere and the upper layers of the convection zone. The box has periodic boundaries in the horizontal direction and is closed at the top. The bottom boundary is open to flows of a constant entropy density. This allows for control of the effective temperature of the simulation boxes (Beeck, 2014). The simulations use the OPAL equation-of-state (Rogers, 1994; Rogers et al., 1996). Opacity is accounted for using four wavelength bins derived from the ATLAS9 opacity distribution functions (ODFs – Kurucz, 1993). More detail can be found in Beeck (2014).

Simulations were performed for five combinations of effective temperature and gravitational acceleration to represent stellar spectral types between F3V and M2V. The metallicity of the simulations was adopted from the ATLAS9 ODFs that corre-

Table 2.1: Spectral types and simulation parameters. Effective temperatures, $T_{\rm eff}$, are calculated from the limb-dependent synthetic spectra calculated with ATLAS9 in this study. The gravitational field strength is given in cgs units. Resolution is given in kilometers. # is "number of".

Spectral type [tranche]	# snapshots	field-free $T_{\rm eff}$ [K]	$\log g$ [cgs]	# z points	Resolution [km] z	x/y
F3V	6	6885.5 ± 6.7	4.301	500	11.25	58.5938
G2V [B]	10	5814.2 ± 5.9	4.438	300	10.03	17.5781
G2V [A]	6	5792.4 ± 5.4	4.438	300	10.03	17.5781
K0V	6	4893.6 ± 5.7	4.6083	300	6.0	11.7188
M0V	6	3848.9 ± 0.3	4.8271	225	4.0	4.8828
M2V	6	3601.6 ± 1.1	4.8271	250	3.2	3.0469

spond to solar values (Castelli & Kurucz, 2001). Each spectral type has a different horizontal and vertical resolution so that the simulation box covers an appropriate sized region to incorporate a similar number of granules (approximately 25 for field-free simulations). All simulations are 512 by 512 pixels in the horizontal direction with a different number of depth pixels. Table 2.1 shows the parameters used for each spectral type. The table includes the magnetic field-free effective temperature (calculated from the limb dependent spectral intensities calculated with ATLAS9 for this thesis); the logarithmic gravitational acceleration input to the MURaM simulations; the number of depth (z) points; and the vertical (z) and horizontal (x/y) resolution.

Magnetic field-free (henceforth hydrodynamic or field-free) simulations are run for several hours, a time comparable to the Kelvin-Helmholtz times of the simulation boxes. After this time, we select six snapshots at constant time intervals for a given spectral type. On average this time interval is 6 minutes for field-free simulations. This time interval is chosen to allow the granulation patterns to evolve sufficiently between snapshots to make them independent. However, on the timescales of these snapshots, granules tend to re-appear in similar locations, thus, the granule positions will be correlated across the snapshots (Cegla et al., 2018). The average total radiative flux of these six snapshots is close to the average over the whole relaxed portion of the simulation. Translated into effective temperature, the standard deviation for the snapshots is given in Table 2.1.

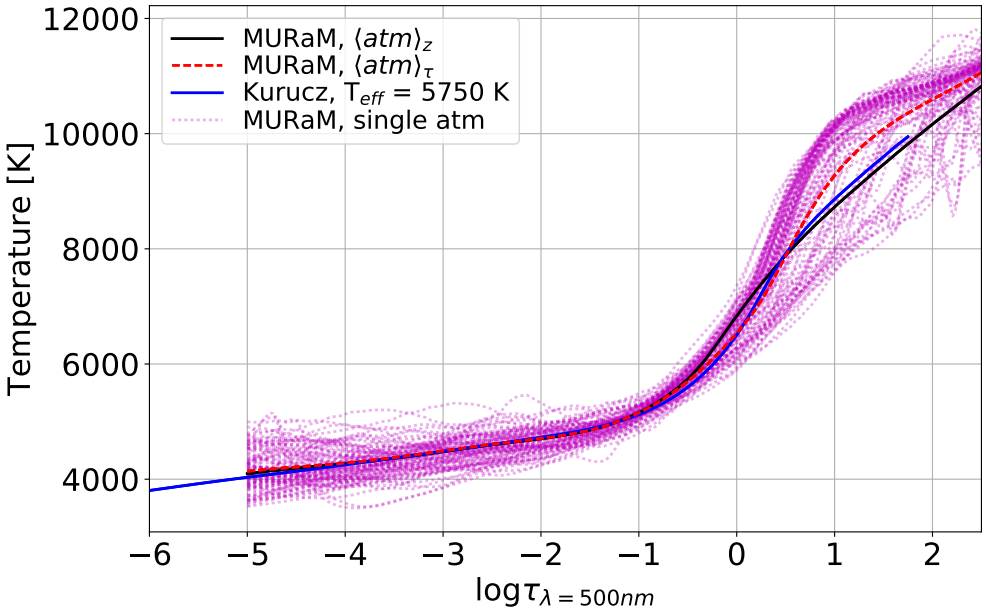
Homogeneous vertical magnetic fields of 20 G, 100 G and 500 G are injected into one of the relaxed hydrodynamic snapshots to represent a range of activity levels. On the Sun, areas of this size with an average magnetic field of 500 G are not so common. Here, they are mainly included to allow for comparison with stars

of different activity levels. For each initial average vertical magnetic field, $\langle B_z \rangle$, the simulations are allowed to relax. To determine whether simulations are relaxed, the effective temperature, $T_{\rm eff}$, and the horizontally averaged magnetic energy density of the simulation are confirmed to be quasi-stationary. See Beeck (2014) for more information on this relaxation criteria. Snapshots are taken at intervals that allow for sufficient evolution of the granulation pattern. As in the case of the field-free simulations, the average total radiative flux for a given magnetisation is close to the average over the whole relaxed portion of the simulation. We limit the number of snapshots to six for each of our chosen average magnetic fields as the number of surface elements is large and synthesising spectra is time costly.

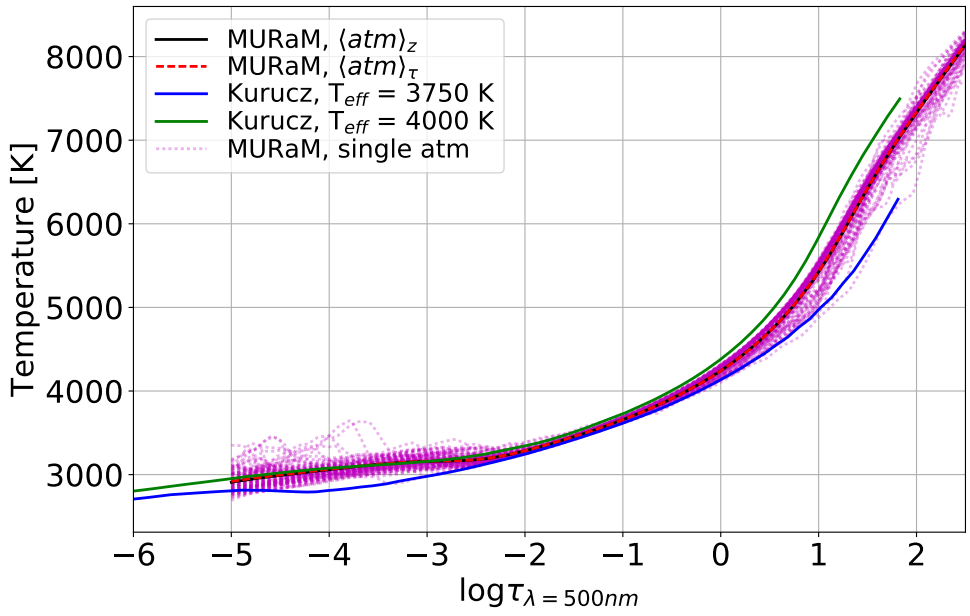
A second simulation for G2V stars was performed at a lower height in the atmosphere (henceforth tranche B G2V, while the previously described six snapshot set will be tranche A G2V). This run includes hydrodynamic snapshots and $\langle B_z \rangle$ = 100 G, 200 G, 300 G, 400 G and 500 G snapshots, allowing for a more in depth study with regards to different magnetic field strengths. Ten snapshots were taken from each magnetic configuration of this simulation. This data set has been published in Norris et al. (2017) and is discussed in Chapter 4. It also forms the basis for our reconstruction of solar TSI (Yeo et al., 2017).

As an example of simulation and snapshot timings, field-free simulations are run for 5 hours of solar time and allowed to relax for the first 3 hours for the tranche B G2V simulation. After this relaxation time, the ten snapshots are selected at approximately 10 minute intervals. The standard deviation of the effective temperature for the ten snapshots is 6 K and very similar to the value of 7 K for the whole duration of the relaxed phase (Beeck et al., 2013). For each injected homogeneous average vertical magnetic field, $\langle B_z \rangle$, the simulations are allowed to relax for two hours of simulated solar time. Snapshots are taken at approximately 7-minute intervals.

As an illustration of the atmospheric structure in the simulations, Figure 2.1 shows the temperature as a function of optical depth at a wavelength of 500 nm, τ_{500}, for example disc-centre, field-free atmospheres for a G2V type star (top) and an M0V star (bottom). The dotted magenta lines show a selection of 90 MURaM snapshot pixels (15 from each of the six snapshots), with cut-offs at $\log(\tau_{500}) = -5$ and 2.5. Mean MURaM atmospheres taken over all hydrodynamic snapshot pixels are shown averaged over constant geometrical depth (z) surfaces, $\langle \mathrm{atm} \rangle_z$ (black line), and averaged over constant $\log(\tau_{500})$ surfaces, $\langle \mathrm{atm} \rangle_\tau$ (red dashed line). In addition to these, 1D Kurucz atmospheres are plotted in green and blue. For the G2V star, a Kurucz atmosphere with $\log\ g = 4.5$ and $T_{\rm eff} = 5750$ K (close to the G2V MURaM



(a) G2V



(b) M0V

Figure 2.1: Temperature vs. logarithmic optical depth at 500 nm for two spectral types: G2V (top) and M0V (bottom). Single pixels of MURaM snapshots are shown by dotted magenta lines. The mean of all pixels (averaged over optical depth) is shown by the red dashed line. The profile when averaging over the geometrical depth is given by the black solid line. The blue and green solid lines shows Kurucz 1D atmospheres. The blue line for G2V is an atmosphere at 5750 K with log $g = 4.5$. Both Kurucz atmospheres in the M0V graph have log $g = 5.0$. Green is for an effective temperature of 4000 K and blue for 3750 K (Kurucz, 1990).

simulation values) is plotted. For the M0V star, Kurucz atmospheres with log $g = 5.0$ and effective temperatures of 3750 K (blue) and 4000 K (green) are plotted as these temperatures are the closest to the effective temperature of the M0V MURaM simulation.

For the G2V star, a large variety of atmospheric structures are present in the simulation, even with no magnetic field (see e.g., magenta dotted lines in Fig. 2.1a). The 1D Kurucz atmosphere and average MURaM atmospheres for the G2V star (Fig. 2.1a) are very similar for above $\log(\tau_{500}) = -1$. However, at this height, temperatures and temperature gradients show large differences between the different pixels in the simulation box. When averaging the atmospheres, we would expect this information to be lost as the gradients are smoothed. The 1D Kurucz temperatures and average MURaM atmospheres deviate in the deeper atmospheric layers. For the G2V simulations, the difference is particularly stark between the average taken over geometrical depth and the average over $\log(\tau_{500})$. From these deviations, it can be seen that differences in spectra produced from 3D atmospheres (for each snapshot pixel) and spectra calculated from the 1D equivalent atmosphere (averaging over z surfaces) are likely to be significant. Unsurprisingly, taking an average of the atmospheres across geometrical depth to produce a 1D atmosphere will remove much of the information that is gained by simulating the atmospheres in 3D in the first place.

For the M0V star (Fig. 2.1b), both $\langle \text{atm} \rangle_\tau$ and $\langle \text{atm} \rangle_z$ are very similar, and lie between the Kurucz atmospheres. Additionally, the individual pixels are much less spread than those of the G2V star. Therefore, unlike for the G2V star, this comparatively simple, single wavelength opacity calculation done here does not much change the structure obtained from an average, and thus the radiation produced from these 1D atmospheres, at least near 500 nm, may be similar and the spread of intensities seen from individual pixels may be smaller. However, the full 3D set of spectra should be calculated, as other wavelengths may yield different results, individual features can be investigated with 3D calculations, and the possible variety of atmospheric structures introduced by magnetic fields has not yet been considered.

Figure 2.2 shows the vertical magnetic field, B_z, in a snapshot of a tranche B G2V simulation that had an initial average vertical magnetic field of 300 G. The magnetic field is shown for constant optical depths at 500 nm, τ_{500}, of 1 (bottom panel), and 10^{-2} (top panel). The field is concentrated in the intergranular lanes due to the convective motions of the plasma. The vertical magnetic field strength within the granules is low, e.g. less than 15 G at $\tau_{500} = 1$ in the $\langle B_z \rangle = 300\ G$ box. The field is more diffuse higher in the atmosphere as the surrounding gas pressure

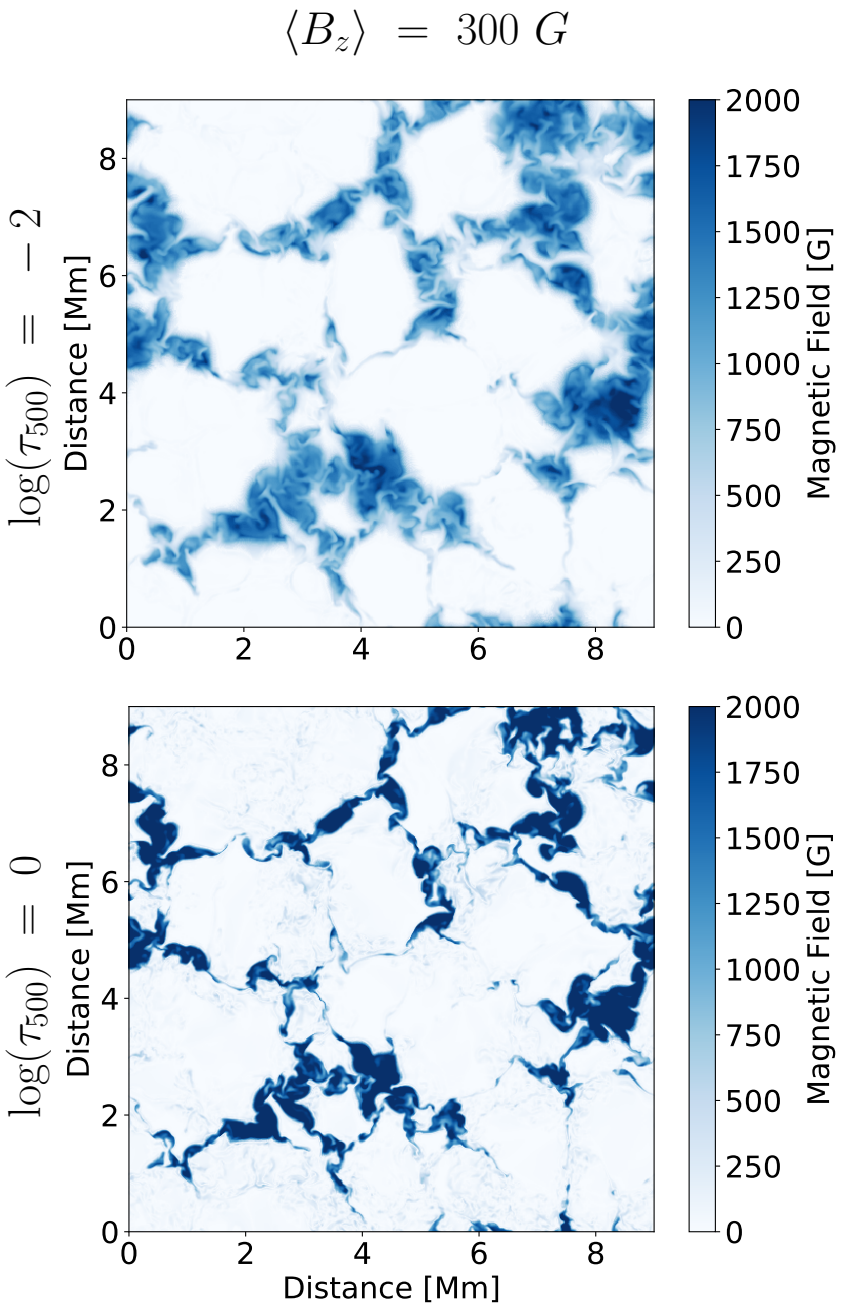


Figure 2.2: The distribution of the unsigned vertical magnetic field component, B_z, at disc centre ($\mu = 1$) for a tranche B G2V $\langle B_z \rangle = 300$ G snapshot. The field is shown for a surface corresponding to a constant logarithmic optical depth at 500 nm, $\log(\tau_{500})$, are -2 (top) and 0 (bottom). Credit: Norris et al., A&A, 605, A45, 15pp., 2017, reproduced with permission © ESO.

in the atmosphere is lower.

To illustrate the effect of the magnetic field on the convection, Figure 2.3 shows the temperatures for a tranche B G2V hydrodynamic box (panels a and c) and a 300 G box (panels b and d). The panels show the same constant optical depth selection as in Fig. 2.2: $\log(\tau_{500}) = -2$ (a and b) and $\log(\tau_{500}) = 0$ (c and d). The snapshot displayed in the $\langle B_z \rangle = 300$ G image is the same as shown in Fig. 2.2. Images of the vertical velocities at a constant τ_{500} of 1 are displayed in Fig. 2.3 e and f in order to show the positions of the up-welling convective granules and the down-flowing intergranular lanes. A granular structure can be seen in both hydrodynamic and $\langle B_z \rangle = 300$ G images. At $\log(\tau_{500}) = 0$ the granules are hot and the temperature is cooler in the intergranular lanes. In the magnetic run, a larger number of high-temperature features are observed compared to the field-free simulations. These additional temperature peaks tend to align with peaks of the magnetic field in the intergranular lanes. However, there are some exceptions where large areas of strong magnetic field appear cooler than granules (Spruit, 1976). In the upper layers of the atmosphere we begin to see reversed granulation, i.e., at $\log(\tau_{500}) = -2$ the centre of granules appear cooler than their edges. The higher atmospheric layers for both the no-field and the 300 G simulation have a more diffuse distribution than the deeper layers, as seen for the magnetic field. Detailed investigations into the structure of MURaM simulations and how they change between spectral type and when a magnetic field has been introduced are shown by Beeck et al. (2013, 2015a).

2.2 Line of sight algorithm

We calculate emergent intensity spectra along rays that are laid through each pixel of the simulation box. To model different viewing angles, corresponding to different positions on the star, these rays were inclined at angles θ to the local normal (θ is the heliocentric angle, also referred to as limb angle). Specifically, we compute rays with inclinations corresponding to limb distances of $\mu = \cos\theta$ between 0.2 and 1.0 in steps of 0.1. Calculations are not performed beyond $\mu = 0.2$ due to the required number of depth points becoming unfeasibly large and the plane parallel nature of the MURaM models becoming less effective, meaning that, for accurate results, a different approach using simulations with a spherical setup would be needed. The small annulus beyond $\mu = 0.2$ accounts for only 4% of the area of the stellar disc. Due to the low relative brightness beyond $\mu = 0.2$ resulting from limb darkening in most wavelengths, significantly less than 4% of the flux is missing when this annulus is neglected. For ease of visual interpretation, feature positions were maintained in

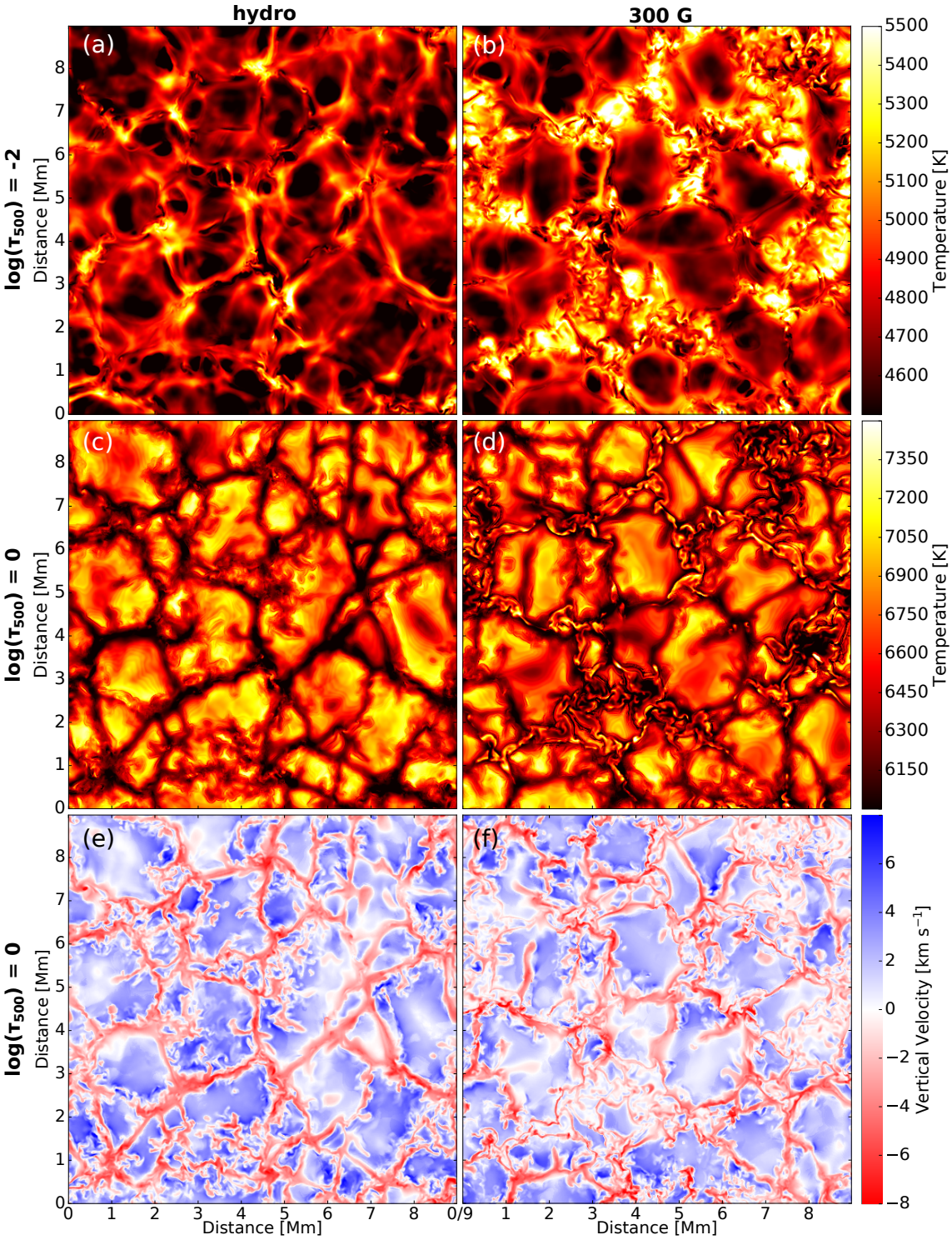


Figure 2.3: The temperatures (a-d) and vertical velocities (e and f) at disc centre for a G2V field-free simulation (left) and a G2V $\langle B_z \rangle = 300$ G simulation (right). The temperatures and velocities are shown at a constant logarithmic optical depth at 500 nm, $\log(\tau_{500}) = -2$ (top) and $\log(\tau_{500}) = 0$ (middle and bottom). Note the different, distinct temperature scales for images at $\log(\tau_{500}) = -2$ and $\log(\tau_{500}) = 0$. Credit: Norris et al., A&A, 605, A45, 15pp., 2017, reproduced with permission © ESO.

images of emergent intensity by pivoting the sight lines at the mean geometrical depth, $\langle z \rangle$, where the disc centre optical depth at 500 nm, τ_{500}, is unity. Using a plane-parallel atmosphere means that the results from sight lines further towards the limb may start to be affected by the lack of spherical structure.

MURaM provides temperature, pressure, density, magnetic field, velocity and geometric depth for each each grid point. The atmospheric quantities at the locations of the rays are obtained by performing a 2D linear interpolation along the line of sight for each pixel with a vertical resolution equal to that of the simulations. Double resolution was tested for tranche B G2V and found to have negligible effect on the calculated emergent intensities. Along each ray, the column mass, electron number density and continuum absorption coefficient at 500 nm were derived for use in the ATLAS9 spectral calculation. The atmospheric parameters along the sight lines were then linearly interpolated onto a 256 point grid. A range of upper limits and distributions of optical depths were tested for calculating emergent intensities. An evenly spaced grid in logarithmic optical depth with values between $\log(\tau_{500})=-5.0$ and 2.5 was selected as this is where most of the radiation is produced. Also, this range of optical depths is completely contained within the simulation box at each spatial pixel.

2.3 ATLAS9

To calculate the emergent intensities, the radiative transfer code ATLAS9 (Kurucz, 1992a; Castelli & Kurucz, 1994) was used. ATLAS9 allows for fast and accurate computation of continuum intensities across a wide wavelength range. Spectra were synthesised for each sight line of the MURaM boxes. This calculation is done under the assumption of local thermodynamic equilibrium (LTE) using an opacity distribution function (ODF) table (Castelli & Kurucz, 2001) to account for the opacity of the millions of atomic and molecular spectral lines in a stellar atmosphere, particularly in the UV. The ODF table used was calculated for solar metallicity with a microturbulence of 1 km/s, apart from in the case of F3V stars where a microturbulence of 2 km/s was chosen. These microturbulent velocities are the nearest tabulations to the RMS speeds found at an optical depth of unity for the MURaM simulation snapshots. For each pixel, we calculate spectra ranging from 149.5 nm to 160 000 nm. The spectra are calculated for 1040 wavelength bins that correspond to the resolution provided by the ATLAS9 ODFs. The resolution of the spectra thus ranges from 1 nm in the UV, to 2 nm in the visible, and up to 20 000 nm in the far infrared.

As ATLAS9 assumes LTE for its calculations, for wavelengths below 300 nm the absolute values of emergent intensity begin to deviate significantly from the values found when allowing for non-LTE. However, relative values continue to be reasonably accurate down to 164 nm (Krivova et al., 2006). Thus, contrasts calculated from ATLAS9 synthesised spectra down to 164 nm are reliable and only wavelengths above 164 nm are discussed in this thesis.

Two different sets of ODFs were used in this study. An outdated version of ODFs (Kurucz, 1990) were used to synthesise spectra from the tranche B G2V snapshots (10 snapshot set). These ODFs use abundances from Anders & Grevesse (1989). Updated ODFs (Castelli & Kurucz, 2004), with additionally updated H_2O contributions produced in 2012, were used to synthesise spectra from the tranche A G2Vs and other stellar snapshots (6 snapshot sets). The new ODFs use abundances from Grevesse & Sauval (1998), as well as TiO lines from Schwenke (1998). Other improvements for the new ODFs are described in Castelli & Kurucz (2004). Tranche B G2Vs will be re-run with the updated ODFs in the future.

ATLAS9 allows for different opacity sources to be included or excluded through the use of switches for separate modules that account for different opacity sources. For example, Fig. 1.2 shows the spectra produced with ATLAS9 for the Kurucz' quiet-Sun model atmosphere with the same switch setup as used in this study in black, and with the ODF switch deactivated in red. The large difference in spectra between the two setups shows the vast number of important opacity sources that are accounted for by the ODFs. Without the ODFs, several absorption edges that are included within other modules in ATLAS9 can be seen more clearly, e.g., the aluminium and magnesium absorption edges at 207.7 nm and 251.4 nm, respectively (both accounted for in the COOLOP module of ATLAS9), and the hydrogen Balmer absorption edge at 364.7 nm (accounted for in the HOP module). The modules that were activated for calculations in this study were HOP, H2PLOP, HMINOP, HRAYOP, HE1OP, HE2OP, HEMINOP, HERAOP, COOLOP, LUKEOP, HOTOP, ELECOP, H2RAOP and LINOPL(ODF).

ATLAS9 can also be used to iterate to find an equilibrium atmosphere, but in this case, where a 3D simulation is used with a 1D radiative transfer code (1.5D calculation), this feature is disabled in order to retain the structures in each of the 1D atmospheres that would not necessarily be stable without the surrounding pixels.

The remaining chapters in this thesis present the spectra calculated from these 3D MURaM simulation snapshots at multiple limb angles and discuss the variations across spectral type and limb position.

Chapter 3

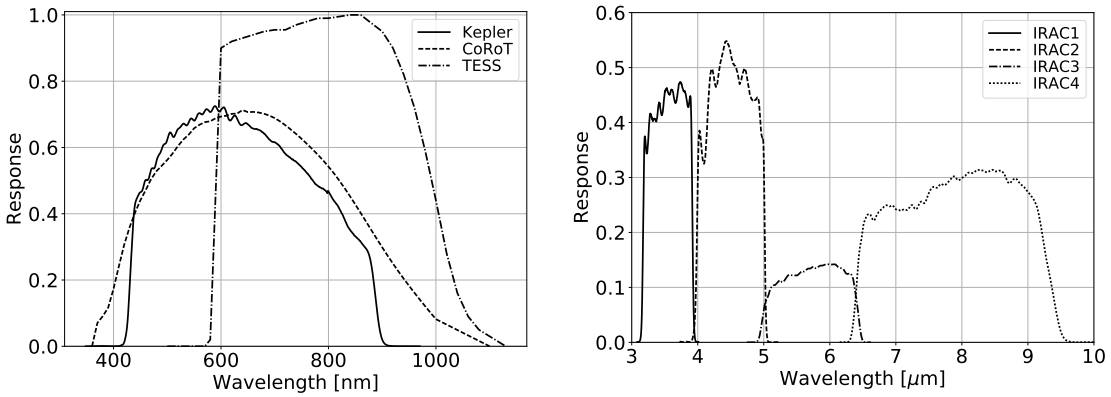
Centre-to-limb variations of magnetic field-free snapshots

The effects of viewing angle through the atmosphere of a star leads to an effect called limb darkening, described in Sect. 1.2.4. This is observed on the Sun (Pierce & Slaughter, 1977; Neckel & Labs, 1994), and seen in transits of planets across other stars. At most wavelengths, the intensity observed will decrease when viewing towards the limb of the star (Gray, 2005). This will occur at different rates for different wavelengths, and intensity will instead increase at some wavelengths, e.g., in the UV and X-ray. The form of this limb-darkening function for both the Sun (Neckel & Labs, 1994) and other stars has been investigated and modelled by many (Sing, 2010; Magic et al., 2015; Morello et al., 2017).

Sing (2010) uses 1D Kurucz stellar atmospheres to calculate spectra and fit limb darkening curves for *Kepler* and CoRoT filters. Magic et al. (2015) use 3D Stagger simulations to calculate spectra and fit to *Kepler* filter limb darkening. Both Sing (2010) and Magic et al. (2015) are further described in Sect. 3.2.

Figure 3.1 shows some commonly used filters in planetary transits. *Kepler*, CoRoT and TESS filters, which cover a range of visible wavelengths, are shown in Fig. 3.1a, and the *Spitzer* IRAC filters, for infrared wavelengths, are shown in Fig. 3.1b. The *Spitzer* IRAC filters include the, now out of use, 5.8 and 8.0 μm filters for use with previously collected data. By calculating limb darkening for this selection of filters we can compare fits from 3D modelling with the fits derived from 1D models in the case of *Kepler* and CoRoT, and provide limb darkening coefficients for a wider range of wavelength filters for use in stellar models and planetary transit calculations.

Here, limb darkening is derived by calculating the mean spectra over all pixels in all magnetic field-free snapshots at each given limb distance, μ. Filters can then



(a) Visible filters **(b)** *Spitzer* filters

Figure 3.1: Filter responses as a function of wavelength for investigation in this study. Figure (a) shows the filters in visible wavelengths (*Kepler*, CoRoT and TESS), while Fig. (b) shows the *Spitzer* IRAC filters in the infrared.

be applied to the mean spectra, if required. For each wavelength or filter, the data points are normalised by the corresponding disc-centre value.

This chapter presents evidence that limb darkening coefficients derived from 1D model atmospheres that are commonly used in stellar and planetary transit studies are insufficient to represent the darkening on some spectral types. Validation of the method used for calculating changes in radiation towards the limb is performed by comparing our calculated solar limb darkening with measured values. Finally, limb darkening coefficients are derived from MURaM atmospheres for selected exoplanetary mission filters.

3.1 Comparison of G2V centre-to-limb variations with solar observations

Neckel & Labs (1994) provide limb darkening polynomials at multiple wavelengths fitted to observed values on the Sun. We use this data to compare limb darkening values obtained from synthesised spectra from the G2V (solar-type) simulations. This comparison was presented in Norris et al. (2017).

To demonstrate the effect of limb darkening, Figure 3.2 shows the emergent intensities at a wavelength of 601 nm for a single hydrodynamic snapshot seen at a range of viewing angles from disc centre ($\mu = 1.0$) to near the stellar limb ($\mu = 0.2$). Darkening of the images can be seen towards the limb, as expected in visible wavelengths, and a foreshortening of the horizontal observed distance is

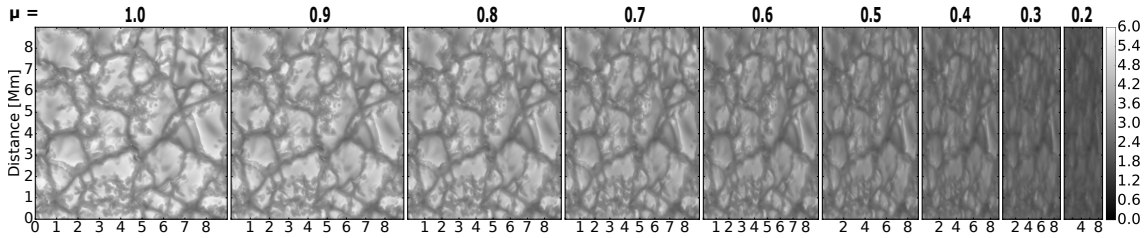


Figure 3.2: Emergent intensities (10^{-8} W m^{-2} sr^{-1} Hz^{-1}) at a wavelength of 601 nm for a simulated G2V hydrodynamic snapshot viewed at limb distances ranging from $\mu = 1.0$ in the left most image, to $\mu = 0.2$ in the right most image. The distance shown is the distance on the surface of the Sun in Mm, the boxes are foreshortened in the horizontal direction to show the box as observed on the solar disc. The employed grey-scale is indicated on the right of the figure. Credit: Norris et al., A&A, 605, A45, 15pp., 2017, reproduced with permission © ESO.

shown to demonstrate the box's appearance on the solar disc.

We confirmed that the mean spectra derived from the field-free simulations reproduce observed limb darkening laws, by comparing to limb darkening polynomials previously derived from observations by Neckel & Labs (1994). Limb darkening derived from the $\langle B_z \rangle = 100$ G snapshots was also compared, as the true field-free quiet solar surface may never actually be observed. As such, the observed limb darkening should lie between field-free and low magnetic field values. The Neckel & Labs (1994) polynomials are tabulated for wavelengths between 303 nm and 1 099 nm. In Fig. 3.3, the width of the solid lines indicates the limb darkening derived from non-magnetic convection simulations (lower bounds) and the 100 G snapshots (upper bounds) for wavelengths of 391 nm (blue), 611 nm (green), 1 097.5 nm (red) and 1 597.5 nm (magenta). These are compared to the Neckel & Labs tabulations at 391 nm (blue), 611 nm (green) and 1 099 nm (red) in dashed lines. Overall, the calculated and observed limb darkening laws agree well, although, in the visible, the limb darkening gradient of the polynomials is slightly shallower than than that of the MURaM-derived hydrodynamic values. These differences may in part be accounted for by the fact that we never observe the truly field-free quiet sun. When a magnetic field is present, the appearance of faculae, that are bright at the limb and have low contrast at disc centre (Spruit, 1976), leads to atmospheres that have a shallower limb darkening gradient than those that are field-free. This is seen in the $\langle B_z \rangle = 100$ G simulations shown by the upper limit of the solid line in Fig. 3.3. At some wavelengths, particularly towards the UV, missing opacity sources may also contribute to the differences between the simulations and the measurements, although these should have a minor effect when the intensities are normalised, as they are in Fig. 3.3. For the MURaM limb darkening values in Fig. 3.3, there is a

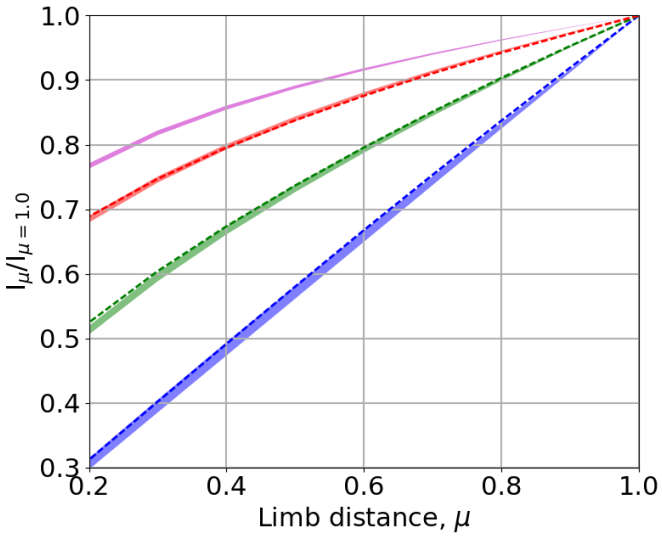


Figure 3.3: Comparisons of the observed solar limb darkening polynomials (Neckel & Labs, 1994) (shown by dashed lines at wavelengths of 390.9 nm (blue), 611.0 nm (green) and 1 099.0 nm (red)) with MURaM-derived G2V limb darkening. The width of the solid line shows the average intensity of snapshots as a function of limb distance, μ, between the hydrodynamic values (lower limit) and the 100 G snapshots (upper limit) for wavelength bins centred on 391.0 nm (blue), 611.0 nm (green), 1 097.5 nm (red) and 1 597.5 nm (magenta). The intensities have been normalised to unity at disc centre. There are no published measurements of limb darkening above 1 098 nm. Credit: Norris et al., A&A, 605, A45, 15pp., 2017, reproduced with permission © ESO.

visible change in gradient at $\mu = 0.3$, particularly for the longer wavelengths. This is due to the limb darkening not being calculated at enough intermediate μ values between $\mu = 0.3$ and 0.2 to smoothly account for the steepening of gradient that occurs close to the limb in the MURaM synthetic spectra.

3.2 3D centre-to-limb variations compared to 1D modelling capabilities

One-dimensional models of limb darkening are currently in wide use throughout the stellar and exoplanetary community. Three-dimensional models should provide more accurate limb darkening values and therefore improve these studies. This section compares limb darkening derived from the 3D MURaM models and those derived from two different 1D models: previously published 1D limb darkening fits from Sing (2010) and limb darkening fits derived from 1D mean atmospheres of the MURaM simulations used in this study.

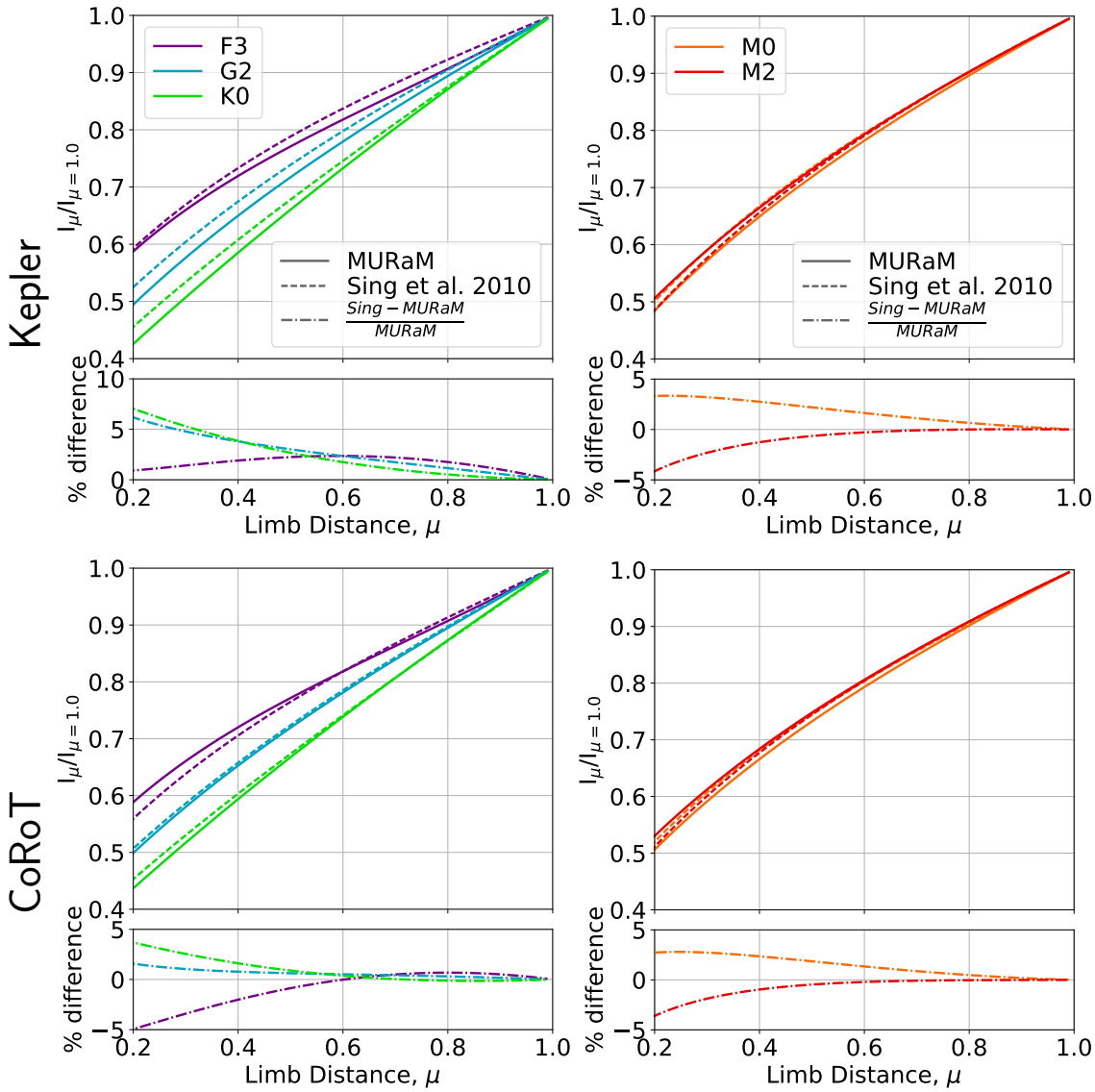


Figure 3.4: Limb darkening derived from 3D MURaM models (solid lines) compared with fits from 1D models in Sing (2010) (dashed lines), both shown in the top axes of each panel, for the *Kepler* (top panels) and CoRoT (bottom panels) filters. The percentage difference between the models is shown with a dot-dashed line in the lower axes of each panel. The left-hand panels show the hotter stars, K0V, G2V and F3V, while the right hand panels show the cooler stars, M0V and M2V.

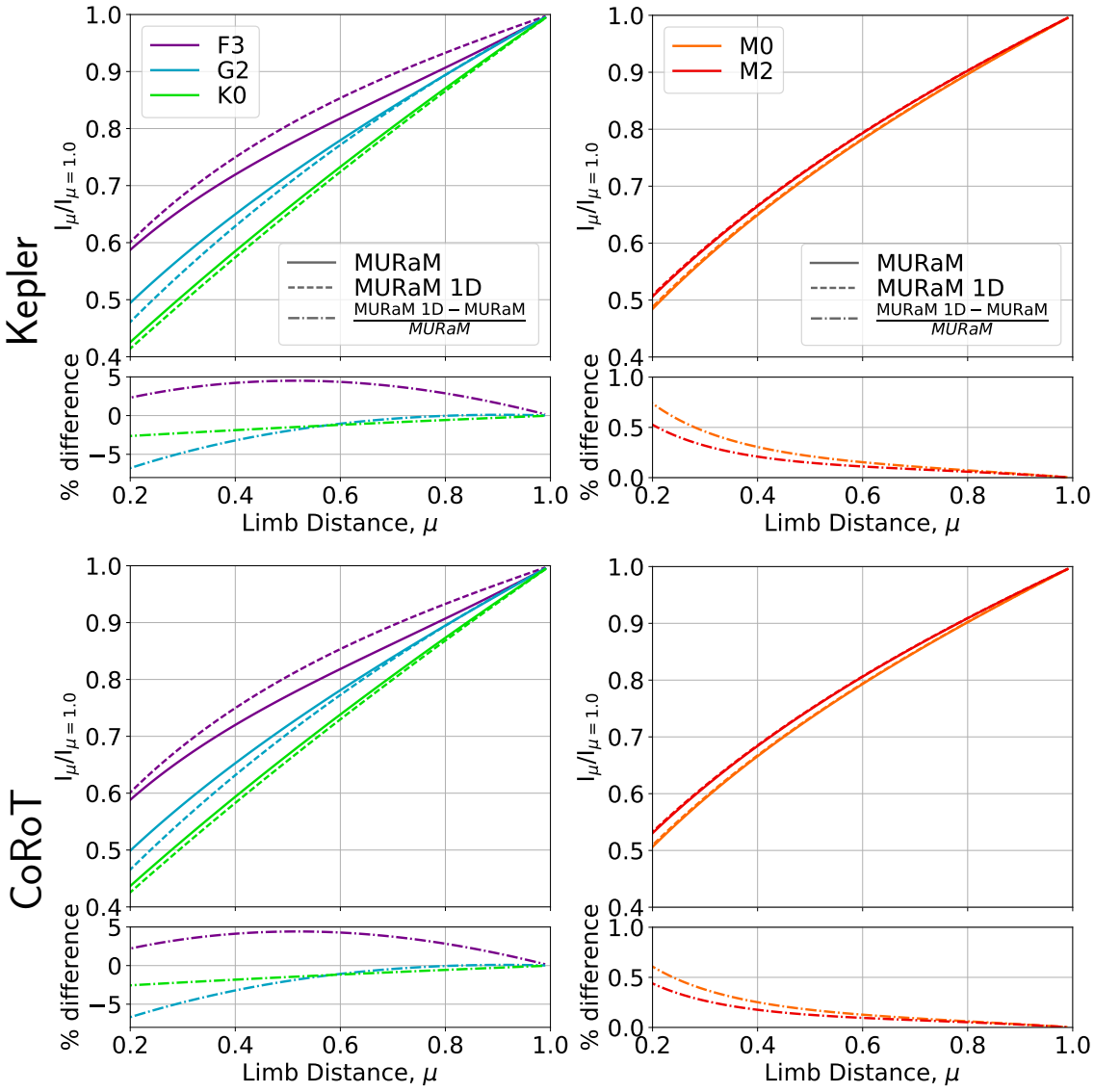


Figure 3.5: Same as in Fig. 3.4, but dashed lines now represent fits from limb darkening calculated from 1D mean MURaM atmospheres.

Figure 3.4 shows limb darkening in the *Kepler* (top) and CoRoT (bottom) filters. Values derived from 1D models by Sing (2010) are shown as dashed lines and 3D MURaM derived limb darkenings are shown as solid lines. The percentage differences between 1D Sing and 3D MURaM models are shown as dot-dashed lines in the lower axis of each panel. The colours represent different spectral types, as seen in the legends. The Sing (2010) values are calculated using Kurucz 1D stellar atmospheres (Kurucz, 1990) and the same spectral synthesis code (ATLAS9) as in this study. However, an older ODF table is used in Sing (2010), meaning there are some slight differences in abundances. Additionally, Kurucz atmospheres are calculated for $T_{\rm eff}$ intervals of 250 K, and $\log g$ intervals of 0.5. Sing (2010) provide a linear interpolation program which was used, in this case, to obtain limb darkening coefficients for the 1D cases with effective temperatures and strengths of gravity that match those of the MURaM simulations. These parameters are shown in Tab. 2.1 in Sect. 2.1.

We find that for hotter stars, K0V-F3V, limb darkening in the *Kepler* filter is steeper when calculated in 3D. This agrees with trends found in Magic et al. (2015). In Magic et al. (2015), *Kepler* limb darkening coefficients from 3D Stagger simulations (see Magic et al., 2013) are compared with Sing (2010) 1D limb darkening laws for atmospheres of solar metallicity at $\log g = 4.5$ and matching effective temperatures. The magnitude of the differences they find between 1D and 3D are slightly smaller at most limb distances than those found in Figure 3.4. The larger difference of our calculations may arise from the interpolation of the Sing (2010) coefficients to match the $\log g$ and $T_{\rm eff}$ values of the MURaM simulations. The coefficients are assumed to change linearly between Sing (2010) grid points in $\log g$ and temperature. As the change in coefficients found with $T_{\rm eff}$ in Sing (2010) does not appear to be linear, this interpolation could cause the 1D coefficients used in our comparison to be inconsistent with limb darkening coefficients found directly from a 1D atmosphere of the chosen $T_{\rm eff}$. In addition to this, both Magic et al. (2015) and Sing (2010) use different abundances to MURaM and the ODFs used for our spectral synthesis. For the CoRoT filter, 1D and 3D are very similar for $\mu > 0.6$ in the hotter stars, with deviations occurring further towards the limb. For the *Kepler* filter, the largest deviations are also seen towards the limb for G2V to M2V stars, while the F3V star appears to have a peak in 1D to 3D deviation at approximately $\mu = 0.7$ and this deviation decreases closer to the limb. Magic et al. (2015) found that for the *Kepler* filter, deviations were largest towards the limb.

These differences in limb darkening can affect the planetary parameters extracted from transit observations when these models are used. In order to determine

the magnitude of this effect, simulations of various transits should be performed for the 3D limb darkening case, and the planetary parameters should be extracted assuming the 1D limb darkening to find the errors produced.

To ensure that differences between 1D and 3D models do not only arise due to inconsistencies in abundance between the models, a comparison is made between limb darkening calculated from 3D MURaM models, and limb darkening derived by calculating spectra at multiple limb angles from a 1D mean atmosphere of all atmospheres of non-magnetic MURaM snapshots, using ATLAS9 (as in Sing, 2010). The results are shown in Figure 3.5. For hotter, lower gravity stellar surfaces, the 1D and 3D limb darkening profiles deviate from one another more with increasing effective temperature. This highlights the importance of taking into account the 3D structure of the atmosphere to calculate accurate limb darkening, particularly for these spectral types in visible filters. The larger differences that are seen in results from 1D and 3D atmospheres are perhaps not surprising in the light of Fig. 2.1a in Sect. 2.1, where the G2V MURaM atmospheres averaged over $\log(\tau_{500})$ and geometrical depth were seen to differ significantly.

However, for M0V and M2V stars, very little difference is seen between the 1D and 3D limb darkening calculations in the *Kepler* and CoRoT filters (Fig. 3.5, right). This similarity in visible radiation from fully 3D treated atmospheres and averaged atmospheres was foreseen when sampling averaged M0V atmospheres in Sect. 2.1. Fig. 2.1b shows that calculating optical depth at 500 nm for individual disc-centre M0V pixels and averaging over the resultant atmosphere led to a similar temperature vs. optical depth profile as for an atmosphere averaged over geometrical depth only. Additionally, the spread of temperatures across individual pixels were relatively small compared to the hotter star (G2V), suggesting that a plane-parallel approach to limb darkening (in the field-free case) could produce similar results to the 3D treatment of viewing angle at this wavelength.

3.3 Centre-to-limb variation coefficients for past, present and future planetary missions

In this section limb darkening is calculated for a variety of filters from past, present and future star observing missions (shown in Fig. 3.1). These are fit with common

limb darkening laws,

$$I_\mu/I_1 = 1 - a(1-\mu), \tag{3.1}$$

$$I_\mu/I_1 = 1 - a(1-\mu) - b(1-\mu)^2, \tag{3.2}$$

$$I_\mu/I_1 = 1 - a(1-\mu) - b(1-\sqrt{\mu}), \tag{3.3}$$

$$I_\mu/I_1 = 1 - a(1-\mu) - b(1-\mu^{3/2}) - c(1-\mu^2), \tag{3.4}$$

$$I_\mu/I_1 = 1 - a(1-\mu^{1/2}) - b(1-\mu) - c(1-\mu^{3/2}) - d(1-\mu^2). \tag{3.5}$$

Equations 3.1 to 3.3 are the widely used linear, quadratic and square root laws, respectively (e.g., Neckel & Labs, 1994). Equation 3.4 is a three-parameter non-linear law introduced by Sing et al. (2009) and equation 3.5 is the four-parameter non-linear limb darkening law introduced by Claret (2000).

As our calculations do not go beyond $\mu = 0.2$ (as discussed in Sect. 2.2), and have only nine data points, four parameters may not be required to sufficiently fit this data. Figure 3.6 shows some examples of fits using Eqs 3.1 to 3.5 for two filters, *Kepler* (top panels) and *Spitzer* IRAC2 (bottom panels), and two stars, G2 (left) and M2 (right). The upper axes of each panels show the fits in various colours and line styles, shown in the legend, with the data points shown by black crosses. The lower axes show the percentage difference between the fits and the data points. The three-parameter non-linear fit provides a sufficient fit to the data for all chosen filters and all spectral types, with each point of the fit being within 0.1% of the calculated values. This is on the order of the temporal variations in the limb darkening across the six snapshots taken. While the four-parameter non-linear law produces smaller differences, of within 0.01%, these are a factor of ten less than the temporal spread found in the limb darkening, in addition to there only being nine data points for each fit. This suggests that the additional parameter may be unnecessary in this case. However, Magic et al. (2015) find that the four-parameter non-linear law fits more completely to their 3D simulated limb darkenings than the three-parameter law. This is likely due to Magic et al. (2015) being able to calculate limb darkening down to $\mu = 0.01$, where it becomes very steep. This is accounted for more accurately with four parameters.

Figures 3.7 and 3.8 show the three-parameter non-linear fit for multiple filters. All stars seen in all filters show a limb darkening that becomes steeper towards the limb. The hottest, lowest surface gravity star, F3V, has the shallowest limb darkening in all shown filters. For cooler and smaller (i.e., higher $\log g$) stars, limb darkening increases until a turnover point where limb darkening begins to become shallower. This occurs around the temperature of the K0V star, giving K0V the

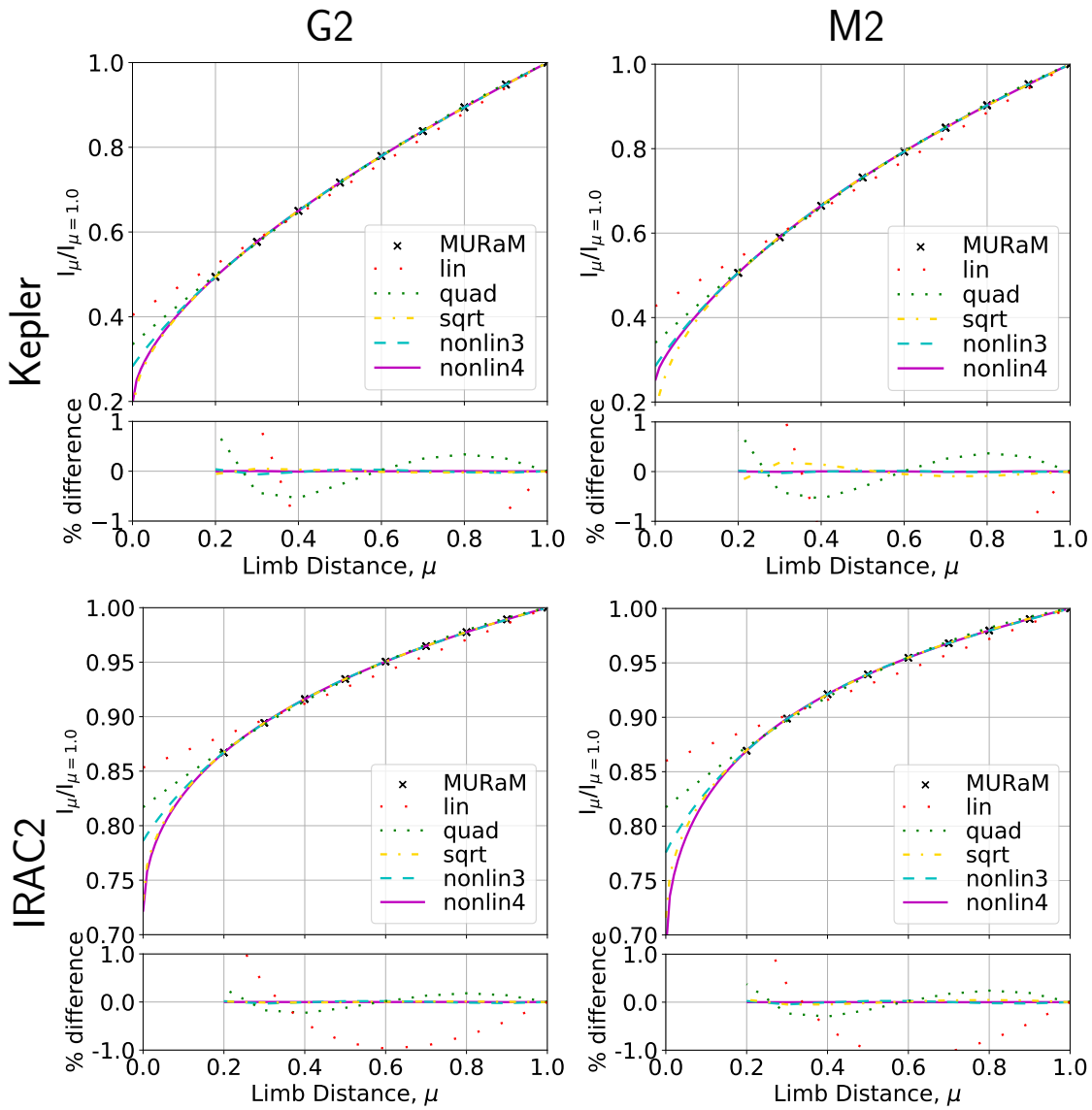
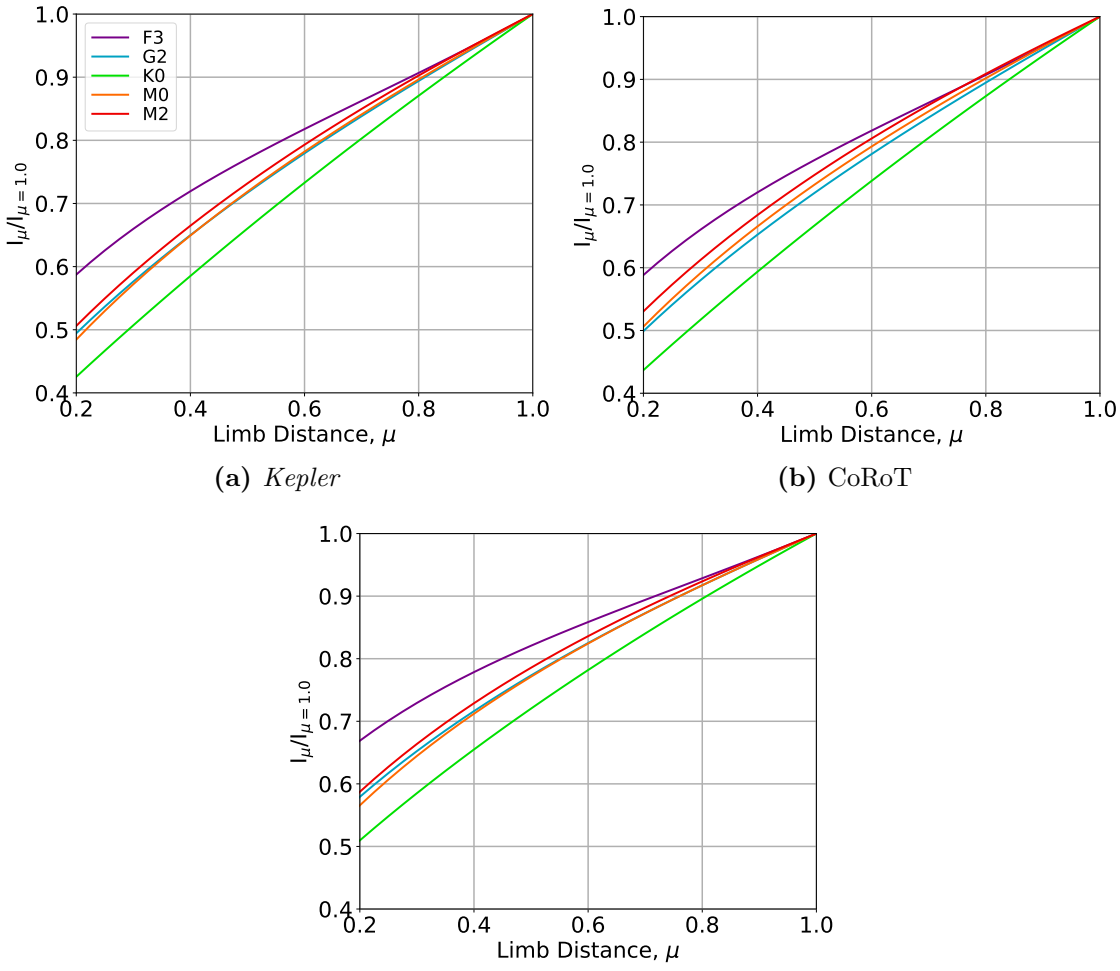


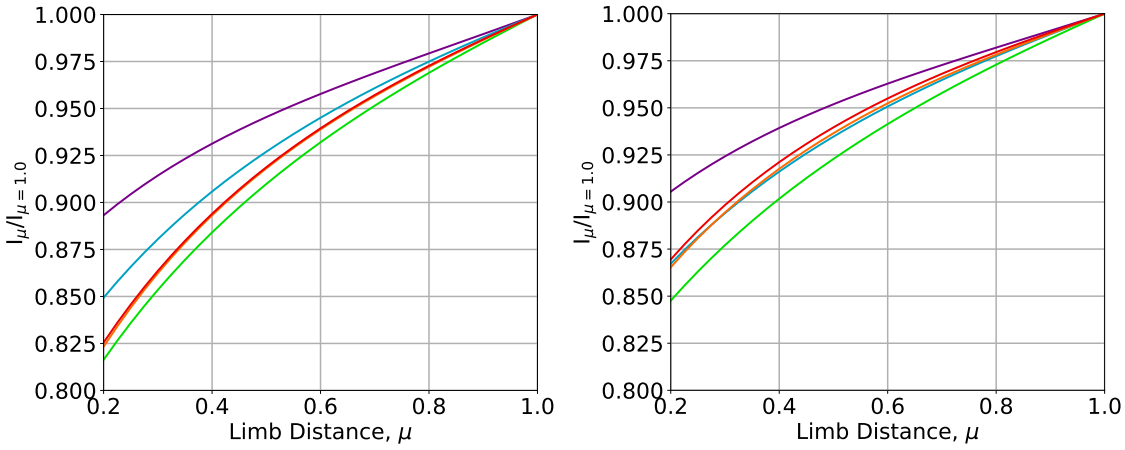
Figure 3.6: A variety of fits to the MURaM field-free limb darkening data for the *Kepler* filter (top panels) and *Spitzer* IRAC2 filter (bottom panels) for stellar spectral type G2 (left) and M2 (right). The top axes in each panel shows the MURaM data points with black crosses and fits to this data using equations 3.1 to 3.5, represented by different line styles and colours – shown in the legend. The bottom axes in each panel shows the percentage difference between the MURaM data points and the fits, represented by the same line styles and colours.



(a) *Kepler* **(b)** CoRoT

(c) TESS

Figure 3.7: MURaM field-free limb darkening for all spectral types, shown in the legend, in various visible filters.



(a) IRAC1 **(b)** IRAC2

(c) IRAC3 **(d)** IRAC4

Figure 3.8: MURaM field-free limb darkening for all spectral types in the four *Spitzer* IRAC bands. The different spectral types are denoted by the same colours as shown on the legend in Fig. 3.7 from purple (F3V) through to red (M2V).

steepest limb darkening in all filters except *Spitzer* IRAC4, where M0V is the steepest.

Limb darkening is strongest in the visible wavelength filters (*Kepler*, CoRoT and TESS, see Fig. 3.7), whereas in the infrared (*Spitzer*, Fig. 3.8) limb darkening is a much smaller effect (note the smaller y-scale in Fig. 3.8 compared to Fig. 3.7). As wavelength increases, from IRAC1 through to IRAC4, limb darkening decreases. Tables 3.1 to 3.7 show limb darkening coefficients for different parameterizations of limb darkening, defined by Eqs 3.1 to 3.5, for the same filters as shown in Figs. 3.7 and 3.8.

Table 3.1: *Kepler* field-free centre-to-limb variation coefficients.

	I(1.0)	linear	quad		sqrt		non-linear 3			non-linear 4			
Star	[10^5 W m^{-2} sr^{-1}]	a	a	b	a	b	a	b	c	a	b	c	d
F3V	148.878	0.48	0.41	0.12	0.20	0.44	2.09	-2.60	1.15	-2.95	8.44	-8.48	3.14
G2V	75.8658	0.60	0.48	0.19	0.20	0.63	1.50	-1.17	0.38	0.51	0.40	-0.15	0.04
K0V	35.6138	0.70	0.62	0.12	0.44	0.40	1.00	-0.24	-0.00	0.22	0.52	0.21	-0.16
M0V	7.94901	0.60	0.45	0.23	0.11	0.78	1.73	-1.45	0.48	0.45	0.75	-0.55	0.17
M2V	5.01176	0.57	0.42	0.24	0.08	0.79	1.59	-1.25	0.37	0.20	1.16	-0.85	0.24

Table 3.2: CoRoT field-free centre-to-limb variation coefficients.

	I(1.0)	linear	quad		sqrt		non-linear 3			non-linear 4			
Star	[10^5 W m^{-2} sr^{-1}]	a	a	b	a	b	a	b	c	a	b	c	d
F3V	167.933	0.48	0.40	0.12	0.20	0.45	2.09	-2.58	1.14	-2.93	8.38	-8.42	3.12
G2V	85.3756	0.59	0.47	0.19	0.20	0.62	1.48	-1.15	0.37	0.50	0.40	-0.15	0.04
K0V	40.2554	0.68	0.61	0.12	0.43	0.40	1.00	-0.27	0.01	0.24	0.48	0.21	-0.15
M0V	9.54094	0.57	0.42	0.23	0.08	0.78	1.72	-1.50	0.50	0.53	0.59	-0.44	0.14
M2V	6.19356	0.54	0.39	0.24	0.04	0.80	1.62	-1.36	0.43	0.33	0.91	-0.70	0.20

Table 3.3: TESS field-free centre-to-limb variation coefficients.

	I(1.0)	linear	quad		sqrt		non-linear 3			non-linear 4			
Star	[10^5 W m^{-2} sr^{-1}]	a	a	b	a	b	a	b	c	a	b	c	d
F3V	137.623	0.38	0.30	0.13	0.10	0.45	1.74	-2.13	0.91	-1.93	5.89	-5.98	2.22
G2V	81.2216	0.49	0.35	0.21	0.05	0.69	1.47	-1.27	0.41	0.71	-0.05	0.15	-0.07
K0V	44.4041	0.58	0.48	0.16	0.24	0.54	1.13	-0.59	0.12	0.29	0.51	-0.01	-0.07
M0V	13.8767	0.50	0.34	0.24	-0.01	0.81	1.74	-1.64	0.56	0.72	0.19	-0.20	0.07
M2V	9.71390	0.47	0.31	0.25	-0.06	0.83	1.69	-1.59	0.53	0.61	0.38	-0.38	0.12

Table 3.4: *Spitzer* IRAC1 field-free centre-to-limb variation coefficients.

	I(1.0)	linear	quad		sqrt		non-linear 3			non-linear 4			
Star	[10^4 W m^{-2} sr^{-1}]	a	a	b	a	b	a	b	c	a	b	c	d
F3V	8.34292	0.12	0.08	0.06	-0.01	0.21	0.61	-0.74	0.30	-0.45	1.58	-1.63	0.60
G2V	7.05601	0.17	0.09	0.12	-0.09	0.40	0.80	-0.85	0.30	0.52	-0.32	0.19	-0.05
K0V	5.96684	0.20	0.11	0.14	-0.09	0.46	0.92	-0.95	0.33	0.52	-0.19	0.08	-0.02
M0V	4.21959	0.19	0.09	0.16	-0.14	0.53	1.11	-1.28	0.47	0.79	-0.58	0.29	-0.06
M2V	3.68881	0.19	0.09	0.15	-0.14	0.52	1.05	-1.17	0.42	0.57	-0.18	-0.02	0.03

Table 3.5: *Spitzer* IRAC2 field-free centre-to-limb variation coefficients.

	I(1.0)	linear	quad		sqrt		non-linear 3			non-linear 4			
Star	[10^4 W m^{-2} sr^{-1}]	a	a	b	a	b	a	b	c	a	b	c	d
F3V	4.90184	0.11	0.07	0.06	-0.02	0.19	0.53	-0.63	0.25	-0.30	1.17	-1.22	0.45
G2V	4.06944	0.15	0.08	0.10	-0.06	0.33	0.67	-0.70	0.24	0.38	-0.15	0.07	-0.02
K0V	3.33578	0.17	0.11	0.10	-0.05	0.34	0.69	-0.69	0.23	0.36	-0.08	0.03	-0.01
M0V	2.45015	0.15	0.07	0.11	-0.10	0.38	0.81	-0.92	0.34	0.57	-0.42	0.22	-0.05
M2V	2.22896	0.14	0.07	0.12	-0.11	0.39	0.82	-0.94	0.34	0.53	-0.32	0.12	-0.02

Table 3.6: *Spitzer* IRAC3 field-free centre-to-limb variation coefficients.

	I(1.0)	linear	quad		sqrt		non-linear 3			non-linear 4			
Star	[10^3 W m^{-2} sr^{-1}]	a	a	b	a	b	a	b	c	a	b	c	d
F3V	7.27702	0.09	0.06	0.04	-0.00	0.14	0.42	-0.50	0.20	-0.33	1.13	-1.15	0.42
G2V	6.05936	0.13	0.08	0.08	-0.04	0.27	0.53	-0.53	0.18	0.28	-0.06	0.01	-0.00
K0V	5.02453	0.15	0.09	0.08	-0.03	0.28	0.57	-0.56	0.19	0.27	-0.02	-0.01	0.00
M0V	3.80138	0.14	0.07	0.11	-0.09	0.36	0.74	-0.82	0.29	0.44	-0.21	0.06	-0.00
M2V	3.43703	0.14	0.07	0.10	-0.07	0.32	0.64	-0.67	0.23	0.28	0.03	-0.11	0.04

Table 3.7: *Spitzer* IRAC4 centre-to-limb variation coefficients.

	I(1.0)	linear	quad		sqrt		non-linear 3			non-linear 4			
Star	[10^3 W m^{-2} sr^{-1}]	a	a	b	a	b	a	b	c	a	b	c	d
F3V	9.67041	0.07	0.05	0.02	0.02	0.08	0.31	-0.38	0.16	-0.44	1.26	-1.26	0.46
G2V	8.12498	0.10	0.06	0.06	-0.02	0.19	0.38	-0.36	0.12	0.17	0.01	-0.02	0.01
K0V	6.87666	0.12	0.08	0.07	-0.03	0.24	0.48	-0.48	0.16	0.22	0.01	-0.04	0.01
M0V	5.16180	0.13	0.08	0.08	-0.04	0.28	0.53	-0.51	0.17	0.18	0.14	-0.15	0.04
M2V	4.62051	0.11	0.08	0.05	-0.00	0.18	0.35	-0.30	0.09	0.09	0.15	-0.12	0.03

Chapter 4

Magnetic regions on G2V stars

The following chapter is based on work published in Norris et al. (2017) where synthetic spectra from simulated solar-type magnetic regions of various field strengths were calculated and analysed. For Norris et al. (2017), and this thesis chapter, the simulation with 10 snapshots each for hydrodynamic and injected vertical magnetic fields, $\langle B_z \rangle$, of 100 G, 200 G, 300 G, 400 G and 500 G was selected (see description in Sect. 2.1). This set of snapshots allows exploration of a finely spaced range of injected magnetic fields for solar-type stars[1]. In the first part of this chapter, the effect of the injected magnetic field on the structure of the stellar surface is discussed and the resulting synthesised radiation is presented. Finally, the spectral contrasts of the magnetic regions with respect to the non-magnetic snapshots are provided.

4.1 Radiation from magnetic regions on G2V stars

In this section we present the calculated synthetic spectra for solar-type snapshots. We discuss the structures that arise as a consequence of the injection of different magnetic field strengths and how these structures affect the distribution of radiation emerging from the region.

Figures 4.1 and 4.2 show images of the emergent intensities from example snapshots. The two columns of Fig. 4.1 show images of a hydrodynamic simulation (left

[1]For comparison with other spectral types, in Chapters 3 and 5, the six snapshot set with $\langle B_z \rangle$ = 20 G, 100 G and 500 G only, described in Sect. 2.1, is used. The results found from the 6 snapshot set of simulations are very similar to those seen in this chapter. The main differences arise at the wavelengths where the ODF table was updated, as described in Sect. 2.3, i.e., in the UV and a few spectral bands (e.g. around 4.5 μm, the use of old ODFs decreases the field-free mean intensity by almost 5 % compared to using the new ODF).

column, the same snapshot as in Figs. 2.3a, 2.3c, and 3.2) and a 100 G simulation (right column), while Fig. 4.2 shows a 300 G simulation (left column, the same snapshot as in Figs. 2.2, 2.3b and 2.3d) and a 500 G simulation (right column). For both figures, each column contains images at two different viewing angles ($\mu = 1.0$, left, and 0.5, right). Images are displayed for bolometric intensity (top) and for three ATLAS9 wavelength bins centred on 214.5 nm, 387 nm and 1597.5 nm, respectively. These wavelengths were selected to represent regions that typically have distinct behaviour, 214.5 nm, 387 nm and 1597.5 nm are representative of the UV, the NUV to visible transition, and the NIR regions, respectively. The bolometric intensity is plotted in order to display the overall brightness. Visible wavelengths are not shown in this figure, as the irradiance in the visible dominates the bolometric intensity for G2V stars, and therefore would not provide any additional information. The images in Figs. 4.1 and 4.2 have been divided by the mean intensity of all pixels in the hydrodynamic simulations at each limb angle. This removes the effect of limb darkening and allows direct comparison of the differences in structure seen at different viewing angles as well as between non-magnetic and magnetic snapshots. Colour scales vary between wavelength bins so that structures can be seen more easily.

Faculae can be seen to appear between the convective granules in the magnetic images (Fig. 4.2 and right column, Fig. 4.1), whereas in the hydrodynamic images (left column, Fig. 4.1) only bright granules and dark intergranular lanes are seen. The facular regions in the 300 G images align with regions of concentrated magnetic field (see Fig. 2.2 in Sect. 2.1 where B_z at $\tau_{500} = 1$ for the same snapshot). The 3D nature of the solar atmosphere, and particularly the facular regions, described in Sect. 1.3.1, can be clearly seen in the $\mu = 0.5$ images. The shapes of the bright areas change as they are viewed towards the limb. Parts of the faculae are obscured by the granules and the brightness of these regions increases as the hot walls of the faculae come into view (Spruit, 1976). The hot walls correspond to the sides of the background granules (Carlsson et al., 2004; Keller et al., 2004). For a given simulation, the features observed remain the same throughout the wavelength range, however their relative brightness clearly changes. The magnetic bright regions stand out more at shorter wavelengths (see also Fig. 4.6) and in molecular bands such as the CN violet band or the G band where the opacity decreases with increasing temperature, allowing the hot magnetic features to stand out even when seen at disc centre (see, e.g., Schüssler et al., 2003; Shelyag et al., 2004; Sánchez Almeida et al., 2001; Shapiro et al., 2015).

The brightest faculae, at both plotted μ values, have contrasts in excess of a factor of 4 of the average field-free value at 214 nm, whereas at 387 nm this value

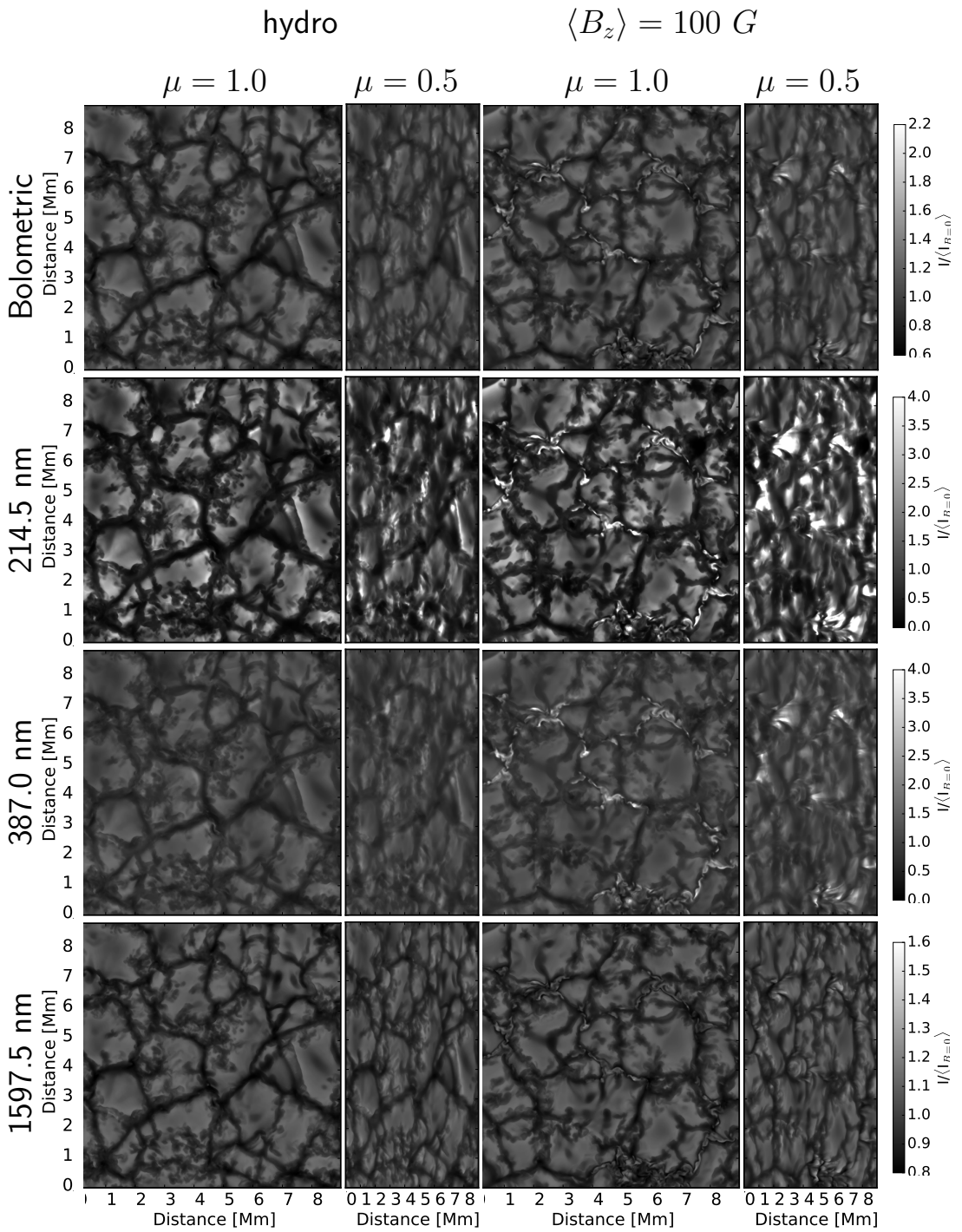


Figure 4.1: Images of the emergent intensities from a G2V simulated atmospheric snapshot divided by the mean intensity of the field-free simulations for the same wavelengths and limb angles. The images are shown for a field-free snapshot (left column) and $\langle B_z \rangle = 100$ G (right column). Two limb distances are shown in each column $\mu = 1.0$ (left) and 0.5 (right). Images from top to bottom: bolometric intensity and intensities for the 214.5 nm, 387 nm and 1 597.5 nm ATLAS9 wavelength bins. Note the different normalised intensity ranges for the different wavelength bins (grey-scale bars on the right). The hydrodynamic snapshot is the same as shown in Fig. 2.3. Credit: Norris et al., A&A, 605, A45, 15pp., 2017, reproduced with permission © ESO.

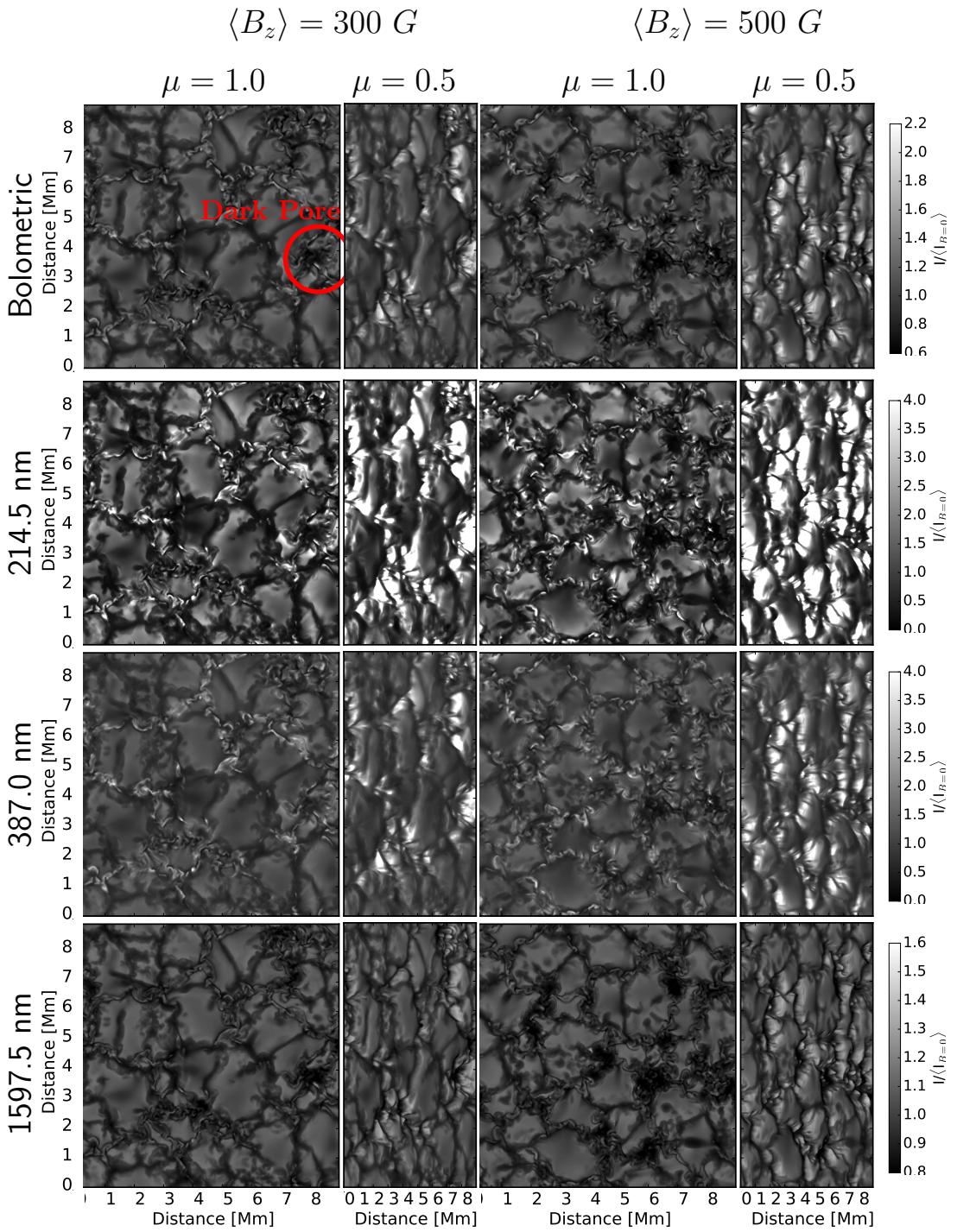


Figure 4.2: Images of the emergent intensities from a G2V simulated atmospheric snapshot divided by the mean intensity of the field-free simulations for the same wavelengths and limb angles. Same as Fig. 4.1 but for $\langle B_z \rangle = 300$ G (left column) and $\langle B_z \rangle = 500$ G (right column). The $\langle B_z \rangle = 300$ G snapshot is the same as shown in Fig. 2.3. The red circle and label indicate an example of a dark magnetic feature. Note the different normalised intensity ranges for the different wavelength bins (grey-scale bars on the right). Credit: Norris et al., A&A, 605, A45, 15pp., 2017, reproduced with permission © ESO. Fig. C.1, in Appendix A, shows equivalent images from the remaining injected magnetic field simulations.

is reached only at $\mu = 0.5$. This is in qualitative agreement with the results of the SuFI imager (Gandorfer et al., 2011) on the Sunrise balloon-borne solar observatory (Solanki et al., 2010; Barthol et al., 2011; Berkefeld et al., 2011), which delivered seeing-free, high-resolution UV images with low scattered light. Thus Riethmüller et al. (2010) found contrasts of up to a factor of 5 at 214 nm, but only up to a factor of 2.4 at 388 nm. Note that the observational values are somewhat lower than in the magnetoconvection simulations due to the influence of the point-spread function of the telescope on the observations (Riethmüller et al., 2014).

In the 300 G snapshot, and in snapshots with larger initial vertical magnetic fields ($\langle B_z \rangle = 400$ G shown in Appendix C, and $\langle B_z \rangle = 500$ G in Fig. 4.2), additional dark magnetic features, larger than faculae, can be seen at $\mu = 1$. An example of one of these dark features is circled, in red, in the $\langle B_z \rangle = 300$ G bolometric image in Fig. 4.2. These are small pores and have a broadly similar magnetic structure to that of facular magnetic concentrations in that both are often described by flux tubes or flux sheets (Spruit & Zwaan, 1981). For this particular example, when viewing at $\mu = 0.5$ the hot wall can be clearly seen. The mechanism for the production of dark pores is described in Section 1.3.1.

A histogram of the intensities between 150 and 3 000 nm in the ATLAS9 frequency bins of all 2 621 440 pixels from all ten disc-centre hydrodynamic snapshots is shown in the top panel of Fig. 4.3. The same type of histogram for all ten disc-centre snapshots with $\langle B_z \rangle = 300$ G is shown in the bottom panel. Logarithmic values of the counts of pixels in each bin are indicated by the colour bar. Each histogram is overlaid with a solid black line displaying the mean intensity spectrum of all pixels in the corresponding set of simulations (same μ and $\langle B_z \rangle$); dotted lines indicate the 5th and 95th percentile of the pixel intensities. Histograms of the pixel values normalised by the total mean intensity spectra are shown in the Appendix, Fig. C.2, for easier interpretation of the fractional variations. The histograms in Fig. 4.3 reveal the distribution of emergent intensities across a snapshot to be asymmetric and highly non-Gaussian.

A broadening of the histogram in intensity can be seen in the visible wavelengths, where the mean intensity is largest. Much less spread in absolute intensity is seen at longer wavelengths, and in the UV. This is due to the lower values of emergent intensities at these wavelengths. The spread of intensities relative to the mean value is in fact larger in the UV than in the visible. This will be discussed in more detail later in this section. The histograms tend to be narrower at positions where spectral lines appear in the mean spectrum, e.g., at Hα (~ 656 nm). These spectral lines lower the intensity significantly and are strongly saturated, i.e., even

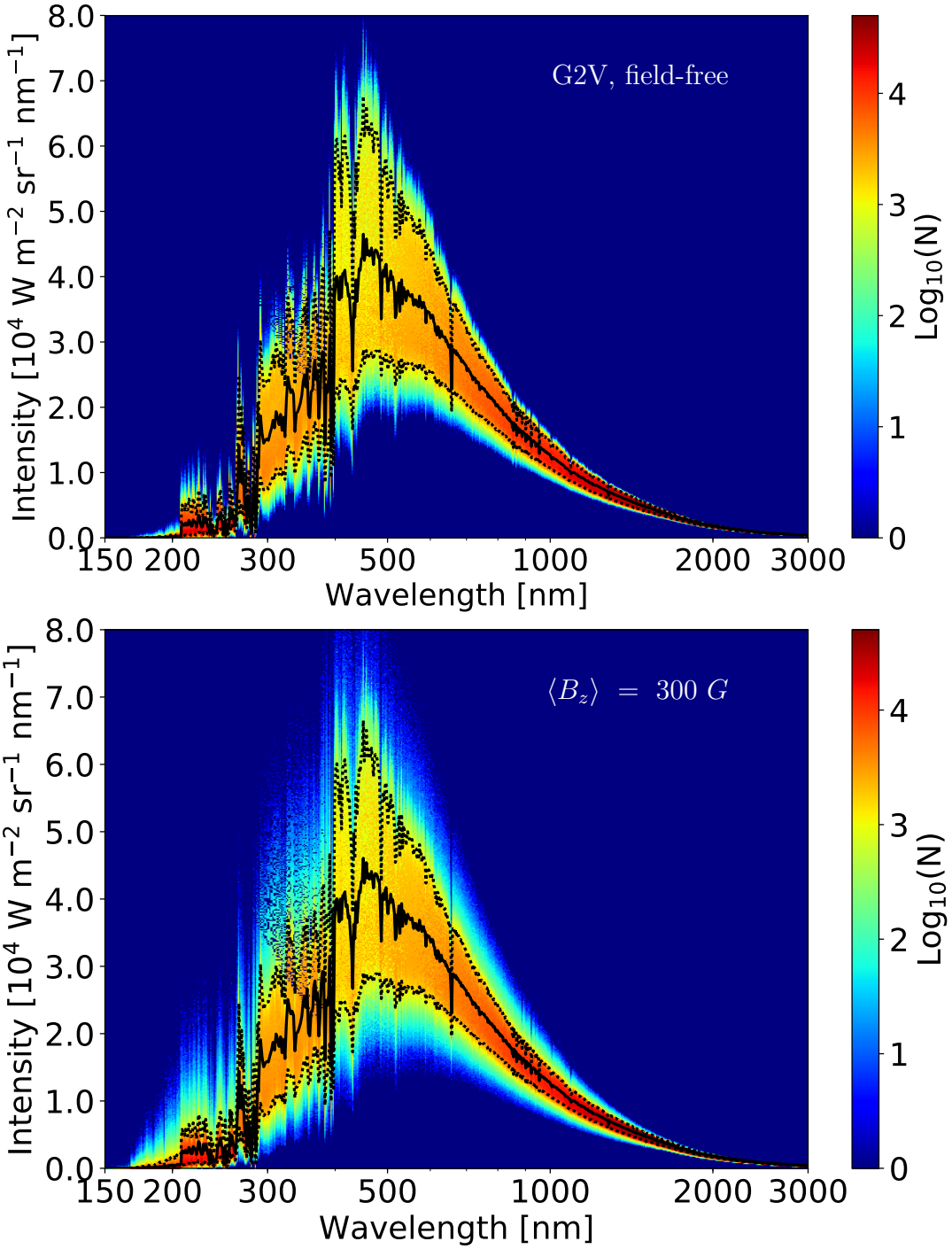


Figure 4.3: Histograms of intensity in each ATLAS9 wavelength bin for all pixels in all G2V snapshots for a given $\langle B_z \rangle$ at disc centre. The field-free histogram is shown in the top panel, while the $\langle B_z \rangle = 300$ G histogram is shown in the bottom panel. The mean intensity spectra of all pixels in all corresponding simulations overlaid in a solid black line and the 5th and 95th percentile overlaid in dotted black lines. The intensity bin size is 30 W m^{-2} sr^{-1} nm^{-1}. The wavelength bins are various sizes, as detailed in Section 2.3, and are displayed in log space. Histograms of the pixel values normalised by the total mean intensity spectra are shown in the Appendix, Figure C.2.

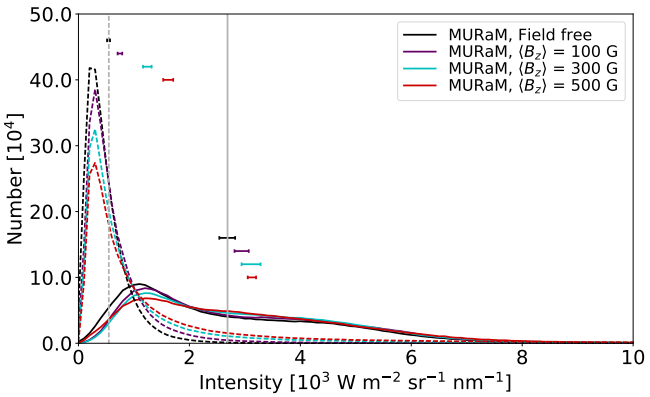
large fluctuations in temperature will not produce significant changes in the line core intensities, leading to less variation in intensities across the simulations.

The tails of the 300 G snapshot histograms are extended in intensity compared with the hydrodynamic simulations. Note the larger green-blue shaded region in the lower frame of Fig. 4.3 compared with the upper frame. Because of the logarithmic scale, these wings correspond to relatively few pixels. This is illustrated in more detail in Fig. 4.4 where we show example histograms at two limb distances ($\mu = 0.5$ and 1.0) at four different wavelengths for the non-magnetic (black), 100 G (purple), 300 G (cyan) and 500 G (red) magnetic snapshots. The field-free mean intensities for each limb distance are indicated by vertical grey lines. Minimum and maximum values from the mean intensities over each of the 10 single snapshots are shown in the corresponding colour as horizontal bars. The four panels show, from top to bottom, histograms for wavelength bins centred on 214.5 nm, 387 nm, 601.0 nm and 1 597.5 nm (referred to as 1.6 μm), i.e., in the UV, NUV, visible and NIR. Note the different intensity bin widths used for the different wavelengths, these bin widths are listed in the caption.

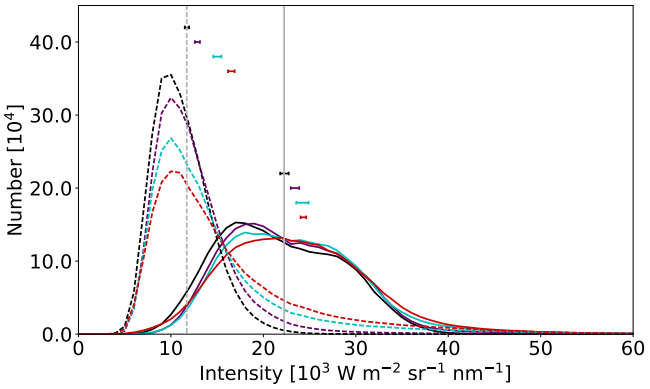
At disc centre, the intensity distribution of the non-magnetic snapshots clearly shows the signature of convection: the distributions for all of the wavelengths shown are double peaked with the peak at lower intensities capturing predominantly pixels in the dark intergranular lanes and the peak at higher intensity values capturing pixels in the bright granules. This bimodal distribution of intensities does not necessarily indicate a more variable region. Granules, and therefore intergranular lanes will tend to reemerge in the same positions, leading to a similar distribution of emergent intensities across the region for the timescales investigated here.

At 601 nm, the dark and bright peaks caused by convection are centred at intensities approximately 15% below and above the mean intensity in the non-magnetic snapshots (see solid black line in Fig. 4.4(c)). As $\langle B_z \rangle$ increases, the distributions tend towards a more centrally peaked shape, with slightly longer tails at lower intensities. This is consistent with results found by Afram et al. (2011). The field-free and magnetic simulations have comparable disc-centre intensities with minimal extension in the tails (compared to at the limb) because small-scale features here have low contrast relative to the quiet Sun, therefore very little dynamic range is added.

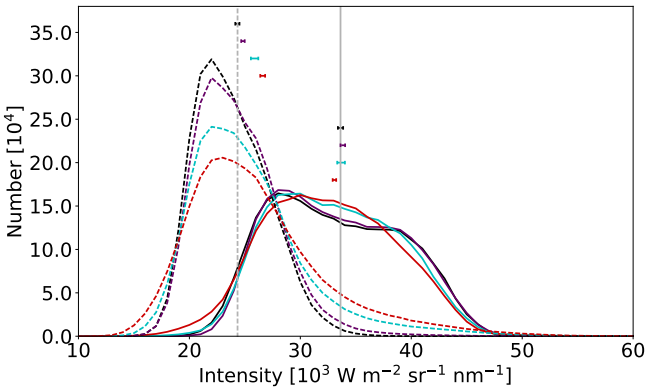
Similar behaviour is seen at disc centre for the CN violet band at approximately 387 nm, though the histogram distributions are wider and show more extended high-intensity tails, especially for simulations with $\langle B_z \rangle \geq 300$ G. Schüssler et al. (2003) found that the high temperature and low density in magnetic regions strongly reduces the concentration of molecules, reducing the absorption at their associated



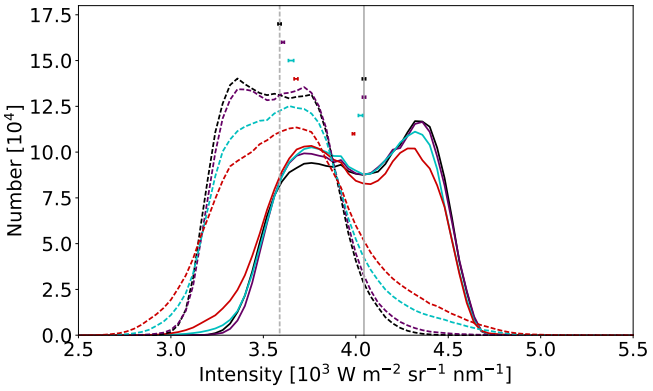
(a) 214.5 nm



(b) 387 nm



(c) 601 nm



(d) 1597.5 nm

Figure 4.4: Histograms of intensity for all pixels in all G2V snapshots for a given $\langle B_z \rangle$, as shown in the legend. The field-free mean intensities (averaged over all field-free snapshots) are marked by grey vertical lines. Minimum and maximum values of the mean intensities of the individual snapshots, separated by $\langle B_z \rangle$, are indicated by horizontal bars. Also shown are histograms of snapshot-averaged intensities for simulations with $\langle B_z \rangle$ of 100 G (purple), 300 G (cyan) and 500 G (red). The histograms are shown at two different limb positions: $\mu = 1.0$ (solid curves) and $\mu = 0.5$ (dashed curves). Fig. 4.4a shows histograms for a wavelength of 214.5 nm with a bin width of 100 W m^{-2} sr^{-1} nm^{-1}. Figs. 4.4b and c show wavelengths of 387 nm and 601 nm, respectively, with a bin width of 1×10^3 W m^{-2} sr^{-1} nm^{-1}. Fig. 4.4d shows the wavelength of 1 597.5 nm with a bin width of 40 W m^{-2} sr^{-1} nm^{-1}. Both the x and the y scale vary between graphs.

wavelengths, and therefore increasing the brightness compared to the surrounding photosphere. Schüssler et al. (2003) look specifically at the G-band, caused by CH molecules, but it is expected that this mechanism is relevant for other molecules in stellar atmospheres.

The disc-centre intensity distribution at 214.5 nm, relative to the mean intensity of the boxes, is very broad. The dominant lower-intensity peak (at approximately 60% of the mean intensity, $\langle I_{215} \rangle$) weakens gradually with increasing magnetic field. The secondary bright peak (centred near $2\langle I_{215} \rangle$) is very extended with tails stretching to beyond $4\langle I_{215} \rangle$, as discussed for the images earlier in this section. This large spread is due to the high temperature sensitivity of the radiation at short wavelengths and the large number of spectral lines present in the UV.

In parts of the NIR, and in particular around 1.6 μm, deeper atmospheric layers are seen due to the H^- opacity being at a minimum for these wavelengths. As illustrated by the histograms at 1597.5 nm shown in Fig. 4.4(d), the disc-centre histograms at this wavelength are strongly double peaked with the brighter peak dominating. This difference between the histograms in the visible and NIR is likely due to the narrowing of intergranular down-flow lanes with depth, leading to fewer pixels in the low intensity peak of the NIR histogram, where deeper layers of the atmosphere are observed. Additionally, the spread of intensities at this wavelength is much smaller than for 601 nm leading to higher peaks for both low and high intensities.

At smaller μ (dashed lines in Fig. 4.4) the distributions for the wavelengths shown here are shifted to lower intensities due to limb darkening. At the same time, the distributions become more single peaked with narrower central widths but more extended tails, particularly for the high-intensity tails. Although the width of the peaks at $\mu = 0.5$ are narrower than at disc centre, the largest intensities seen in the tails match, or exceed, those seen at disc centre. At 1.6 μm, where radiation emerges from deeper layers, the distribution retains its double-peaked shape further towards the limb and can still be seen for small $\langle B_z \rangle$ at $\mu = 0.5$. This wavelength also shows much less of a high-intensity tail than the other wavelengths displayed.

Towards the limb, the counts in the peaks for all wavelengths decrease significantly with increasing $\langle B_z \rangle$: the tails are lengthened both towards brighter and darker intensities, though with a larger effect on the higher intensities. This effect of lengthening tails with increasing $\langle B_z \rangle$ is due to the magnetic field introducing a larger variety of atmospheric structures. As the magnetic field increases, larger and more numerous magnetic features begin to appear. Hot walls associated with the magnetic features are more visible towards the limb of the star which gives rise to

the lengthened tails at high intensities. Dark lanes arise by the faculae due to the cool gas above the neighbouring granules and in the magnetic flux tube dominating the radiation in these pixels and increasing the length of the low-intensity tail as seen in Keller et al. (2004) and Carlsson et al. (2004). For more detail on these limb effects, see Section 1.3.2.

For a given mean magnetic field, the shape of an individual snapshot's intensity histogram is very similar to that of the full histogram that combines all snapshots. The mean intensity value, however, changes slightly from one snapshot to another, reflecting the evolving granulation. The minimum and maximum values shown by horizontal bars in Fig. 4.4 give the range of temporal variations of the mean intensities of the ten snapshots of a given initial $\langle B_z \rangle$. These ranges are based on subsets of ten snapshots from each simulation, though for each subset, the mean effective temperature and its standard deviation are typically representative of the full relaxed phase of the simulations (see Sec. 2.1).

The temporal variations of the mean intensity are much smaller than the spatial variations displayed within a snapshot. Relative to the mean intensity, the temporal variations show very little dependence on the viewing angle or mean magnetic field. Temporal variability is larger for shorter wavelengths, particularly in the UV, due to the larger dependence on temperatures of the Planck function at shorter wavelengths. The many spectral lines and the higher layers of the atmosphere from which the radiation arises also contribute.

4.2 Contrasts of magnetic regions on G2V stars

As faculae often appear in groups and can rarely be fully resolved in observations, contrasts were calculated based on the mean spectra of all pixels in all MURaM snapshots of a given $\langle B_z \rangle$ and μ, including those in the granules, i.e., with small magnetic field strengths and low, but positive, contrasts. The contrasts were calculated relative to the total mean over all the hydrodynamic snapshots at the same limb distance, μ,

$$C(\langle B_z \rangle, \lambda, \mu) \; = \; \frac{I(\langle B_z \rangle, \lambda, \mu) - I(0, \lambda, \mu)}{I(0, \lambda, \mu)}. \tag{4.1}$$

$C(\langle B_z \rangle, \lambda, \mu)$ is the spectral contrast for a given average vertical magnetic field, $\langle B_z \rangle$, and limb angle, μ; $I(\langle B_z \rangle, \lambda, \mu)$ is the mean spectral intensity over all pixels in all simulations for $\langle B_z \rangle$, at a given μ; and $I(0, \lambda, \mu)$ is the mean spectral intensity over all pixels in all hydrodynamic boxes at a given μ. This approach was chosen

with stellar applications in mind, where the spatial resolution is low (at best) and hence spatially averaged intensities and contrasts are more appropriate. It is worth noting that by averaging over a large area, we take into account not only the bright component of the magnetic features, but cover all the types of magnetic features that are created for a given spatially averaged magnetic field. Therefore, in that sense our "facular" contrasts for the large flux simulations can be somewhat different from what stellar astronomers traditionally consider them to be, i.e., the purely bright component.

The complicated nature of the dependence of contrast on wavelength, average vertical magnetic field and limb distance can be seen in Figs. 4.5 and 4.6. Figure 4.5 shows the spatially averaged contrasts for given injected vertical magnetic fields, $\langle B_z \rangle$, of 100 G (magenta), 200 G (blue), 300 G (cyan), 400 G (orange) and 500 G (red) as they vary with limb angle, for wavelengths of 214.5 nm (top), 387 nm (middle top), 601 nm (middle bottom) and 1597.5 nm (bottom). The black curves are contrasts derived from the 1D facular model used in the SATIRE solar irradiance reconstructions that is based on the FAL P model by Fontenla et al. (1993). As Fontenla et al. (1993) do not provide the average magnetic field strength to which the FAL P model refers to, it is unclear to which of the simulation curves the 1D model should be compared. For that reason we have also multiplied the contrast with 0.25 (corresponding to a filling factor of 25% of FAL P) and have plotted these curves for comparison. The coloured shaded regions show the standard deviation of the spatially averaged contrasts calculated by propagating the standard deviations of the means of the snapshot intensities, including both the given $\langle B_z \rangle$ and the hydrodynamic values. The shaded regions thus provide a view of the short term temporal variation of the spatially averaged contrasts.

Figure 4.5 shows that the mean contrast tends to increase as limb distance decreases. The steepness of these increases varies with both $\langle B_z \rangle$ and wavelength. An exception are contrasts in the UV, as illustrated in the top plot at 214.5 nm, where the mean contrast levels off at $\mu = 0.3$ for most magnetisations and begins to decrease again between $\mu = 0.3$ and 0.2. This has been explained by the theory of magnetic flux tubes. When observed at an angle towards the limb, the hot walls of the faculae come into view and the contrast increases. The contrast reaches a maximum value and begins to decrease further towards the limb as the hot wall begins to be obscured by the granules lying immediately in front of the flux tube (Spruit, 1976). This effect has been observed on the Sun (e.g., Auffret & Muller, 1990; Ortiz et al., 2002; Yeo et al., 2013). As illustrated by the black lines, 1D atmospheric models cannot account for the obscuration and thus produce unrealistically steep

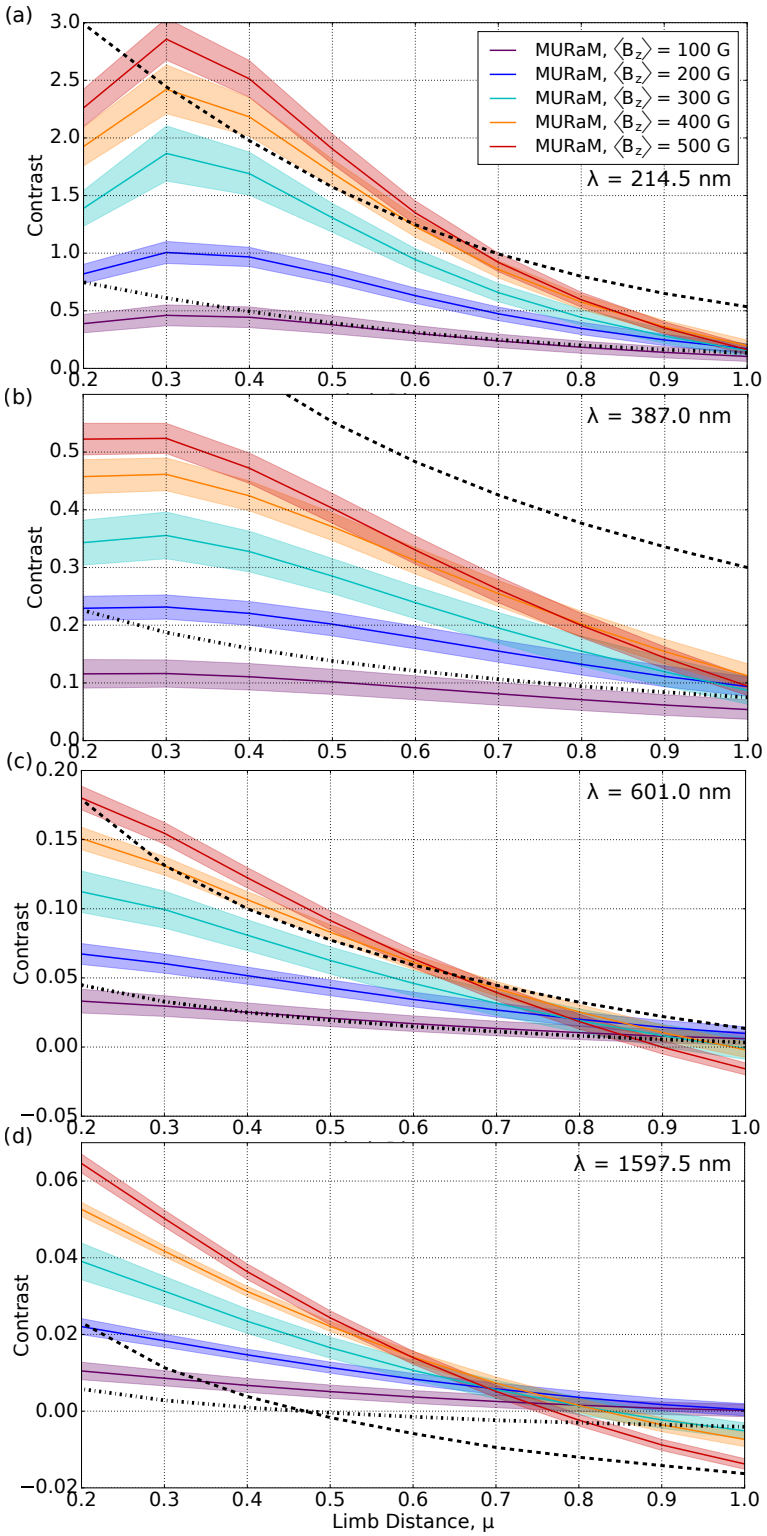


Figure 4.5: The average contrast as a function of limb distance, μ, of all pixels for all G2V snapshots of a given $\langle B_z \rangle$ relative to the average intensity of the hydrodynamic snapshots. These are shown for 214.5 nm (a), 387 nm (b), 601 nm (c) and 1 597.5 nm (d). The shaded regions show the spread calculated from the standard deviations of the means of the snapshots at each μ, incorporating both the magnetic and hydrodynamic spreads. Colours corresponding to $\langle B_z \rangle$ are given in the legend of the figure. The dashed and dash-dotted lines show contrasts derived for a 1D facular model of unspecified magnetic field strength with 100 % and 25 % filling factor, respectively (see text in Sects. 1.3.2 and 4.2 for descriptions of 1D model). Credit: Norris et al., A&A, 605, A45, 15pp., 2017, reproduced with permission © ESO.

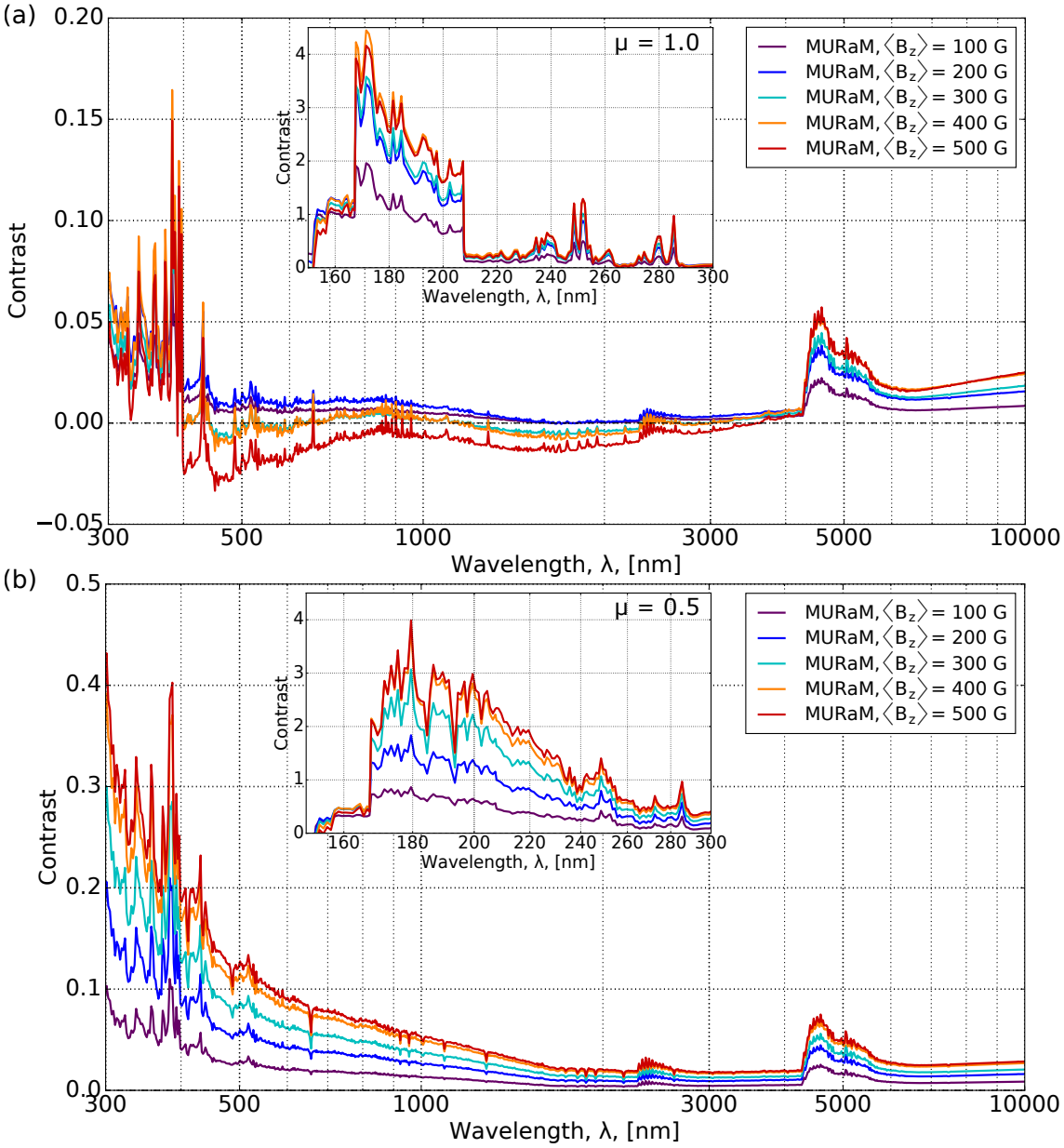


Figure 4.6: The average contrast spectra of all pixels for all G2V snapshots of a given $\langle B_z \rangle$ relative to the average of the hydrodynamic snapshots shown for a wavelength range of 150 nm to 10 000 nm. The main plots show wavelengths of 300 nm to 10 000 nm using logarithmic x axes, while the insets show 150 nm to 300 nm using linear axes. These are shown at $\mu = 1.0$ (top) and $\mu = 0.5$ (bottom). Note the different vertical scales. Credit: Norris et al., A&A, 605, A45, 15pp., 2017, reproduced with permission © ESO.

contrasts near the limb.

Contrasts are much larger in the UV than in the visible and IR (note the difference in y axis scales in Fig. 4.5). Mean contrasts at 214.5 nm reach a value of approximately three at $\mu = 0.3$ when $\langle B_z \rangle = 500$ G, while at 601 nm in the visible the largest mean contrast remains below 0.2. The UV also shows most temporal variability, i.e., the range of contrasts observed across a series of snapshots is much larger than at 601 nm or 1597.5 nm.

A more detailed view of the wavelength dependence is shown in Fig. 4.6, where wavelengths of 150 nm to 10 000 nm are displayed for disc centre, $\mu = 1$ (top), and at $\mu = 0.5$ (bottom). The colour coding for the different $\langle B_z \rangle$ values is the same as in Fig. 4.5. Figure 4.6 illustrates the larger contrast in the UV, particularly at $\mu = 0.5$, where contrasts at ~ 200 nm reach levels approximately 10–20 times those seen in the visible.

Towards the limb, contrasts are always positive and increase for larger $\langle B_z \rangle$ values (see also Fig. 4.5). This holds for all wavelengths, down to approximately 170 nm, displayed in the bottom plot of Fig. 4.6 where the $\mu = 0.5$ contrast spectra are shown. However, towards disc centre, the relationship with $\langle B_z \rangle$ is more complex (see Fig. 4.6(a)). Below 400 nm and above roughly 4000 nm, contrasts are always positive. For wavelengths between 400 nm and approximately 1500 nm, contrasts initially increase as $\langle B_z \rangle$ increases from 100 G to 200 G, but then decrease for stronger fields and become negative when $\langle B_z \rangle$ reaches 500 G. As magnetic field in the region increases, more large, dark concentrations of magnetic field emerge, as seen in the images in Fig. 4.2. When dark features emerge, the mean contrast of the region decreases. When enough pixels are contained within dark features, they counteract the effect of the bright features, causing the contrast to become negative. In the UV and the IR the bright features have higher contrast, increasing the threshold for dark features to cause the total mean contrast to be negative. At 1.6 μm, close to the H^- opacity minimum, features that are bright at most wavelengths appear low contrast, therefore, contrasts for all $\langle B_z \rangle$ are very low or negative at this wavelength.

The 'turnover' and sign change of the visible and NIR contrast with increasing magnetic field is not accounted for in irradiance variability models that use 1D modelled facular contrasts. In SATIRE, for example, the 1D contrasts are linearly scaled with the observed magnetic field, up to a saturated magnetic field strength. This means that larger measured magnetic fields, up to this saturated value, lead to larger (positive or negative) contrasts that always maintain their sign. This is illustrated in Fig. 4.5 where the dashed and dot-dashed lines illustrate two different

scalings; such linear scaling fails to capture the changing limb dependence of the contrast as a function of magnetic field.

In Fig. 4.6 some spectral features stand out. For example, a marked rise in contrast is seen between approximately 4300 and 5500 nm and, to a lesser extent, also around 2300 nm. Both regions are dominated by rovibrational CO lines (Wallace et al., 1996) that are sensitive to the atmospheric structure near the temperature minimum (Noyes & Hall, 1972; Uitenbroek et al., 1994). A large jump is also seen at 400 nm at disc centre, which is due to the hydrogen Balmer series absorption edge (364.6 nm) and multiple absorption lines including the Ca II H and K lines (396.9 nm and 393.4 nm respectively), and the CN violet system (385.8 and 388.8 nm). Below 300 nm, in the insets, multiple spectral lines are seen. Of particular note are the Mg II h & k lines at 279.6 nm and 280.3 nm, that combine to form a peak at 280 nm, as well as the Mg I line at 285.2 nm. A large jump is seen at 208 nm at disc centre, this is an aluminium absorption edge.

The contrasts derived compare well with those measured by Yeo et al. (2013), where continuum intensity contrast with respect to the quiet Sun over a resolution element in SDO/HMI was measured near the 617.3 nm Fe spectral line. Contrast measurements in Yeo et al. (2013) are grouped in terms of $\frac{\langle B_l \rangle}{\mu}$, where $\langle B_l \rangle$ is the unsigned longitudinal magnetogram signal, a measure of the magnetic field in the direction of the line of sight. As the magnetic field in features, such as faculae, is approximately radial, only the line of sight component of the field is measured in these observations. The magnetic field is, therefore, scaled by $\frac{1}{\mu}$ to better represent the radial field within the features. Figure 4.7 shows the solar centre-to-limb continuum contrasts measured by Yeo et al. (2013) with solid lines compared with the centre-to-limb contrasts at 617 nm calculated from the G2V simulations used in this chapter, shown by dashed lines. The magnetic field values shown, $\frac{\langle B_l \rangle}{\mu}$ in the case of Yeo et al. (2013) and $\langle B_z \rangle$ (i.e., the injected magnetic field in the radial direction) in the case of the simulations, are 100, 200, 300, 400 and 500 G, represented by the colours in the figure legend. The figure shows that across magnetic field, the simulations and measurements have similar ranges for $\mu > 0.5$.

For positions closer to the limb, the measurements indicate a levelling and then a decrease in contrast beyond $\mu = 0.3$ that are absent in simulations at 617 nm. Differences are expected in exact values as our derived contrasts are taken by averaging over a larger area than the spatial resolution of measurements taken by Yeo et al. (2013). Additionally, for the contrasts used here, only the initial average vertical (radial) magnetic field is considered, whereas Yeo et al. (2013) consider the line-of-sight magnetic field measured in a single spectral line, Fe I 617.3 nm, (which

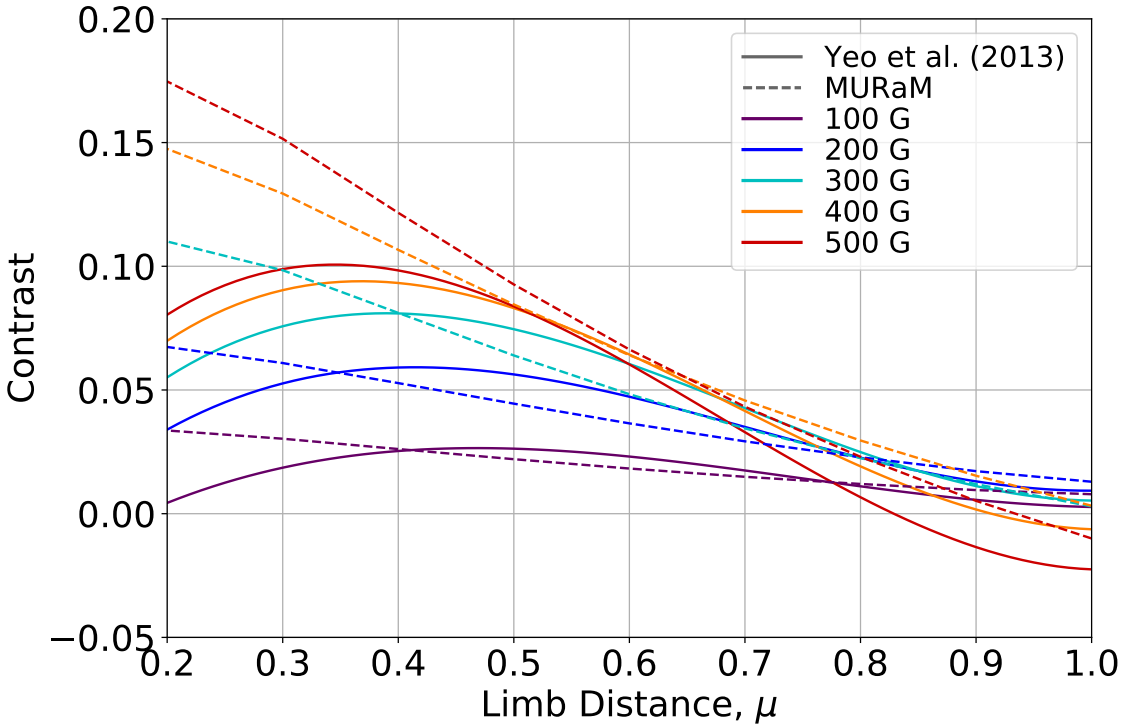


Figure 4.7: The average contrast centre-to-limb variations (CLV) of all pixels for all G2V snapshots (dashed lines) of a given $\langle B_z \rangle$ (given by different colours shown in the legend) relative to the average of the hydrodynamic snapshots for a wavelength of 617.0 nm. These are plotted with fits to measured facular contrasts from Yeo et al. (2013) (solid lines) for $\frac{\langle B_l \rangle}{\mu}$ values (given by different colours shown in the legend) that match the $\langle B_z \rangle$ run with MURaM. Note that the resolution of the measurements are different from those of the MURaM average contrast CLV.

corresponds to a specific atmospheric height). Although the latter is scaled by $\frac{1}{\mu}$ to better represent the radial magnetic field, the magnetic fluxes in the two studies are not directly comparable.

Chapter 5

Contrasts of magnetic regions on M2V to F3V stars

Magnetic regions on low-mass main-sequence stars other than the Sun are currently unresolvable. To understand how magnetism affects the variability of other spectral types, simulations must be used to predict the features that can arise and the effects they can have on the observed variability. This chapter explores differences in the radiation emitted from simulated magnetic regions on various main-sequence spectral types from M2V to F3V. The snapshots used are from the magnetic companion simulations to the field-free ones presented in Chap. 3. Disc-centre variations in spectra are addressed in Section 5.1. Limb effects are discussed in Section 5.2. Finally, the mean contrast spectra, described by Eq. 4.1 in Chap. 4, and limb-dependence of these are explored in Section 5.3. The mean contrast spectra are used to compare different spectral types and activities for regions of otherwise similar properties (e.g., the number of granules). The spectral types compared in this section are characterised by different effective temperatures, $T_{\rm eff}$, and strengths of gravitational acceleration, $\log g$, defined in Table 2.1.

5.1 Effect of the stellar spectral type on disc centre snapshots

5.1.1 Images

Figures 5.1 to 5.4 show disc-centre images of a snapshot of each of the spectral types at four different wavelengths: 214.5 nm, 387 nm, 601 nm and 1 597.5 nm from top to bottom. As in Chapter 4, these wavelengths were selected to represent a

variety of regions in wavelength space with typically distinct behaviour. The image at 601 nm is shown in place of the bolometric images seen in Chap. 4 as the visible does not dominate the bolometric intensity for all stellar spectral types. I want to stress that all calculations have been carried out under the assumption of LTE. This means that the results presented for the UV (in particular for wavelengths below about 300 nm) can at best be taken as indicative and will need to be confirmed with more detailed and time-consuming nLTE calculations. In the solar case, the UV variability between 1D facular and quiet-Sun atmospheres is well captured even with LTE calculations, even though absolute intensities are not (see Krivova et al., 2006; Yeo et al., 2014). The columns in Figs. 5.1 to 5.4, from left to right, show field-free, $\langle B_z \rangle = 100$ G and $\langle B_z \rangle = 500$ G snapshots. The colour bars to the right of the images indicate the intensity. Note that this colour scale changes for each spectral type and wavelength. When magnetic field is injected into the simulation, convective motions of the plasma sweep the flux into the intergranular lanes. The images in Figs. 5.1 to 5.4 show the variety of features that emerge, and how these differ across spectral types.

For all spectral types, granulation, caused by convection, is seen (see Sect. 1.3 for more detail). For K0V to M2V stars for all field-free and magnetic snapshots in the UV (e.g., images of 214.5 nm in the top rows of Figs. 5.2 to 5.4), granules appear dark and the intergranular lanes appear bright. This is known as reversed granulation. This occurs due to the reversal of horizontal temperature fluctuations in the middle to upper photosphere due to the balance of adiabatic expansion and radiative heating, as described in Cheung et al. (2007). These intergranular lanes appear much wider in the UV, where they are bright, than at other wavelengths shown in Figs. 5.2 to 5.4, this is due to the pressure in the atmosphere being lower at the height where UV radiation is formed leading to more diffuse features.

For all stars, with an injected vertical magnetic field, $\langle B_z \rangle$, of 100 G, mainly bright features are present. In some selected wavelength regions, the predominantly bright features occasionally appear dark or show very low contrast compared to the granules, particularly near 1.6 μm. This is due to this wavelength being close to the H^- opacity minimum, as seen for G2V stars in chapter 4. The low opacity at this wavelength region allows radiation from deeper in the star to emerge, meaning radiation seen in the granules will be produced in a hotter layer, and its intensity more likely to match or exceed that of the radiation from the magnetic feature. For $\langle B_z \rangle = 500$ G, in addition to bright features, larger dark features emerge for all spectral types, these vary in size, number and spectral dependence, as discussed in the following paragraphs. The resulting contrast of a magnetic region is produced

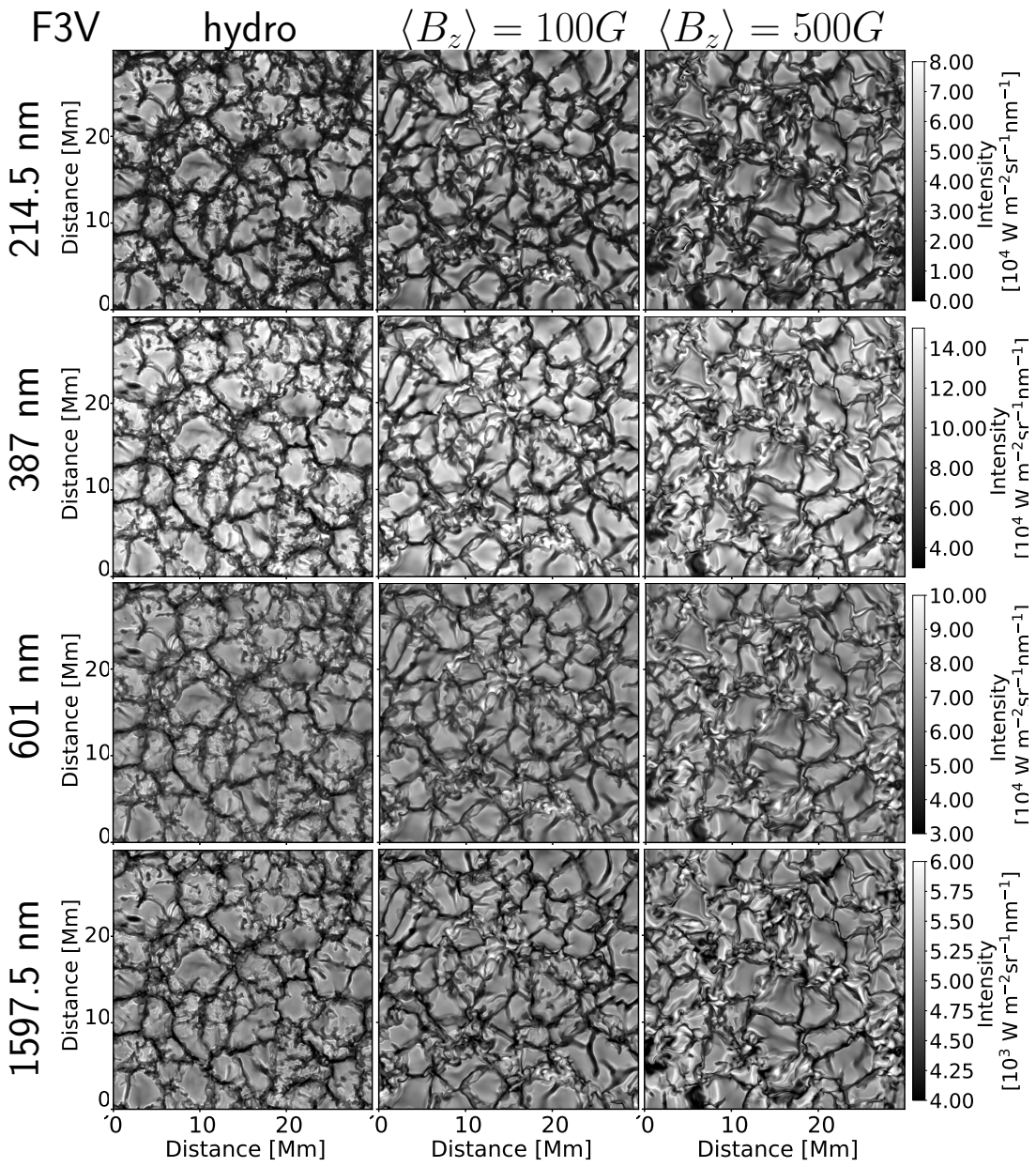


Figure 5.1: Images of the disc-centre emergent intensities from F3V simulated atmospheric snapshots. The images are shown for a field-free snapshot (left column), $\langle B_z \rangle = 100$ G (middle column) and $\langle B_z \rangle = 500$ G (right column). Rows show ATLAS9 wavelength bins of 214.5 nm, 387 nm, 601 nm and 1 597.5 nm from top to bottom respectively. Note the different normalised intensity ranges for the different wavelength bins (grey-scale bars on the right).

by the sum of these dark and bright features.

The F3V snapshot, in Fig. 5.1, shows very few high contrast features for both injected vertical magnetic field strengths, although the number of bright magnetic features does increase with increasing field strength. The lack of bright magnetic features in these F3V snapshots compared to the snapshots of other spectral types

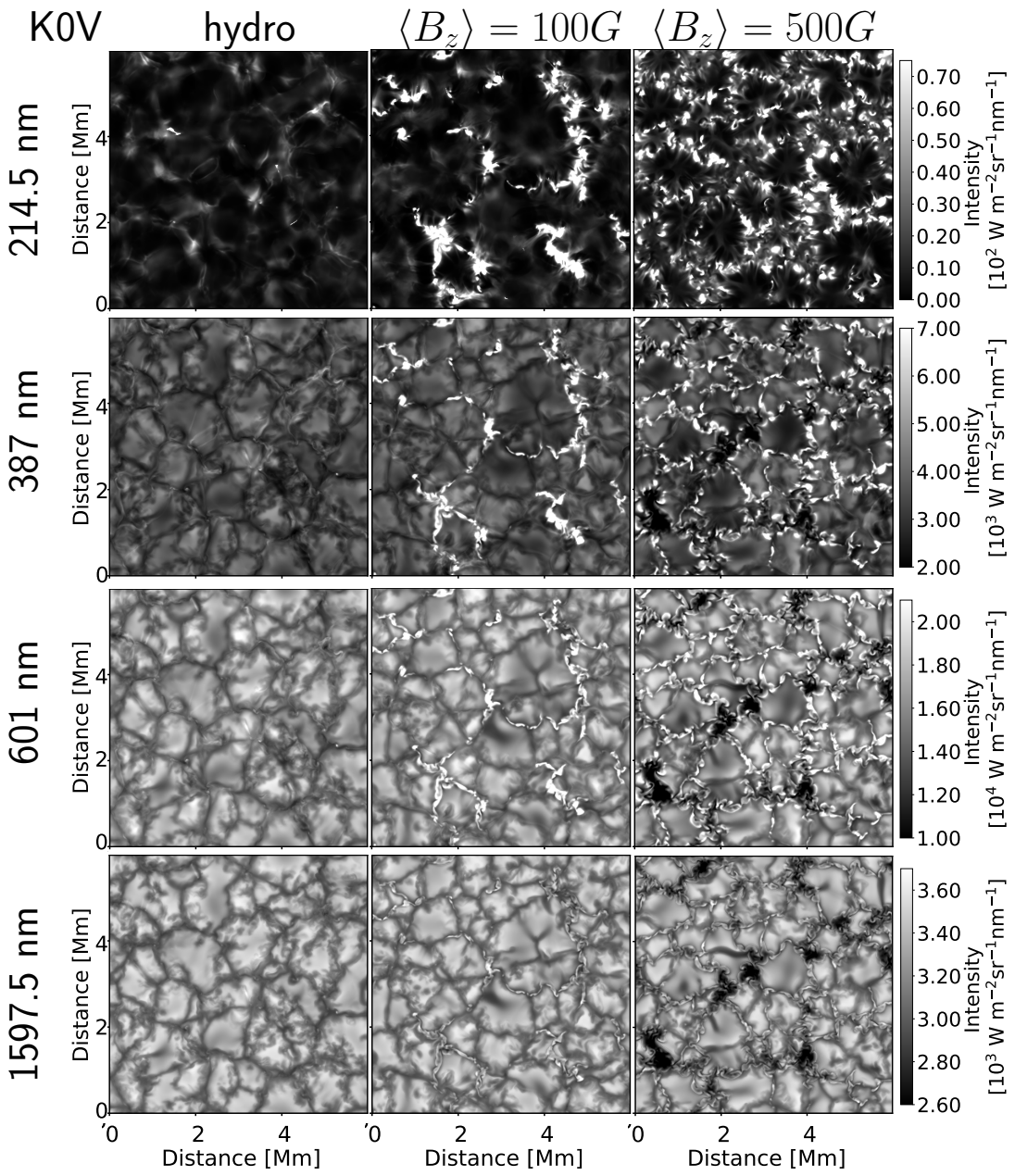


Figure 5.2: Images of the disc-centre emergent intensities from K0V simulated atmospheric snapshots. Same as Fig. 5.1 for K0V snapshots.

with the same injected magnetic fields could, in part, be due to the lower spatial resolution of the F3V simulations (e.g. the F3V resolution elements are approximately five times larger than those of the K0V simulations), meaning that small magnetic features may be unable to manifest themselves. This could be tested in the future by comparing to a similar F3V simulation with higher spatial resolution. At $\langle B_z \rangle = 500$ G some small dark features emerge, seen most clearly in the bottom left of the snapshot. Only a small number of dark features are seen for this spectral

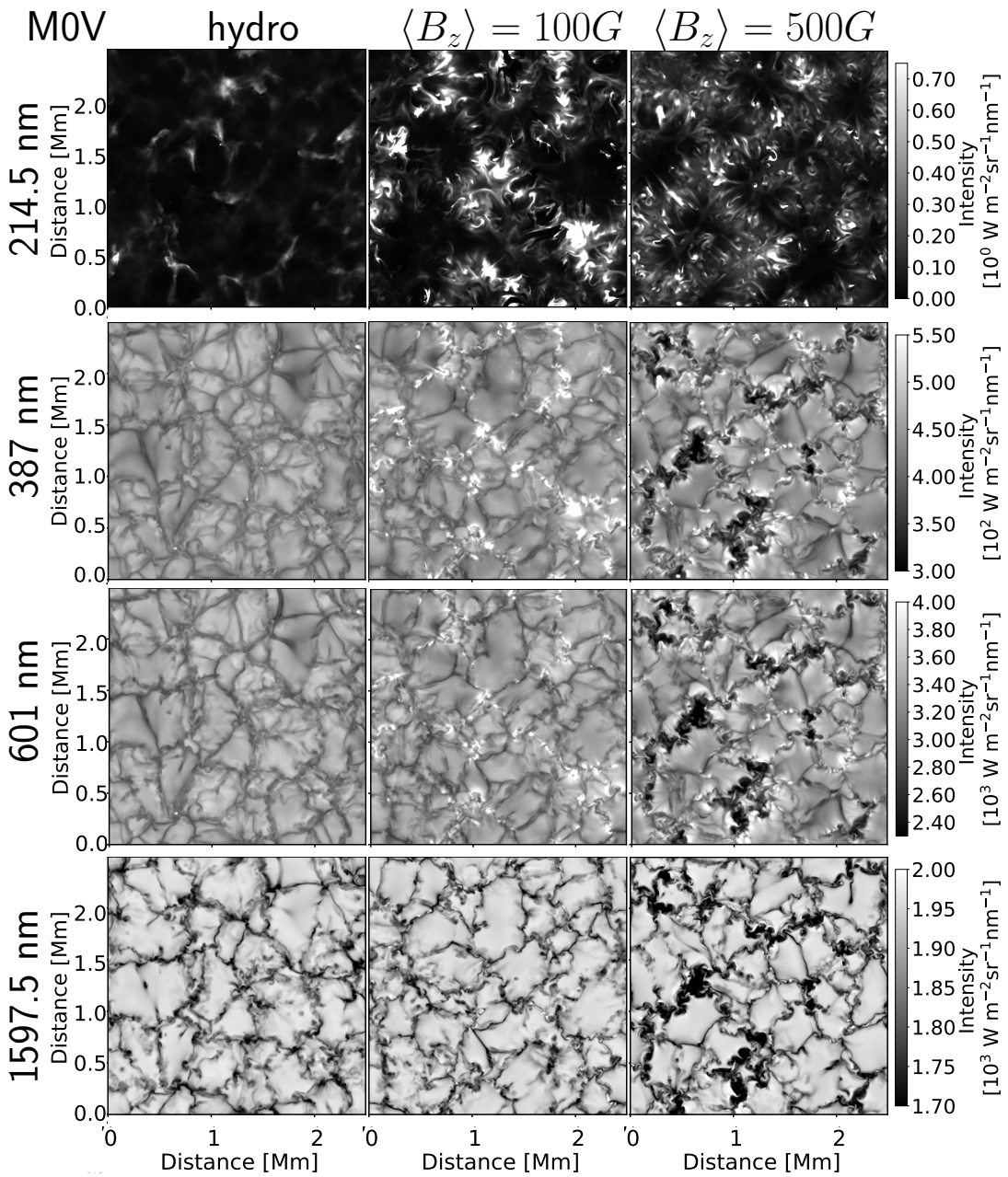


Figure 5.3: Images of the disc-centre emergent intensities from M0V simulated atmospheric snapshots. Same as Fig. 5.1 for M0V snapshots.

type.

In Fig. 5.2, K0V stars have noticeable bright features for $\langle B_z \rangle = 100$ G that increase in number for $\langle B_z \rangle = 500$ G. At $\langle B_z \rangle = 500$ G both the granules and the bright magnetic features are fragmented into smaller sections and most of the intergranular lanes are filled with magnetic features. Although the small magnetic features are bright in images from the UV to the visible, they are very low contrast, if not dark, around 1.6 nm for both injected magnetic fields. With the presence of a

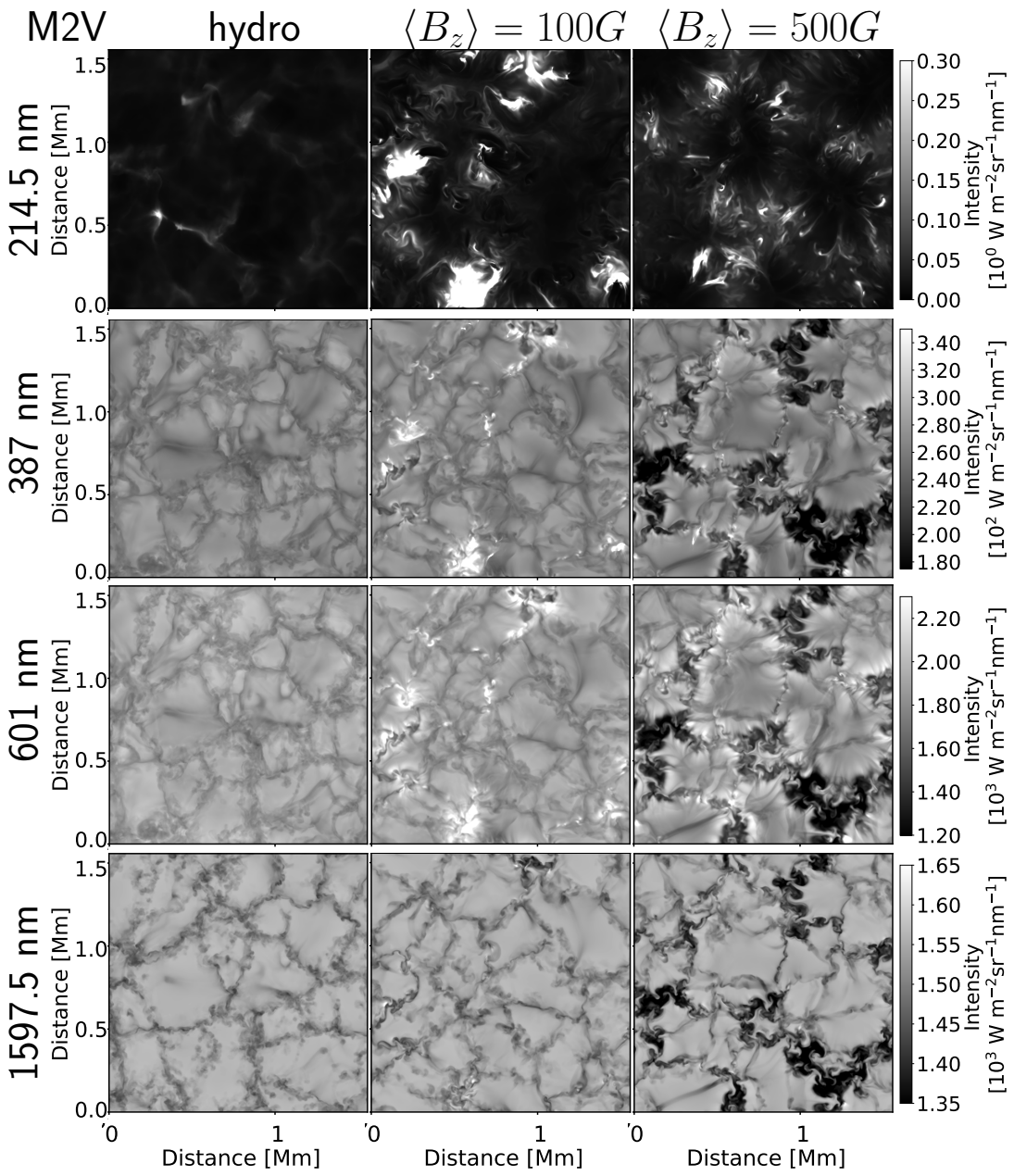


Figure 5.4: Images of the disc-centre emergent intensities from M2V simulated atmospheric snapshots. Same as Fig. 5.1 for M2V snapshots.

mean magnetic field of 500 G, a larger number of dark features, in comparison to the F3V images, develop across the snapshot in addition to the smaller bright features. These dark features stand out clearly at 601 nm and 1.6 μm, their contrast becomes low at 387 nm. Therefore, at different wavelengths the balance between dark and bright features varies, resulting in changes in the overall contrast of the magnetic region. For example, the mean contrast of the $\langle B_z \rangle = 500$ G snapshot shown, with respect to the mean hydrodynamic intensity, is positive at 214.5 nm and 387 nm,

while being negative for the same snapshot at 601 nm and 1 597.5 nm.

For M0V and M2V snapshots with $\langle B_z \rangle = 100$ G, in the central columns of Figs. 5.3 and 5.4, magnetic features are low contrast or dark at 1597.5 nm, but have high contrasts for 214.5 nm to 601 nm. For both M stars with $\langle B_z \rangle = 500$ G large dark features are present, with very few bright features. For M0V snapshots, the dark features are elongated and filament-like in shape. They, similarly to the dark features for the K0V snapshot, become less dark at 387 nm than at 601 nm or 1597.5 nm. For M2V simulations, the dark features are larger, and are dark throughout the NUV to the NIR. For K0V to M2V stars, these dark features seen for large mean magnetic fields show strong UV brightening, perhaps suggesting overlying clouds of hot gas.

5.1.2 Histograms

To see the effect these different features have on the distribution of intensities at disc centre on the stars, Figures 5.5 to 5.8 show histograms of pixel intensities for all 1 572 864 pixels from all six of the disc centre snapshots for each hydrodynamic (top), $\langle B_z \rangle = 100$ G (middle) and $\langle B_z \rangle = 500$ G (bottom) simulation for each spectral type. This gives a basic view of how the spectra differ between spectral types and as more magnetic field is introduced. All histograms show intensity in W m^{-2} sr^{-1} nm^{-1} as a function of wavelength (in nm) for a range of 150 nm to 5000 nm in log space. The number counts correspond to the colour bars shown, and are also in log space. Different intensity bin sizes were chosen for each star to best represent the spread of the pixel values. These bin sizes are given in the captions of each figure. For each star and magnetisation, the mean spectra calculated from all pixels of all six snapshots are plotted in solid black lines, with the 5th and 95th percentiles of these pixel values shown by dotted black lines. Equivalent histograms of the pixel values normalised by the total mean intensity spectra are shown in the Appendix, Figs. C.3 to C.6, for easier interpretation of the fractional variations.

Figs. 5.5 to 5.8 show an increase in the peak wavelength as stellar temperature decreases (from F3V to M2V). This effect is expected from blackbody emission. The spectra also change shape according to spectral type due to the differing continuum opacities as well as the absorption that occurs in the outer layers of the star. This absorption varies across spectral type as different atomic and molecular lines become important at different temperatures, pressures and densities. For example, a large jump in intensity can be seen at around 400 nm for F3V stars. This is caused by absorption below 400 nm at the hydrogen Balmer series absorption edge and in Ca

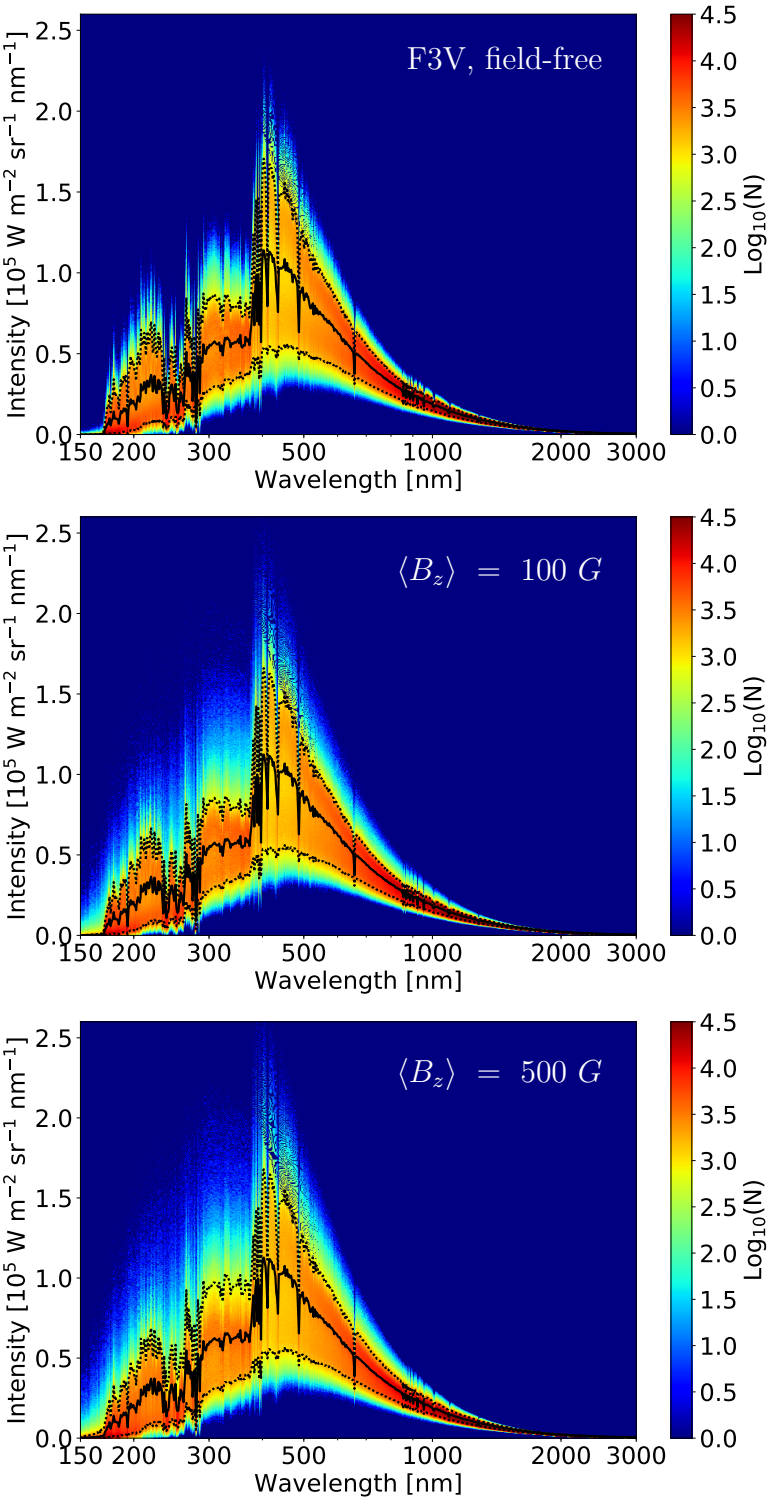


Figure 5.5: Histograms of disc-centre intensity in each ATLAS9 wavelength bin for the F3V snapshots. The mean intensity spectrum is overlaid in a solid black line and the 5th and 95th percentile overlaid in dotted black lines. Histograms, mean spectra and percentiles are for all pixels in all snapshots for a given $\langle B_z \rangle$. The intensity bin size is 1×10^2 W m^{-2} sr^{-1} nm^{-1}. From top to bottom, histograms are displayed for field-free, $\langle B_z \rangle$ = 100 G and $\langle B_z \rangle$ = 500 G snapshots. The wavelength bins are as detailed in Section 2.3, and are displayed in log space. Equivalent histograms of the pixel values normalised by the total mean intensity spectra are shown in the Appendix, Figure C.3.

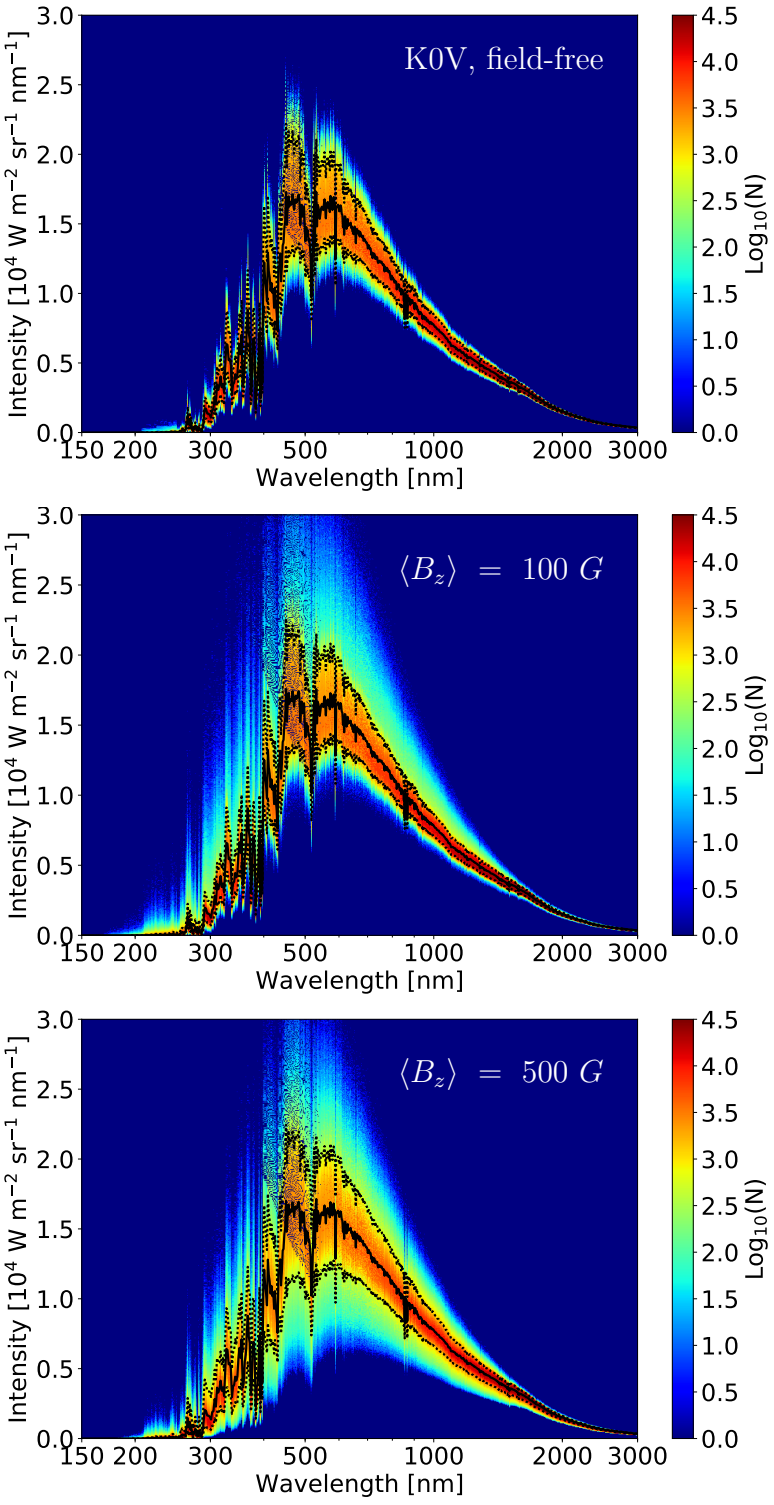


Figure 5.6: Histograms as in Figure 5.5 for the K0V star with an intensity bin width of 10 W m^{-2} sr^{-1} nm^{-1}. Equivalent histograms of the pixel values normalised by the total mean intensity spectra are shown in the Appendix, Figure C.4.

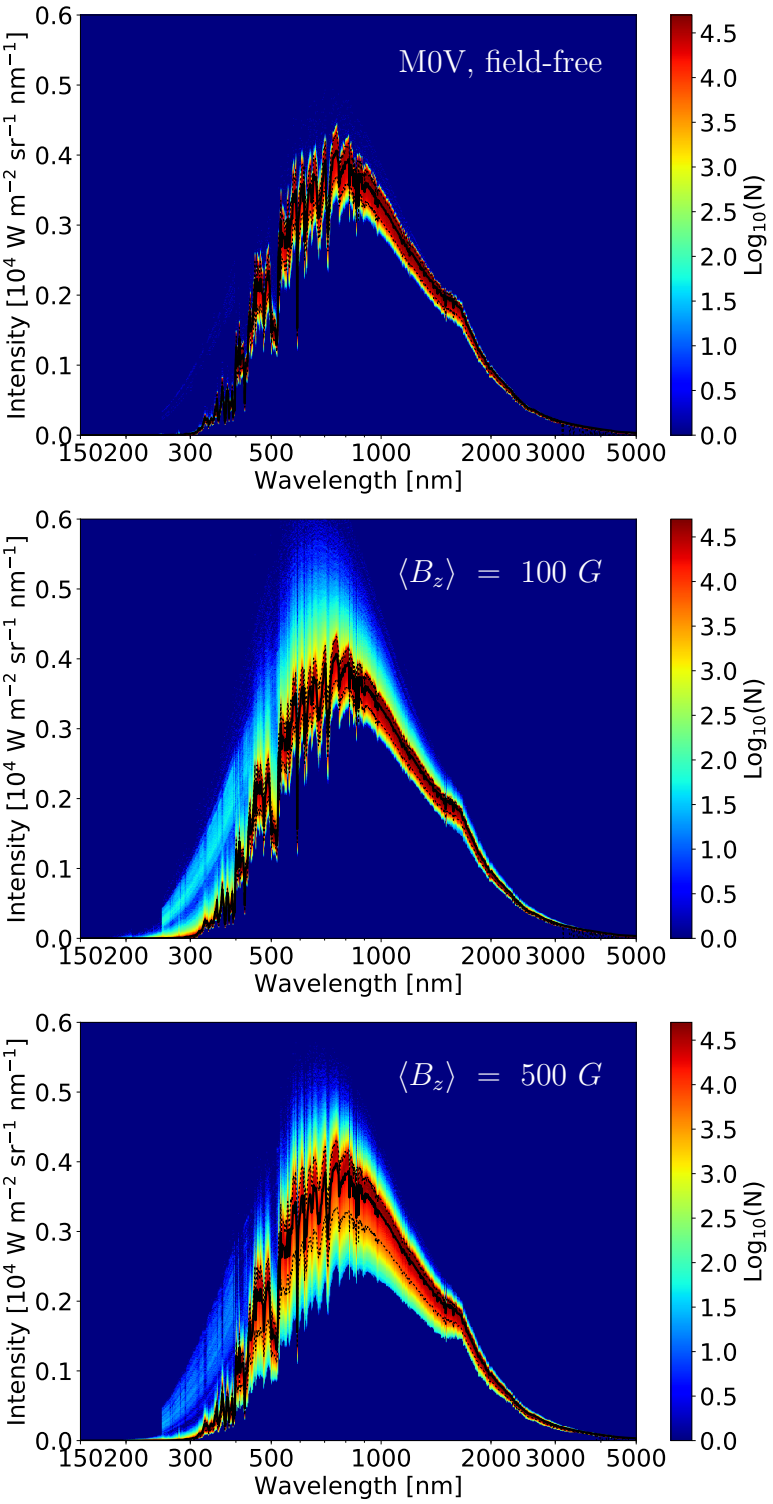


Figure 5.7: Histograms as in Figure 5.5 for the M0V star with an intensity bin width of 10 W m^{-2} sr^{-1} nm^{-1}. Equivalent histograms of the pixel values normalised by the total mean intensity spectra are shown in the Appendix, Figure C.5.

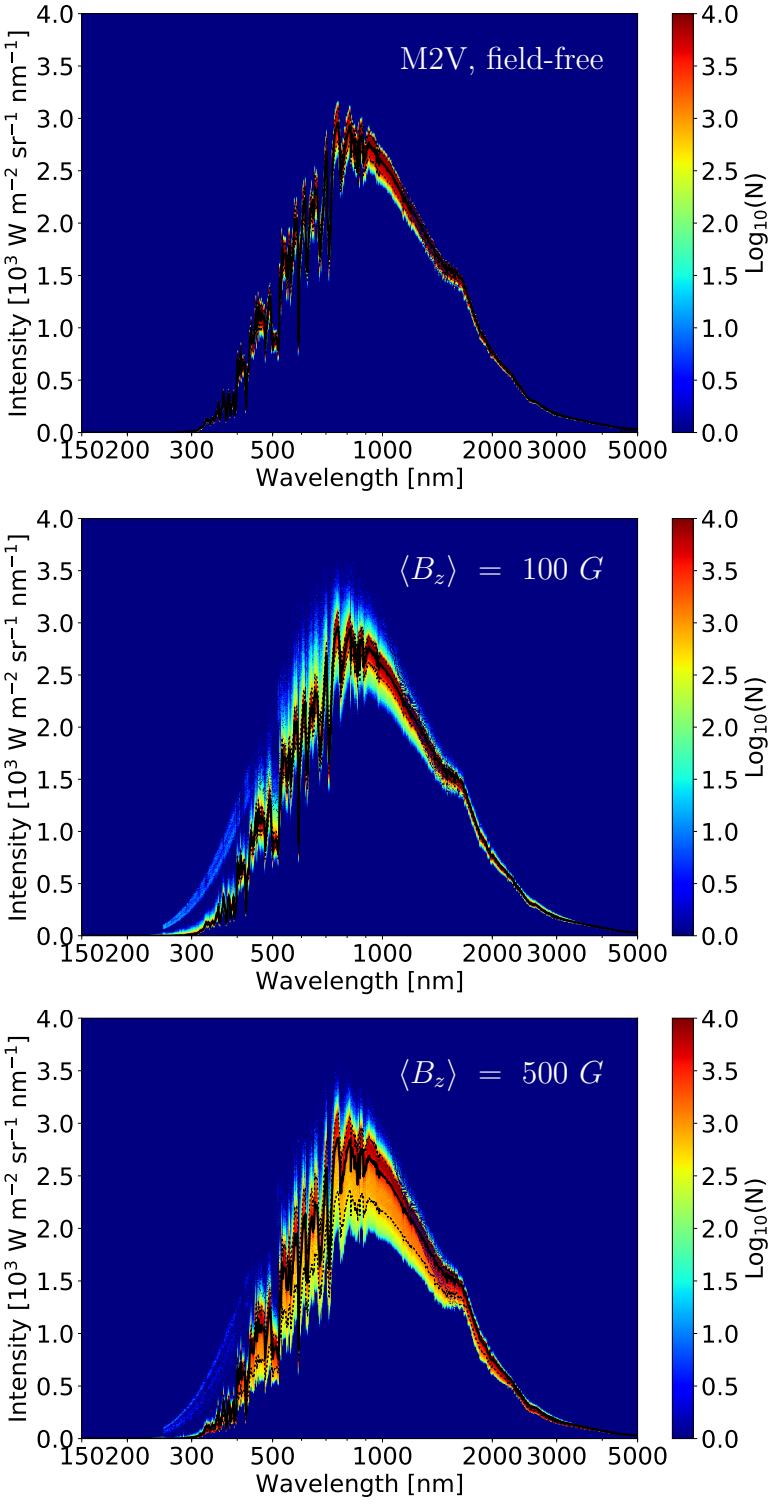


Figure 5.8: Histograms as in Figure 5.5 for the M2V star with an intensity bin width of 1 W m^{-2} sr^{-1} nm^{-1}. Equivalent histograms of the pixel values normalised by the total mean intensity spectra are shown in the Appendix, Figure C.6.

II H & K lines and the CN violet system (the same species that cause an increased contrast below 400 nm for the G2V star in chapter 4). This jump is seen only very weakly in the histograms of other spectral types as the intensity at this wavelength is much lower for cooler stellar temperatures. The many atomic and molecular lines that occur for wavelengths below 400 nm lead to a continuum-like opacity that is accounted for by ODFs (described in Section 2.3). Magnetic variability in Sun-like stars can mostly be attributed to line opacity effects (Shapiro et al., 2015), meaning that metallicity plays a crucial role in determining the amplitude of variability. For different spectral types, there are a number of spectral features that stand out. These features will be discussed in Section 5.3.

As with the G2V star in chapter 4, all stars have a larger spread in intensity for the magnetised snapshots than for the hydrodynamic snapshots, particularly in the visible. This is due to the increased variety of features within the snapshots when a magnetic field is present introducing a wider range of intensities emitted.

The presence of a relatively weak field (here $\langle B_z \rangle = 100$ G) can, depending on spectral type and wavelength, reduce the range of intensities for the central 90% of pixels (shown by the 5 and 95 percentiles on Figs. 5.5 to 5.8) compared to magnetic field-free snapshots (e.g., for the F3V spectral type, decreases in the spread occur at most wavelengths from 375 nm to 2 455 nm when a magnetic field of 100 G is present. At approximately 1 μm, there is a 3% decrease in the spread). This narrower range is due to many of the magnetic features present at this field strength being small and low contrast compared to the granules, particularly in the visible and NIR, as seen in the images in the central columns of Figs. 5.1 to 5.4. Furthermore, the magnetic features form mostly in the place of dark intergranular lane pixels. Some of these pixels are spread to the extreme values, but the majority have intensities closer to those of the main peak caused by the granules.

For $\langle B_z \rangle = 500$ G, the 90% central spread tends to be larger than that of the field-free snapshots. This larger spread is due to more magnetic features developing in the presence of a larger magnetic field. Some of these features have large contrasts compared to the granules, meaning a larger number of pixels will be more diverse in value.

The histograms for the cooler stars (K0V-M2V) in Figs. 5.6 to 5.8 show that low intensity tails for $\langle B_z \rangle = 500$ G extend significantly, while $\langle B_z \rangle = 100$ G histograms mainly have long tails towards higher intensities. This is due to multiple large, dark magnetic features manifesting only when a stronger magnetic field is present in the simulation. These large, dark features are seen clearly in the $\langle B_z \rangle = 500$ G (right column) images in Figs. 5.2 to 5.4. For M2V stars the 500 G central 90% is seen to

have a particularly large increase in range from the magnetic field-free histogram, mostly in the low intensity direction. This large, low intensity spread is caused by the dark magnetic features covering a large percentage of the pixels in the M2V $\langle B_z \rangle$ = 500 G snapshots. The transition from $\langle B_z \rangle$ = 100 G to $\langle B_z \rangle$ = 500 G is quite dramatic for all stars. As such, results from an intermediate mean magnetic field would be interesting (see Chapter 7).

The following section continues discussion on aspects of disc-centre dependence on spectral type, and furthers this discussion to include the effect that spectral type has on the radiation observed towards the limb.

5.2 Effect of the stellar spectral type on limb dependence

For a more detailed view of intensity distributions for different spectral types, and to highlight their limb dependence, Figs. 5.9 to 5.12 show histograms for each star for magnetic field-free (black lines), $\langle B_z \rangle$ = 100 G (purple lines) and $\langle B_z \rangle$ = 500 G (red lines). The four graphs in each figure show the four selected wavelengths of 214.5 nm, 387 nm, 601 nm and 1 597.5 nm from top to bottom (also seen in Figs. 5.1 to 5.4). Intensity bin sizes of the histograms vary across wavelength and spectral type, and are given in the captions of each figure. Vertical grey lines give the mean magnetic field-free values for each μ value. Disc-centre values are shown with solid lines, while μ = 0.5 histograms are shown by dashed lines. The horizontal bars at the top of each graph show the range of means of all snapshots at a given μ and $\langle B_z \rangle$. These represent the temporal variations, see Section 2.1.

Very little temporal variation in mean snapshot intensity is seen compared with the width of the distribution of pixel values except for late types at UV wavelengths (these variations could be due to the use of the LTE approximation, see comment in Sect 5.1.1). For all spectral types and wavelengths, these temporal variations are possibly underestimated due to granules generally re-appearing in the same positions over these timescales.

For some of the histograms, numerical spikes are seen. The most clear of which are seen for the M2 star at 1597.5 nm in Fig. 5.12. These spikes are caused by the intensity bin sizes not being an integer multiple of the steps in value associated with the recorded precision of the intensity. Due to the conversion of intensity units from the calculated W m^{-2} sr^{-1} Hz^{-1} to the displayed W m^{-2} sr^{-1} nm^{-1}, these steps in value are different at each wavelength. Therefore, to remove these numerical spikes,

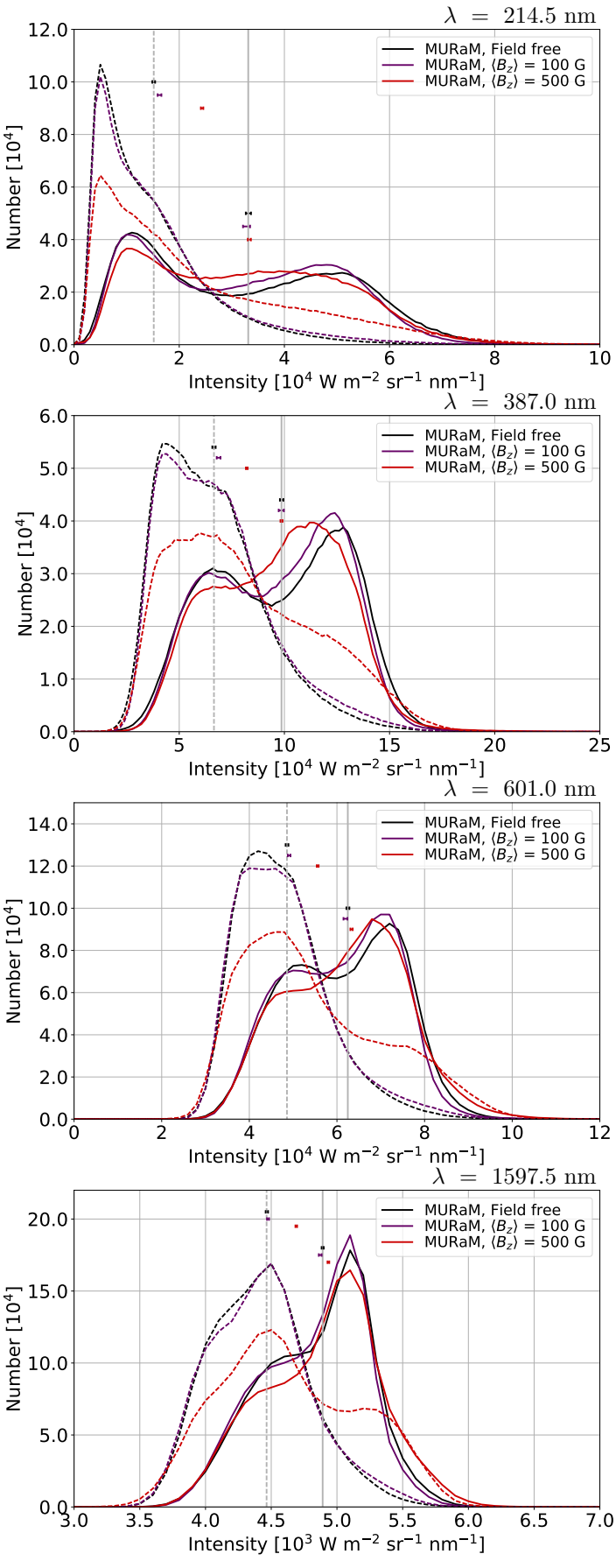


Figure 5.9: Histograms of intensity for all pixels in all F3V snapshots for a given $\langle B_z \rangle$ shown in the legend. The field-free mean intensities (averaged over all field-free snapshots) are marked by grey vertical lines with the minimum and maximum values of the mean intensities of the individual field-free snapshots indicated by black horizontal bars. Also shown are histograms and the range of snapshot-averaged intensities for simulations with $\langle B_z \rangle$ of 100 G (purple) and 500 G (red). The histograms are shown at two different limb positions: $\mu = 1.0$ (solid curves) and $\mu = 0.5$ (dashed curves). Histograms are shown for four wavelengths, each with a different intensity bin size. From top to bottom graphs show wavelengths of 214.5 nm, 387 nm, 601 nm and 1597.5 nm, with bin widths of 1×10^3, 2×10^3, 2×10^3 and 1×10^2 W m^{-2} sr^{-1} nm^{-1}, respectively. Both, the x and the y scales vary between graphs.

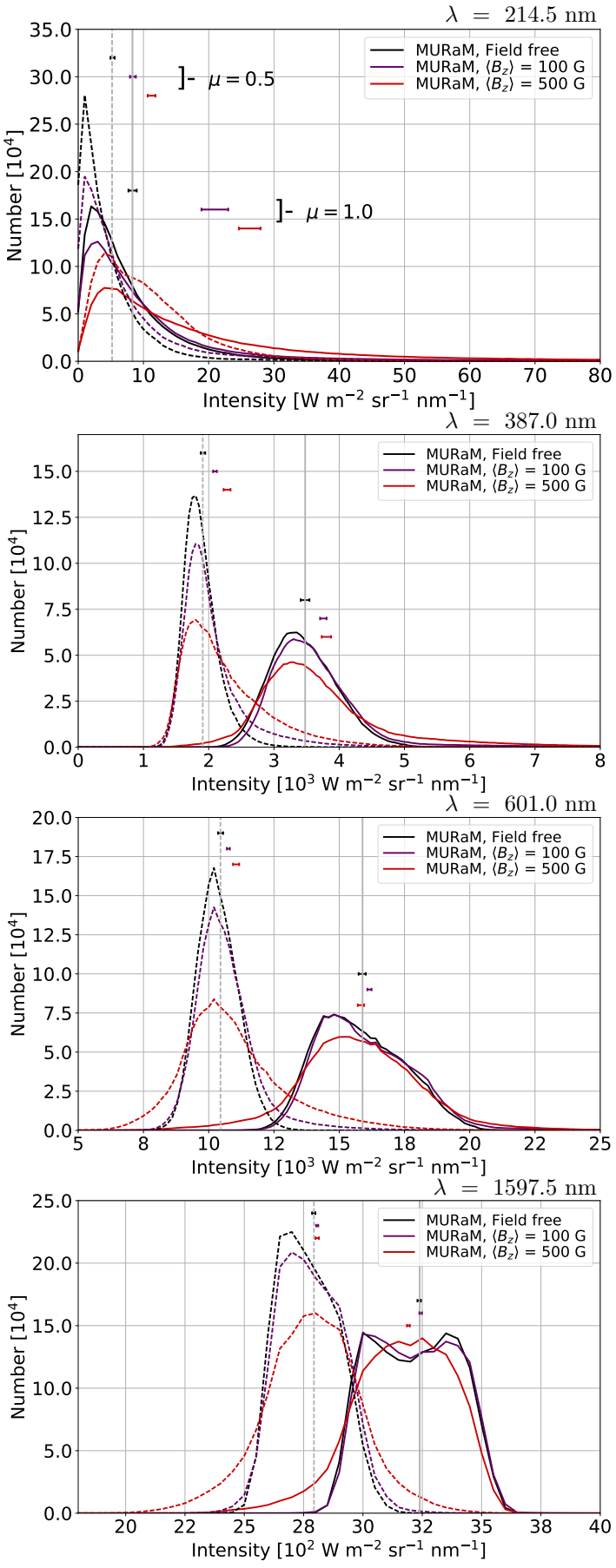


Figure 5.10: Same as Figure 5.9 for K0V stars with bin sizes of 1, 50, 200 and 50 W m^{-2} sr^{-1} nm^{-1}.

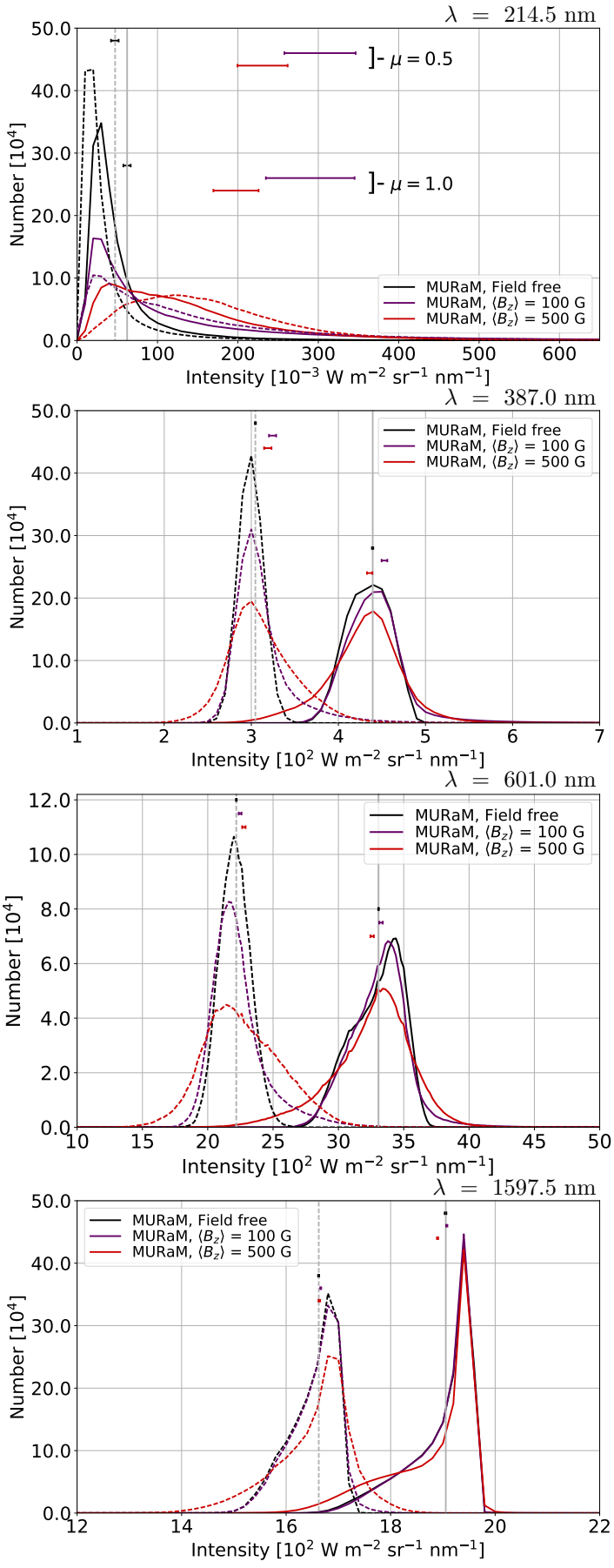


Figure 5.11: Same as Figure 5.9 for M0V stars with bin sizes of 0.01, 10, 20 and 20 W m^{-2} sr^{-1} nm^{-1}.

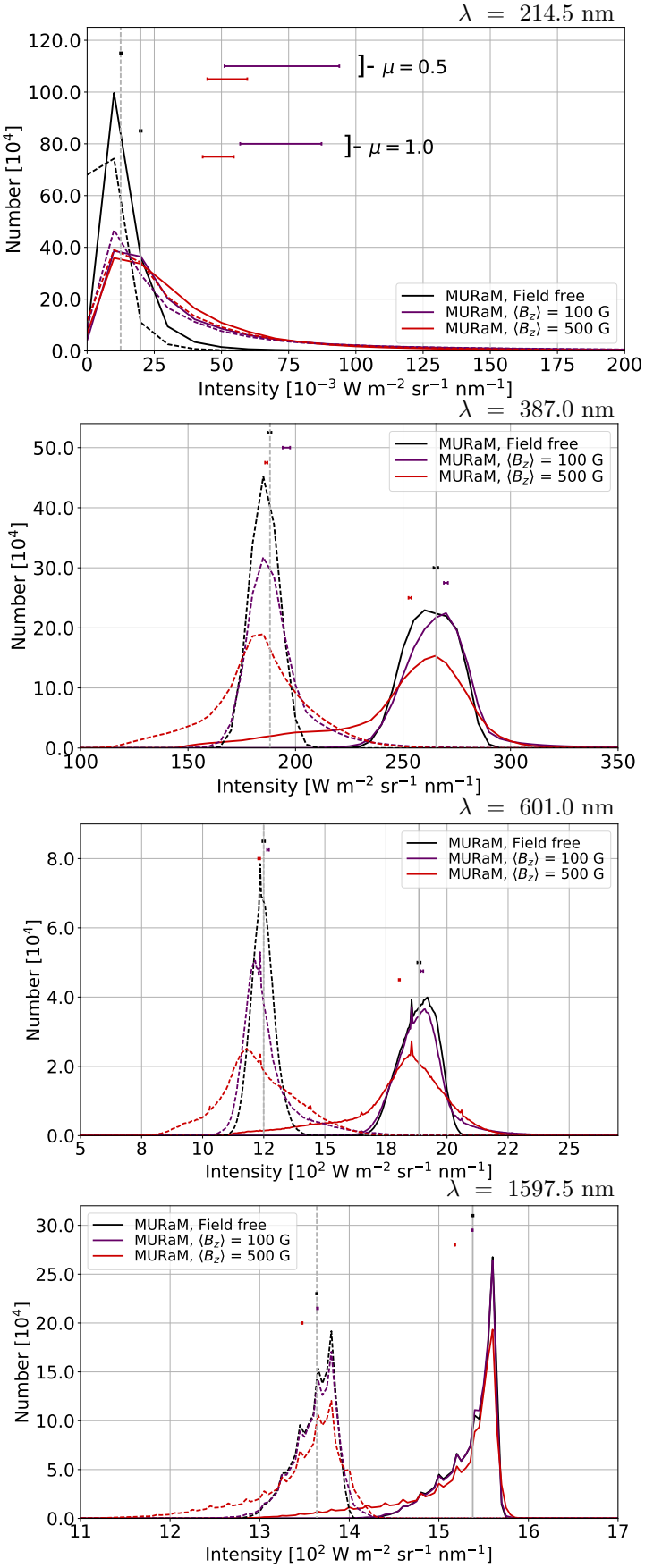


Figure 5.12: Same as Figure 5.9 for M2V stars with bin sizes of 0.01, 5, 5 and 5 W m^{-2} sr^{-1} nm^{-1}. The numerical spikes seen in this figure (particularly the bottom two panels), are explained in Sect. 5.2. The shapes of the histograms are not significantly affected when the spikes are removed.

the histograms must be calculated for a different bin size at each wavelength. When the spikes are removed, the histograms remain a very similar shape.

The mean intensities of the magnetic field-free snapshots (vertical grey lines in Figs. 5.9 to 5.12) decrease from disc centre to $\mu = 0.5$ in all plots. This demonstrates that limb darkening is occurring for these wavelengths for all chosen spectral types. At disc centre, all stars show only a small difference between magnetic field-free and $\langle B_z \rangle = 100$ G histograms for all wavelengths in Figs. 5.9 to 5.12 except 214.5 nm. This is in line with the larger sensitivity of UV radiation to the presence of surface features and is also observed in Fig. 4.4 for the G2V histograms. Differences between $\langle B_z \rangle = 100$ G and $\langle B_z \rangle = 500$ G histograms tend to be larger. The following paragraphs discuss peculiarities for different spectral types.

F3V: The largest differences between field-free and $\langle B_z \rangle = 100$ G histograms occur for the F3V spectral type in Fig. 5.9. At disc centre, histograms for the F3V spectral type are double peaked, with both a dark and a bright peak. These peaks arise due to granulation on the surface of the star. The higher intensity histogram peak is formed of pixels in the granules while the lower intensity peak is formed from pixels in the intergranular lanes. In the visible and infrared, the brighter peak is larger as the granules cover a larger area of the surface, and therefore more pixels. In the UV, the range of intensities in the granules is larger than in the intergranular lanes, so the high intensity peak is wider and less peaked than the low intensity peak, despite still containing a larger number of pixels (e.g., at 214.5 nm, in the top panel of Fig. 5.9).

At disc centre, for all wavelengths, the F3V $\langle B_z \rangle = 100$ G histogram's low-intensity peak is decreased compared to field-free, while the high-intensity peak is increased. This is due to a few low contrast, but bright, magnetic concentrations forming in the dark intergranular lanes lowering the low-intensity peak and adding to the high-intensity peak. The low-intensity peak is further diminished for $\langle B_z \rangle = 500$ G at disc centre as more magnetic field is concentrated in the intergranular lanes forming more bright regions. In the UV to the visible, the higher intensity peak shifts to slightly lower intensities and broadens due to magnetic features being generally brighter than intergranular lanes, but darker than the brightest granule pixels, as seen in the images in Fig. 5.1. For the visible and NIR, some magnetic features are brighter than the granules in these snapshots so the high-intensity tail is lengthened.

At $\mu = 0.5$, there is little difference between the F3V $\langle B_z \rangle = 100$ G and field-free histograms. There is a slight decrease in the peak and an increase in the high-intensity tail when the magnetic field is introduced. This small shift of pixels from

the peak to the tail is due to a small number of small-scale magnetic concentrations that emerge in the intergranular lanes, producing bright pixels. Although these features have low contrast compared to granule brightness at disc centre, towards the limb the viewing angle causes observed granular brightness to decrease, and allows radiation from the deeper layers of the hot walls of the feature to emerge, producing higher contrast regions. The $\langle B_z \rangle = 500$ G histograms show a larger decrease in the peak and a large increase in the high-intensity tail when compared to the field-free histograms, sometimes creating a second peak. This is caused by the larger magnetic features produced with this magnetic field strength allowing larger areas of the high contrast hot walls of the features to become visible.

G2V: G2V stars are discussed in detail in chapter 4.

K0V: Fig. 5.10 shows that the histograms for K0V stars mainly have single asymmetric peaks at both disc centre and $\mu = 0.5$. This smoother profile is due to the less discrete transition between granules and intergranular lanes for this star, demonstrated by images in Fig. 5.2. This leads to less separation between the intensities seen in each feature type. Disc-centre histograms in the NIR (see, e.g., 1597.5 nm histograms in Fig. 5.2) are the only exception as a double peak is seen for both magnetic field-free and $\langle B_z \rangle = 100$ G simulations, this is due to the granules being more defined at this wavelength.

When the magnetic field is increased to $\langle B_z \rangle = 500$ G, low-intensity tails increase in the NUV to the NIR. These dark tails are due to the emergence of large magnetic features, as seen in the right hand images in Fig. 5.2. Due to their large diameter, the surrounding atmosphere is unable to heat the features sufficiently, so they appear dark by comparison. At short wavelengths (UV to the visible), longer high-intensity tails are seen as more high-contrast small features emerge. The combination of bright and dark features results in a flattening of the peak (or peaks in the case of NIR) and emergence of high and low intensity tails. The relative importance of bright and dark features changes with wavelength, for example, the distribution is close to symmetric at 387 nm, and there is a large low intensity tail, with a very small high intensity tail in the NIR.

Looking towards the limb, at $\mu = 0.5$, the histogram peak height decreases with increasing magnetic field as more magnetic concentrations form in the intergranular lanes. These magnetic features allow radiation from deeper layers of the hot granular walls to emerge when viewing angle is increased, lengthening the high-intensity tails. For K0V $\langle B_z \rangle = 500$ G, at $\mu = 0.5$, there is also an increase in the low-intensity tails for the visible and NIR (illustrated in 601 nm and 1597.5 nm histograms). This increase in low intensities is due to larger, cool, magnetic features, which are dark

at these wavelengths. When viewed at an angle, these features allow more of the hot walls to be visible (hence larger high intensity tails), but, due to their size, some dark areas of the features will still remain visible, increasing the number of dark pixels in comparison to $\langle B_z \rangle = 100$ G histograms.

M stars: As with K0V stars, Figs. 5.11 and 5.12 show that M-star snapshots tend to have singly peaked distributions of intensity. At 214.5 nm this distribution has a long high-intensity tail for all magnetic fields. With the proviso that the calculations here are carried out assuming LTE, as magnetic field is increased, the height of the peak decreases and the high intensity tail lengthens. This change in distribution is due to the emergent magnetic features appearing either low contrast or bright at this wavelength, as can be seen in the top rows of images in Figs. 5.3 and 5.4. Whether the extreme long tail is an artefact of LTE will need to await confirmation until faster nLTE codes are available that can be applied to these simulations. For longer wavelengths, the low-intensity tails increase more strongly than the high-intensity tails when moving to $\langle B_z \rangle = 500$ G due to the emergence of large features that are dark at these wavelengths. These features are seen in the right hand images of Figs. 5.3 and 5.4. Towards the limb, again similar to K0V stars, the higher intensity tails increase as the hot and bright walls of the magnetic features are revealed, while dark tails remain present due to darks areas of the features still being visible.

The histograms in Figs. 5.5 to 5.12 show that the distribution of intensities seen in a stellar atmosphere changes significantly across spectral type, wavelength and magnetic field strength. The following section explores how these changes affect the total brightness of a magnetic region compared to the quiet star.

5.3 Contrast spectra of magnetic regions on F, K and early M stars

Figures 5.13 and 5.14 show mean contrast spectra with respect to field-free simulations, calculated using equation 4.1, for all spectral types for $\langle B_z \rangle = 100$ G and $\langle B_z \rangle = 500$ G, respectively. The top panel in each figure shows the disc-centre contrasts, while the bottom panel shows contrasts at $\mu = 0.5$. For both magnetisations contrast is a complicated function of wavelength and this relationship depends heavily on spectral type. By and large contrasts decrease from the UV to the visible and NIR, before increasing slightly in the band at 4.5 μm (dominantly caused by rovibrational CO lines). Complexity is introduced by different atmospheric species

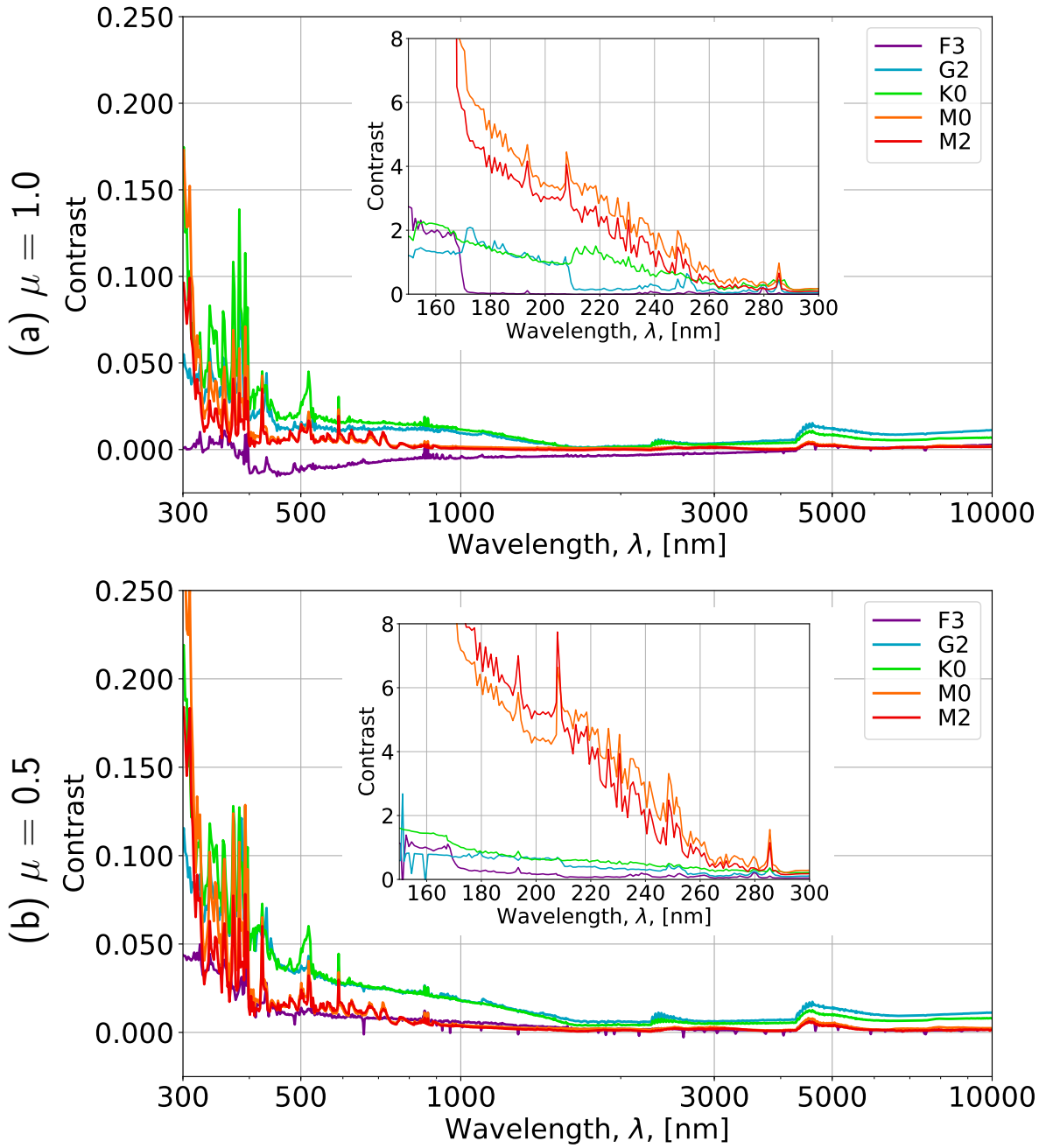


Figure 5.13: Average contrast spectra relative to field-free simulations for all MURaM spectral types for snapshots with $\langle B_z \rangle = 100$ G. Contrasts are shown at disc centre, panel a (top), and $\mu = 0.5$, panel b (bottom). The main plots show wavelengths of 300 nm to 10 000 nm using logarithmic x axes, while the insets show 150 nm to 300 nm using linear axes. Note the different vertical scales.

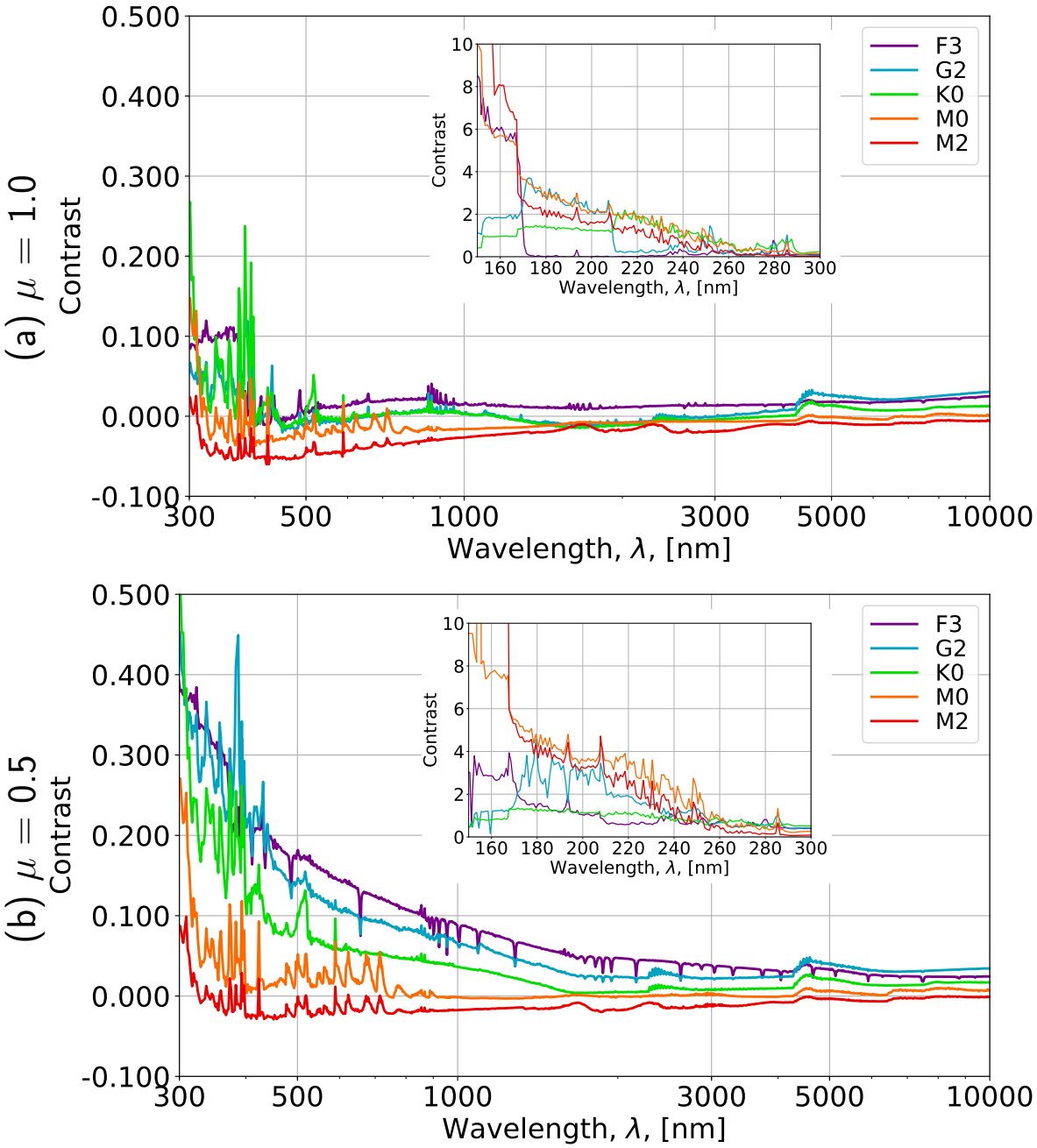


Figure 5.14: Average contrast spectra relative to field-free simulations for all MURaM spectral types for $\langle B_z \rangle = 500$ G. Contrasts are shown at disc centre, panel a (top), and $\mu = 0.5$, panel b (bottom). The main plots show wavelengths of 300 nm to 10 000 nm using logarithmic x axes, while the insets show 150 nm to 300 nm using linear axes. Note the different vertical scales.

Table 5.1: Bolometric intensities and standard deviation across snapshots for all F-K and magnetisations at all limb angles. In units of 10^4 W m^{-2} sr^{-1}.

Star	mag	$\mu = 1.0$	$\mu = 0.9$	$\mu = 0.8$	$\mu = 0.7$	$\mu = 0.6$
F3V	hydro	4968.4 ± 19.8	4692.8 ± 18.8	4484.2 ± 18.4	4266.6 ± 17.9	4039.1 ± 17.2
F3V	20G	4903.0 ± 16.4	4647.3 ± 16.8	4433.1 ± 16.6	4210.6 ± 16.7	3979.3 ± 17.3
F3V	100G	4940.5 ± 27.0	4696.3 ± 26.1	4499.9 ± 24.2	4295.1 ± 22.1	4081.1 ± 19.8
F3V	500G	5091.1 ± 14.0	4905.5 ± 10.4	4804.5 ± 10.2	4694.8 ± 11.5	4573.5 ± 12.4
G2V	hydro	2521.4 ± 10.4	2399.5 ± 9.9	2273.6 ± 9.0	2143.3 ± 8.1	2007.2 ± 7.2
G2V	20G	2549.5 ± 14.2	2427.0 ± 13.4	2300.6 ± 12.5	2169.8 ± 11.7	2033.3 ± 11.0
G2V	100G	2559.4 ± 10.9	2440.7 ± 10.4	2318.7 ± 10.1	2191.7 ± 9.5	2058.5 ± 8.8
G2V	500G	2536.2 ± 14.4	2452.2 ± 15.7	2366.3 ± 16.2	2275.0 ± 16.4	2176.6 ± 16.5
K0V	hydro	1293.2 ± 6.0	1228.5 ± 5.7	1161.1 ± 5.4	1091.4 ± 5.0	1018.8 ± 4.7
K0V	20G	1295.2 ± 3.3	1230.5 ± 3.1	1163.3 ± 2.8	1093.7 ± 2.6	1021.2 ± 2.3
K0V	100G	1312.1 ± 4.6	1247.7 ± 4.3	1180.9 ± 4.0	1111.5 ± 3.7	1039.2 ± 3.4
K0V	500G	1294.9 ± 6.4	1238.1 ± 6.5	1179.2 ± 6.5	1117.6 ± 6.4	1053.0 ± 6.2

Star	mag	$\mu = 0.5$	$\mu = 0.4$	$\mu = 0.3$	$\mu = 0.2$
F3V	hydro	3799.3 ± 16.3	3538.0 ± 15.2	3248.6 ± 13.9	2910.0 ± 11.4
F3V	20G	3736.8 ± 18.4	3476.9 ± 19.8	3192.0 ± 20.9	2861.5 ± 22.0
F3V	100G	3854.8 ± 17.2	3607.6 ± 15.4	3328.6 ± 15.3	2991.1 ± 16.6
F3V	500G	4436.4 ± 12.2	4272.5 ± 12.6	4065.0 ± 15.0	3751.2 ± 22.5
G2V	hydro	1863.8 ± 6.3	1711.0 ± 5.5	1544.5 ± 4.8	1356.9 ± 4.3
G2V	20G	1889.4 ± 10.2	1736.3 ± 9.5	1569.5 ± 8.6	1381.7 ± 7.5
G2V	100G	1917.0 ± 8.0	1764.7 ± 7.2	1596.7 ± 6.5	1405.3 ± 6.2
G2V	500G	2067.9 ± 16.3	1943.3 ± 16.2	1793.3 ± 15.6	1597.7 ± 15.3
K0V	hydro	943.1 ± 4.4	863.4 ± 4.1	778.6 ± 3.8	686.2 ± 3.6
K0V	20G	945.5 ± 2.0	865.8 ± 1.7	781.0 ± 1.4	688.4 ± 1.2
K0V	100G	963.4 ± 3.1	883.3 ± 2.8	797.6 ± 2.5	703.6 ± 2.2
K0V	500G	984.8 ± 6.0	912.1 ± 5.7	832.9 ± 5.3	742.4 ± 4.5

Table 5.2: Bolometric intensities and standard deviation across snapshots for all magnetisations of M spectral types at all limb angles. In units of 10^3 W m^{-2} sr^{-1}.

Star	mag	$\mu = 1.0$	$\mu = 0.9$	$\mu = 0.8$	$\mu = 0.7$	$\mu = 0.6$
M0V	hydro	4639.5 ± 1.6	4495.1 ± 1.4	4342.2 ± 1.3	4178.3 ± 1.2	4000.8 ± 1.2
M0V	20G	4654.3 ± 1.8	4510.0 ± 1.6	4357.2 ± 1.5	4193.4 ± 1.5	4016.2 ± 1.6
M0V	100G	4650.7 ± 6.6	4508.4 ± 6.4	4357.2 ± 6.2	4195.0 ± 5.9	4019.1 ± 5.6
M0V	500G	4580.6 ± 5.4	4451.5 ± 5.3	4312.6 ± 5.3	4163.0 ± 5.5	3999.9 ± 5.7
M2V	hydro	3507.7 ± 3.8	3413.6 ± 3.9	3312.8 ± 3.9	3203.4 ± 3.9	3083.0 ± 3.8
M2V	20G	3512.0 ± 7.1	3418.2 ± 7.0	3317.7 ± 6.9	3208.6 ± 6.7	3088.6 ± 6.5
M2V	100G	3512.8 ± 2.5	3420.2 ± 2.5	3320.8 ± 2.5	3212.5 ± 2.5	3093.4 ± 2.5
M2V	500G	3422.6 ± 1.6	3336.5 ± 1.8	3243.2 ± 1.8	3141.2 ± 1.9	3028.9 ± 2.0

Star	mag	$\mu = 0.5$	$\mu = 0.4$	$\mu = 0.3$	$\mu = 0.2$
M0V	hydro	3805.8 ± 1.3	3586.8 ± 1.5	3333.1 ± 1.7	3023.4 ± 1.7
M0V	20G	3821.7 ± 1.8	3603.4 ± 2.0	3351.2 ± 2.2	3044.4 ± 2.2
M0V	100G	3825.7 ± 5.2	3608.0 ± 4.9	3355.8 ± 4.7	3047.4 ± 4.6
M0V	500G	3820.3 ± 5.9	3617.7 ± 6.1	3382.7 ± 6.3	3094.0 ± 6.4
M2V	hydro	2948.7 ± 3.8	2795.4 ± 3.6	2615.2 ± 3.4	2391.6 ± 3.0
M2V	20G	2954.7 ± 6.3	2801.9 ± 6.0	2622.3 ± 5.6	2399.5 ± 5.1
M2V	100G	2960.4 ± 2.5	2808.4 ± 2.5	2629.5 ± 2.3	2406.6 ± 2.0
M2V	500G	2903.9 ± 2.1	2761.6 ± 2.2	2594.9 ± 2.3	2388.4 ± 2.2

becoming more dominant in the spectra for different spectral types. E.g., contrasts for M0V and M2V stars show strong variations between 400 and 900 nm due to molecular bands, such as the TiO band heads at 517 nm, 619 nm and 709 nm, while other stars vary more smoothly at these wavelengths. These differences in molecular bands are important as if they are ignored in planetary transit spectroscopy they can lead to spurious detections of molecules that are not present in the planetary atmosphere, or mask those that are there.

Figs. 5.13 and 5.14 reveal that there is no obvious trend with stellar temperature that can be used to scale spectral contrasts. In the presence of a strong mean magnetic field at disc centre (Fig. 5.14(a)), contrasts tend to increase with increasing stellar temperature between 400 nm and 1.5 μm. At around 1.5 μm contrasts of both K0V and G2V decrease to coincide with and cross those of the M0V and M2V simulations. Away from disc centre (see Fig. 5.14(b)), the trend of increasing contrast with increasing effective temperature is more persistent across all wavelengths between 400 nm and 4 μm. However, even in this case, strong atomic or molecular lines, present for some spectral types, affect the relationship at given wavelengths. E.g., M0V shows stronger features in the visible and flat contrasts in the IR, while M2V contrasts shows broad molecular lines at 1.8 and 2.4 μm, despite both spectral types looking very similar at $\langle B_z \rangle = 100$ G. At both disc positions shown, the contrast increase at approximately 4.5 μm varies with spectral type such that the F3V contrast is no longer the greatest.

For strong mean fields at disc centre and weaker mean fields for both disc positions (Figs. 5.13 and 5.14(a)), the G2V and K0V simulations have very similar spectral contrasts. Slight differences are seen, the most striking one being the strength of the molecular band at approximately 500 nm, which could be a TiO feature. Here, the K0V contrast is enhanced compared to that of G2V.

For the M stars with $\langle B_z \rangle = 500$ G (Fig. 5.14a), disc centre contrasts above 300 nm are negative. This negative contrast is due to the magnetic features becoming large enough that the surrounding hot atmosphere is unable to heat the cooled magnetic region by radiation, therefore the features appear dark compared to the surrounding atmosphere. However, in a few molecular bands for the M0V simulation the contrast is increased enough to become positive. In certain wavelength regions, negative contrasts are also seen for other stars with $\langle B_z \rangle = 500$ G at disc centre, but these stars also have significant wavelength regions of positive contrast. Tables 5.1 and 5.2 show the mean bolometric intensities for each spectral type at all calculated limb distances, μ. The tables also show the standard deviation of the snapshot means, i.e., the temporal variation. For the M stars at disc centre, for $\langle B_z \rangle = 500$ G,

bolometric contrast is negative, while the other stars, although having wavelength regions of negative contrast, have positive disc-centre bolometric contrast.

At $\langle B_z \rangle = 100$ G (shown in Fig. 5.13), G2V and K0V spectral types, despite being in the middle of the effective temperature range, have the largest contrasts at most wavelengths between 400 nm and 10 000 nm at both disc centre and $\mu = 0.5$. Below 300 nm, the M-star spectral contrasts increase with shortening wavelength at a much higher rate than the other stars, such that their contrasts become much higher than those of the hotter spectral types (see inserts in Fig. 5.13).

For the F3V stars with $\langle B_z \rangle = 100$ G, the mean disc-centre bolometric contrast appears to be negative for the six snapshots considered here (bolometric intensities seen in Tab. 5.1). However, bolometric averages over longer runs, shown in table 1 in Beeck et al. (2015b), indicate that the bolometric contrast is very small, but positive. I have included the 100 G F3V run here, but given the intrinsic variability, confirmation of these contrasts require simulations of additional snapshots.

5.4 Centre-to-limb contrast variations for F, K and early M stars

Figures 5.13 and 5.14 do not fully demonstrate the changes in centre-to-limb variation with spectral type. Fig. 5.15 shows mean contrasts for all calculated limb distances for a selection of wavelengths that match those shown in Figs. 5.9 to 5.12 (214.5 nm, 387 nm, 601 nm and 1597.5 nm from top to bottom). Stellar simulations at $\langle B_z \rangle = 100$ G are displayed in the left column and $\langle B_z \rangle = 500$ G in the right column. The standard deviation of the mean contrasts of each of the six snapshots from the overall mean of the snapshots for each spectral type, incorporating both the magnetic and hydrodynamic spreads, is shown by shaded regions. This gives an idea of temporal variations seen in the mean snapshot contrasts.

The form of the centre-to-limb contrast variations is dependent on spectral type as well as wavelength and magnetic field strength. All stars generally increase in contrast towards the limb at all selected wavelengths for both magnetic field strengths in Fig. 5.15. This brightening is caused by lower opacity in the magnetic features compared to the surrounding atmosphere. The decreased opacity in the features allows radiation from deeper in the atmosphere to emerge. At disc centre this can be brighter or darker than the radiation that is seen in the surrounding atmosphere, depending on the balance of optical depth and reheating of the feature by the surrounding atmosphere, as in previous discussion (Sect. 1.3.1). As viewing

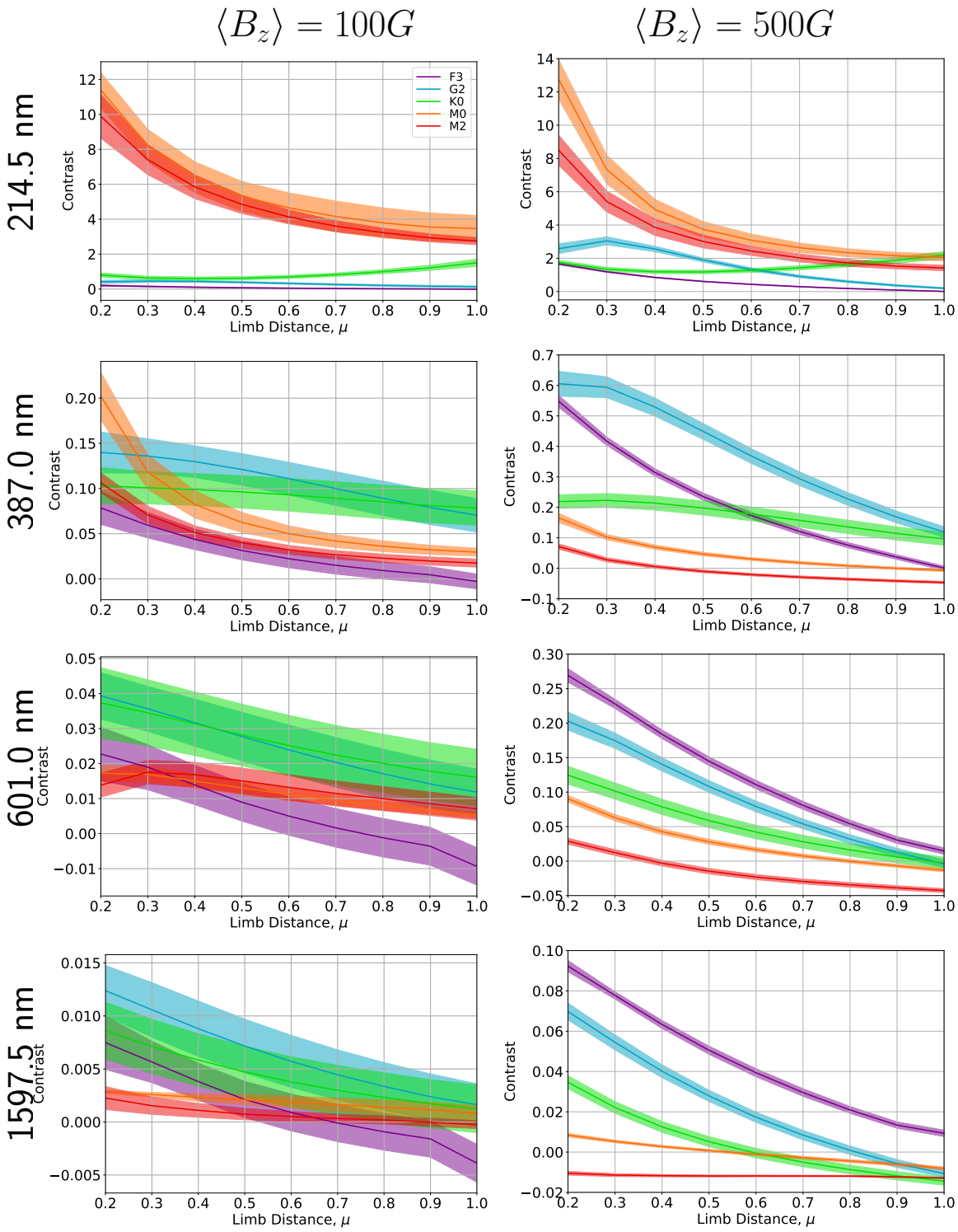


Figure 5.15: The average contrast relative to the average intensity of the hydrodynamic snapshots as a function of limb distance, μ. These are shown for 214.5 nm, 387 nm, 601 nm and 1 597.5 nm from top to bottom and for $\langle B_z \rangle =$ 100 G (left) and $\langle B_z \rangle = 500$ G (right). The shaded regions show the spread calculated from the standard deviations of the means of the snapshots at each μ. Colours corresponding to spectral type are given in the legend of the figure.

angle is increased, radiation from the hot walls of the feature will become visible. Therefore, as more and more wall is revealed, in conjunction with the field-free limb darkening effect explored in Chapter 3, contrast tends to increase. Only K0V simulations at 214.5 nm have a lower contrast at $\mu = 0.2$ than at disc centre. Given the LTE nature of the ATLAS9 calculations, UV contrasts will need confirmation with nLTE codes.

For those contrasts that brighten towards the limb, the functional form of this increase differs. Some functions exhibit slight decreases in contrast when they are viewed close to the limb, leading to the maximum contrast occurring away from the limb (e.g. M2V at 601 nm and $\langle B_z \rangle = 100$ G). The turnover in some centre-to-limb variations of the contrast is due to the atmosphere at the top of the granules becoming opaque enough at certain wavelengths to block the bright radiation from the hot walls at large viewing angles, producing dark lanes, as discussed in Sect. 1.3.1. However, the contrasts at $\mu = 0.2$ tend to remain brighter than at disc centre. This turnover is observed on the Sun in the visible continuum in Yeo et al. (2013), where facular contrasts are observed to continue decreasing to $\mu = 0.1$. For some magnetic field strengths at this limb angle the contrast is seen to match that of the disc centre value. Calculations with $\mu < 0.1$, i.e., closer to the limb, would be required to determine whether contrast continues to decrease.

The standard deviations of the mean contrasts of each snapshot, shown by the shaded regions in Figs. 5.15, are comparable across magnetic field strength and stellar spectral type. Although they appear larger for $\langle B_z \rangle = 100$ G, the spread itself is of similar value. Due to the lower contrasts of the $\langle B_z \rangle = 100$ G, the fractional variation is larger for $\langle B_z \rangle = 100$ G than for $\langle B_z \rangle = 500$ G. The variations stay fairly constant from disc centre to limb for all stars. For longer wavelengths (visible and NIR), the hotter, lower gravity stars (F-K types) have larger variations. In the UV (214.5 nm) the M stars have the largest absolute variations, but as the mean contrast itself is larger for M stars at this wavelength, the fractional variations are similar across spectral type, particularly at disc centre.

5.5 Contrasts of magnetic regions for past, present and future planetary missions

Observations of stars tend to be taken in certain spectral bands that are different for each spacecraft. To allow for use of our calculated contrasts, coefficients for centre-to-limb variations (CLVs) for the paramaterisations described in Chap. 3, Eqs 3.1

to 3.5 for $\langle B_z \rangle = 20$ G, $\langle B_z \rangle = 100$ G and $\langle B_z \rangle = 500$ G snapshots are supplied in this section. Tables 5.3 to 5.5 contain the coefficients for a variety of instruments on multiple spacecraft (the filters are shown in Fig. 3.1). Additional coefficients can be found in Tables B.1 to B.4 in App. B. Contrasts can be calculated relative to field-free CLVs, detailed in Chap. 3, Tabs 3.1 to 3.7, or relative to $\langle B_z \rangle = 20$ G CLVs to account for the 'quiet' stellar surface not being entirely field-free.

In Figs. 5.16 and 5.17, contrasts relative to field-free snapshots in each of the chosen filters are calculated as follows,

$$c = \frac{f(\theta_{i,\langle B_z \rangle}) I(1.0, \langle B_z \rangle)}{f(\theta_{i,hydro}) I(1.0, hydro)} - 1, \tag{5.1}$$

where f is the fitting function chosen, $\theta_{i,\langle B_z \rangle}$ are the various coefficients for that fit for a given filter and $\langle B_z \rangle$, and $I(1.0, \langle B_z \rangle)$ is the disc centre intensity for the given $\langle B_z \rangle$.

For $\langle B_z \rangle = 500$ G, contrasts with respect to field-free simulations in all filters tend to increase with increasing stellar effective temperature at all limb distances. For *Kepler*, CoRoT and TESS, K0V and G2V contrasts do not follow this trend at disc centre, with K0V having a slightly higher contrast than G2V. Additionally, for *Spitzer* IRAC 2-4 filters with $\langle B_z \rangle = 500$ G the F3V star has a lower contrast than the G2V star at all limb distances. Although, as stated in Sect. 5.3, F3V contrasts, particularly those for $\langle B_z \rangle = 100$ G, will need to be confirmed with an increased number of snapshots and will therefore not be further discussed.

For $\langle B_z \rangle = 100$ G, the increase in contrast towards the limb for *Kepler*, CoRoT and TESS filters becomes steeper with increasing stellar temperature. However, the disc centre intensities do not scale with temperature. This leads to K0V having the highest contrast in these filters at disc centre and G2V having the largest contrast at $\mu = 0.5$. For the *Spitzer* IRAC filters at $\langle B_z \rangle = 100$ G, contrasts tend to increase with stellar temperature. For the IRAC4 band, M-stars have a turnover to a negative gradient at about $\mu = 0.4$, that leads to the contrast becoming smaller at the limb than at disc centre. Perhaps surprisingly, the contrast at the limb is negative for M2V.

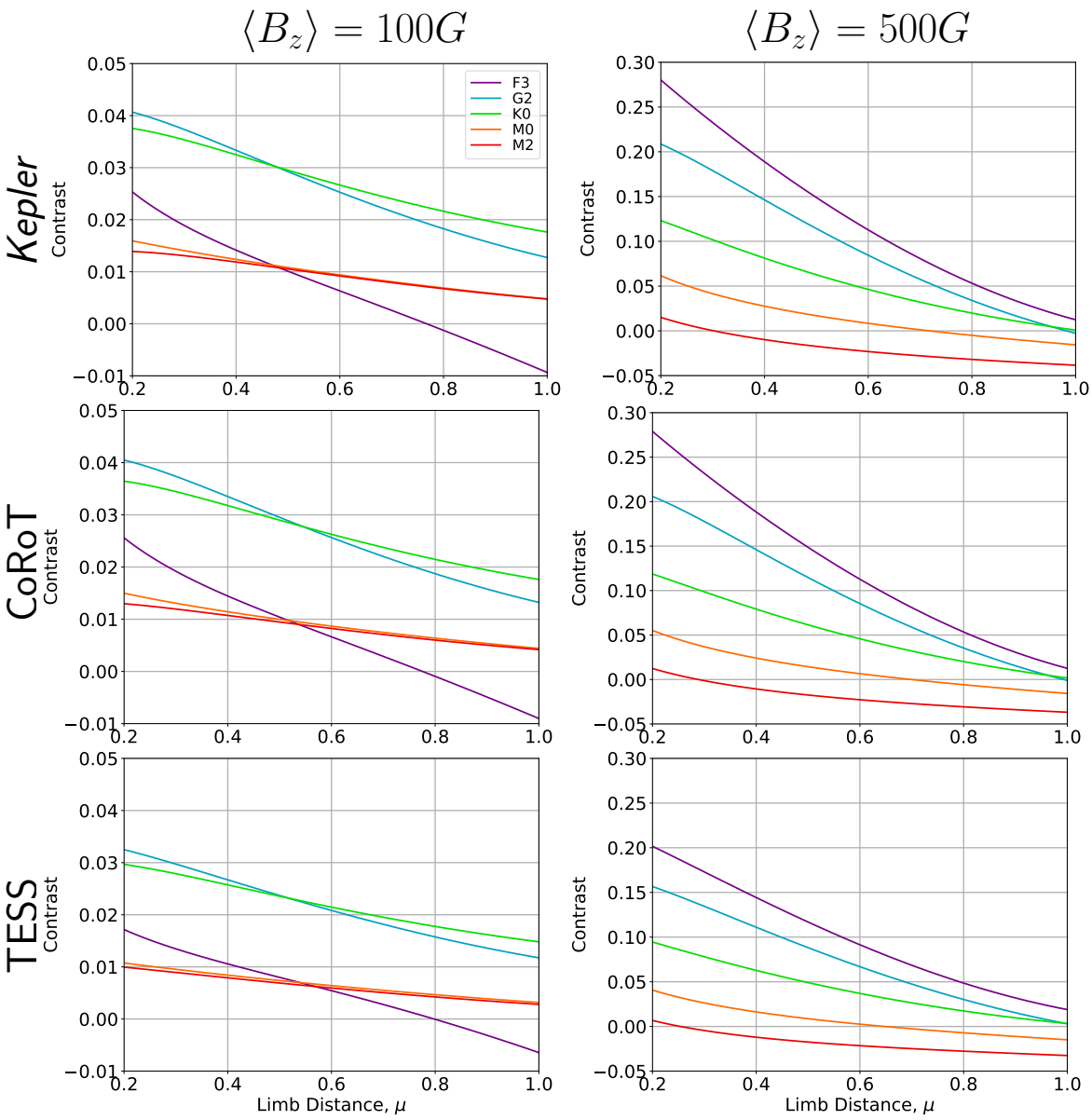


Figure 5.16: The average contrast relative to the average intensity of the hydrodynamic snapshots as a function of limb distance, μ. These are calculated using the magnetic and hydrodynamic CLV non-linear 3 parameter fits. These are shown for *Kepler*, CoRoT and TESS filters from top to bottom and for $\langle B_z \rangle$ = 100 G (left) and $\langle B_z \rangle$ = 500 G (right). Colours corresponding to spectral type are given in the legend of the figure.

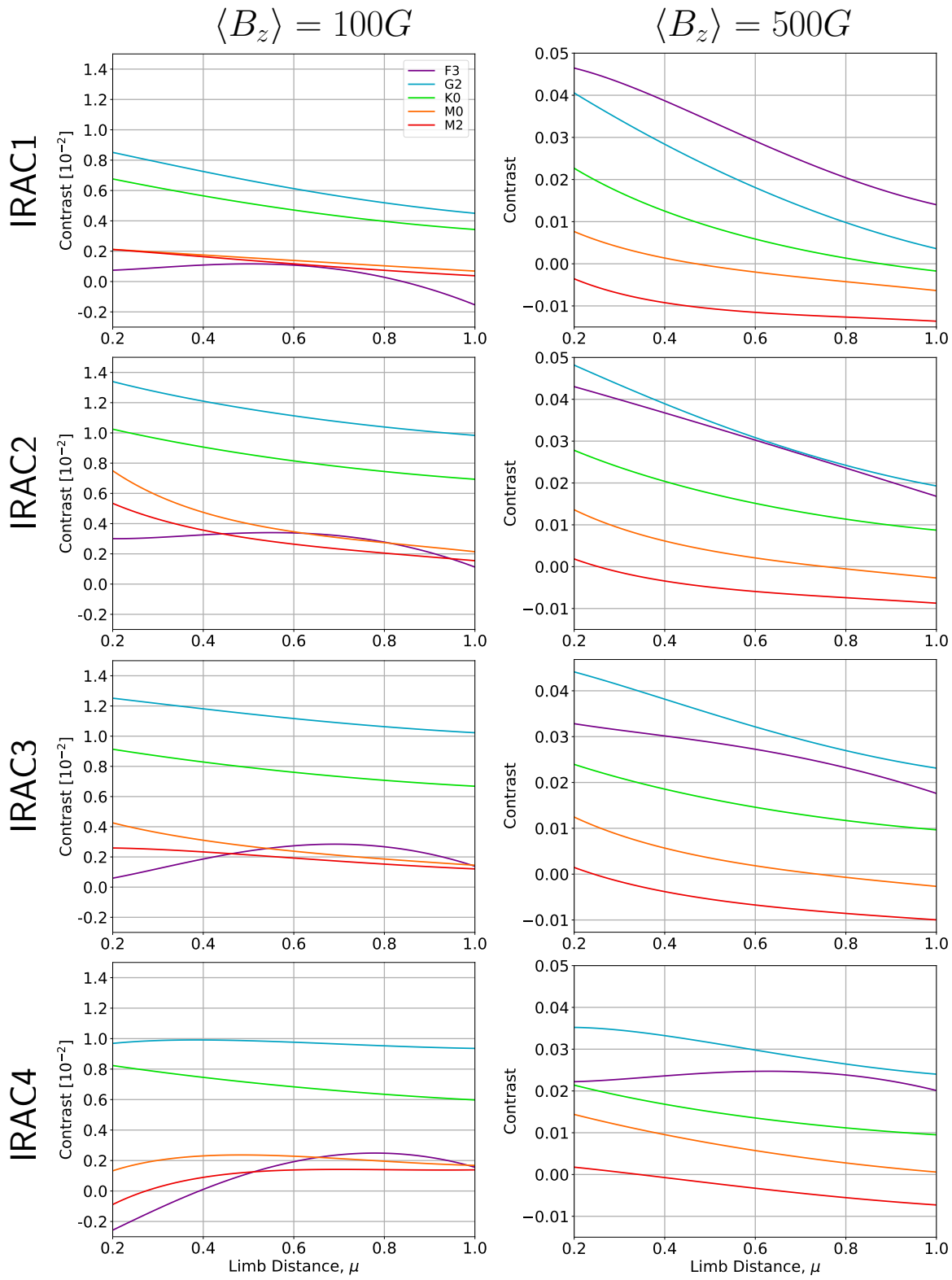


Figure 5.17: The average contrast relative to the average intensity of the hydrodynamic snapshots as a function of limb distance, μ. These are shown for *Spitzer* IRAC 1-4 filters and for $\langle B_z \rangle = 100$ G (left) and $\langle B_z \rangle = 500$ G (right). Colours corresponding to spectral type are given in the legend of the figure.

Table 5.3: *Kepler* centre-to-limb variation coefficients.

		I(1.0)	linear	quad		sqrt		non-linear 3			non-linear 4			
Star	mag	[10^5 W m^{-2} sr^{-1}]	a	a	b	a	b	a	b	c	a	b	c	d
F3V	20G	146.877	0.49	0.41	0.13	0.20	0.45	1.79	-2.01	0.86	-1.45	4.89	-4.90	1.83
F3V	100G	147.486	0.46	0.37	0.14	0.14	0.50	2.04	-2.51	1.09	-1.42	5.10	-5.35	2.05
F3V	500G	150.724	0.28	0.20	0.13	-0.02	0.49	2.76	-4.14	1.89	-2.28	7.64	-8.67	3.43
G2V	20G	76.6588	0.59	0.47	0.19	0.20	0.62	1.49	-1.16	0.38	0.53	0.34	-0.09	0.02
G2V	100G	76.8314	0.58	0.45	0.21	0.14	0.69	1.62	-1.38	0.47	0.43	0.70	-0.52	0.18
G2V	500G	75.6653	0.45	0.27	0.27	-0.14	0.92	2.37	-2.80	1.10	1.81	-1.51	0.80	-0.12
K0V	20G	35.6787	0.70	0.62	0.13	0.44	0.41	1.02	-0.27	0.01	0.22	0.55	0.16	-0.14
K0V	100G	36.2413	0.68	0.60	0.14	0.40	0.45	1.08	-0.37	0.05	0.18	0.69	-0.02	-0.07
K0V	500G	35.6450	0.62	0.52	0.16	0.28	0.54	1.32	-0.86	0.26	0.72	-0.24	0.59	-0.23
M0V	20G	8.00391	0.59	0.45	0.23	0.11	0.76	1.67	-1.37	0.44	0.39	0.83	-0.60	0.18
M0V	100G	7.98687	0.59	0.44	0.24	0.09	0.80	1.75	-1.50	0.49	0.53	0.61	-0.44	0.13
M0V	500G	7.82484	0.55	0.40	0.24	0.06	0.78	1.67	-1.43	0.46	0.78	-0.02	0.13	-0.07
M2V	20G	5.03042	0.57	0.42	0.24	0.07	0.78	1.57	-1.23	0.37	0.19	1.16	-0.85	0.24
M2V	100G	5.03560	0.57	0.41	0.24	0.05	0.81	1.64	-1.34	0.41	0.40	0.79	-0.55	0.14
M2V	500G	4.81937	0.54	0.39	0.23	0.06	0.76	1.51	-1.19	0.35	0.67	0.07	0.15	-0.10

Table 5.4: CoRoT centre-to-limb variation coefficients.

		I(1.0)	linear	quad		sqrt		non-linear 3			non-linear 4			
Star	mag	$[10^5$ W m^{-2} sr$^{-1}]$	a	a	b	a	b	a	b	c	a	b	c	d
F3V	20G	165.707	0.49	0.40	0.13	0.20	0.46	1.78	-2.00	0.85	-1.44	4.88	-4.88	1.82
F3V	100G	166.420	0.46	0.36	0.14	0.14	0.50	2.03	-2.50	1.08	-1.41	5.07	-5.31	2.03
F3V	500G	170.043	0.28	0.20	0.13	-0.03	0.49	2.73	-4.09	1.87	-2.19	7.45	-8.46	3.35
G2V	20G	86.2858	0.59	0.47	0.18	0.20	0.61	1.46	-1.13	0.37	0.52	0.35	-0.10	0.02
G2V	100G	86.5049	0.57	0.44	0.20	0.14	0.67	1.60	-1.35	0.46	0.41	0.71	-0.53	0.18
G2V	500G	85.2835	0.44	0.27	0.27	-0.14	0.91	2.34	-2.76	1.08	1.76	-1.45	0.75	-0.11
K0V	20G	40.3310	0.68	0.60	0.12	0.42	0.41	1.02	-0.30	0.02	0.23	0.51	0.17	-0.14
K0V	100G	40.9647	0.67	0.58	0.13	0.39	0.44	1.07	-0.40	0.06	0.20	0.65	-0.01	-0.07
K0V	500G	40.3257	0.61	0.51	0.16	0.28	0.53	1.31	-0.86	0.26	0.72	-0.24	0.58	-0.23
M0V	20G	9.60074	0.57	0.42	0.23	0.09	0.76	1.67	-1.42	0.47	0.46	0.67	-0.50	0.15
M0V	100G	9.58307	0.57	0.41	0.24	0.06	0.80	1.74	-1.53	0.51	0.59	0.47	-0.35	0.11
M0V	500G	9.39119	0.53	0.38	0.23	0.04	0.78	1.65	-1.45	0.48	0.81	-0.09	0.17	-0.07
M2V	20G	6.21377	0.54	0.39	0.24	0.04	0.79	1.61	-1.34	0.42	0.32	0.92	-0.70	0.20
M2V	100G	6.21948	0.53	0.38	0.25	0.02	0.82	1.66	-1.43	0.45	0.50	0.58	-0.43	0.11
M2V	500G	5.96568	0.51	0.36	0.23	0.03	0.76	1.53	-1.27	0.39	0.73	-0.03	0.18	-0.10

Table 5.5: TESS centre-to-limb variation coefficients.

		I(1.0)	linear	quad		sqrt		non-linear 3				non-linear 4			
Star	mag	[10^5 W m^{-2} sr^{-1}]	a	a	b	a	b	a	b	c	a	b	c	d
F3V	20G	136.024	0.39	0.30	0.14	0.09	0.47	1.51	-1.69	0.69	-0.71	3.04	-3.11	1.17
F3V	100G	136.738	0.36	0.27	0.14	0.05	0.50	1.70	-2.05	0.86	-0.68	3.16	-3.41	1.32
F3V	500G	140.223	0.23	0.15	0.12	-0.06	0.45	2.25	-3.35	1.51	-1.31	5.07	-5.95	2.40
G2V	20G	81.9268	0.48	0.35	0.20	0.05	0.68	1.45	-1.25	0.41	0.72	-0.09	0.18	-0.08
G2V	100G	82.1753	0.47	0.33	0.22	0.01	0.72	1.54	-1.41	0.47	0.67	0.10	-0.06	0.02
G2V	500G	81.4651	0.36	0.21	0.25	-0.17	0.84	2.01	-2.35	0.90	1.83	-1.93	1.30	-0.34
K0V	20G	44.4784	0.58	0.48	0.16	0.24	0.54	1.14	-0.61	0.13	0.29	0.53	-0.04	-0.06
K0V	100G	45.0620	0.57	0.46	0.17	0.22	0.56	1.19	-0.68	0.16	0.27	0.61	-0.15	-0.02
K0V	500G	44.5496	0.52	0.41	0.18	0.15	0.59	1.33	-1.01	0.32	0.73	-0.24	0.44	-0.17
M0V	20G	13.9415	0.49	0.34	0.24	-0.01	0.79	1.70	-1.58	0.54	0.69	0.22	-0.22	0.08
M0V	100G	13.9207	0.49	0.33	0.24	-0.03	0.82	1.75	-1.67	0.57	0.80	0.03	-0.07	0.03
M0V	500G	13.6699	0.46	0.31	0.23	-0.04	0.78	1.63	-1.54	0.52	0.91	-0.32	0.27	-0.09
M2V	20G	9.73654	0.47	0.31	0.25	-0.05	0.82	1.68	-1.57	0.52	0.60	0.39	-0.38	0.12
M2V	100G	9.74118	0.46	0.30	0.25	-0.07	0.84	1.71	-1.64	0.55	0.74	0.12	-0.16	0.05
M2V	500G	9.39799	0.44	0.29	0.23	-0.05	0.78	1.56	-1.44	0.47	0.85	-0.27	0.26	-0.11

Chapter 6

Small-scale magnetic structures

6.1 Applications to total solar irradiance

The total solar irradiance variability, on timescales of longer than a day, is attributed mainly to magnetic features on the surface of the Sun (Krivova et al., 2003). TSI reconstructions (e.g., SATIRE-S, discussed in Sect. 1.5) use facular contrasts derived from 1D atmospheric models that do not directly link to the magnetic field strength of a facular region. Facular brightness depends on the magnetic field strength of the facular region (Ortiz et al., 2002; Yeo et al., 2013). As such, for adequate reconstructions, 1D derived facular contrasts must be scaled to the the observed field strength. This requires using a free parameter that is calibrated using the observed TSI itself (Fligge & Solanki, 2000).

In Yeo et al. (2017), the need for such a free parameter was removed. The TSI reconstruction in Yeo et al. (2017) was an extension of SATIRE-S, using observed full-disc magnetograms to locate quiet Sun, spot (separated into umbral and penumbral) and facular pixels. In this case, the magnetograms were from the Helioseismic and Magnetic Imager (HMI) instrument on board the Solar Dynamics Observatory (SDO), Schou et al. (2012). Bolometric intensities derived from 1D models were used for the quiet Sun and spot pixels as spot darkening is successfully reproduced by 1D models. However, the intensities for faculae, usually derived from a 1D atmospheric model, were replaced with bolometric intensities calculated from the spectra derived from 3D MURaM atmospheres, presented in Chap. 4. Instead of using a filling factor to scale the facular contrast to the observed magnetogram signal (see Sect. 1.5) – a process that introduces a free parameter – we calculated the observed magnetic field by using the same MURaM atmospheres and performing spectral line synthesis for the Fe I 617.3 nm line before degrading to the HMI pixel size and calculating the magnetic flux density as would be measured by HMI. Each simulated

magnetic pixel can then be linked to a simulated bolometric intensity [1].

The 3D magnetised MURaM simulations with $\langle B_z \rangle$ = 100 G, 200 G and 300 G were used to obtain realistic bolometric intensities for facular regions on the Sun. These were calculated by degrading the spatial resolution of the spectra, such that the resulting bolometric intensities are for SDO/HMI pixel size. This approach was done for disc centre as well as along inclined rays, allowing us to derive the bolometric intensities as a function of the observed magnetogram signal and position on the Sun. This process is described in more detail in Yeo et al. (2017).

Figure 6.1 is taken from Yeo et al. (2017). It shows the bolometric intensity as a function of the magnetic field for SDO/HMI pixels calculated using the method described above for each limb distance (differentiated by colour), for all the snapshots combined. The crosses indicate the mean values of the HMI pixels binned by magnetic field strength. The solid lines are fits to the crosses and the dashed lines are the quiet Sun bolometric intensities at each limb distance, calculated from bolometric images of the hydrodynamic MURaM snapshots. The bolometric intensities were used to reconstruct the TSI based on solar-disc images following the method described in Fligge & Solanki (2000); Krivova et al. (2003); Yeo et al. (2014). This reconstruction showed that at least 95% of the TSI variations can be accounted for by magnetic activity without any need for adjusting the facular contrasts according to the observed TSI (Yeo et al., 2017).

At disc centre, at low magnetic field strengths, bolometric intensity decreases with increasing magnetic field. The highest intensities are those in granular pixels. Magnetic field is swept into intergranular lanes, leaving areas of dark intergranular lane with low magnetic field strengths. As magnetic field increases further, small magnetic features form, which tend to increase in size with increasing magnetic field. As the magnetic field concentrates, the gas from the feature evacuates, lowering the density (see Sect. 1.3.1 for more detail). This allows deeper layers in the feature to be observed. These deeper layers are heated by the features' hot walls and, as the features are small enough to be sufficiently heated, are brighter than the observed surrounding atmosphere for lower magnetic fields. As magnetic field increases further, intensity will begin to decrease as the features become too large for the walls to heat the gas within. Towards the limb, the increase in intensity with increasing magnetic field is enhanced as the hot walls of the features are revealed. More hot wall is revealed for larger, higher magnetic field features and for more inclined viewing angles. Therefore, the decrease at low magnetic field strength is limited

[1] My main contribution to this work was to calculate and provide the bolometric intensities for magnetised simulations of multiple activities and limb angles.

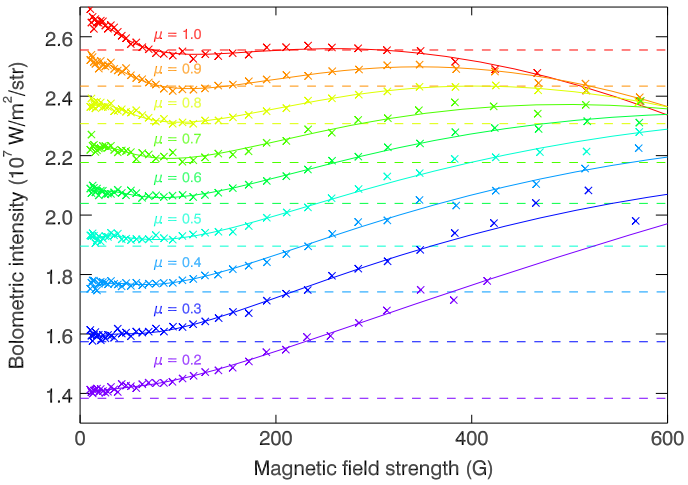
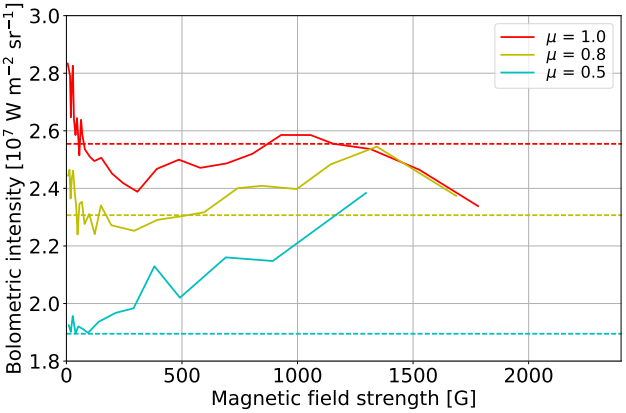


Figure 6.1: Average bolometric intensity as a function of average instrumental magnetic field strength in bins of 1000 pixels for HMI pixel size for all snapshots of G2V, $\langle B_z \rangle$ = 100 G, 200 G and 300 G simulations presented in Chap. 4 (solid lines). Dashed lines show the mean bolometric intensity for all hydrodynamic snapshots at each limb distance, μ. Limb distances of 1.0, 0.9, 0.8, 0.7, 0.6, 0.5, 0.4, 0.3 and 0.2 are shown by different colours, labelled on the figure. Credit: Yeo et al. (2017), © American Physical Society.

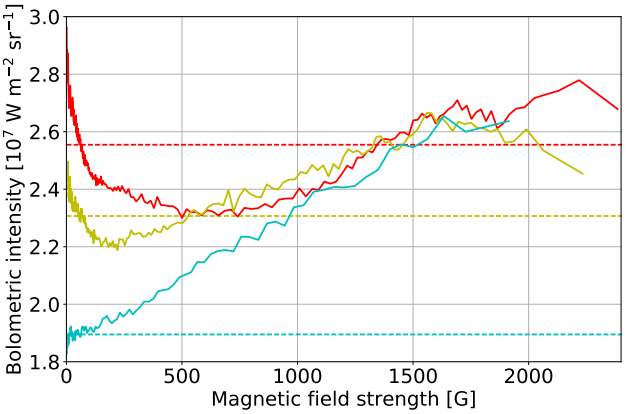
and pixels remain bright compared to the hydrodynamic bolometric intensity at all magnetic fields.

As the calculations performed in Yeo et al. (2017) were aimed at reconstructing solar irradiance from SDO images with specific passbands and instrumental characteristics, they involved a more in-depth calculation to obtain the magnetic field strength. Here, a broader view of the relationship between the radiation from facular regions and magnetic field is presented.

In the remaining calculations of this chapter magnetic fields relevant to the synthetic spectra were obtained by averaging over total magnetic fields in an optical depth range relevant to the wavelength being investigated. For Sections 6.1, 6.2 and 6.4, bolometric intensity is compared with total magnetic field averaged over the line of sight between $\log(\tau_{500}) = -2$ and -0.5. This range of optical depths should be representative of the magnetic field present in the layers where the bulk of the radiation is produced though the resulting magnetic field (denoted B) does not correspond to any observed field strength. Observed magnetic field strengths tend to measure the magnetic field in the direction of the line of sight, and therefore may not fully capture the radial field strength of a feature towards the limb. This may lead to calculations using the total magnetic field from the simulations having larger magnetic fields close to the limb than would be observed. Each of the following proof-of-concept calculations performed in Sects 6.1, 6.2 and 6.4 use only single



(a) 20×20 averaged pixels



(b) Full-resolution

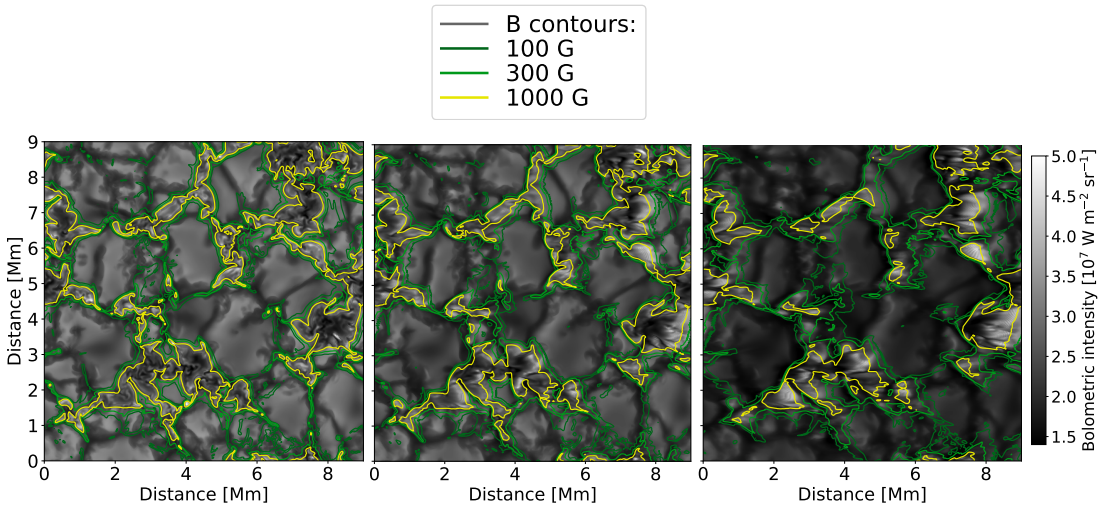
Figure 6.2: Mean bolometric intensity as a function of mean magnetic field in bins of 20 averaged pixels (a), or bins of 1000 full-resolution pixels (b), for a single snapshot of the G2V, $\langle B_z \rangle = 300$ G simulation (solid lines). Averaged pixels are of size 20 by 20 original pixels at disc centre (and equivalent for other limb distances). The magnetic field used is the mean over the total magnetic field recorded at each point in the simulation between optical depths, $\log(\tau_{500}) = -2$ and -0.5 along the line of sight. These are shown for disc centre (red) and limb distances, $\mu = 0.8$ (yellow) and $\mu = 0.5$ (cyan). Dashed lines show the mean bolometric intensity of all hydrodynamic snapshots at each limb distance.

snapshots. Further calculations could be improved by including all snapshots of the selected simulation. The calculations performed here do not take into account any stray light or instrumental effects.

For Figure 6.2a, the bolometric intensity images and magnetic fields were spatially averaged to obtain pixel sizes similar to that of the SDO/HMI pixels used in Yeo et al. (2017). This was achieved by averaging over 20×20, 20×25 and 20×40 pixels for disc centre, $\mu = 0.8$ and $\mu = 0.5$, respectively. These larger pixels will henceforth be referred to as "averaged pixels". A single $\langle B_z \rangle = 300\ G$ snapshot was chosen, as the $\langle B_z \rangle = 300\ G$ snapshots show the greatest variety of magnetic features and range of magnetic fields from the simulations used in the Yeo et al. (2017) paper.

Averaged pixels were ordered according to magnetic field and means of both magnetic field and the associated pixel intensities were taken for bins of 20 averaged pixels. Bolometric intensity as a function of magnetic field for disc centre (red), $\mu = 0.8$ (yellow) and $\mu = 0.5$ (cyan) are shown with solid lines in Fig. 6.2a. The dashed lines show the mean bolometric intensity over all G2V hydrodynamic snapshots. Due to the limited number of pixels in a single snapshot, the trends seen in Fig. 6.2a are much less smooth than those found in Yeo et al. (2017) (see Fig. 6.1). However, the lines are similar in shape. At a viewing angle of $\mu = 0.5$ both remain flat until approximately 100 G, where an increase in bolometric intensity with magnetic field then occurs, with values remaining above the mean hydrodynamic intensity. The gradient of the increase in Fig. 6.2a is smaller than that of Fig. 6.1. This could be due to the use of total magnetic field for the calculation in this chapter, rather than the line of sight magnetic field (as would be observed), leading to magnetic field strengths being larger in Fig. 6.2a.

For both Yeo et al. (2017) (seen in Fig. 6.1) and Fig. 6.2a, the disc-centre and $\mu = 0.8$ graphs show an initial decrease of intensity with increasing magnetic field strength. For Fig. 6.1, there is a slight increase in intensity with magnetic field from B $\sim$ 100 G onwards, while Fig. 6.2a shows a steeper increase starting at approximately 300 G. At higher magnetic fields a turnover to decreasing intensity is seen. This turnover occurs above B = 300 G for disc centre and at about 400 G for $\mu = 0.8$ for Fig. 6.1 and at B $\sim$ 1000 G and 1300 G for Fig. 6.2a at disc centre and $\mu = 0.8$, respectively. While Yeo et al. (2017) found almost flat values of disc-centre bolometric intensities at the hydrodynamic mean for magnetic fields between 100 and 300 G, disc-centre intensities in Fig. 6.2a deviate from the hydrodynamic bolometric intensity between 100 and 800 G. This deviation is only of the order of a few percent, and may be an artefact of the low number of averaged pixels available



(a) $\mu = 1.0$ **(b)** $\mu = 0.8$ **(c)** $\mu = 0.5$

Figure 6.3: Bolometric intensity images for a G2V $\langle B_z \rangle = 300$ G snapshot at disc centre (left), $\mu = 0.8$ (middle) and $\mu = 0.5$ (right). Intensities are given by the colour bar. Contours of total magnetic field averaged between $\log(\tau_{500}) = -2$ and -0.5 along the line of sight are overlaid at values given by the legend.

in a single snapshot and temporal variation. Thus, if the remaining $\langle B_z \rangle = 300$ G snapshots and the $\langle B_z \rangle = 100$ G and 200 G snapshots were included, as in Fig. 6.1, this may produce a flatter relationship. Alternatively, the Yeo et al. (2017) include straylight and instrumental noise, which may also smooth this relationship.

The similarities between these two sets of results suggest that by selecting relevant optical depths, and a good range of snapshots with varied magnetic features, magnetic field can be calculated and the expected relationship between intensity and magnetic field can be estimated. In order to use the resulting contrasts, the range over which the magnetic field is calculated will have to be adjusted according to the observable that is used to infer stellar magnetic fields.

6.2 Effect of instrument pixel size on bolometric intensity as a function of magnetic field

For different instruments and applications, the resolution needed will vary. Figure 6.3 shows images of the bolometric intensity for the G2V, $\langle B_z \rangle = 300$ G snapshot used in Fig. 6.2a at full simulation resolution. The images are shown at disc centre (Fig. 6.3a), $\mu = 0.8$ (Fig. 6.3b) and $\mu = 0.5$ (Fig. 6.3c) and displayed with the physical distances on the stellar surface preserved to better display the features. The colour bar on the right shows the intensity scale. Contours of total magnetic

field averaged between optical depths at 500 nm of -2 and -0.5 along the line of sight are overlaid to show the alignment of high magnetic field and certain features.

At disc centre, the areas of high magnetic field align well with the bright as well as the large, dark magnetic features. As an area contained within a 1000 G contour increases, the bolometric intensity in the centre of this area tends to be darker. As the snapshot is viewed at larger angles, it can be seen that the shapes of the magnetic field contours change in a similar way to the surface features. However, some detail associated with high-strength magnetic regions at disc centre may not correspond with a high level of magnetic field towards the limb. For example, the large dark feature seen in the lower right hand side of the snapshot is fully contained within the 1000 G contour at disc centre. However, when looking toward the limb, the hot bright wall of the granule is revealed (due to the evacuation caused by the magnetic field). This leads to a bright region. At $\mu = 0.5$, the bright wall of this feature is partially within the 1000 G contour, and partially outside, although staying within the 300 G contour. The range chosen for the averaging method used to calculate the magnetic fields is an estimate of where most of the radiation is formed, therefore, it may not provide the best possible representation of the magnetic field associated with the features. However, it can be seen that there is a good correlation between calculated magnetic field and associated features.

Figure 6.2b shows the extent to which intensity as a function of magnetic field will change for differing resolution. Each data point shown on Fig. 6.2b represents the average over 1000 (full-resolution) pixels and has been produced following the same process as for Fig. 6.2a.

In Fig. 6.2b, a larger range of magnetic fields are seen than with averaged pixels, as high magnetic field pixels are not averaged out with surrounding low magnetic field pixels. In the case of larger pixels, features smaller than the averaged pixel size would be diluted by the surrounding granules when averaged. Consequently, the pixel intensities tend more towards the hydrodynamic intensity and the magnetic field will be pushed towards low magnetic fields. This effect leads to the differences seen at both disc centre and $\mu = 0.8$. These lines maintain similar shapes as in Fig. 6.2a, but the dips into negative contrast (i.e., intensities below the value of the mean hydrodynamic intensity) reach lower intensities than those seen in the averaged pixels of Fig. 6.2a. This shows that intensities of pixels of this magnetic field can be much darker than suggested by lower resolution calculations or observations.

The turnover seen at disc centre for the averaged pixels, in Fig. 6.2a, at about 1000 G is not seen for the higher resolution in Fig. 6.2b and the bolometric intensity seen for higher magnetic fields continues to increase. However, at $\mu = 0.8$, a turnover

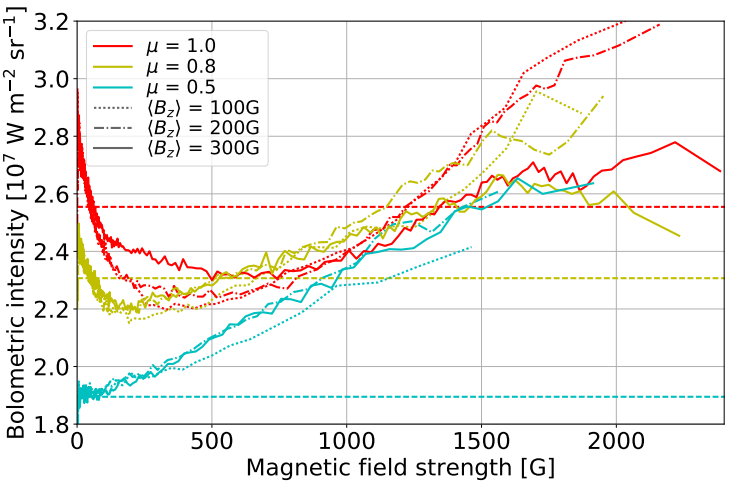


Figure 6.4: The average bolometric intensity as a function of average magnetic field between $\log(\tau_{500}) = -2$ and -0.5 in bins of 1000 pixels for a single G2V snapshot each of the $\langle B_z \rangle = 100$ G (dotted lines), 200 G (dot-dashed lines) and 300 G (solid lines) simulations. Limb distances $\mu = 1.0$ (red), $\mu = 0.8$ (yellow), and $\mu = 0.5$ (cyan) are shown. Dashed lines show the mean hydrodynamic bolometric intensity at each μ.

is seen, albeit, possibly at a higher magnetic field than for the lower resolution.

In the single pixel approach, the magnetic field that is obtained from a single pixel does not take into account that it may be positioned in the centre of a large feature surrounded by highly magnetised pixels, which could cause the intensity in the pixel itself to be lower. Conversely, a pixel with the same magnetic field could be positioned in a small feature, and appear brighter due to the nature of the surrounding pixels. Thus, averaging over a larger region containing an entire feature can allow for a better representation of each of the features as a whole. However, due to the large range of feature sizes, and the constant pixel size of observations it is more useful to calculate these parameters for a given pixel size.

6.3 Effect of activity on bolometric intensity as a function of magnetic field

As the magnetic activity of a star increases, the magnetic field that may be injected into regions of the surface is increased. The level of injected magnetic field, $\langle B_z \rangle$, affects the types of features that form in an area, therefore affecting the range of intensities that are observed. In this section, the effect of activity on the relationship between bolometric intensity and the total magnetic field averaged along the line of sight (B) is examined. G2V snapshots from the 10 snapshot set of simulations

are used as they have a high $\langle B_z \rangle$ resolution (see Sect. 2.1 for details). Figure 6.4 shows the pixel intensity as a function of average total magnetic field for three snapshots of different activities; one from each of the $\langle B_z \rangle$ = 100 G (dotted lines), 200 G (dot-dashed lines) and 300 G (solid lines) simulations. Three limb angles are shown in Fig. 6.4: $\mu = 1.0$ (red), $\mu = 0.8$ (yellow) and $\mu = 0.5$ (cyan). The mean hydrodynamic bolometric intensity is shown for each limb angle with a dashed horizontal line. The $\langle B_z \rangle$ = 300 G snapshot here is the same as used for Figs. 6.2a and 6.2b.

In Fig. 6.4, at very low magnetic fields, B < 100 G, all levels of activity show similar decreases (in the case of $\mu = 1.0$ or 0.8), or constant values (in the case of $\mu = 0.5$). These pixels are those in the granules. At limb distance, $\mu = 0.5$, all snapshots show very similar increases in intensity with magnetic field, throughout the magnetic field range. This is due to the viewing angle being large enough that most of the features observed appear bright, due to the hot walls being revealed, even when they are dark towards disc centre.

Up to 1000 G for limb distance, $\mu = 0.8$, intensities remain similar across the activity levels, while at disc centre between 100 G and 700 G, where the contrast compared to the hydrodynamic mean is negative, the $\langle B_z \rangle$ = 100 G and 200 G (lower activity) snapshots have lower intensities than the $\langle B_z \rangle$ = 300 G (higher activity) snapshot. This may be due to more of the dark intergranular lanes being filled with bright magnetic features at this level of activity, increasing the average intensities seen with these magnetic fields. Above 1000 G, for both disc centre and $\mu = 0.8$, the lower activity snapshot intensities are larger than those seen in the $\langle B_z \rangle$ = 300 G snapshot, with the lower activity intensities increasing with magnetic field, even when the highest activity line begins to flatten and, in the case of the $\mu = 0.8$ snapshot, turn over. This is due to there being no large, dark features in the $\langle B_z \rangle$ = 100 G and 200 G simulations, so all of the high magnetic field pixels are within bright features.

The data in Fig. 6.4 suggests that when viewing at small angles (e.g., disc centre and $\mu = 0.8$) in areas of high activity, regions of high magnetic field (above 1000 G) are more likely to be darker than in lower activity regions. However, for all activities viewed here, the contrast compared to the hydrodynamic mean remains positive above magnetic fields of 1300 G, and thus pixels of high magnetic field are on average bright. At disc centre, in mid-range magnetic fields (100 G to 900 G), the opposite appears to be true, with the majority of pixels being dark compared to the hydrodynamic mean, and this contrast becoming closer to zero with increased activity.

As seen in Sect. 6.2, the resolution at which intensity as a function of magnetic field is observed affects the outcome. See Fig. C.7 in Appendix C for the equivalent of Fig. 6.4 for averaged pixels.

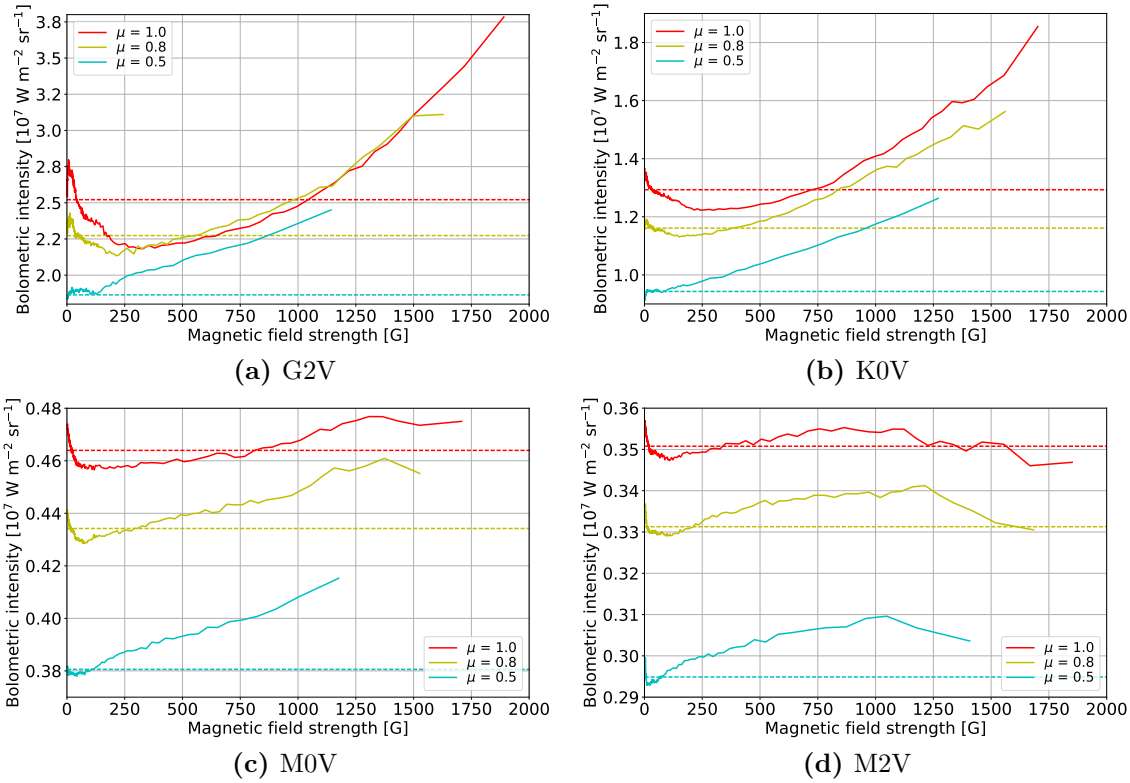
6.4 Effect of spectral type on bolometric intensity as a function of magnetic field

In order to compare the relationship of intensity to pixel magnetic field of different spectral types, calculations were performed using the $\langle B_z \rangle = 100$ G simulations. As seen in Figs. 5.1 to 5.4, this means that only small magnetic features are present in these simulations. If $\langle B_z \rangle = 500$ G snapshots were used (see Figures C.8a to C.8d in App. C), mainly large dark features would be included. To allow for a wide range of features and magnetic fields, simulations with intermediate values of $\langle B_z \rangle$ would need to be performed, as for G2V stars in Chap. 4.

Figures 6.5a to 6.5d show mean bolometric intensity as a function of mean magnetic field in bins of 1000 pixels for a single snapshot of each star from G2V to M2V spectral types with solid lines. The dashed lines show the mean bolometric intensity over all pixels of all hydrodynamic snapshots. Limb distances of 1.0, 0.8 and 0.5 show how the relationship changes at different viewing angles.

For the G2V star, in Fig. 6.5a, it can be seen that the shapes of the graphs at all limb positions remain largely the same as when looking at a $\langle B_z \rangle = 300$ G snapshot (as in Fig. 6.2b). The graph is, however, cut off at 2000 G as higher magnetic fields are not seen in the $\langle B_z \rangle = 100$ G snapshot. Therefore, the turnover in bolometric intensity at high magnetic fields is not seen. The negative contrast portion of the $\mu = 0.8$ graph occurs at the same magnetic fields for both snapshots. The increase of bolometric intensity with increasing magnetic field has a larger gradient for the $\langle B_z \rangle = 100$ G snapshot for both disc centre and $\mu = 0.8$. These differences could be due to the pixels with these magnetic fields largely being in small, bright magnetic features for $\langle B_z \rangle = 100$ G snapshots, while in the $\langle B_z \rangle = 300$ G snapshot, pixels with this magnetic field may occur at the edges of larger, dark magnetic features, therefore decreasing the average bolometric intensity typically seen at this magnetic field.

The shapes of the graphs for G2V (Fig. 6.5a) and K0V (Fig. 6.5b) stars are similar. The main difference is the gradients of the increase in the graphs, leading to the bolometric contrast becoming positive at a lower magnetic field for K0V stars than for G2V stars for both μ =1.0 and 0.8. Additionally, this difference in gradients



(a) G2V **(b)** K0V

(c) M0V **(d)** M2V

Figure 6.5: The average bolometric intensity as a function of average magnetic field between $\log(\tau_{500}) = -2$ and -0.5 in bins of 1000 pixels for a single snapshot of the $\langle B_z \rangle = 100$ G simulations. These are shown by solid lines for $\mu = 1.0$ (red), $\mu = 0.8$ (yellow), and $\mu = 0.5$ (cyan). Dashed lines show the mean hydrodynamic bolometric intensity at each μ. The top row shows G2V (left) and K0V (right) snapshots. The bottom row shows M0V (left) and M2V (right) snapshots.

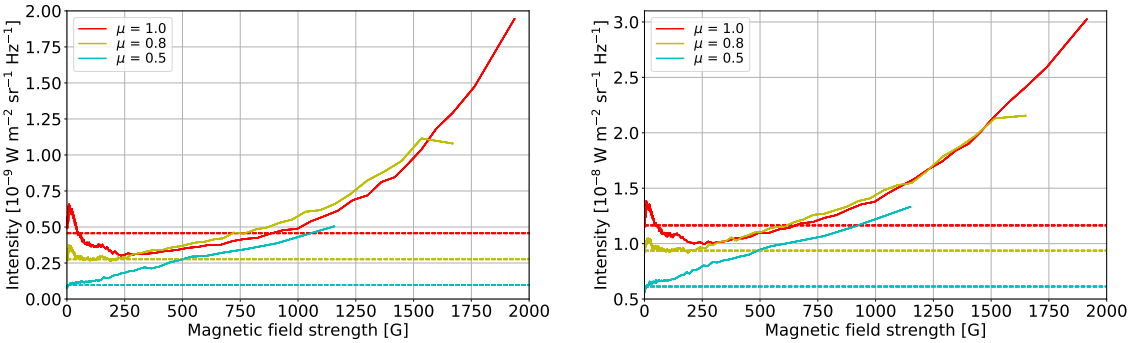
causes the $\mu = 0.8$ average bolometric intensity at a given B to never exceed that of the disc-centre intensities, as they do for G2V stars.

The M0V star, in Fig. 6.5c, has similar ranges of magnetic field for negative bolometric intensities as the K0V snapshot for all limb distances. However, the rate of increase of bolometric intensity with increasing magnetic field is much less for M0V stars. Similarly, the M2V snapshot in Fig. 6.5d has a low rate of increase in bolometric intensity. The M2V snapshot is also the only star for the 100 G snapshots that shows a decrease in intensity at high magnetic fields and the contrast even becomes negative again at approximately 1600 G. The presence of a turnover for M2V stars could be due to the emergence of larger features for this spectral type, even at $\langle B_z \rangle = 100$ G, where only small, predominantly bright, features are present for the other spectral types.

The comparisons made here are for different pixels sizes for each spectral type, see Tab. 2.1 in Chap. 2 for resolutions of simulations. Therefore differences may vary if the spectral types were observed with the same resolution at the same distance. While this approach of finding the average intensity seen for a given magnetic field can be useful for estimating the intensity that will be seen for an instrument of a given resolution (as in Yeo et al. (2017)), care must be taken as there is a distribution of intensity values at a given B, that depends on the types of features that are present.

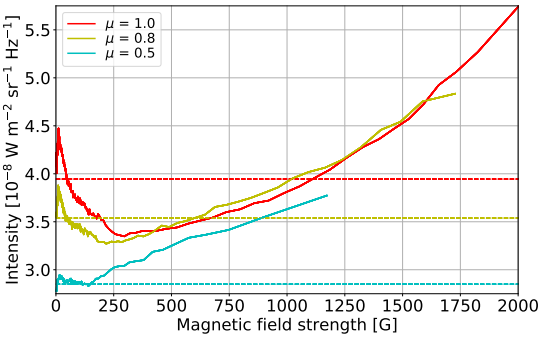
6.5 Effect of wavelength on intensity as a function of magnetic field

Figures 6.6a to 6.6d show how the relationship between intensity and magnetic field (B) changes over wavelength for a G2V, $\langle B_z \rangle = 100$ G snapshot. The graphs show the average intensity as a function of the average magnetic field for bins of 1000 pixels at four different wavelengths, matching those seen in Chap. 5 (214.5 nm, 387 nm, 601 nm and 1597.5 nm). To calculate the magnetic field in a pixel, the total magnetic field along the line of sight is averaged (as for the bolometric case). However, as the formation heights for different wavelengths vary, the lower edge of the optical depth range averaged over ($\log(\tau_{500,bot})$) is set at the approximate optical depth (calculated at 500 nm) where the brightness temperature of the chosen wavelength occurs. The magnetic field is calculated over a range of $\log(\tau_{500}) = 1.5$ in the line of sight above this $\log(\tau_{500,bot})$ ($\log(\tau_{500,bot}) = -0.35$, -0.41, -0.18 and -0.06 for 214.5 nm, 387 nm, 601 nm and 1597.5 nm, respectively).

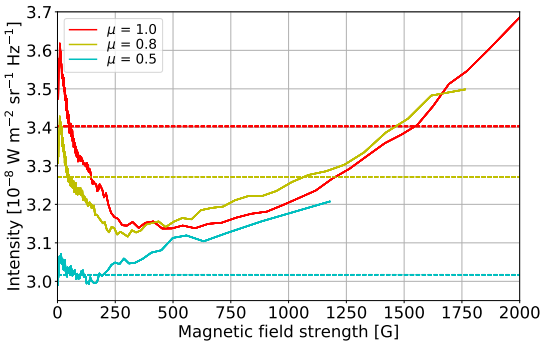


(a) 214.0 nm

(b) 387.0 nm



(c) 601.0 nm



(d) 1597.5 nm

Figure 6.6: The average intensity as a function of average magnetic field over a range of $\log(\tau_{500}) = 1.5$ in bins of 1000 pixels for a single G2V snapshot of the $\langle B_z \rangle = 100$ G simulations. These are shown by solid lines for $\mu = 1.0$ (red), $\mu = 0.8$ (yellow), and $\mu = 0.5$ (cyan). Dashed lines show the mean hydrodynamic intensity at each μ and λ. The top row shows 214.5 nm (left) and 387 nm (right). The bottom row shows 601 nm (left) and 1597.5 nm (right) snapshots.

At first glance, the shapes of the curves at all limb distances are similar across the wavelength range, though the extent of the intensity changes varies dramatically. The UV wavelengths show the largest changes, going from a minimum value of approximately 60% of the mean hydrodynamic value at disc centre to 300% at 1800 G, while the disc-centre NIR only goes from a minimum of 93% of the mean hydrodynamic value to only 104% at 1800 G.

At $\mu = 1.0$ and $\mu = 0.8$ the intensity initially decreases with increasing magnetic field. The intensity values for $\mu = 0.8$ are lower than the disc-centre intensity values throughout this decrease. At all wavelengths, the $\mu = 1.0$ contrasts always become negative, i.e., intensity becomes less than the mean hydrodynamic intensity (red, dotted line), whereas, $\mu = 0.8$ intensities only become negative at longer wavelengths (601 nm and 1.6 μm). The magnetic field at which the disc centre contrast becomes negative is similar for all wavelengths.

At approximately 250 G, for both disc centre and $\mu = 0.8$, the graph flattens, or intensity begins to increase with increasing magnetic field. The $\mu = 0.8$ intensities begin to exceed those of the disc centre. The disc-centre contrast becomes positive again during this increase, as do the $\mu = 0.8$ contrasts that were negative. The magnetic field at which this occurs varies significantly across wavelength. For example, at disc centre in the NUV (e.g., 387 nm in Fig. 6.6b) intensity rises above the mean hydrodynamic value at $\sim$700 G, and in the NIR (see Fig. 6.6d) intensity does not exceed the hydrodynamic value until over 1500 G. For 601 nm, this crossing point occurs at approximately the same magnetic field as it does for bolometric intensities (seen in Fig. 6.5a). This is due to the visible light dominating the bolometric intensity for G2V stars.

In the UV (Figs. 6.6a and 6.6b), $\mu = 0.5$ intensity increases linearly with increasing magnetic field, while in the visible and NIR (Figs. 6.6c and 6.6d) it is initially near constant or slightly decreasing before again showing an almost linear increase. The value of intensity for $\mu = 0.5$ remains below that of the intensity at disc centre and $\mu = 0.8$, meaning features are darker. However, due to limb darkening, with comparison to the hydrodynamic mean intensities (dashed lines), contrast at $\mu = 0.5$ remains positive even for magnetic fields where disc centre and $\mu = 0.8$ contrasts are negative.

The relationship between intensity at a given wavelength and magnetic field varies across spectral type. See Figs. C.9a to C.9d in Appendix C for the M0V equivalent to Figs. 6.6a to 6.6d.

6.6 Summary

The results presented in Yeo et al. (2017) and Sect. 6.1 show that linking the intensities calculated from these simulations with magnetic field strengths can supply valuable information to better understand the relative importance of the magnetic activity for the variability of the Sun. While Yeo et al. (2017) provides an in-depth calculation for a specific solar-observing mission, linking intensity with magnetic field using the magnetic field values from the MURaM simulations, as has been done in Sects 6.2 to 6.5, can provide inputs for stellar simulations to estimate the role of magnetic activity on other stars.

The results in Sections 6.2 to 6.5 are preliminary and based on pixels from only one of the six, or ten in the case of the G2V simulations used for Yeo et al. (2017), available snapshots for each $\langle B_z \rangle$. These investigations would benefit from inclusion of all pixels from these snapshots. For better comparison with observable magnetic field strengths, the magnetic field used in these intensity as a function of magnetic field investigations could use the line of sight magnetic field calculated from the snapshots, rather than the total magnetic field. Additionally, more information about the populations of magnetic features that cause the shape of the relationship between intensity and magnetic field could be provided by looking at how the intensities are spread for single magnetic field values.

Chapter 7

Conclusion

7.1 Summary of thesis achievements

In this thesis, I explore the spectral radiation from small-scale magnetic features on cool main-sequence stars. As we lack the ability to resolve these features on other stars, this has been achieved by the synthesis of spectra from 3D magneto-convection models. LTE spectra between 149.5 and 160 000 nm from magneto-convection simulations for 5 spectral types between F3V to M2V of multiple activity levels (i.e., with different injected magnetic fields), each for limb distances from $\mu = 0.2$ to 1.0 have been calculated and presented. The work within demonstrates the effectiveness and the necessity of using 3D simulations to provide accurate representations of small-scale magnetic features.

In Chapter 2, the magneto-convection simulations, and selection of snapshots used for this study are described. I discuss the temperature structure of the 3D atmospheres compared with 1D equivalents for two spectral types and find that 3D atmospheres for the hotter type (G2V) have a larger spread of temperatures and temperature gradients than the cooler type (M0V). Magnetic field, temperature and velocities in constant $\log(\tau_{500})$ planes in a MURaM simulation show the shapes of the structures that form and their temperatures. To prepare the 3D MURaM atmospheres for spectral synthesis for different viewing angles, they are interpolated along different sight lines. This method is described in Chapter 2. Finally, this chapter concludes with a description of the chosen spectral synthesis code (ATLAS9) and the approximations used to allow for the large number of calculations that are necessary to calculate spectra for a range of spectral types and activities for 3-dimensional simulations.

In Chapter 3, observed solar limb darkening laws are compared with the G2V limb darkening coefficients derived from the 3D MURaM simulation. Assuming the

true field-free quiet solar surface is never truly seen, the derived 3D limb darkening represents the observed limb darkening well from the UV to the NIR, as seen in Norris et al. (2017). Limb darkening is derived for all simulated spectral types and coefficients are provided for a number of star-observing missions. For *Kepler* and CoRoT filters, limb darkenings are compared to the limb darkening derived from 1D Kurucz atmospheres (Sing, 2010). Differences for all spectral types are seen in both filters. For hotter stars, limb darkening in the *Kepler* filter is steeper in 3D than for 1D models, in agreement with Magic et al. (2015). Limb darkening laws derived from 3D atmospheres are then compared with those derived from a 1D mean atmosphere of the 3D simulations. As expected, for hotter stars in both filters, the limb darkening behaviour differs between the two derivations. This was concluded to be due to the large variety of atmospheric structures, seen in Chapter 2 for the G2V snapshots, that are averaged out in the 1D case. Surprisingly, the difference between the averaged 1D and 3D derived limb darkening laws for M stars is much smaller. This could be due to the low variation in temperature structure seen across the snapshot pixels, discussed in Chapter 2 for M2V snapshots.

A set of G2V snapshots from MURaM simulations with a high resolution of injected vertical magnetic field, $\langle B_z \rangle$ (representing stellar activity), were obtained. This led to an investigation of how the spectra of magnetic regions changes with activity. In Chapter 4, I explore the variety of features that emerge as injected magnetic field is increased in a region of a solar-type star. By comparing these magnetic simulations to spectra from field-free simulations, we were, for the first time, able to construct facular contrast as a function of μ, $\langle B_z \rangle$ and λ over a large wavelength range. We find that the contrast spectra display a complex dependence on magnetic field and limb distance that cannot be fully reproduced by commonly used 1D models. For example, as the average vertical magnetic field increases, contrasts initially increase, but eventually 'turn over' and decrease, particularly at disc centre for wavelengths between 400 and 2000 nm. This effect is not accounted for in currently available reconstructions of the total and spectral solar irradiance, TSI and SSI, respectively. The results from this chapter have been published in Norris et al. (2017).

Chapter 5 presents calculated spectra and contrasts for the remaining spectral types (F3V-M2V). Using MURaM simulations of stellar atmospheres at appropriate effective temperatures and strengths of gravity, snapshots are obtained that show the types of features that would emerge. I investigate how the features observed for different spectral types vary with injected magnetic field and wavelength. To demonstrate the effect of such magnetic features on stellar spectra, I calculated

mean contrasts with respect to the mean of the hydrodynamic snapshots across wavelength and μ. These calculations confirm that there is no simple scaling of facular contrast between spectral types. In molecular bands, such as the TiO bands, the shape of spectral contrast varies drastically between spectral types. Even when considering only a single wavelength band, the shape of the centre-to-limb variation of the contrast changes with effective temperature. The complicated nature of the emergence of these magnetic flux concentrations at different levels of activity and the complex relationship of facular contrasts with μ, $\langle B_z \rangle$ and λ leads to the conclusion that one-dimensional models must always omit detail that can only be captured with these types of simulations. For initial ease of use of this data, coefficients for fits to contrasts in commonly used filters as a function of limb position and activity are provided for all spectral types.

In Chapter 6, work from Yeo et al. (2017) is summarised. The G2V synthetic spectra, presented in Chap. 4, and the corresponding MURaM atmospheres, are used to calculate bolometric intensity as a function of magnetic field strength as would be observed on the Sun in SDO/HMI pixels. This is calculated for multiple limb distances. SDO/HMI pixels would contain approximately 20×20 full-resolution simulation pixels, as such, the bolometric intensities calculated from the synthetic spectra are averaged to obtain these data. Magnetic field strength is calculated from the MURaM atmospheres by using spectral line synthesis and extracting the magnetic field as they would for solar observations. The relationship calculated is used to reconstruct TSI variability without the need for the previously used free parameter, that has, until now, been required due to the use of facular spectra derived from 1D atmospheric models. This confirms, without calibration to the observed TSI, that the TSI variability on timescale of longer than a day can almost completely (over 95%) be accounted for by solar surface magnetic activity. This also indicates that the photometric variability on timescales of longer than a day on other cool stars could primarily be caused by stellar surface magnetism.

Having seen the effectiveness of calculating intensity as a function of magnetic field strength for smaller regions of the snapshots, I perform preliminary calculations to find this relationship for single pixels. I investigate how this relationship varies with wavelength for G2V stars, and across spectral type for bolometric intensity. I find that at a given limb distance, μ, the shape of the function is largely similar across wavelength for G2V stars, and across spectral type for bolometric intensities, although spreads in the intensity across magnetic field strengths vary enormously.

In conclusion, this thesis provides evidence that 3D modelling is necessary for accurate representation of small-scale magnetic features on cool main-sequence stars.

A large array of spectral data for multiple spectral types and magnetic activities has been produced that can be used in solar or stellar physics, as well as planetary transit models.

7.2 Future work

The calculations presented in this thesis provide spectral information for many pixels containing a large range of magnetised atmospheres for multiple spectral types. In addition to the application already achieved and presented in Sect. 6.1 and published in Yeo et al. (2017), the vast amount of information contained in these synthesised spectra, along with the snapshots that they were derived from can be applied to many areas. This section suggests future uses for the data presented here as well as detailing some of the work still to be done in the areas of this thesis.

Firstly, the spectral synthesis for snapshots in Chap. 4 was performed with an old version of the ODF tables. As these tables have been updated, these snapshots will be re-run with the new ODF tables. These new G2V spectra can then be used to perform spectral solar irradiance variability reconstructions with a similar method as that seen for TSI in Chap. 6 for Yeo et al. (2017). This could determine the extent to which solar surface magnetic activity is responsible for variability in different parts of the solar spectrum.

The simulations used in this thesis, and the spectral synthesis performed are for solar metallicity. Metallicity plays an important role in the opacities in a stellar atmosphere, as it affects both line and continuum opacity sources (particularly H^-). Spectral lines have been found to be the main source of variability on timescales of a day and longer on the Sun (Shapiro et al., 2015). As such, understanding the role of metallicity is important for accurate modelling of limb darkening, facular contrasts and stellar variability. Higher metallicity has been observed to be associated with higher variability in Karoff et al. (2018) and attributed to the larger facular contrasts resulting from the metallicity increase. 1D atmospheric models have also been used to demonstrate this increase of facular contrast and variability with increased metallicity (Witzke et al., 2018). To account for these changes with metallicity in stellar variability studies and in planetary observing techniques, these 3D simulations and spectral synthesis must be repeated for various values of metallicity. To achieve this, the equation of state within the MURaM simulations must be changed to reflect the metallicity, and, for the radiative transfer calculations, an ODF table used that corresponds to the metallicity.

The low spatial resolution contrasts calculated in this thesis can be used to

improve our understanding of micro-variability of late-type stars as recorded by *Kepler* and CoRoT, and as will be provided in future by TESS (Ricker et al., 2015) and PLATO (Rauer et al., 2014). To improve the range of activities available for these contrasts, simulations with $\langle B_z \rangle = 300$ G are being run for the spectral types shown in this thesis. Snapshots from these simulations will allow us to provide facular contrasts for a greater resolution of magnetic field strength. They will also potentially provide evidence for a similar turnover in contrast with $\langle B_z \rangle$ on other late-type stars as is seen for the G2V type.

Stellar magnetic activity is recognised as a significant source of noise and systematics for the detection and characterisation of exoplanets. To model the effects of this activity, simulated stars are covered with spots and faculae, and an observation including an orbiting planet is simulated. An example of this method for a transiting planet is Herrero et al. (2016). Typically, for transit simulations, the faculae are taken to emit a black-body like spectrum, resulting in facular contrasts that do not reproduce the observed wavelength and limb-angle dependence. The contrasts and centre-to-limb variations of magnetic regions presented in Chap. 4 and 5 are averages over a simulation box. As the observed resolution is low for other stars, these spectral contrasts can thus be used to enhance planetary transit spectroscopy by enabling more accurate modelling of facular regions on exoplanet host stars. For example, TiO can be an important opacity source in the atmospheres of hot Jupiters (Haynes et al., 2015; Evans et al., 2016), but, as we see in this thesis, the contrasts of magnetic regions in the TiO bands tend to be higher and vary with stellar spectral type. Therefore, the abundances in the planetary atmosphere can be miscalculated when magnetic activity is ignored or misrepresented. The spectral contrasts calculated in this thesis can be used to constrain the stellar contribution in transit observations, and thus allow for more accurate results regarding the planetary atmosphere itself.

In turn, by using observed transiting planets as a probe, star light blocked by the planet at multiple positions across the stellar disc can be measured. These measurements allow for the validation of the limb darkening coefficients and magnetic region contrasts calculated in this thesis. This would require multi-wavelength or spectroscopic observations. Additionally, these measurements could be used to trace the positions of active regions on the stellar surface. Due to the degeneracy between stellar and planetary parameters in planetary transit measurements, for accurate information on the star, ideally the transiting planet would be rocky with minimal atmosphere, to limit its spectral response.

The preliminary investigations of intensity as a function of magnetic field in

Chap. 6 provide an insight into the information that could be extracted from such simulations. However, to obtain more accurate representation of this particular relationship, all pixels of all snapshots should be included in the calculations. Additionally, for comparison with observable magnetic field that may be obtained with star-observing missions, the line-of-sight magnetic field could be calculated from the simulation magnetic field vectors.

As it is difficult to measure magnetic field on stars other than the Sun, intensity as a function of magnetic field may not be the best way for this information to be transfered to stellar and exoplanetary applications. While Ca II H & K is one of the more easily observable measures of magnetic activity, the simulations used in this thesis do not include the chromosphere and therefore these lines cannot be accurately synthesised. However, the spectra calculated in this thesis could potentially be used to identify typical magnetic features found on a given spectral type and therefore provide typical feature, i.e., facular, contrasts for each simulated spectral type.

As full spectra for a variety of spectral types and activities have been calculated, further calculations using these spectra for different instrument filters can provide facular models for many star-observing missions.

Bibliography

Afram N., Unruh Y. C., Solanki S. K., Schüssler M., Lagg A., Vögler A., 2011, A&A, 526, A120

Agol E., 2007, MNRAS, 374, 1271

Anders E., Grevesse N., 1989, Grochim. Cosmochim. Acta, 53, 197

Auffret H., Muller R., 1990, Publications of Debrecen Heliophysical Observatory, 7, 162

Baliunas S. L., Donahue R. A., Soon W., Henry G. W., 1998, in Astronomical Society of the Pacific Conference Series, Vol. 154, Cool Stars, Stellar Systems, and the Sun, Donahue R. A., Bookbinder J. A., eds., p. 153

Baliunas S. L., Donahue R. A., Soon W. H., Horne J. H., Frazer J., Woodard-Eklund L., Bradford M., Rao L. M., Wilson O. C., Zhang Q., Bennett W., Briggs J., Carroll S. M., Duncan D. K., Figueroa D., Lanning H. H., Misch T., Mueller J., Noyes R. W., Poppe D., Porter A. C., Robinson C. R., Russell J., Shelton J. C., Soyumer T., Vaughan A. H., Whitney J. H., 1995, ApJ, 438, 269

Barthol P., Gandorfer A., Solanki S. K., Schüssler M., Chares B., Curdt W., Deutsch W., Feller A., Germerott D., Grauf B., Heerlein K., Hirzberger J., Kolleck M., Meller R., Müller R., Riethmüller T. L., Tomasch G., Knölker M., Lites B. W., Card G., Elmore D., Fox J., Lecinski A., Nelson P., Summers R., Watt A., Martínez Pillet V., Bonet J. A., Schmidt W., Berkefeld T., Title A. M., Domingo V., Gasent Blesa J. L., Del Toro Iniesta J. C., López Jiménez A., Álvarez-Herrero A., Sabau-Graziati L., Widani C., Haberler P., Härtel K., Kampf D., Levin T., Pérez Grande I., Sanz-Andrés A., Schmidt E., 2011, Sol. Phys., 268, 1

Basri G., Walkowicz L. M., Batalha N., Gilliland R. L., Jenkins J., Borucki W. J., Koch D., Caldwell D., Dupree A. K., Latham D. W., Marcy G. W., Meibom S., Brown T., 2011, AJ, 141, 20

Basri G., Walkowicz L. M., Batalha N., Gilliland R. L., Jenkins J., Borucki W. J., Koch D., Caldwell D., Dupree A. K., Latham D. W., Meibom S., Howell S., Brown T., 2010, ApJL, 713, L155

Basri G., Walkowicz L. M., Reiners A., 2013, ApJ, 769, 37

Beeck B., 2014, PhD thesis, International Max Planck Research School for Solar System Science at the University of Gttingen

Beeck B., Cameron R. H., Reiners A., Schüssler M., 2013, A&A, 558, A48

Beeck B., Collet R., Steffen M., Asplund M., Cameron R. H., Freytag B., Hayek W., Ludwig H.-G., Schüssler M., 2012, A&A, 539, A121

Beeck B., Schüssler M., Cameron R. H., Reiners A., 2015a, A&A, 581, A42

—, 2015b, A&A, 581, A43

Berkefeld T., Schmidt W., Soltau D., Bell A., Doerr H. P., Feger B., Friedlein R., Gerber K., Heidecke F., Kentischer T., v. D. Lühe O., Sigwarth M., Wälde E., Barthol P., Deutsch W., Gandorfer A., Germerott D., Grauf B., Meller R., Álvarez-Herrero A., Knölker M., Martínez Pillet V., Solanki S. K., Title A. M., 2011, Sol. Phys., 268, 103

Bray R. J., Loughhead R. E., 1964, Sunspots

Broomhall A.-M., Chatterjee P., Howe R., Norton A. A., Thompson M. J., 2014, Space Sci. Rev., 186, 191

Brun A. S., Browning M. K., 2017, Living Reviews in Solar Physics, 14, 4

Carlsson M., Stein R. F., Nordlund Å., Scharmer G. B., 2004, ApJL, 610, L137

Castelli F., 2005, Memorie della Societa Astronomica Italiana Supplementi, 8, 25

Castelli F., Kurucz R. L., 1994, A&A, 281, 817

—, 2001, A&A, 372, 260

—, 2004, ArXiv Astrophysics e-prints

Cegla H. M., Lovis C., Bourrier V., Beeck B., Watson C. A., Pepe F., 2016, A&A, 588, A127

Cegla H. M., Shelyag S., Watson C. A., Mathioudakis M., 2013, ApJ, 763, 95

Cegla H. M., Watson C. A., Shelyag S., Chaplin W. J., Davies G. R., Mathioudakis M., Palumbo III M. L., Saar S. H., Haywood R. D., 2018, ApJ, 866, 55

Cegla H. M., Watson C. A., Shelyag S., Mathioudakis M., 2015, in Cambridge Workshop on Cool Stars, Stellar Systems, and the Sun, Vol. 18, 18th Cambridge Workshop on Cool Stars, Stellar Systems, and the Sun, van Belle G. T., Harris H. C., eds., pp. 567–574

Chapman G. A., McGuire T. E., 1977, ApJ, 217, 657

Charbonneau P., 2010, Living Reviews in Solar Physics, 7, 3

Cheung M. C. M., Schüssler M., Moreno-Insertis F., 2007, A&A, 461, 1163

Claret A., 2000, A&A, 363, 1081

Collier Cameron A., Bruce V. A., Miller G. R. M., Triaud A. H. M. J., Queloz D., 2010, MNRAS, 403, 151

Czesla S., Huber K. F., Wolter U., Schröter S., Schmitt J. H. M. M., 2009, A&A, 505, 1277

Dasi-Espuig M., Jiang J., Krivova N. A., Solanki S. K., Unruh Y. C., Yeo K. L., 2016, A&A, 590, A63

Domingo V., Ermolli I., Fox P., Fröhlich C., Haberreiter M., Krivova N., Kopp G., Schmutz W., Solanki S. K., Spruit H. C., Unruh Y., Vögler A., 2009, Space Sci. Rev., 145, 337

Donati J.-F., Landstreet J. D., 2009, ARA&A, 47, 333

Dravins D., Lindegren L., Nordlund A., 1981, A&A, 96, 345

Duncan D. K., Vaughan A. H., Wilson O. C., Preston G. W., Frazer J., Lanning H., Misch A., Mueller J., Soyumer D., Woodard L., Baliunas S. L., Noyes R. W., Hartmann L. W., Porter A., Zwaan C., Middelkoop F., Rutten R. G. M., Mihalas D., 1991, ApJS, 76, 383

Ermolli I., Matthes K., Dudok de Wit T., Krivova N. A., Tourpali K., Weber M., Unruh Y. C., Gray L., Langematz U., Pilewskie P., Rozanov E., Schmutz W., Shapiro A., Solanki S. K., Woods T. N., 2013, Atmospheric Chemistry & Physics, 13, 3945

Espinoza N., \ Rackham B. V., Jordán A., Apai D., López-Morales M., Osip D. J., Grimm S. L., Hoeijmakers J., Wilson P. A., Bixel A., McGruder C., Rodler F., Weaver I., Lewis N. K., Fortney J. J., Fraine J., 2018, ArXiv e-prints

Evans T. M., Sing D. K., Wakeford H. R., Nikolov N., Ballester G. E., Drummond B., Kataria T., Gibson N. P., Amundsen D. S., Spake J., 2016, ApJL, 822, L4

Fan Y., 2009, Living Reviews in Solar Physics, 6, 4

Fligge M., Solanki S. K., 2000, Journal of Astrophysics and Astronomy, 21, 275

Fligge M., Solanki S. K., Unruh Y. C., Froehlich C., Wehrli C., 1998, A&A, 335, 709

Floyd L., Rottman G., Deland M., Pap J., 2003, in ESA Special Publication, Vol. 535, Solar Variability as an Input to the Earth's Environment, Wilson A., ed., pp. 195–203

Fontenla J. M., Avrett E., Thuillier G., Harder J., 2006, ApJ, 639, 441

Fontenla J. M., Avrett E. H., Loeser R., 1993, ApJ, 406, 319

Fontenla J. M., Avrett E. H., Loeser R., 2002, ApJ, 572, 636

Fontenla J. M., White O. R., Fox P. A., Avrett E. H., Kurucz R. L., 1999, ApJ, 518, 480

Foukal P., Little R., Graves J., Rabin D., Lynch D., 1990, ApJ, 353, 712

Frazier E. N., 1971, Sol. Phys., 21, 42

Freytag B., Steffen M., Dorch B., 2002, Astronomische Nachrichten, 323, 213

Fröhlich C., 2006, Space Sci. Rev., 125, 53

—, 2009, A&A, 501, L27

Fröhlich C., Lean J., 2004, The Astronomy and Astrophysics Review, 12, 273

Galsgaard K., Nordlund Å., 1996, Journal of Geophysical Research, 101, 13445

Gandorfer A., Grauf B., Barthol P., Riethmüller T. L., Solanki S. K., Chares B., Deutsch W., Ebert S., Feller A., Germerott D., Heerlein K., Heinrichs J., Hirche D., Hirzberger J., Kolleck M., Meller R., Müller R., Schäfer R., Tomasch G., Knölker M., Martínez Pillet V., Bonet J. A., Schmidt W., Berkefeld T., Feger B., Heidecke F., Soltau D., Tischenberg A., Fischer A., Title A., Anwand H., Schmidt E., 2011, Sol. Phys., 268, 35

Gilliland R. L., Brown T. M., Christensen-Dalsgaard J., Kjeldsen H., Aerts C., Appourchaux T., Basu S., Bedding T. R., Chaplin W. J., Cunha M. S., De Cat P., De Ridder J., Guzik J. A., Handler G., Kawaler S., Kiss L., Kolenberg K., Kurtz D. W., Metcalfe T. S., Monteiro M. J. P. F. G., Szabó R., Arentoft T., Balona L., Debosscher J., Elsworth Y. P., Quirion P.-O., Stello D., Suárez J. C., Borucki W. J., Jenkins J. M., Koch D., Kondo Y., Latham D. W., Rowe J. F., Steffen J. H., 2010, PASP, 122, 131

Goldberg L., Noyes R. W., Parkinson W. H., Reeves E. M., Withbroe G. L., 1968, Science, 162, 95

Gray D. F., 1992, The Observation and Analysis of Stellar Photospheres. Camb. Astrophys. Ser., Vol. 20,

—, 2005, The Observation and Analysis of Stellar Photospheres. “The Observation and Analysis of Stellar Photospheres, 3rd Edition, by D.F. Gray. ISBN 0521851866. ¡A href=”http://www.cambridge.org/us/catalogue/catalogue.asp?isbn=0521851866. Cambridge“¿http://www.cambridge.org/us/catalogue/catalogue.asp?isbn=0521851866. Cambridge¡/A¿, UK: Cambridge University Press, 2005.”

Grevesse N., Sauval A. J., 1998, Space Sci. Rev., 85, 161

Hall J. C., 2008, Living Reviews in Solar Physics, 5, 2

Haynes K., Mandell A. M., Madhusudhan N., Deming D., Knutson H., 2015, ApJ, 806, 146

Haywood R. D., 2015, PhD thesis, University of St Andrews

Henry G. W., 1999, PASP, 111, 845

Herrero E., Ribas I., Jordi C., Morales J. C., Perger M., Rosich A., 2016, A&A, 586, A131

Hoyt D. V., Schatten K. H., 1998, Sol. Phys., 181, 491

Karoff C., Metcalfe T. S., Santos Â. R. G., Montet B. T., Isaacson H., Witzke V., Shapiro A. I., Mathur S., Davies G. R., Lund M. N., Garcia R. A., Brun A. S., Salabert D., Avelino P. P., van Saders J., Egeland R., Cunha M. S., Campante T. L., Chaplin W. J., Krivova N., Solanki S. K., Stritzinger M., Knudsen M. F., 2018, ApJ, 852, 46

Keller C. U., Schüssler M., Vögler A., Zakharov V., 2004, ApJL, 607, L59

Kirk J., Wheatley P. J., Louden T., Littlefair S. P., Copperwheat C. M., Armstrong D. J., Marsh T. R., Dhillon V. S., 2016, MNRAS, 463, 2922

Kobel P., Solanki S. K., Borrero J. M., 2011, A&A, 531, A112

—, 2012, A&A, 542, A96

Kochukhov O., 2016, in Lecture Notes in Physics, Berlin Springer Verlag, Vol. 914, Lecture Notes in Physics, Berlin Springer Verlag, Rozelot J.-P., Neiner C., eds., p. 177

Kopp G., 2016, Journal of Space Weather and Space Climate, 6, A30

Krivova N. A., Solanki S. K., Fligge M., Unruh Y. C., 2003, A&A, 399, L1

Krivova N. A., Solanki S. K., Floyd L., 2006, A&A, 452, 631

Kurucz R. L., 1990, NATO Asi Ser., ed. L. Crivellari et al., 441

—, 1992a, Rev. Mexicana Astron. Astrof., 23

—, 1992b, Rev. Mexicana Astron. Astrof., 23, 181

—, 1992c, Rev. Mexicana Astron. Astrof., 23

—, 1993, ATLAS9 Stellar Atmosphere Programs and 2 km/s grid. Kurucz CD-ROM No. 13. Cambridge, Mass.: Smithsonian Astrophysical Observatory, 1993., 13

Lagrange A.-M., Desort M., Meunier N., 2010, A&A, 512, A38

Lean J., 1987, Journal of Geophysical Research, 92, 839

—, 1997, ARA&A, 35, 33

Lemaire P., Gouttebroze P., Vial J. C., Artzner G. E., 1981, A&A, 103, 160

Lites B. W., Elmore D. F., Seagraves P., Skumanich A. P., 1993, ApJ, 418, 928

Llama J., Shkolnik E. L., 2015, ApJ, 802, 41

Lockwood G. W., Skiff B. A., Henry G. W., Henry S., Radick R. R., Baliunas S. L., Donahue R. a., Soon W., 2007, ApJS, 171, 260

Lockwood G. W., Skiff B. A., Radick R. R., 1997, ApJ, 485, 789

Magic Z., Chiavassa A., Collet R., Asplund M., 2015, A&A, 573, A90

Magic Z., Collet R., Asplund M., Trampedach R., Hayek W., Chiavassa A., Stein R. F., Nordlund Å., 2013, A&A, 557, A26

McQuillan A., Aigrain S., Roberts S., 2012, A&A, 539, A137

Meunier N., Desort M., Lagrange A.-M., 2010, A&A, 512, A39

Mihalas D., 1978, Stellar atmospheres /2nd edition/

Milne E. A., 1928, The Observatory, 51, 88

Morello G., Tsiaras A., Howarth I. D., Homeier D., 2017, AJ, 154, 111

Morris B. M., Hebb L., Davenport J. R. A., Rohn G., Hawley S. L., 2017, ApJ, 846, 99

Nascimbeni V., Piotto G., Pagano I., Scandariato G., Sani E., Fumana M., 2013, A&A, 559, A32

Neckel H., Labs D., 1994, Sol. Phys., 153, 91

Nordlund r., Stein R. F., Asplund M., 2009, Living Reviews in Solar Physics, 6, 2

Norris C. M., Beeck B., Unruh Y. C., Solanki S. K., Krivova N. A., Yeo K. L., 2017, A&A, 605, A45

Noyes R. W., Hall D. N. B., 1972, ApJL, 176, L89

Noyes R. W., Hartmann L. W., Baliunas S. L., Duncan D. K., Vaughan A. H., 1984, ApJ, 279, 763

Ortiz A., Solanki S. K., Domingo V., Fligge M., Sanahuja B., 2002, A&A, 388, 1036

Oshagh M., Santos N. C., Ehrenreich D., Haghighipour N., Figueira P., Santerne A., Montalto M., 2014, A&A, 568, A99

Parker E. N., 1978, ApJ, 221, 368

Pierce A. K., Slaughter C. D., 1977, Sol. Phys., 51, 25

Pont F., Sing D. K., Gibson N. P., Aigrain S., Henry G., Husnoo N., 2013, MNRAS, 432, 2917

Posener D. W., 1959, Australian Journal of Physics, 12, 184

Rabus M., Alonso R., Belmonte J. A., Deeg H. J., Gilliland R. L., Almenara J. M., Brown T. M., Charbonneau D., Mandushev G., 2009, A&A, 494, 391

Radick R. R., Lockwood G. W., Henry G. W., Hall J. C., Pevtsov A. A., 2018, ApJ, 855, 75

Radick R. R., Mihalas D., Lockwood G. W., Thompson D. T., Warnock III A., Hartmann L. W., Worden S. P., Henry G. W., Sherlin J. M., 1983a, PASP, 95, 621

Radick R. R., Wilkerson M. S., Worden S. P., Africano J. L., Klimke A., Ruden S., Rogers W., Armandroff T. E., Giampapa M. S., 1983b, PASP, 95, 300

Rauer H., Catala C., Aerts C., Appourchaux T., Benz W., Brandeker A., Christensen-Dalsgaard J., Deleuil M., Gizon L., Goupil M.-J., Güdel M., Janot-Pacheco E., Mas-Hesse M., Pagano I., Piotto G., Pollacco D., Santos Ċ., Smith A., Suárez J.-C., Szabó R., Udry S., Adibekyan V., Alibert Y., Almenara J.-M., Amaro-Seoane P., Eiff M. A.-v., Asplund M., Antonello E., Barnes S., Baudin F., Belkacem K., Bergemann M., Bihain G., Birch A. C., Bonfils X., Boisse I., Bonomo A. S., Borsa F., Brandão I. M., Brocato E., Brun S., Burleigh M., Burston R., Cabrera J., Cassisi S., Chaplin W., Charpinet S., Chiappini C., Church R. P., Csizmadia S., Cunha M., Damasso M., Davies M. B., Deeg H. J., Díaz R. F., Dreizler S., Dreyer C., Eggenberger P., Ehrenreich D., Eigmüller P., Erikson A., Farmer R., Feltzing S., de Oliveira Fialho F., Figueira P., Forveille T., Fridlund M., García R. A., Giommi P., Giuffrida G., Godolt M., Gomes da Silva J., Granzer T., Grenfell J. L., Grotsch-Noels A., Günther E., Haswell C. A., Hatzes A. P., Hébrard G., Hekker S., Helled R., Heng K., Jenkins J. M., Johansen A., Khodachenko M. L., Kislyakova K. G., Kley W., Kolb U., Krivova N., Kupka F., Lammer H., Lanza A. F., Lebreton Y., Magrin D., Marcos-Arenal P., Marrese P. M., Marques J. P., Martins J., Mathis S., Mathur S., Messina S., Miglio A., Montalban J., Montalto M., Monteiro M. J. P. F. G., Moradi H., Moravveji E., Mordasini C., Morel T., Mortier A., Nascimbeni V., Nelson R. P., Nielsen M. B., Noack L., Norton A. J., Ofir A., Oshagh M., Ouazzani

R.-M., Pápics P., Parro V. C., Petit P., Plez B., Poretti E., Quirrenbach A., Ragazzoni R., Raimondo G., Rainer M., Reese D. R., Redmer R., Reffert S., Rojas-Ayala B., Roxburgh I. W., Salmon S., Santerne A., Schneider J., Schou J., Schuh S., Schunker H., Silva-Valio A., Silvotti R., Skillen I., Snellen I., Sohl F., Sousa S. G., Sozzetti A., Stello D., Strassmeier K. G., Švanda M., Szabó G. M., Tkachenko A., Valencia D., Van Grootel V., Vauclair S. D., Ventura P., Wagner F. W., Walton N. A., Weingrill J., Wern-er S. C., Wheatley P. J., Zwintz K., 2014, Experimental Astronomy, 38, 249

Reiners A., Basri G., 2006, ApJ, 644, 497

—, 2010, ApJ, 710, 924

Ricker G. R., Winn J. N., Vanderspek R., Latham D. W., Bakos G. Á., Bean J. L., Berta-Thompson Z. K., Brown T. M., Buchhave L., Butler N. R., Butler R. P., Chaplin W. J., Charbonneau D., Christensen-Dalsgaard J., Clampin M., Deming D., Doty J., De Lee N., Dressing C., Dunham E. W., Endl M., Fressin F., Ge J., Henning T., Holman M. J., Howard A. W., Ida S., Jenkins J. M., Jernigan G., Johnson J. A., Kaltenegger L., Kawai N., Kjeldsen H., Laughlin G., Levine A. M., Lin D., Lissauer J. J., MacQueen P., Marcy G., McCullough P. R., Morton T. D., Narita N., Paegert M., Palle E., Pepe F., Pepper J., Quirrenbach A., Rinehart S. A., Sasselov D., Sato B., Seager S., Sozzetti A., Stassun K. G., Sullivan P., Szentgyorgyi A., Torres G., Udry S., Villasenor J., 2015, Journal of Astronomical Telescopes, Instruments, and Systems, 1, 014003

Riethmüller T. L., Solanki S. K., Berdyugina S. V., Schüssler M., Martínez Pillet V., Feller A., Gandorfer A., Hirzberger J., 2014, A&A, 568, A13

Riethmüller T. L., Solanki S. K., Martínez Pillet V., Hirzberger J., Feller A., Bonet J. A., Bello González N., Franz M., Schüssler M., Barthol P., Berkefeld T., del Toro Iniesta J. C., Domingo V., Gandorfer A., Knölker M., Schmidt W., 2010, ApJL, 723, L169

Robinson Jr. R. D., 1980, ApJ, 239, 961

Roettenbacher R. M., Monnier J. D., Harmon R. O., Korhonen H. H., 2014, in IAU Symposium, Vol. 302, Magnetic Fields throughout Stellar Evolution, Petit P., Jardine M., Spruit H. C., eds., pp. 212–215

Roettenbacher R. M., Monnier J. D., Korhonen H., Harmon R. O., Baron F., Hackman T., Henry G. W., Schaefer G. H., Strassmeier K. G., Weber M., ten Brummelaar T. A., 2017, ApJ, 849, 120

Rogers F. J., 1994, in IAU Colloq. 147: The Equation of State in Astrophysics, Chabrier G., Schatzman E., eds., Vol. 147, p. 16

Rogers F. J., Swenson F. J., Iglesias C. A., 1996, ApJ, 456, 902

Sánchez Almeida J., Asensio Ramos A., Trujillo Bueno J., Cernicharo J., 2001, ApJ, 555, 978

Schad T. A., 2014, Sol. Phys., 289, 1477

Schou J., Scherrer P. H., Bush R. I., Wachter R., Couvidat S., Rabello-Soares M. C., Bogart R. S., Hoeksema J. T., Liu Y., Duvall T. L., Akin D. J., Allard B. A., Miles J. W., Rairden R., Shine R. A., Tarbell T. D., Title A. M., Wolfson C. J., Elmore D. F., Norton A. A., Tomczyk S., 2012, Sol. Phys., 275, 229

Schüssler M., Shelyag S., Berdyugina S., Vögler A., Solanki S. K., 2003, ApJL, 597, L173

Schwenke D. W., 1998, Faraday Discussions, 109, 321

Semel M., 1989, A&A, 225, 456

Shapiro A. I., Solanki S. K., Krivova N. A., Cameron R. H., Yeo K. L., Schmutz W. K., 2017, Nature Astronomy, 1, 612

Shapiro A. I., Solanki S. K., Krivova N. A., Schmutz W. K., Ball W. T., Knaack R., Rozanov E. V., Unruh Y. C., 2014, A&A, 569, A38

Shapiro A. I., Solanki S. K., Krivova N. A., Tagirov R. V., Schmutz W. K., 2015, A&A, 581, A116

Shelyag S., Schüssler M., Solanki S. K., Berdyugina S. V., Vögler A., 2004, A&A, 427, 335

Sing D. K., 2010, A&A, 510, A21

Sing D. K., Désert J.-M., Lecavelier Des Etangs A., Ballester G. E., Vidal-Madjar A., Parmentier V., Hebrard G., Henry G. W., 2009, A&A, 505, 891

Sing D. K., Pont F., Aigrain S., Charbonneau D., Désert J.-M., Gibson N., Gilliland R., Hayek W., Henry G., Knutson H., Lecavelier Des Etangs A., Mazeh T., Shporer A., 2011, MNRAS, 416, 1443

Solanki S. K., 2003, The Astronomy and Astrophysics Review, 11, 153

Solanki S. K., Barthol P., Danilovic S., Feller A., Gandorfer A., Hirzberger J., Riethmüller T. L., Schüssler M., Bonet J. A., Martínez Pillet V., del Toro Iniesta J. C., Domingo V., Palacios J., Knölker M., Bello González N., Berkefeld T., Franz M., Schmidt W., Title A. M., 2010, ApJL, 723, L127

Solanki S. K., Unruh Y. C., 1998, A&A, 329, 747

—, 2013, Astronomische Nachrichten, 334, 145

Spruit H. C., 1976, Sol. Phys., 50, 269

Spruit H. C., Zwaan C., 1981, Sol. Phys., 70, 207

Stein R. F., 2012, Living Reviews in Solar Physics, 9, 4

Taylor S. F., Varsik J. R., Woodard M. F., Libbrecht K. G., 1998, Sol. Phys., 178, 1

Title A. M., Frank Z. A., Shine R. A., Tarbell T. D., Topka K. P., Scharmer G., Schmidt W., 1993, ApJ, 403, 780

Title A. M., Topka K. P., Tarbell T. D., Schmidt W., Balke C., Scharmer G., 1992, ApJ, 393, 782

Topka K. P., Tarbell T. D., Title A. M., 1992, ApJ, 396, 351

—, 1997, ApJ, 484, 479

Triaud A. H. M. J., 2011, A&A, 534, L6

Uitenbroek H., Noyes R. W., Rabin D., 1994, ApJL, 432

Unruh Y. C., Solanki S. K., Fligge M., 1999, A&A, 345, 635

Vernazza J. E., Avrett E. H., Loeser R., 1981, ApJS, 45, 635

Vögler A., Shelyag S., Schüssler M., Cattaneo F., Emonet T., Linde T., 2005, A&A, 429, 335

Vogt S. S., Penrod G. D., 1983, PASP, 95, 565

Voigt H. H., 1956, Zeitschrift für Astrophysik, 40, 157

—, 1959, Zeitschrift für Astrophysik, 47, 144

Walkowicz L. M., Basri G. S., 2013, MNRAS, 436, 1883

Wallace L., Livingston W., Hinkle K., Bernath P., 1996, ApJS, 106, 165

Wiegelmann T., Thalmann J. K., Solanki S. K., 2014, The Astronomy and Astrophysics Review, 22, 78

Willson R. C., Gulkis S., Janssen M., Hudson H. S., Chapman G. A., 1981, Science, 211, 700

Willson R. C., Hudson H. S., 1991, Nature, 351, 42

Wilson O. C., 1978, ApJ, 226, 379

Winn J. N., Fabrycky D., Albrecht S., Johnson J. A., 2010, ApJL, 718, L145

Withbroe G. L., 1970, Sol. Phys., 11, 42

Witzke V., Shapiro A. I., Solanki S. K., Krivova N. A., Schmutz W., 2018, ArXiv e-prints

Wright J. T., Gaudi B. S., 2013, Exoplanet Detection Methods, Oswalt T. D., French L. M., Kalas P., eds., p. 489

Yeo K. L., Krivova N. A., Solanki S. K., Glassmeier K. H., 2014, A&A, 570, A85

Yeo K. L., Solanki S. K., Krivova N. a., 2013, A&A, 550, A95

Yeo K. L., Solanki S. K., Norris C. M., Beeck B., Unruh Y. C., Krivova N. A., 2017, Physical Review Letters, 119

Appendix A

Abbreviations

$\langle B_z \rangle$ – initial average vertical magnetic field
$\langle B_l \rangle$ – Unsigned longitudinal magnetogram signal (i.e., along the line of sight.)
CLV – Centre-to-Limb Variation
CoRoT – Convection, Rotation and planetary Transits
FAL – 1D atmospheric models from Fontenla, Avrett, & Loeser (1993)
g – Surface gravity (in cgs units in this thesis)
IRAC – InfraRed Array Camera (instrument on-board *Spitzer*)
LOS – Line Of Sight
LTE – Local Thermodynamic Equilibrium
μ – Limb distance, $\mu = \cos\theta$, where θ is the heliocentric angle
MHD – MagnetoHydroDynamic
MURaM – The Max-Planck-Institute for Aeronomy/ University of Chicago RadiationMagnetohydrodynamics code
nLTE – non Local Thermodynamic Equilibrium
ODF – Opacity Distribution Function
OPAL – Equation of state, see Rogers et al. (1996)
SATIRE(-S) – Spectral and Total Irradiance Reconstructions (for the Satellite era)
SDO/HMI – Solar Dynamics Observatory, Helioseismic and Magnetic Imager
SOHO/MDI – SOlar and Heliospheric Observatory, Michelson Doppler Interferometer
SSI – Solar Spectral Irradiance
$T_{\rm eff}$– Effective temperature
TESS – Transiting Exoplanet Survey Satellite
TSI – Total Solar Irradiance
τ_{500} – optical depth at a wavelength of 500 nm

Appendix B

Centre-to-limb coefficient tables for *Spitzer* IRAC

Tables B.1 to B.4 contain the coefficients for the *Spitzer* IRAC filters. These filter responses are shown in Fig. 3.1. These can be used along with coefficients in Tabs 3.4 to 3.7 to calculate contrasts, as described by Eq. 5.1 in Sect. 5.5.

Table B.1: *Spitzer* IRAC1 centre-to-limb variation coefficients.

		I(1.0)	linear	quad		sqrt		non-linear 3			non-linear 4			
Star	mag	[10^4 W m^{-2} sr^{-1}]	a	a	b	a	b	a	b	c	a	b	c	d
F3V	20G	8.29991	0.12	0.08	0.07	-0.03	0.23	0.56	-0.61	0.23	-0.02	0.60	-0.65	0.24
F3V	100G	8.33010	0.12	0.07	0.07	-0.04	0.24	0.60	-0.69	0.26	0.01	0.57	-0.66	0.26
F3V	500G	8.45986	0.08	0.05	0.06	-0.05	0.21	0.74	-1.04	0.45	-0.08	0.90	-1.19	0.50
G2V	20G	7.07466	0.16	0.09	0.12	-0.08	0.39	0.79	-0.83	0.29	0.51	-0.32	0.19	-0.06
G2V	100G	7.08776	0.16	0.09	0.12	-0.09	0.39	0.80	-0.87	0.31	0.53	-0.34	0.19	-0.05
G2V	500G	7.08135	0.13	0.06	0.11	-0.10	0.36	0.80	-0.95	0.36	0.87	-1.07	0.79	-0.23
K0V	20G	5.96907	0.20	0.11	0.14	-0.09	0.46	0.92	-0.96	0.33	0.52	-0.19	0.08	-0.02
K0V	100G	5.98731	0.20	0.11	0.14	-0.09	0.46	0.92	-0.97	0.33	0.53	-0.20	0.08	-0.02
K0V	500G	5.95656	0.18	0.10	0.12	-0.08	0.41	0.85	-0.91	0.32	0.62	-0.49	0.34	-0.10
M0V	20G	4.22504	0.19	0.09	0.16	-0.14	0.52	1.10	-1.26	0.46	0.78	-0.56	0.28	-0.06
M0V	100G	4.22250	0.19	0.09	0.16	-0.15	0.53	1.12	-1.28	0.47	0.81	-0.63	0.33	-0.08
M0V	500G	4.19279	0.18	0.08	0.15	-0.14	0.50	1.02	-1.15	0.42	0.75	-0.59	0.34	-0.09
M2V	20G	3.69067	0.19	0.09	0.15	-0.14	0.52	1.04	-1.16	0.41	0.58	-0.19	-0.02	0.03
M2V	100G	3.69022	0.19	0.09	0.15	-0.14	0.52	1.05	-1.18	0.42	0.63	-0.30	0.08	-0.00
M2V	500G	3.63855	0.18	0.09	0.14	-0.12	0.48	0.93	-1.00	0.35	0.56	-0.27	0.11	-0.03

Table B.2: *Spitzer* IRAC2 centre-to-limb variation coefficients.

		I(1.0)	linear	quad		sqrt		non-linear 3			non-linear 4			
Star	mag	[10^4 W m^{-2} sr^{-1}]	a	a	b	a	b	a	b	c	a	b	c	d
F3V	20G	4.88384	0.11	0.07	0.06	-0.03	0.21	0.49	-0.53	0.20	0.05	0.38	-0.44	0.17
F3V	100G	4.90736	0.10	0.06	0.07	-0.04	0.22	0.50	-0.56	0.21	0.08	0.33	-0.40	0.16
F3V	500G	4.98428	0.08	0.04	0.06	-0.06	0.21	0.53	-0.66	0.26	0.26	-0.03	-0.14	0.08
G2V	20G	4.09055	0.14	0.08	0.10	-0.06	0.32	0.65	-0.68	0.23	0.37	-0.14	0.06	-0.02
G2V	100G	4.10947	0.14	0.08	0.10	-0.06	0.33	0.66	-0.69	0.24	0.38	-0.15	0.06	-0.01
G2V	500G	4.14796	0.12	0.06	0.09	-0.07	0.30	0.68	-0.79	0.30	0.63	-0.69	0.48	-0.13
K0V	20G	3.33905	0.17	0.11	0.10	-0.05	0.34	0.69	-0.68	0.23	0.35	-0.08	0.03	-0.01
K0V	100G	3.35891	0.17	0.10	0.10	-0.05	0.34	0.69	-0.69	0.24	0.36	-0.09	0.04	-0.01
K0V	500G	3.36489	0.15	0.10	0.09	-0.04	0.30	0.65	-0.67	0.24	0.44	-0.31	0.22	-0.06
M0V	20G	2.45575	0.14	0.07	0.11	-0.09	0.36	0.76	-0.84	0.31	0.49	-0.30	0.14	-0.03
M0V	100G	2.45540	0.14	0.07	0.11	-0.09	0.36	0.76	-0.85	0.31	0.51	-0.32	0.16	-0.03
M0V	500G	2.44354	0.13	0.07	0.10	-0.08	0.33	0.70	-0.78	0.28	0.51	-0.39	0.23	-0.06
M2V	20G	2.23085	0.14	0.07	0.12	-0.11	0.39	0.81	-0.92	0.33	0.52	-0.31	0.11	-0.02
M2V	100G	2.23241	0.14	0.06	0.11	-0.10	0.38	0.79	-0.90	0.33	0.51	-0.31	0.13	-0.02
M2V	500G	2.20951	0.13	0.06	0.11	-0.09	0.36	0.72	-0.80	0.28	0.48	-0.32	0.17	-0.04

155

Table B.3: *Spitzer* IRAC3 centre-to-limb variation coefficients.

		I(1.0)	linear	quad		sqrt		non-linear 3			non-linear 4			
Star	mag	[10^3 W m^{-2} sr^{-1}]	a	a	b	a	b	a	b	c	a	b	c	d
F3V	20G	7.24816	0.09	0.06	0.05	-0.01	0.16	0.39	-0.42	0.16	0.00	0.38	-0.41	0.15
F3V	100G	7.28710	0.09	0.05	0.05	-0.02	0.18	0.40	-0.44	0.16	0.03	0.34	-0.38	0.14
F3V	500G	7.40518	0.07	0.03	0.06	-0.05	0.19	0.38	-0.41	0.15	0.27	-0.21	0.13	-0.04
G2V	20G	6.09012	0.12	0.08	0.08	-0.04	0.26	0.52	-0.52	0.18	0.27	-0.05	0.01	-0.00
G2V	100G	6.12133	0.12	0.07	0.08	-0.04	0.26	0.53	-0.54	0.19	0.27	-0.05	-0.00	0.00
G2V	500G	6.19951	0.10	0.06	0.07	-0.05	0.25	0.57	-0.66	0.25	0.48	-0.47	0.31	-0.08
K0V	20G	5.02941	0.14	0.09	0.08	-0.03	0.28	0.56	-0.55	0.19	0.27	-0.02	-0.01	0.00
K0V	100G	5.05811	0.14	0.09	0.08	-0.03	0.27	0.57	-0.56	0.19	0.28	-0.03	-0.00	0.00
K0V	500G	5.07313	0.13	0.08	0.07	-0.03	0.25	0.54	-0.55	0.19	0.35	-0.21	0.14	-0.04
M0V	20G	3.80837	0.14	0.07	0.10	-0.08	0.34	0.70	-0.77	0.27	0.39	-0.14	0.02	0.01
M0V	100G	3.80689	0.14	0.07	0.11	-0.09	0.35	0.73	-0.81	0.29	0.44	-0.21	0.07	-0.01
M0V	500G	3.79125	0.13	0.07	0.09	-0.07	0.31	0.64	-0.70	0.25	0.41	-0.24	0.12	-0.03
M2V	20G	3.44038	0.13	0.07	0.10	-0.07	0.32	0.63	-0.66	0.23	0.28	0.04	-0.11	0.04
M2V	100G	3.44117	0.13	0.07	0.10	-0.07	0.33	0.65	-0.69	0.24	0.33	-0.05	-0.04	0.02
M2V	500G	3.40278	0.12	0.07	0.09	-0.06	0.29	0.56	-0.58	0.20	0.31	-0.11	0.04	-0.01

Table B.4: *Spitzer* IRAC4 centre-to-limb variation coefficients.

		I(1.0)	linear	quad		sqrt		non-linear 3			non-linear 4			
Star	mag	[10^3 W m^{-2} sr^{-1}]	a	a	b	a	b	a	b	c	a	b	c	d
F3V	20G	9.62475	0.07	0.05	0.03	0.00	0.11	0.28	-0.31	0.12	-0.08	0.46	-0.47	0.17
F3V	100G	9.68549	0.07	0.05	0.04	-0.01	0.13	0.30	-0.33	0.12	-0.06	0.43	-0.44	0.16
F3V	500G	9.86489	0.06	0.03	0.05	-0.04	0.15	0.24	-0.20	0.05	0.17	-0.13	0.14	-0.06
G2V	20G	8.15913	0.10	0.06	0.05	-0.02	0.18	0.37	-0.36	0.12	0.17	0.01	-0.02	0.00
G2V	100G	8.20101	0.10	0.06	0.06	-0.02	0.19	0.39	-0.39	0.13	0.18	0.01	-0.04	0.01
G2V	500G	8.32010	0.09	0.05	0.06	-0.04	0.19	0.45	-0.52	0.20	0.36	-0.31	0.19	-0.04
K0V	20G	6.88136	0.12	0.08	0.07	-0.03	0.24	0.48	-0.48	0.16	0.23	-0.01	-0.02	0.01
K0V	100G	6.91775	0.12	0.07	0.07	-0.03	0.23	0.48	-0.48	0.16	0.23	-0.01	-0.02	0.01
K0V	500G	6.94201	0.11	0.07	0.06	-0.02	0.21	0.45	-0.46	0.16	0.28	-0.15	0.10	-0.03
M0V	20G	5.17436	0.13	0.08	0.08	-0.04	0.27	0.51	-0.48	0.15	0.16	0.16	-0.16	0.05
M0V	100G	5.17047	0.13	0.08	0.09	-0.05	0.29	0.57	-0.57	0.19	0.25	0.03	-0.08	0.03
M0V	500G	5.16483	0.12	0.07	0.08	-0.04	0.25	0.51	-0.52	0.18	0.28	-0.10	0.05	-0.01
M2V	20G	4.62731	0.11	0.08	0.05	-0.00	0.18	0.34	-0.29	0.09	0.08	0.16	-0.12	0.03
M2V	100G	4.62692	0.11	0.07	0.06	-0.01	0.20	0.40	-0.38	0.12	0.18	0.02	-0.02	0.00
M2V	500G	4.58683	0.10	0.07	0.05	-0.01	0.17	0.36	-0.34	0.12	0.24	-0.14	0.12	-0.04

157

Appendix C

Additional figures

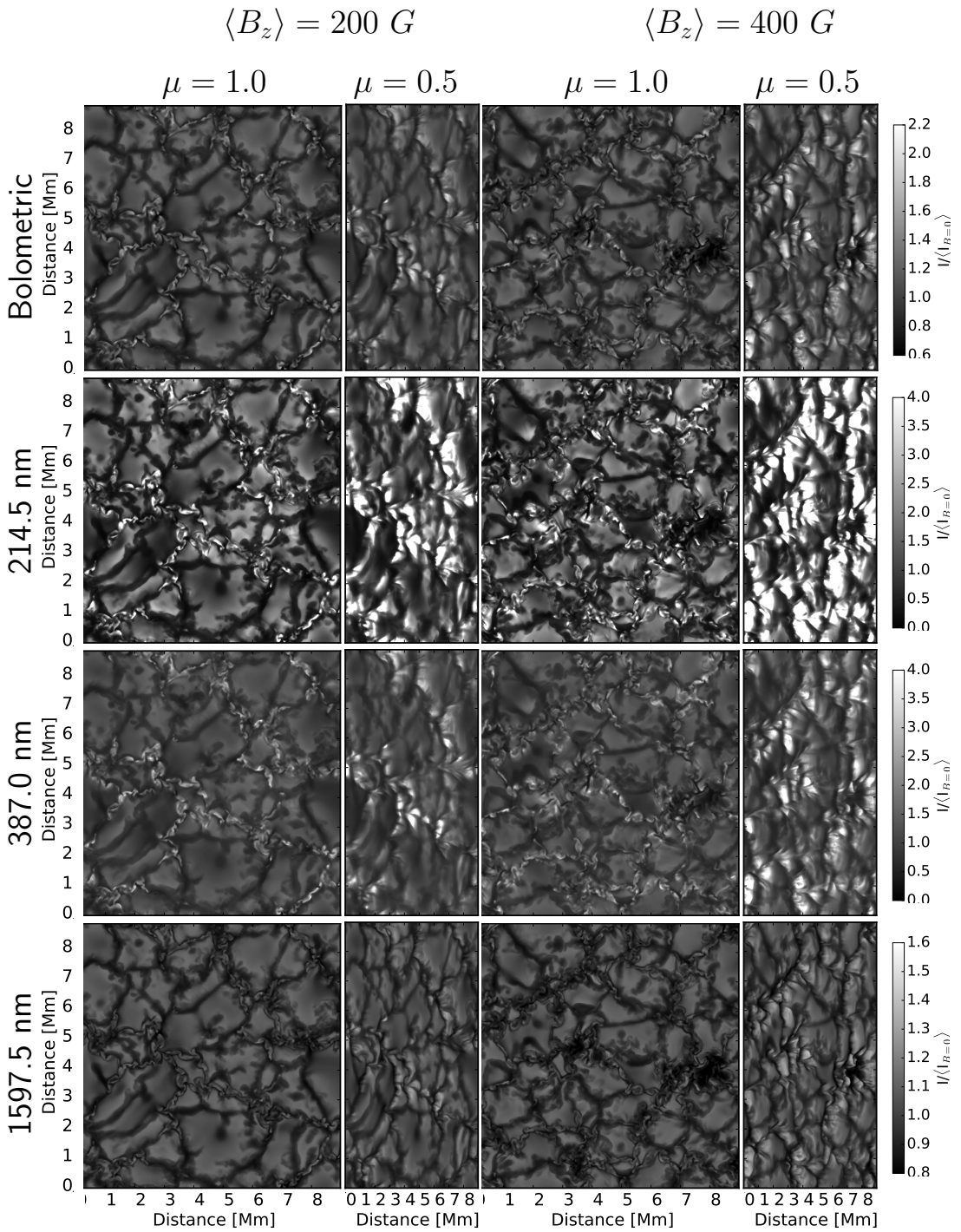


Figure C.1: Emergent intensities for G2V snapshots from initial average magnetic field simulations of 200 G and 400 G. Bolometric images are shown in the top row, along with images for three wavelength bins centred at 214.5 nm, 387 nm and 1597.5 nm (top to bottom). This figure complements Figs. 4.1 and 4.2 in the main text.

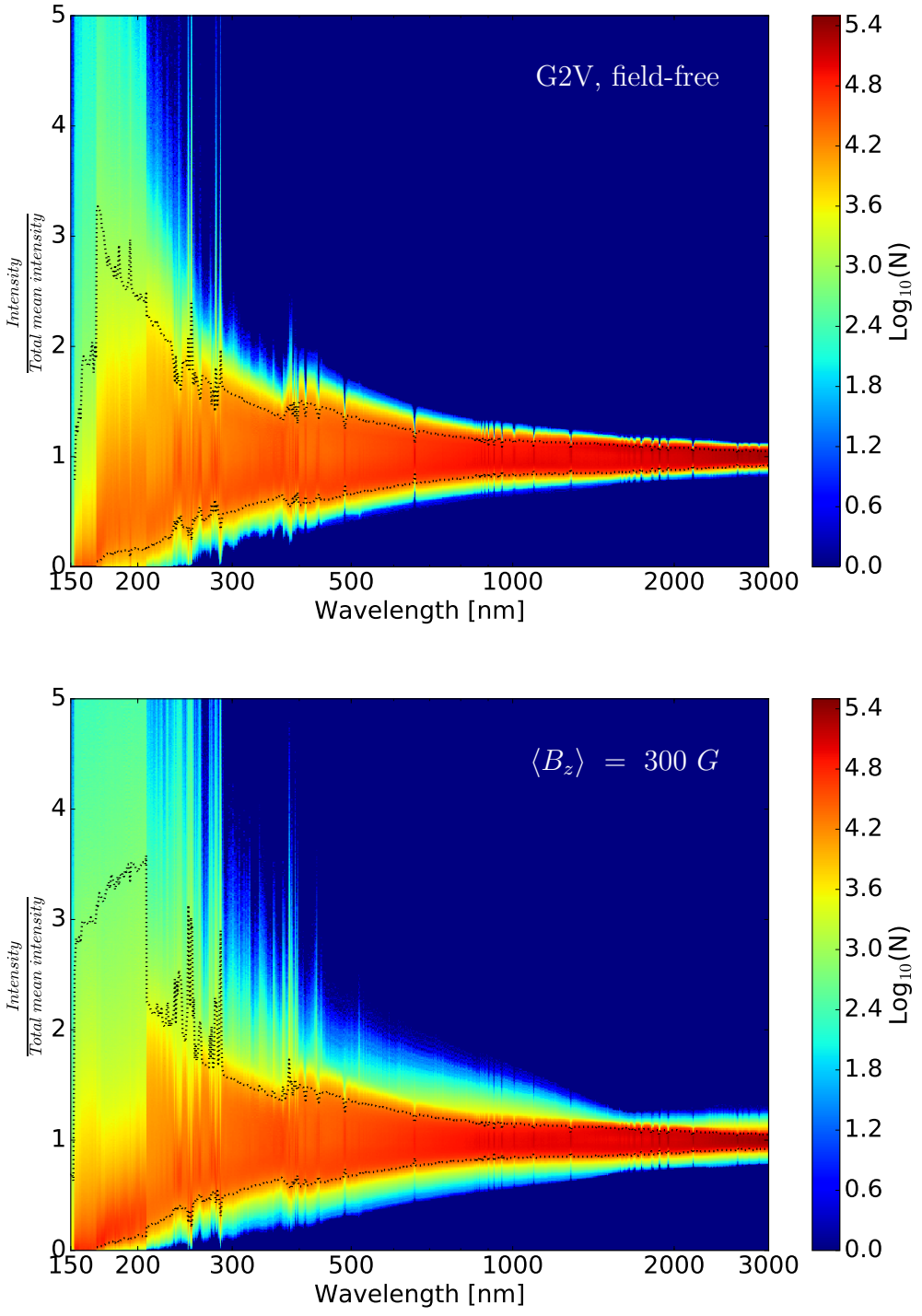


Figure C.2: Histograms of pixel intensities divided by the total mean intensity in each ATLAS9 wavelength bin for all pixels in all G2V snapshots for a given $\langle B_z \rangle$ at disc centre with the 5th and 95th percentiles of all pixels in all corresponding simulations overlaid in dotted black lines. The bin size is 0.01. The wavelength bins are various sizes, as detailed in Section 2.3, and are displayed in log space. The field-free histogram is shown in the top panel, while the $\langle B_z \rangle = 300$ G histogram is shown in the bottom panel.

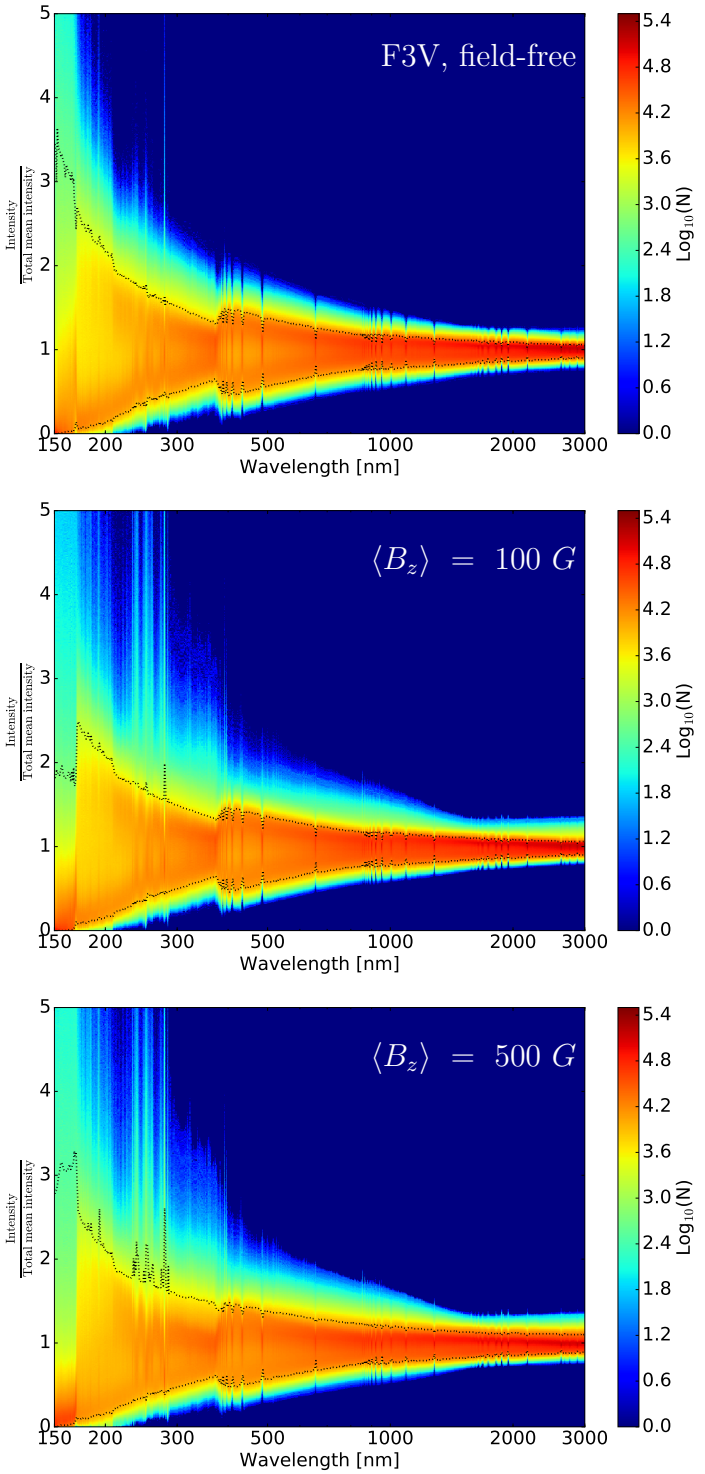


Figure C.3: Histograms of disc-centre pixel intensity divided by the total mean intensity in each ATLAS9 wavelength bin for the F3V snapshots. The 5th and 95th percentiles are overlaid in dotted black lines. Histograms and percentiles are for all pixels in all snapshots for a given $\langle B_z \rangle$. The bin size is 0.01. From top to bottom, histograms are displayed for field-free, $\langle B_z \rangle = 100$ G and $\langle B_z \rangle = 500$ G snapshots. The wavelength bins are as detailed in Section 2.3, and are displayed in log space.

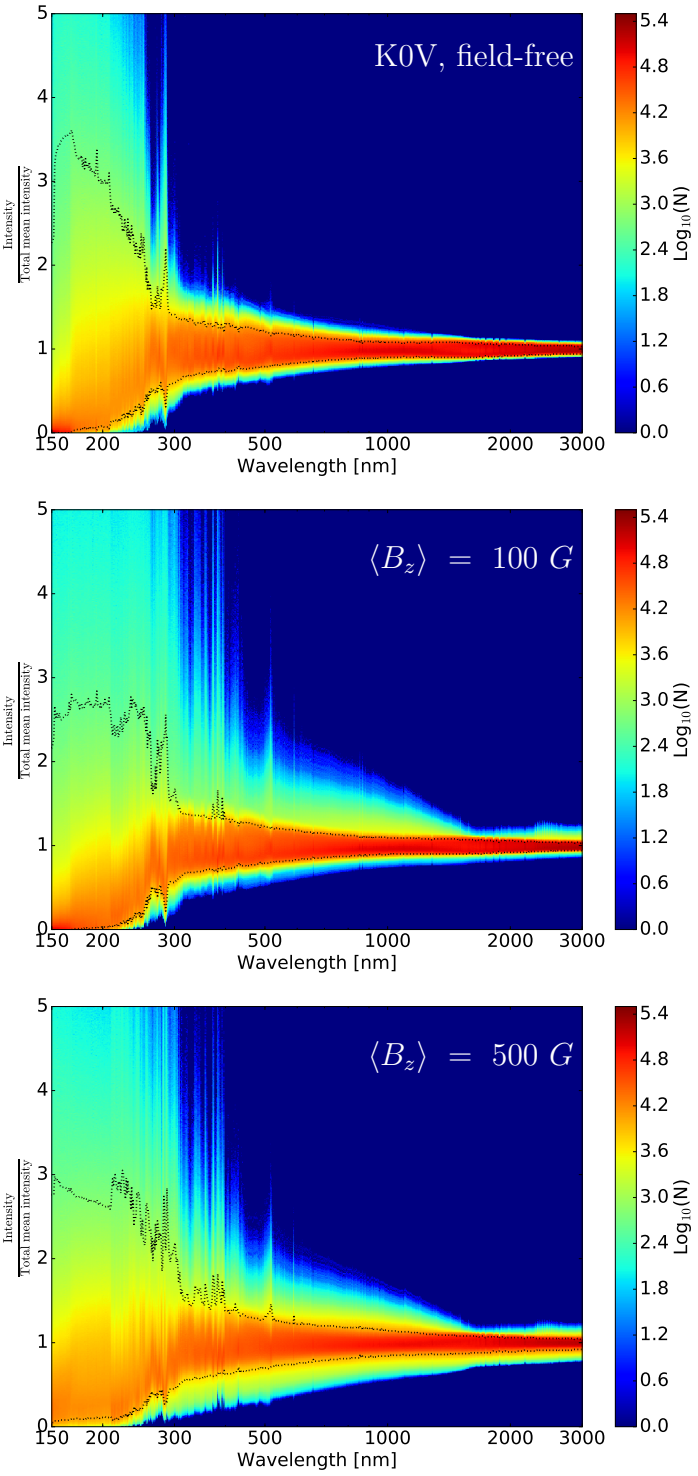


Figure C.4: Normalised histograms as in Figure C.3 for the K0V star with an bin width of 0.01.

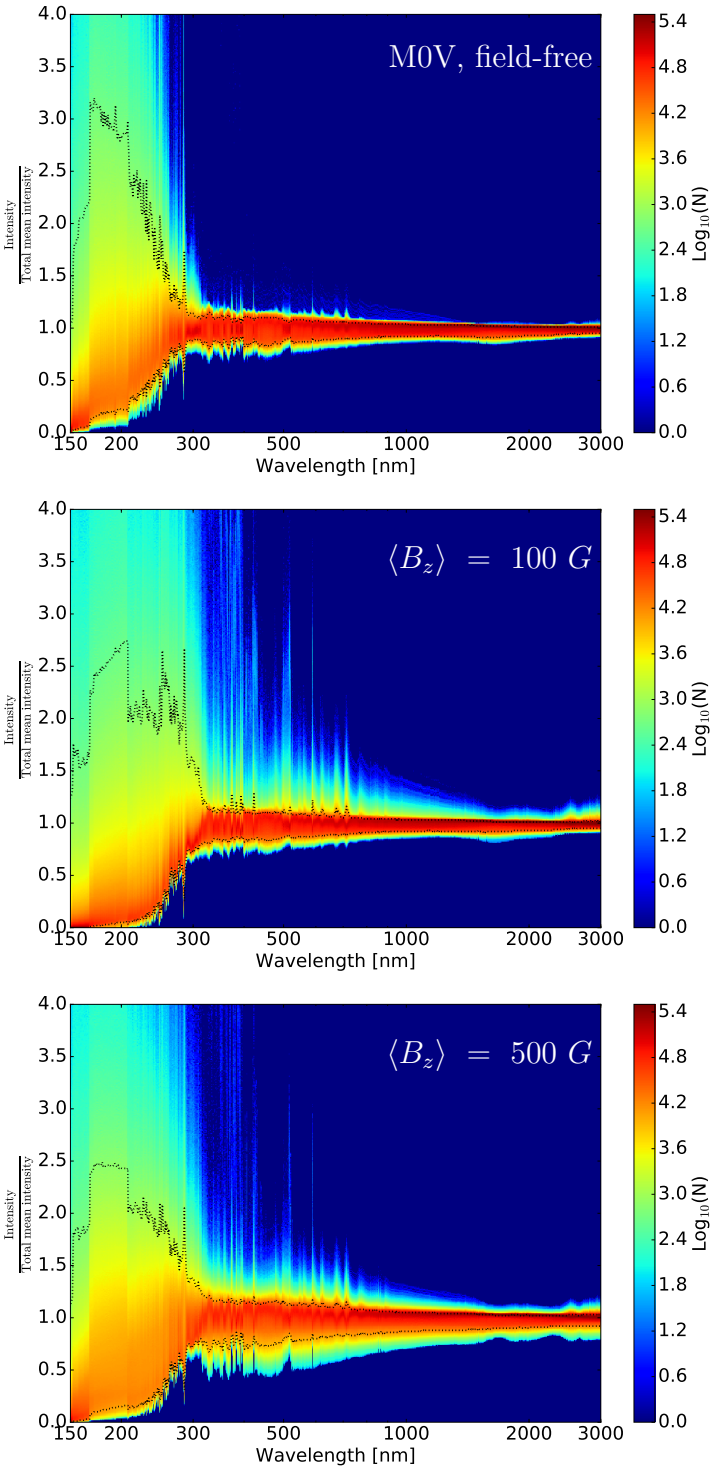


Figure C.5: Normalised histograms as in Figure C.3 for the M0V star with an bin width of 0.01.

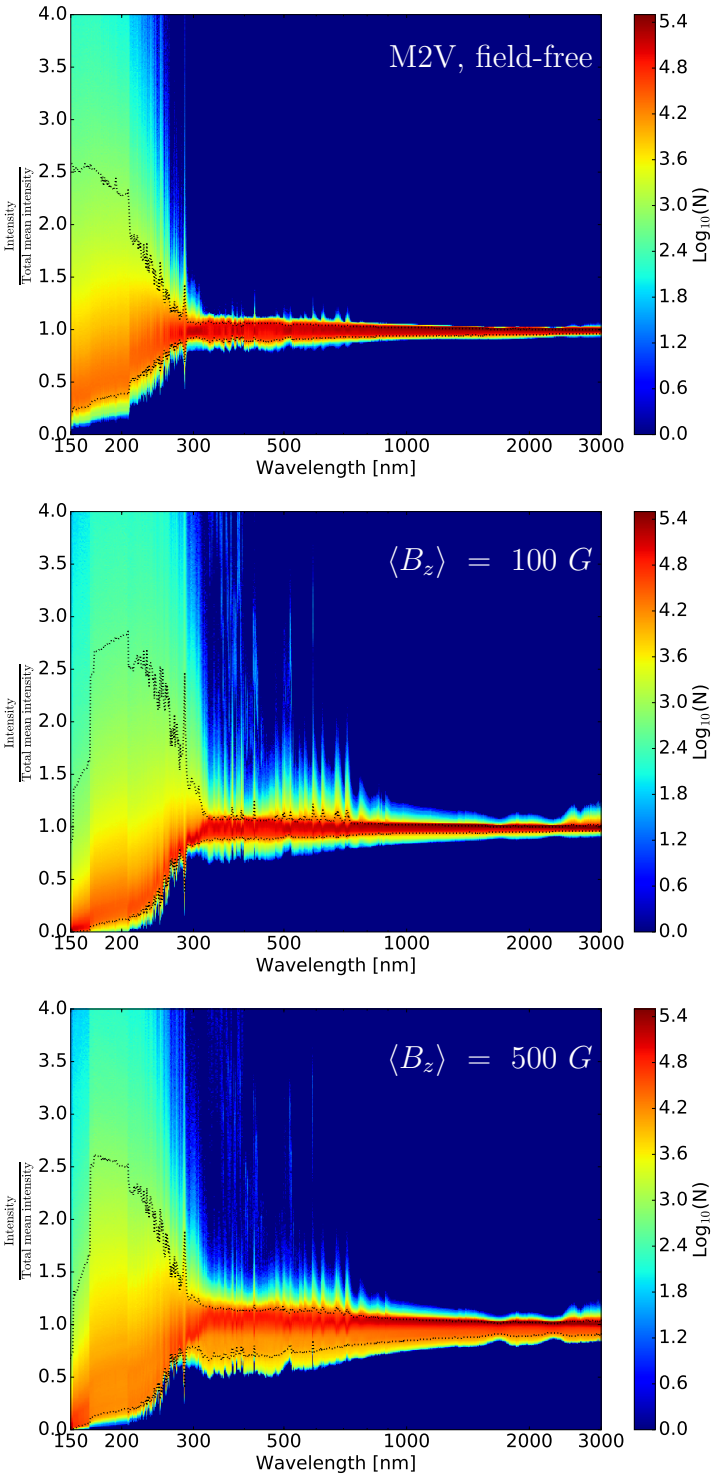


Figure C.6: Normalised histograms as in Figure C.3 for the M2V star with an bin width of 0.01.

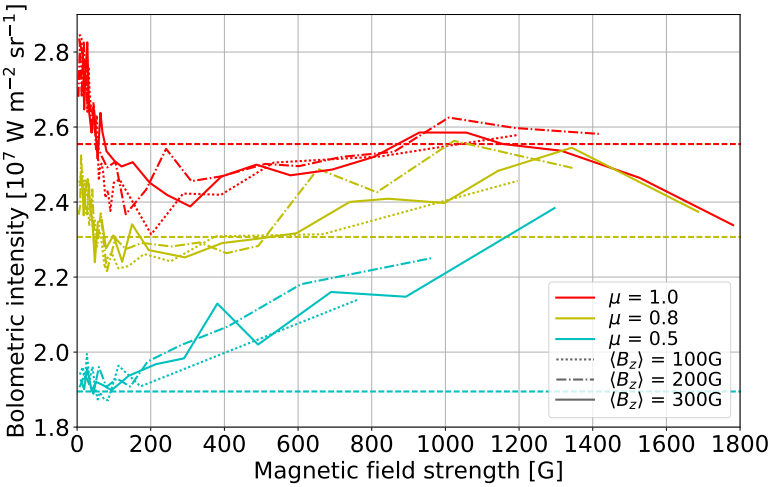
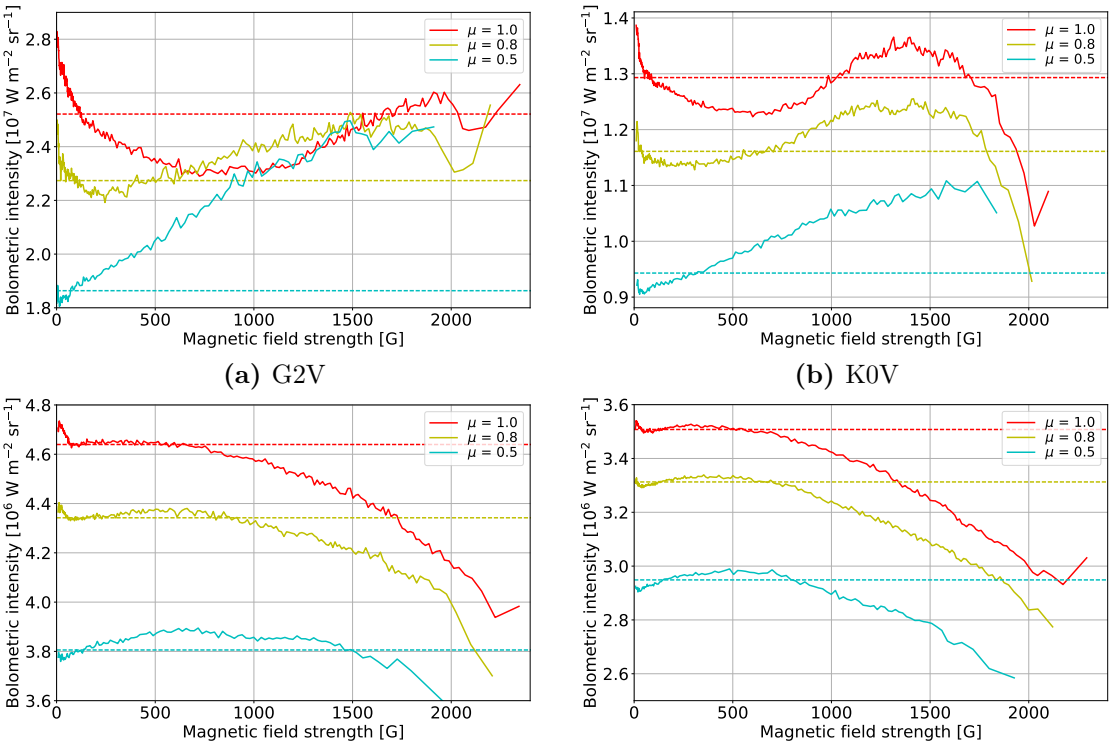


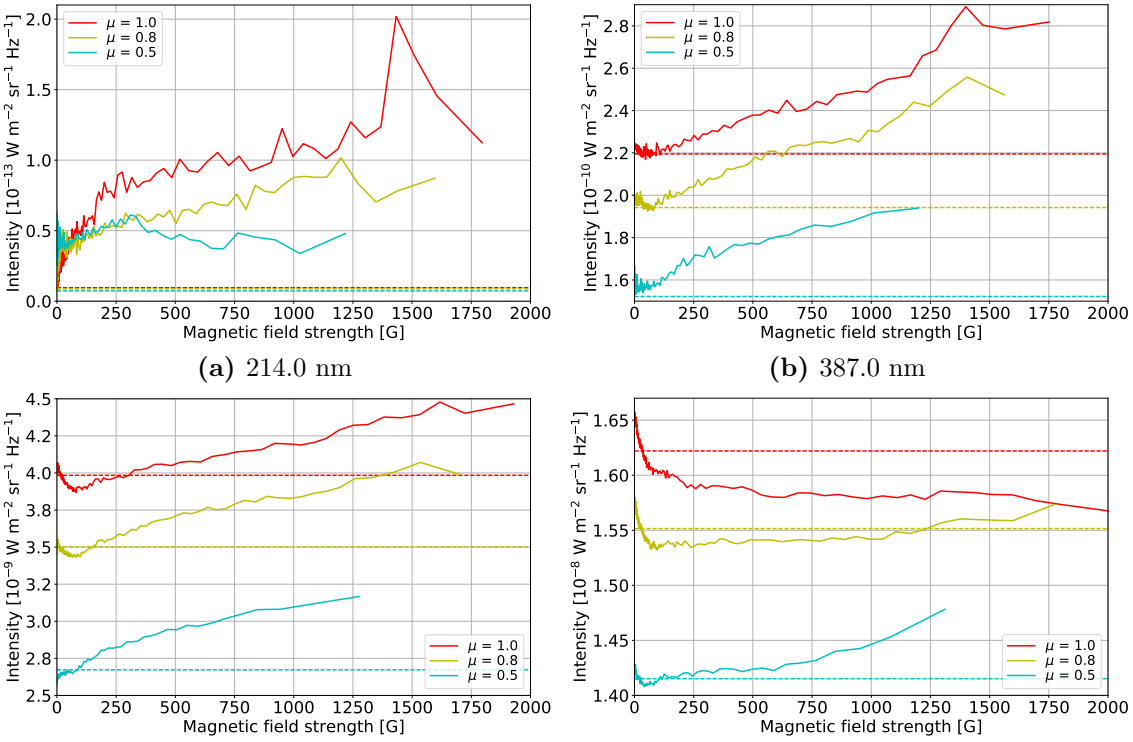
Figure C.7: Same as Fig. 6.4, for averaged pixel size, seen in Fig. 6.2a.



(a) G2V **(b)** K0V

(c) M0V **(d)** M2V

Figure C.8: Same as Figs 6.5a to 6.5d, for $\langle B_z \rangle = 500$ G.



(a) 214.0 nm

(b) 387.0 nm

(c) 601.0 nm

(d) 1597.5 nm

Figure C.9: Same as Figs 6.6a to 6.6d for the M0V star.

Appendix D

Yeo et al. 2017

The following paper is discussed in Chapter 6. Credit: Yeo et al. (2017), ©American Physical Society. The supplementary material is supplied after the paper.

PRL 119, 091102 (2017) PHYSICAL REVIEW LETTERS week ending 1 SEPTEMBER 2017

Solar Irradiance Variability is Caused by the Magnetic Activity on the Solar Surface

Kok Leng Yeo,[1,*] Sami K. Solanki,[1,†] Charlotte M. Norris,[2] Benjamin Beeck,[1] Yvonne C. Unruh,[2] and Natalie A. Krivova[1]
[1]*Max Planck Institute for Solar System Research, Justus-von-Liebig-Weg 3, 37077 Göttingen, Germany*
[2]*Blackett Laboratory, Imperial College London, South Kensington Campus, London SW7 2AZ, United Kingdom*
(Received 12 February 2017; published 1 September 2017; publisher error corrected 19 September 2017)

The variation in the radiative output of the Sun, described in terms of solar irradiance, is important to climatology. A common assumption is that solar irradiance variability is driven by its surface magnetism. Verifying this assumption has, however, been hampered by the fact that models of solar irradiance variability based on solar surface magnetism have to be calibrated to observed variability. Making use of realistic three-dimensional magnetohydrodynamic simulations of the solar atmosphere and state-of-the-art solar magnetograms from the Solar Dynamics Observatory, we present a model of total solar irradiance (TSI) that does not require any such calibration. In doing so, the modeled irradiance variability is entirely independent of the observational record. (The absolute level is calibrated to the TSI record from the Total Irradiance Monitor.) The model replicates 95% of the observed variability between April 2010 and July 2016, leaving little scope for alternative drivers of solar irradiance variability at least over the time scales examined (days to years).

DOI: 10.1103/PhysRevLett.119.091102

The brightness of the Sun is usually described in terms of solar irradiance, defined as the solar radiative flux at 1 AU. The integral over all wavelengths, total solar irradiance (TSI), has been monitored from space since 1978 [1]. The observation of TSI revealed fluctuations with solar activity [2], confirming speculations that the radiative output of the Sun is not constant but modulated by its activity [3]. These fluctuations, while minute (about 0.1% over the 11-year solar cycle), influence Earth's climate, with implications for our assessment of the anthropogenic contribution to climate change [4]. Climate simulations require historical solar irradiance variability as input, and this can be provided only by models since measurements only go back to 1978. Evidently, modeling solar irradiance variability requires an understanding of the underlying physics. This understanding is also vital to our interpretation of the brightness variations of other cool stars, which are beginning to be monitored extensively with missions such as Convection Rotation and Planetary Transits (COROT) [5] and Kepler [6].

The kilogauss-strength magnetic concentrations found in the lower solar atmosphere affect the temperature structure of the enclosed plasma, forming what we observe as dark sunspots and bright faculae and network [7]. (Faculae refers to the bright features in magnetically active regions, which are concentrated at midlatitudes and network to the smaller bright features distributed more uniformly across the solar disk.) Hereafter, we will refer to faculae and network, the fundamental physics of which is similar, collectively as faculae. Observations indicate that TSI is lower and higher around the minima and maxima of the solar cycle [8]. TSI measurements also indicate increases and decreases that coincide with the passage of faculae and sunspots across the disk [2,9,10]. This apparent correlation between solar irradiance variability and solar surface magnetism spurred the development of models aimed at reconstructing solar irradiance variability by ascribing it to magnetic activity on the solar surface [11,12]. This implicitly assumes that the heat blocked by sunspots is redistributed in the convection zone and the excess heat emitted by faculae originates from the convection zone [13]. If the intensity deficit (excess) of surface magnetic features is channeled to (from) their surroundings instead, they would have no net effect on solar irradiance.

Other mechanisms have also been proposed, for example, global oscillations driven by the rotation of the Sun [14], surface temperature fluctuations related to magnetic fields in the interior [15], and the solar dynamo modulating convective flows [16]. There has been no reported attempt to incorporate any of these mechanisms in solar irradiance models. Solar irradiance variability from acoustic oscillations, convection, and flares, which occur at time scales of a day and shorter, and from the thermal and chemical evolution of the Sun, which emerge at time scales exceeding 10^5 yr, are irrelevant over the intermediate, climate-relevant time scales [17].

Solar irradiance variability is modeled as the outcome of solar surface magnetism by inferring the intensity deficit and excess effected by sunspots and faculae from solar observations indicative of its surface magnetism. There are two main approaches, termed proxy and semiempirical [12]. Proxy models employ indirect, disk-integrated measures of solar magnetism such as the Mg II index [18] and the photometric sunspot index [9] as indications of facular brightening and sunspot darkening. Solar irradiance variability is obtained by the regression of these measures to solar irradiance observations [19]. In the semiempirical

 © 2017 American Physical Society

PRL 119, 091102 (2017) PHYSICAL REVIEW LETTERS week ending 1 SEPTEMBER 2017

approach, solar irradiance variability is reconstructed by combining the information about the spatial distribution of solar surface magnetism in resolved full-disk observations (such as magnetograms, which map the magnetic flux density) with the intensity contrast of solar surface features calculated from models of their atmospheric structure by the solution to the radiative transfer equation [20].

While such models have managed to replicate most of the variability in solar irradiance observations [17], they suffer from the shortcoming of having to rely on empirical relationships to establish facular brightening and, in the case of proxy models, sunspot darkening from the solar observations employed [21]. (Semiempirical models return sunspot darkening without taking recourse to empirical relationships.) These empirical relationships are constrained by optimizing the model output to observed solar irradiance variability. Critically, in doing so, the possible contribution to solar irradiance variability by other mechanisms can be wrongly ascribed to solar surface magnetism. The ability of present-day models to replicate observed solar irradiance variability cannot exclude the possibility that mechanisms other than solar surface magnetism might play a significant role. The true relationship between solar irradiance variability and solar surface magnetism will remain an open question for as long as models have to be calibrated to observed variability. It is therefore vital to develop models of solar irradiance that do completely without such calibrations.

Proxy models, by their very definition, have to be optimized to measured solar irradiance. Current semiempirical models represent solar surface features with one-dimensional (1D) model atmospheres, which describe the vertical stratification of their atmospheric structure. As we will explain later in this Letter, the challenge in describing the variation in facular intensity with magnetic flux density [22] with 1D model atmospheres is the reason why existing semiempirical models have to be calibrated to observed solar irradiance variability.

We present the first TSI model to reproduce observed variability without requiring any calibration to the latter [23]. This is achieved by extending the current semiempirical approach to incorporate state-of-the-art 3D model atmospheres. To this end, we made use of 3D magnetohydrodynamic (MHD) simulations of the solar atmosphere generated with the MURaM code [35]. (MURaM denotes the Max-Planck Institute for Solar System Research and University of Chicago Radiation MHD code.) We exploit the realism of MURaM simulations of the solar atmosphere, which have been demonstrated to reproduce a wide range of solar observations [36–39]. We also employed full-disk magnetograms and intensity images from the Helioseismic and Magnetic Imager (HMI) onboard the Solar Dynamics Observatory (SDO), launched in 2010 [40]. Recorded from space, HMI observations are free from atmospheric seeing effects. Also, as compared to other full-disk magnetographs, the spatial resolution is higher and the noise level is, in most cases, lower [41].

The TSI model is a major extension of the semiempirical model Spectral and Total Irradiance Reconstruction for the Satellite Era (SATIRE-S) [20,41]. In SATIRE-S, the wavelength-integrated or bolometric intensity of the quiet Sun, faculae, and sunspots, at various distances from the disk center, is calculated on the basis of 1D model atmospheres with a radiative transfer code [42]. For a given day, the surface coverage by faculae and sunspots is determined by identifying these features in a full-disk magnetogram and the concurrent continuum intensity image. TSI is recovered by assigning the calculated bolometric intensities to each disk position according to this segmentation and integrating the resultant bolometric image over the solar disk. The TSI model presented here assumes a similar architecture, with the crucial exception that the bolometric intensity of the quiet Sun and faculae is calculated from 3D model atmospheres provided by MURaM simulations.

It is known that the intensity of faculae varies not just with distance from the disk center but also with magnetic flux density (see [22,43,44], and references therein). However, in SATIRE-S, facular intensity is determined as a function of the distance from the disk center alone with a 1D model atmosphere that corresponds to faculae of a particular and *a priori* unknown magnetic flux density [42]. In order to relate the calculated facular intensities to measured facular magnetic flux densities, as needed to assign the appropriate intensity to observed faculae, the model introduces an empirical relationship that is constrained by optimizing the model output to measured TSI variability [20]. Other existing semiempirical models face the same issue, as they also employ 1D model atmospheres. The application of the calculated sunspot intensities to observed sunspots yields sunspot darkening without the need to introduce any further calibration to measured TSI variability.

To model facular brightening and therefore TSI variability without optimizing the model output to observed TSI variability, we need to incorporate the variation in facular bolometric intensity with magnetic flux density into the model in a physically self-consistent manner. This is achieved here by synthesizing bolometric images and magnetograms of 3D model atmospheres emulating how they would appear to a bolometric imager and to HMI. From the result, we determined facular bolometric intensity as a function of the distance from the disk center and the HMI magnetogram signal. Such a quantitative relationship is exactly what is missing from existing models. This relationship allows us to assign the appropriate bolometric intensity to faculae identified in HMI magnetograms by their disk position and apparent magnetic flux density alone, making it possible to reconstruct TSI variability from HMI observations without any calibration to observed variability.

PRL 119, 091102 (2017) PHYSICAL REVIEW LETTERS week ending 1 SEPTEMBER 2017

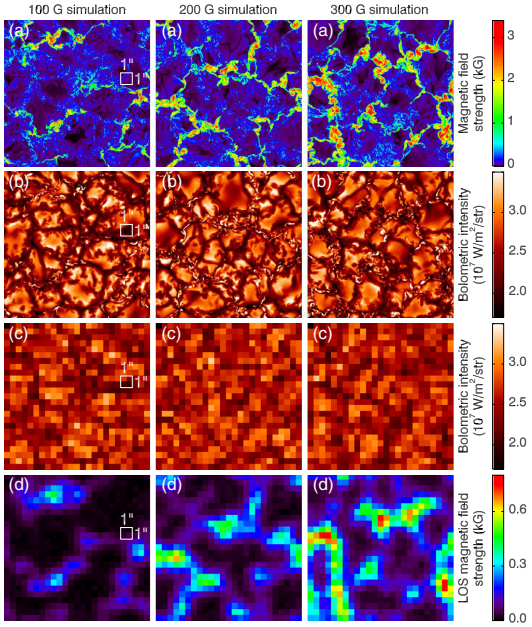


FIG. 1. From top to bottom: (a) Magnetic field strength, at optical depth unity, in a snapshot of each MHD simulation. There are three MHD simulations, initiated with a uniform magnetic field of 100 (left), 200 (center), and 300 G (right), respectively. There is an additional simulation that is purely hydrodynamic (not pictured). The white box on the left panel denotes a $1'' \times 1''$ area. (b) Bolometric image of each snapshot when viewed from above, therefore representing if they were at the solar disk center, synthesized with the snapshots as input to a radiative transfer code. (c) The same bolometric images, resampled to the image pixel scale of HMI. (d) Corresponding longitudinal magnetogram of each snapshot, synthesized emulating the HMI instrument. The longitudinal magnetograms map the line-of-sight (LOS) component of the magnetic field strength.

The MURaM code describes the time evolution of magnetized plasma of solar composition from magnetoconvection in a 3D space [35]. The computational domain of the employed simulations extends 9×9 Mm in the horizontal and 3 Mm in the vertical, set up such that the surface of optical depth unity (i.e., the solar surface) is about 0.7 Mm from the top. We generated three MHD simulations, initiated with a uniform magnetic field of 100, 200, and 300 G, respectively [Fig. 1(a)]. There is an additional simulation to which no magnetic flux was introduced, making it purely hydrodynamic. We took ten snapshots of each simulation. Each snapshot, capturing the state of the given simulation at a particular simulation time, is equivalent to a 3D model atmosphere.

Taking each snapshot, we calculated the emergent intensity spectrum (including the effect of spectral lines) from each horizontal position when viewed from above using a radiative transfer code [45]. Taking the integral over wavelength of each intensity spectrum, we arrive at the bolometric image of the snapshot as it would appear at the disk center [Fig. 1(b)]. This is repeated, inclining the line of sight as needed to synthesize the bolometric images of the snapshot as it would appear at various distances from the disk center. The bolometric images are resampled to the image pixel scale of HMI [Fig. 1(c)].

Next, we synthesized the magnetogram corresponding to each bolometric image by emulating the HMI instrument [Fig. 1(d)]. Applying a spectral line synthesis code [46] to the MHD snapshots in a process similar to the bolometric intensity calculations just described, we calculated the Stokes parameters of the Fe I 6173 Å line (the spectral line HMI observes) corresponding to each point in each bolometric image. The line profiles were processed in such a way as to emulate the spatial resolution, spectral sampling, stray light [47], and noise level [22] of the HMI instrument. We calculated the magnetic flux density from the line profiles employing the same algorithm used in the HMI data reduction pipeline [48], yielding the HMI-like magnetogram corresponding to each bolometric image. From the synthetic images and magnetograms based on the MHD snapshots, we derived a relationship describing bolometric intensity as a function of the distance from the disk center and the HMI magnetogram signal (solid lines, Fig. 2).

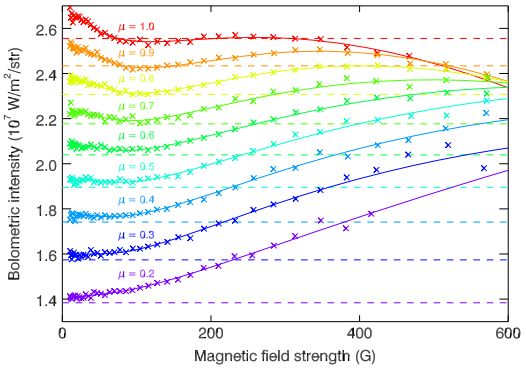


FIG. 2. Bolometric intensity of the quiet Sun and faculae. Let μ denote the cosine of the heliocentric angle, representing the distance from the disk center. The crosses denote the result of taking the bolometric images and the HMI-like longitudinal magnetograms of the MHD snapshots, binning the points by μ and magnetic field strength, and taking the bin-averaged magnetic field strength and bolometric intensity. The solid lines follow the corresponding bivariate polynomial in μ and magnetic field strength fit, taken into the model to describe the bolometric intensity of faculae. The dashed lines denote the quiet Sun bolometric intensity at each value of μ, given by the mean level in the bolometric images of the hydrodynamic snapshots.

PRL 119, 091102 (2017) PHYSICAL REVIEW LETTERS week ending 1 SEPTEMBER 2017

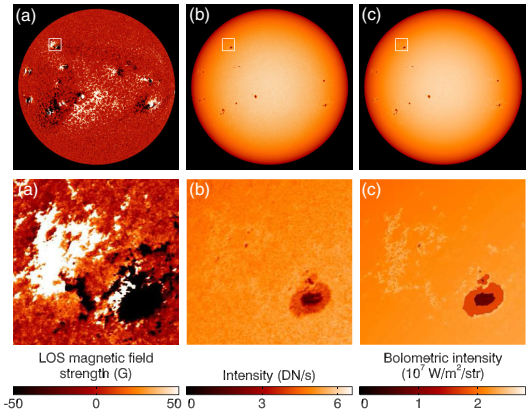


FIG. 3. From left to right: (a) HMI longitudinal magnetogram dated December 16, 2012 (top) and the inset of the boxed area (bottom). Positive and negative values, rendered bright and dark, denote the magnetic field pointed towards and away from the observer, respectively. (b) Simultaneous HMI continuum intensity image, where sunspots are easily apparent. The instrument maps the intensity in the continuum of the Fe I 6173 line in instrumental units of digital number per second (DN/s). (c) Bolometric image reconstructed with the model presented, the full-disk integral of which yields TSI. The model assigns, to each image pixel on the solar disk, the calculated bolometric intensity of either the quiet Sun, faculae, sunspot penumbra, or sunspot umbra depending on what it is identified to be in the HMI observations.

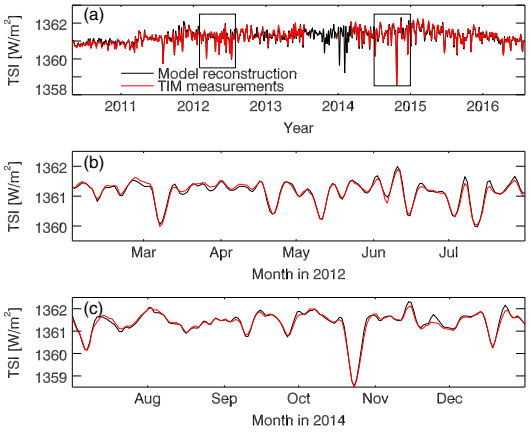


FIG. 4. (a) The TSI reconstruction (black line) and the measurements from TIM (red line), which operated over the period of the reconstruction except between August 2013 and April 2014. (b) The inset of the boxed period in 2012. (c) The inset of the boxed period in 2014.

We determined the bolometric intensity of the quiet Sun from the bolometric images of the hydrodynamic snapshots (dashed lines, Fig. 2). As in SATIRE-S, the bolometric intensity of sunspots is calculated from 1D model atmospheres. Since existing semiempirical models already demonstrate this approach to return sunspot darkening without requiring any calibration to observed solar irradiance variability, there is no need to model it differently here.

HMI has been returning observations continuously since April 30, 2010. For each day up to July 31, 2016, we took a full-disk magnetogram [Fig. 3(a)] and the concurrent continuum image [Fig. 3(b)]. We segmented the solar disk into the quiet Sun, faculae, and sunspots by identifying faculae by the magnetogram signal and sunspots by the contrast in the continuum intensity image following Ref. [41]. We assigned, to each image pixel on the solar disk, the appropriate bolometric intensity by the surface feature type, distance from the disk center, and, in the case of faculae, the magnetogram signal. TSI is then given by the integral of the resultant full-disk bolometric image [Fig. 3(c)]. The reconstructed TSI variability (Fig. 4) is a direct consequence of the day-to-day variation in surface coverage by faculae and sunspots.

We compared the TSI reconstruction to the measurements from the two solar radiometers that operated over the same period, Total Irradiance Monitor onboard the solar radiation and climate experiment (SORCE/TIM) [49] and Variability of Irradiance and Gravity Oscillations instrument onboard the Solar and Heliospheric Observatory (SoHO/VIRGO) [50]. Because it is TSI variability that is of interest rather than the absolute radiative flux, we normalized the reconstruction and the VIRGO record to the TIM record, the absolute radiometry of which is widely accepted as the most accurate [51–53].

The TSI reconstruction is in excellent agreement with both observational records, in particular that from TIM (Table I). The Pearson correlation coefficient R is 0.976, indicating the model replicates 95% of the apparent variability. More importantly, the reconstruction reproduces the amplitude of measured TSI variability remarkably well. The reconstruction and the TIM record run closely parallel to one another, in terms of both the overall

TABLE I. The Pearson correlation coefficient R and rms difference between the TSI reconstruction and the observational records from TIM and VIRGO. The reconstruction spans April 30, 2010 to July 31, 2016, a period of 2285 days, without interruption. As there are gaps in the coverage of this period by TIM and VIRGO, we compared the various time series to one another over just the days where measurements are available from both instruments (1996 days, 87% of the total).

Time series	R	rms difference (W/m^2)
Model and TIM	0.976	0.0836
Model and VIRGO	0.968	0.0941
TIM and VIRGO	0.975	0.0865

PRL 119, 091102 (2017) PHYSICAL REVIEW LETTERS week ending 1 SEPTEMBER 2017

and the day-to-day trend, as visibly evident in Fig. 4 and encapsulated in the minute root-mean-square (rms) difference of 0.0836 W/m^2.

It is worth noting that the agreement between the model reconstruction and each of the two observational records, whether in terms of R or the rms difference, is comparable to that between the two records (Table I). This suggests that the differences between the reconstruction and the two observational records is in no small part due to the uncertainty in the latter.

Coming without any optimization to measured TSI variability, the agreement between the TSI reconstruction and observations is direct evidence that, at least for time scales from days to the solar cycle, solar irradiance variability is mainly driven by solar surface magnetic activity. Recall that the case for this relationship has so far been circumstantial due to the fact that preceding models, without exception, have to be calibrated to observed solar irradiance variability. The fact that the model accounts for the bulk of measured TSI variability (95%) also implies that the contribution by other mechanisms, such as those stated earlier in this Letter [14–16], is very limited (no more than 5% on the time scales examined here).

The ability of the TSI model presented to recreate observed variability confirms the assertion that the energy blocked by sunspots is redistributed in the convection zone and the excess energy released at faculae originates from the convection zone [12,13,17]. The convection zone acts like an energy store due to the high thermal conductivity and slow thermal relaxation. Together with the high heat capacity, the fluctuations in internal energy from these exchanges have essentially no effect on the surface properties. If the intensity deficit (excess) of surface magnetic features is channeled to (from) their surroundings instead, accounting for just that as we have done here should not recreate the observed solar irradiance variability.

Climate simulations rely on model reconstructions of historical solar irradiance variability, and all current models are based on solar surface magnetism. The demonstration here that solar irradiance variability is indeed dominantly driven by solar surface magnetism bolsters the validity of their application to climate simulations.

Finally, the results of this study indicate that the photometric variability of other cool stars, at time scales greater than a day, can be almost completely ascribed to stellar surface magnetism.

We made use of observations from SDO/HMI (level 1.5 [54]), SOHO/VIRGO (version 06_005_1608 [55]), and SORCE/TIM (version 14 [56]), courtesy of the respective instrument teams. The TSI reconstruction presented is available in Ref. [57].

We are very grateful to Yang Liu and Philip Scherrer at Stanford University for the useful discussions and their assistance in implementing the HMI observables algorithm. This work was supported by the German Federal Ministry of Education and Research (Project No. 01LG1209A), the European Research Council (ERC) under the European Union's Horizon 2020 research and innovation program (Grant Agreement No. 695075), and the BK21 plus program of the National Research Foundation (NRF) funded by the Ministry of Education of Korea.

*yeo@mps.mpg.de
†Also at School of Space Research, Kyung Hee University, Yongjin, Gyeonggi 446-701, Korea.

[1] G. Kopp, J. Space Weather Space Clim. **4**, A14 (2014).
[2] R. C. Willson, S. Gulkis, M. Janssen, H. S. Hudson, and G. A. Chapman, Science **211**, 700 (1981).
[3] J. A. Eddy, Science **192**, 1189 (1976).
[4] L. J. Gray, J. Beer, M. Geller, J. D. Haigh, M. Lockwood, K. Matthes, U. Cubasch, D. Fleitmann, G. Harrison, L. Hood, J. Luterbacher, G. A. Meehl, D. Shindell, B. van Geel, and W. White, Rev. Geophys. **48**, RG4001 (2010).
[5] A. Baglin, M. Auvergne, P. Barge, J.-T. Buey, C. Catala, E. Michel, W. Weiss, and (COROT Team), in *Stellar Structure and Habitable Planet Finding*, edited by B. Battrick, F. Favata, I. W. Roxburgh, and D. Galadi, ESA Special Publication Vol. 485 (European Space Agency, Munich, 2002), pp. 17–24.
[6] R. L. Gilliland *et al.*, Publ. Astron. Soc. Pac. **122**, 131 (2010).
[7] H. C. Spruit and B. Roberts, Nature (London) **304**, 401 (1983).
[8] R. C. Willson and H. S. Hudson, Nature (London) **332**, 810 (1988).
[9] H. S. Hudson, S. Silva, M. Woodard, and R. C. Willson, Sol. Phys. **76**, 211 (1982).
[10] L. Oster, K. H. Schatten, and S. Sofia, Astrophys. J. **256**, 768 (1982).
[11] P. Foukal and J. Lean, Astrophys. J. Lett. **302**, 826 (1986).
[12] V. Domingo, I. Ermolli, P. Fox, C. Fröhlich, M. Haberreiter, N. Krivova, G. Kopp, W. Schmutz, S. K. Solanki, H. C. Spruit, Y. Unruh, and A. Vögler, Space Sci. Rev. **145**, 337 (2009).
[13] H. C. Spruit, Astron. Astrophys. **108**, 356 (1982).
[14] C. L. Wolff and J. R. Hickey, Science **235**, 1631 (1987).
[15] J. R. Kuhn, K. G. Libbrecht, and R. H. Dicke, Science **242**, 908 (1988).
[16] J.-F. Cossette, P. Charbonneau, and P. K. Smolarkiewicz, Astrophys. J. Lett. **777**, L29 (2013).
[17] S. K. Solanki, N. A. Krivova, and J. D. Haigh, Annu. Rev. Astron. Astrophys. **51**, 311 (2013).
[18] D. F. Heath and B. M. Schlesinger, J. Geophys. Res. **91**, 8672 (1986).
[19] C. Fröhlich and J. Lean, Astron. Astrophys. Rev. **12**, 273 (2004).
[20] M. Fligge, S. K. Solanki, and Y. C. Unruh, Astron. Astrophys. **353**, 380 (2000).
[21] K. L. Yeo, N. A. Krivova, and S. K. Solanki, Space Sci. Rev. **186**, 137 (2014).
[22] K. L. Yeo, S. K. Solanki, and N. A. Krivova, Astron. Astrophys. **550**, A95 (2013).

[23] See Supplemental Material at http://link.aps.org/supplemental/10.1103/PhysRevLett.119.091102 for a detailed description, which includes Refs. [24–34].
[24] V. Martínez Pillet, B. W. Lites, and A. Skumanich, Astrophys. J. **474**, 810 (1997).
[25] D. Buehler, A. Lagg, S. K. Solanki, and M. van Noort, Astron. Astrophys. **576**, A27 (2015).
[26] F. J. Rogers, F. J. Swenson, and C. A. Iglesias, Astrophys. J. **456**, 902 (1996).
[27] E. Anders and N. Grevesse, Geochim. Cosmochim. Acta **53**, 197 (1989).
[28] A. Vögler, J. H. M. J. Bruls, and M. Schüssler, Astron. Astrophys. **421**, 741 (2004).
[29] B. Beeck, R. H. Cameron, A. Reiners, and M. Schüssler, Astron. Astrophys. **558**, A48 (2013).
[30] N. E. Piskunov, F. Kupka, T. A. Ryabchikova, W. W. Weiss, and C. S. Jeffery, Astron. Astrophys. Suppl. Ser. **112**, 525 (1995).
[31] L. R. Bellot Rubio and J. M. Borrero, Astron. Astrophys. **391**, 331 (2002).
[32] R. J. Rutten and R. I. Kostik, Astron. Astrophys. **115**, 104 (1982).
[33] N. Shchukina and J. Trujillo Bueno, Astrophys. J. **550**, 970 (2001).
[34] N. A. Krivova, S. K. Solanki, and L. Floyd, Astron. Astrophys. **452**, 631 (2006).
[35] A. Vögler, S. Shelyag, M. Schüssler, F. Cattaneo, T. Emonet, and T. Linde, Astron. Astrophys. **429**, 335 (2005).
[36] S. Shelyag, M. Schüssler, S. K. Solanki, S. V. Berdyugina, and A. Vögler, Astron. Astrophys. **427**, 335 (2004).
[37] N. Afram, Y. C. Unruh, S. K. Solanki, M. Schüssler, A. Lagg, and A. Vögler, Astron. Astrophys. **526**, A120 (2011).
[38] S. Danilovic, D. Röhrbein, R. H. Cameron, and M. Schüssler, Astron. Astrophys. **550**, A118 (2013).
[39] T. L. Riethmüller, S. K. Solanki, S. V. Berdyugina, M. Schüssler, V. Martínez Pillet, A. Feller, A. Gandorfer, and J. Hirzberger, Astron. Astrophys. **568**, A13 (2014).
[40] J. Schou *et al.*, Sol. Phys. **275**, 229 (2012).
[41] K. L. Yeo, N. A. Krivova, S. K. Solanki, and K. H. Glassmeier, Astron. Astrophys. **570**, A85 (2014).
[42] Y. C. Unruh, S. K. Solanki, and M. Fligge, Astron. Astrophys. **345**, 635 (1999).
[43] A. M. Title, K. P. Topka, T. D. Tarbell, W. Schmidt, C. Balke, and G. Scharmer, Astrophys. J. **393**, 782 (1992).
[44] A. Ortiz, S. K. Solanki, V. Domingo, M. Fligge, and B. Sanahuja, Astron. Astrophys. **388**, 1036 (2002).
[45] R. L. Kurucz, Rev. Mex. Astron. Astrofis. **23**, 45 (1992).
[46] C. Frutiger, S. K. Solanki, M. Fligge, and J. H. M. J. Bruls, Astron. Astrophys. **358**, 1109 (2000).
[47] K. L. Yeo, A. Feller, S. K. Solanki, S. Couvidat, S. Danilovic, and N. A. Krivova, Astron. Astrophys. **561**, A22 (2014).
[48] S. Couvidat, S. P. Rajaguru, R. Wachter, K. Sankarasubramanian, J. Schou, and P. H. Scherrer, Sol. Phys. **278**, 217 (2012).
[49] G. Kopp, G. Lawrence, and G. Rottman, Sol. Phys. **230**, 129 (2005).
[50] C. Fröhlich *et al.*, Sol. Phys. **162**, 101 (1995).
[51] G. Kopp and J. L. Lean, Geophys. Res. Lett. **38**, n/a (2011).
[52] G. Kopp, A. Fehlmann, W. Finsterle, D. Harber, K. Heuerman, and R. Willson, Metrologia **49**, S29 (2012).
[53] A. Fehlmann, G. Kopp, W. Schmutz, R. Winkler, W. Finsterle, and N. Fox, Metrologia **49**, S34 (2012).
[54] http://jsoc.stanford.edu.
[55] ftp://ftp.pmodwrc.ch/pub/data/.
[56] http://lasp.colorado.edu/lisird.
[57] http://www2.mps.mpg.de/projects/sun-climate/data.html.

Supplementary Material: Solar irradiance variability is caused by the magnetic activity on the solar surface

Kok Leng Yeo,[1,*] Sami K. Solanki,[1,†] Charlotte M. Norris,[2]
Benjamin Beeck,[1] Yvonne C. Unruh,[2] and Natalie A. Krivova[1]

[1] *Max Planck Institute for Solar System Research, Justus-von-Liebig-Weg 3, 37077 Göttingen, Germany.*

[2] *Blackett Laboratory, Imperial College London, South Kensington Campus, London SW7 2AZ, UK.*

(Dated: August 1, 2017)

OVERVIEW OF THE MODEL

Existing models of solar irradiance variability, which describe the variation associated with solar surface magnetic activity, have to be calibrated to observed variability. As a consequence, the true relationship between solar irradiance variability and solar surface magnetism remains an open question. To settle this controversy, we present what is the first model of TSI variability to not require any such calibration. Let us start with an overview of the model.

The architecture of the model broadly follows the semi-empirical model SATIRE-S [1, 2]. The solar surface is taken to comprise of the quiet Sun, faculae and sunspots. The bolometric intensity of the various solar surface features is calculated from models of their atmospheric structure. For each day, the solar disk is segmented into the quiet Sun, faculae and sunspots by identifying faculae and sunspots in full-disk observations of magnetic field strength and continuum intensity (Fig. 1). For this purpose, we make use of full-disc magnetograms and intensity images from SDO/HMI, which are the most precise available. Taking the bolometric intensities of solar surface features calculated from the corresponding model atmospheres, we ascribe to each image pixel on the solar disc the appropriate bolometric intensity according to the segmentation. The integral of the resultant bolometric image (see Fig. 3C in the main text) over the solar disk yields TSI.

In SATIRE-S and other present-day semi-empirical models, the intensity of solar surface features is determined, as a function of distance from disk center, on the basis of 1D model atmospheres. This neglects the variation in facular intensity with magnetic field strength. In order to assign the appropriate intensity to observed faculae, these models introduce empirical relationships relating the calculated facular intensities to measured magnetic flux densities. Such relationships are calibrated by optimizing the model output to measured solar irradiance variability.

The TSI model presented here departs from existing semi-empirical models in that the bolometric intensity of the quiet Sun and faculae is calculated from 3D model atmospheres. The 3D model atmospheres are provided by 3D radiation MHD simulations of the solar atmosphere generated with the MURaM code [3]. Taking these 3D models of the solar atmosphere, we synthesized bolometric images and HMI-like magnetograms that represent how the simulated boxes of the Sun would appear to a bolometric imager and to HMI

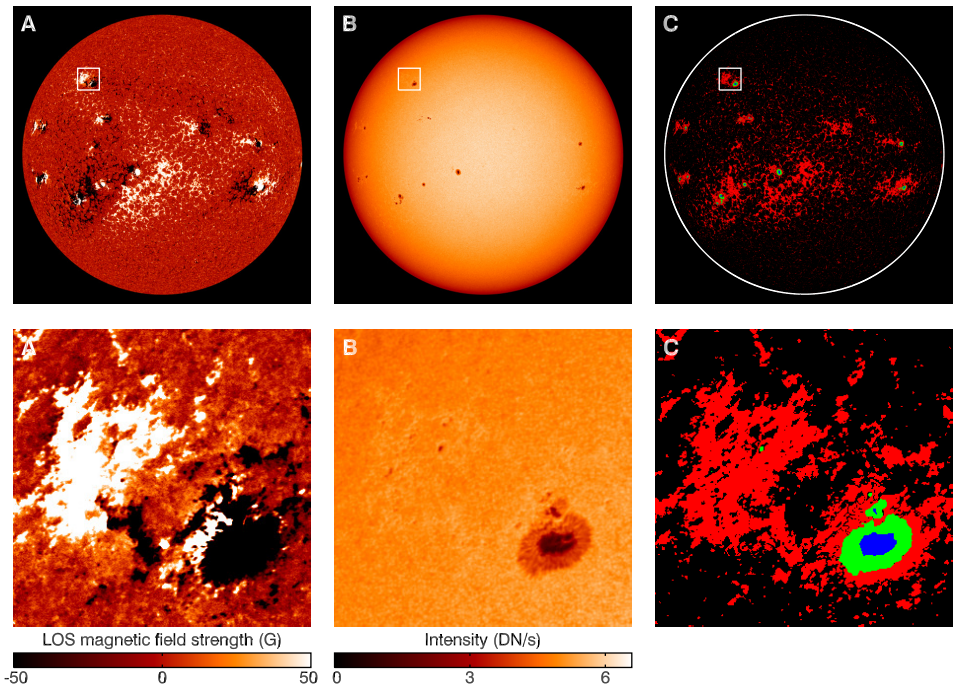


FIG. 1. From left to right: A) HMI longitudinal magnetogram and B) continuum intensity image dated December 16, 2012 (taken from Fig. 3 in the main text). C) Map indicating the location of faculae (red), sunspot penumbra (green) and sunspot umbra (blue) as identified in the HMI longitudinal magnetogram and continuum intensity image. The solar disk is encircled.

if they were at various distances from disk center (Fig. 2). From the result, we derived facular bolometric intensity as a function of not just distance from disk center but also HMI magnetogram signal (Fig. 2 in the main text). This allows us, in the TSI reconstruction process, to determine the bolometric intensity of faculae identified in HMI observations by their position on the solar disk and the apparent magnetic field strength alone. By removing the need to introduce empirical relationships to relate calculated facular intensities to observed faculae, we arrive at a model of TSI variability that does not require any calibration to observed TSI variability.

In the following, we detail the various aspects of the model.

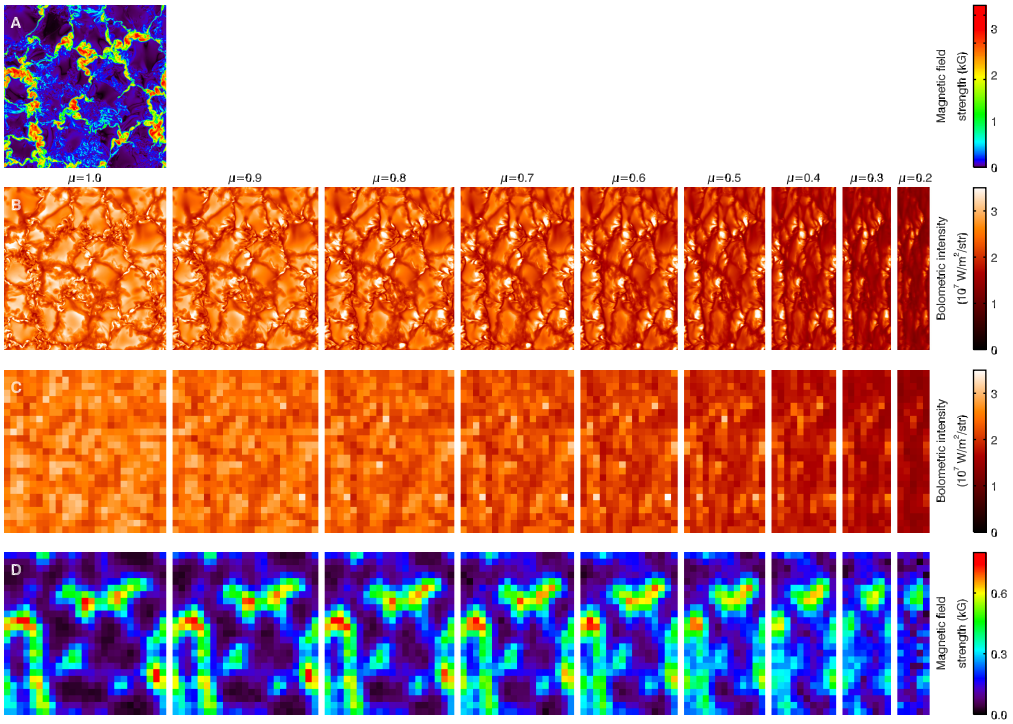


FIG. 2. From top to bottom: A) Magnetic field strength at optical depth unity in a snapshot of the MHD simulation initiated with a uniform magnetic field of 300 G (taken from Fig. 1A in the main text). B) Bolometric image of the snapshot at various μ. C) The same bolometric images, resampled to the image pixel scale of HMI. D) The corresponding HMI-like longitudinal magnetograms of the snapshot. We estimated magnetic field strength by taking the quotient of the longitudinal magnetogram signal with μ. Going from disc center to limb, the magnetic concentrations appear to weaken. This is due to the declining spatial resolution (due to foreshortening) and the combination of the decline in magnetic field strength with height and the greater formation height of the spectral line HMI observes in.

SURFACE COVERAGE BY FACULAE AND SUNSPOTS

The daily surface coverage by faculae and sunspots is determined from HMI full-disk observations of magnetic field strength and continuum intensity. HMI consists of two 4096 × 4096 pixel CCD telescopes, observing the entire solar disk at a pixel scale of 0.5". The instrument has been returning, amongst other data products, longitudinal magnetograms

and images in the continuum of the Fe I 6173 Å line at 45-second intervals since April 30, 2010. For each day, up to July 31, 2016, we took the average of seven consecutive longitudinal magnetograms and of the corresponding continuum images. The result is a set of daily 315-second integral longitudinal magnetograms and continuum images spanning a period of 2285 days.

The longitudinal magnetogram gives the line-of-sight component of the mean magnetic field strength over each resolution element. Magnetic flux tubes tend to stand vertically to the solar surface due to magnetic buoyancy. This allows us to approximate the mean magnetic field strength over a given HMI image pixel, B_{HMI} by the quotient of the longitudinal magnetogram signal and the cosine of the heliocentric angle, μ. This is a typical assumption of facular features in longitudinal magnetograms [4] and is well supported by observations [5, 6].

Sunspots are identified by the continuum intensity and faculae by the longitudinal magnetogram signal essentially following the procedure in SATIRE-S with similar HMI data [detailed in 2]. The image pixels where the continuum intensity is below 0.87 and 0.59 of the quiet Sun level are counted as sunspot penumbra and sunspot umbra, respectively. (The quiet Sun level is given by the polynomial in μ fit to the image pixels where the magnetogram signal is below 10 G.) These thresholds are set in SATIRE-S such that the resultant sunspot area and umbral to penumbral area ratio are consistent with independent sunspot observations [2].

The image pixels where the longitudinal magnetogram signal exceeds three times the noise level, 3σ and are not already identified as sunspots are taken to correspond to faculae (Fig. 1). The noise level of HMI 315-second longitudinal magnetograms is taken from [4], who determined it as a function of disc position (it increases radially from about 5 G about disk center to 9 G near the limb, see Fig. 1 in their paper). The remaining image pixels are assumed to be quiet Sun. To minimize false positives from measurement noise, we reassigned, as quiet Sun, the standalone facular image pixels. We also reclassified the facular image pixels where B_{HMI} exceeds 600 G as quiet Sun. Such points, mainly located close to sunspots near the limb, were found to be mostly false positives from the encroachment of the magnetic canopy of sunspots onto their surroundings [2].

3D MHD SIMULATIONS OF THE SOLAR ATMOSPHERE

The bolometric intensity of the quiet Sun and faculae is determined from 3D model atmospheres provided by 3D radiative MHD simulations of the solar atmosphere performed with the MURaM code.

The MURaM code solves the time-dependent MHD equations for a compressible, partially-ionized plasma in a 3D grid with periodic side boundaries. The system of MHD equations is closed with the OPAL equation of state [7] for a plasma with solar composition [8]. Non-gray radiative heating/cooling is included through the non-grey 3D radiative transfer scheme detailed in [9]. Inflows and outflows are permitted from the bottom boundary. Gas pressure at the bottom boundary, which modulates the inflow, is adaptive such that the total mass in the computational domain is maintained. The entropy density of the inflows is fixed at the value where the average effective temperature of a purely hydrodynamic simulation (that is, no magnetic flux introduced) equals the solar value. The computational domain extends 9×9 Mm in the horizontal and 3 Mm in the vertical in a grid spanning $512 \times 512 \times 300$ points, which translates into a cell size of $17.6 \times 17.6 \times 10.0$ km. The mean level of optical depth unity is about 0.7 Mm below the top boundary.

First, we generated a hydrodynamic simulation, taking a snapshot of the existing hydrodynamic simulation from [10] as the initial condition. This earlier simulation is, apart from the surface of optical depth unity being about 0.3 Mm deeper, similarly set up. We allowed the simulation to run for about five hours in solar time. After the first three hours, with the simulation well into a statistically steady state, 10 snapshots were taken at approximately 10-minute intervals. These snapshots are taken to represent the quiet Sun.

Next, we produced three MHD simulations, initialized by introducing a uniform, unipolar and vertical magnetic field of 100 G, 200 G and 300 G, respectively to one of the snapshots of the hydrodynamic simulation. The introduction of magnetic flux results in a dynamic restructuring over about 20 to 30 minutes in solar time. We ran each simulation for over three hours, taking 10 snapshots at approximately 7-minute intervals after the first two hours. By allowing the simulations to relax for two hours before sampling, we exclude any transients from the dynamic restructuring. The 7-minute interval allows a given simulation to evolve sufficiently between snapshots such that they are independent in terms of the granulation pattern and the distribution of magnetic flux. These snapshots represent facular regions

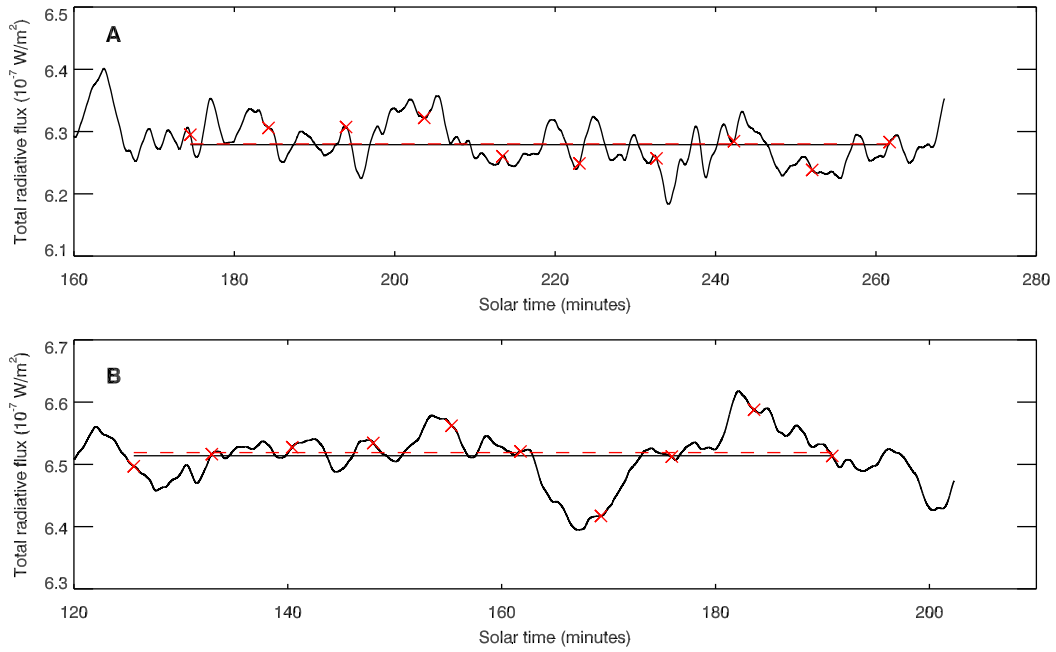


FIG. 3. A) Time series of the total emergent radiative flux in the hydrodynamic simulation. The red crosses mark the ten snapshots. The red line (dashed for visibility) follows the mean of ten snapshots and the black line the mean over the period between the first and last snapshots. B) The same, except for the MHD simulation initiated with a uniform magnetic field of 200 G. The time series for the two other MHD simulations are not included to avoid repetition.

with different levels of magnetic activity.

The MURaM code returns the vertically emergent and the angle-integrated bolometric intensity. In Fig. 3, we display the time series of the total radiative flux emerging from the hydrodynamic simulation and from the MHD simulation initiated with a uniform magnetic field of 200 G. The fluctuations reflect the statistical variability of the simulations from the time evolution of the magneto-convection system. As illustrated in the figure, for each simulation, the 10 snapshots are selected such that the average of the total radiative flux at the sampled times is close to the average over the simulation after it reaches a statistically steady state.

In the following, we will describe how we determined the bolometric intensity of the quiet Sun and faculae from the 10 hydrodynamic and 30 MHD snapshots.

SYNTHETIC BOLOMETRIC IMAGES

MURaM only outputs the vertically emergent and angle-integrated bolometric intensity. Therefore, to synthesized bolometric images of the snapshots that represent how they would appear to a bolometric imager if they were at various distances from disk center, we input them into the radiative transfer code ATLAS9 [11] to solve for the emergent intensity at the required viewing angles.

For a given input 1D model atmosphere, ATLAS9 returns the intensity spectrum under the assumption of local thermodynamic equilibrium (LTE). Spectral lines are represented by opacity distribution function (ODF) tables. We employed the ATLAS9 ODF table corresponding to a micro-turbulent velocity of 1 km/s. This value was chosen on the observation that in the snapshots, the RMS velocity around optical depth unity is close to this value. ATLAS9 can be configured to take the variation in micro-turbulent velocity with depth into account with multiple ODF tables. However, tests revealed this to make no appreciable difference to the output intensity spectra.

Taking each snapshot, we passed a ray through each vertical column in the 3D grid. We input the run of parameters along each ray into ATLAS9, essentially treating the snapshot as a 512×512 array of 1D model atmospheres. The output intensity spectra cover the wavelength range of 168 nm to 160 μm at 1020 points. This wavelength range, extending from the far-ultraviolet (UV) to the far-infrared, encompasses the bulk of the energy in solar radiative flux such that we can take the integral of a given intensity spectrum as the corresponding bolometric intensity. The result is a 512×512 pixel bolometric image of the snapshot as it would appear at disk center.

Bolometric images of the snapshots as they would appear off disk center were synthesized by inclining the rays by the appropriate angle and repeating the above process. We derived, for each snapshot, the bolometric images corresponding to μ of 0.2 (0.98 solar radii from disk center) to 1.0 (disk center) in steps of 0.1 (Fig. 2B). The bolometric images, a total of nine per snapshot, are resampled to the image pixel scale of HMI (Fig. 2C). This resampling is to enable us to relate the calculated bolometric intensities to the magnetogram signal in the HMI-like magnetograms of the same snapshots, derived next. Due to foreshortening in the direction the rays are tilted, the bolometric images extend 25×25 HMI pixels at disk center but only 25×5 HMI pixels at μ of 0.2.

SYNTHETIC HMI LONGITUDINAL MAGNETOGRAMS

Next, we synthesized longitudinal magnetograms of the snapshots, at the same values of μ where we generated bolometric images, emulating the HMI instrument.

HMI captures a full disk image of the Sun every 1.875 seconds, alternating between six filters centered at various positions across the magnetically sensitive Fe I 6173 Å line (Fig. 4) and six polarizations (Stokes I±V, I±Q and I±U). HMI longitudinal magnetograms and continuum intensity images are generated from the Stokes I±V filtergrams in the HMI data reduction pipeline with the algorithm described in [12]. To create HMI-like longitudinal magnetograms of the snapshots, we synthesized HMI-like Stokes I±V filtergrams of them and applied this same algorithm.

Earlier, we generated 512×512 pixel bolometric images of the snapshots by sampling each snapshot in such a way that we treat it as a 512×512 array of 1D model atmospheres. For each snapshot and at each value of μ, we passed the same 512×512 array of 1D model atmospheres into a spectral line synthesis code, SPINOR [Stokes Profiles INversion-O-Routines, 13] to calculate the Stokes parameters of the Fe I 6173 Å line corresponding to each 1D model atmosphere (at 5 mÅ resolution). The SPINOR code solves the radiative transfer equation for polarized light, for a prescribed 1D model atmosphere and atomic parameters, under the assumption of LTE. We took the atomic parameters from the VALD database [14] and the iron abundance from [15]. As demonstrated in Fig. 4A, the output of the code is in good agreement with observation.

We resampled the resultant line profiles with the transmission profile of the six HMI filters (Fig. 4B). The result is, for each snapshot and at each value of μ, 12 512×512 pixel images giving Stokes I±V at each of the six filters (Fig. 5B). Following that, we resampled the filtergrams to the image pixel scale of HMI and convolved the result with the point spread function of the instrument [16] to adopt its spatial resolution and stray light (Fig. 5C). We introduced Gaussian noise to the result to emulate the measurement uncertainty of the instrument. After this process, we arrive at HMI-like Stokes I±V filtergrams of the snapshots, which we then convert to HMI-like longitudinal magnetograms (Fig. 5D). The Gaussian noise introduced to the filtergrams is set at the level where the RMS magnetogram signal in the longitudinal magnetograms of the hydrodynamic snapshots matches the observed noise level of HMI 315-second longitudinal magnetograms [4].

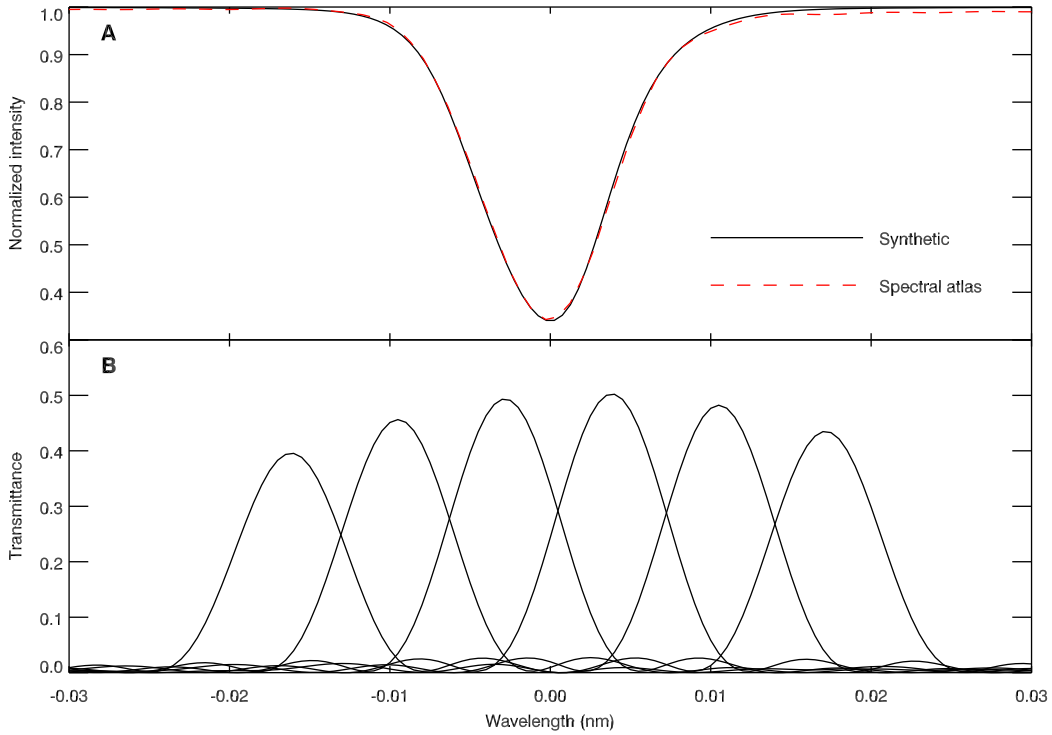


FIG. 4. A) The Fe I 6173 Å line, from the NSO disk center quiet Sun spectral atlas (diglib.nso.edu) and synthesized with the hydrodynamic snapshots, drawn in red and black, respectively. The latter is given by the average calculated line profile of the 10 hydrodynamic snapshots. The minor discrepancy between the two line profiles in the red wing is due to the exclusion of the La II 6172.72 Å line from the line synthesis. B) The transmission profile of the six filters in which HMI makes observations of the Fe I 6173 Å line.

The HMI data reduction pipeline algorithm used in this conversion also yields synthetic HMI continuum intensity images of the snapshots. They are not required by the TSI model but we examined them in a verification of this analysis, to be discussed later.

We had passed the result of resolving each snapshot as a 512×512 array of 1D model atmospheres into both ATLAS9 and SPINOR, and resampled the output from both codes to the image pixel scale of HMI. The synthetic magnetograms are generated from the SPINOR output by emulating the HMI instrument. With these steps, the magnetograms give the HMI magnetogram signal corresponding to each point in the bolometric images.

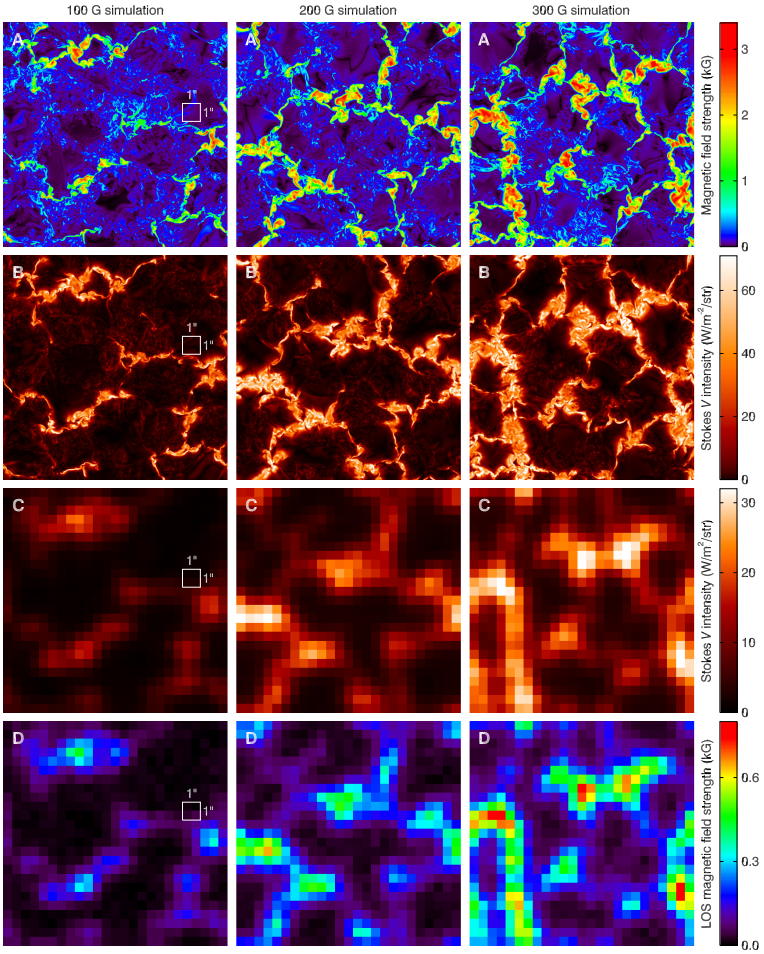


FIG. 5. From top to bottom: A) From Fig. 1A in the main text, magnetic field strength at optical depth unity in a snapshot of each MHD simulation, denoted by the strength of the uniform magnetic field introduced at onset. B) The sum of the Stokes V signal in the six HMI filters. The Stokes V parameters are calculated from the snapshots with a spectral line synthesis code. C) The same, after emulating the spatial resolution, stray light and measurement uncertainty of HMI. This treatment yields HMI-like filtergrams of the snapshots. D) The HMI-like longitudinal magnetogram generated from the HMI-like filtergrams by the same method applied in the HMI data reduction pipeline, taken from Fig. 1D in the main text.

BOLOMETRIC INTENSITY OF SOLAR SURFACE FEATURES

We determined the bolometric intensity of faculae from the bolometric images and the HMI-like longitudinal magnetograms of the 30 MHD snapshots. As done earlier with actual HMI longitudinal magnetograms, magnetic flux density, $B_{\rm HMI}$ is estimated by taking the quotient of the longitudinal magnetogram signal and μ.

At each value of μ where we generated synthetic images and magnetograms of the snapshots, we made a scatter plot of bolometric intensity versus the corresponding $B_{\rm HMI}$, and binned the points by $\log B_{\rm HMI}$ in intervals of 0.1. The average $B_{\rm HMI}$ and bolometric intensity within each bin is drawn in Fig. 2 in the main text (crosses). As visibly evident, bolometric intensity is profoundly influenced by $B_{\rm HMI}$ and μ. The center-to-limb variation (CLV) of bolometric intensity varies with $B_{\rm HMI}$, giving the change in the trend with $B_{\rm HMI}$ as we go from μ=1.0 to μ=0.2.

The bolometric intensity of faculae, $I_{\rm fac}$, as a function of μ and $B_{\rm HMI}$, is given by the bivariate polynomial in $B_{\rm HMI}$ and μ fit to the bin-average bolometric intensities from all values of μ (solid lines, Fig. 2 in the main text). In linear algebra notation, the relationship is

$$I_{\rm fac} = \begin{bmatrix} B^0_{\rm HMI} \\ B^1_{\rm HMI} \\ B^2_{\rm HMI} \\ B^3_{\rm HMI} \\ B^4_{\rm HMI} \\ B^5_{\rm HMI} \end{bmatrix}^{\rm T} \begin{bmatrix} -23.9 & 248 & -700 & 830 & 324 & -21.3 \\ 33.4 & -326 & 924 & -1080 & 408 & 38.0 \\ -17.8 & 173 & -493 & 585 & -228 & -14.7 \\ 4.69 & -45.7 & 132 & -161 & 69.1 & 0.0184 \\ -0.612 & 5.97 & -17.6 & 22.4 & -10.7 & 0.704 \\ 0.0314 & -0.307 & 0.926 & -1.22 & 0.641 & -0.0767 \end{bmatrix} \begin{bmatrix} \mu^0 \\ \mu^1 \\ \mu^2 \\ \mu^3 \\ \mu^4 \\ \mu^5 \end{bmatrix}, \qquad (1)$$

where $I_{\rm fac}$ is in units of 10^7 W/m^2/str. This is a significant advance over current semi-empirical models, where $I_{\rm fac}$ is calculated as a function of μ alone and then related to magnetic flux density empirically. The various models take different approaches but invariably the empirical relationship is calibrated to measured solar irradiance and implicitly assumes that the CLV of facular intensity does not change with magnetic flux density, which is certainly not the case (Fig. 2 in the main text). The relationship between $I_{\rm fac}$ and μ and $B_{\rm HMI}$ derived here (Eq. 1) encapsulates the complex disc position and magnetic field strength dependence of facular bolometric intensity (Fig. 2 in the main text) and does so without the need to be calibrated to solar irradiance observations or to make any assumptions about

the magnetic flux density dependence of the CLV.

Next, we determined the bolometric intensity of the quiet Sun from the bolometric images of the 10 hydrodynamic snapshots. The quiet Sun bolometric intensity at each value of μ where we generated these images is given by the average intensity over all the images, represented in Fig. 2 of in main text by the dashed lines. By deriving the bolometric intensity of both the quiet Sun and faculae from MURaM-based 3D model atmospheres, we are adopting into the TSI model the intensity contrast of faculae as simulated by the MURaM code.

As in existing semi-empirical models, we derived the bolometric intensity of sunspot penumbra and umbra, as a function of μ, on the basis of 1D model atmospheres. Following the arguments of (49), we ascribe an effective temperature of 5450 K to sunspot penumbra and 4500 K to sunspot umbra. Penumbral and umbral bolometric intensities are then calculated by taking the 1D model atmospheres in the ATLAS9 model atmosphere grid (32) corresponding to these effective temperatures as input to the ATLAS9 code. Existing semi-empirical models already demonstrate this approach to yield the influence of sunspots on solar irradiance without requiring any calibration to solar irradiance observations, including SATIRE-S, which assumes the same penumbral and umbral effective temperatures (30). Hence, adopting this approach to obtain the bolometric intensity of sunspot umbrae and penumbrae does not compromise our objective of a model of TSI variability that does not require calibration to measured variability.

As noted earlier, for each day HMI has been operating (up to July 31, 2016), we take HMI observations and segment the solar disc into quiet Sun, faculae and sunspot penumbra and umbra. We assigned to each quiet Sun, penumbral and umbral image pixel the bolometric intensity corresponding to its μ and to each facular image pixel the bolometric intensity corresponding to its μ and $B_{\rm HMI}$ as given by the result of the above analysis. The integral of the resultant bolometric image over the solar disk yields TSI.

TEST OF THE REALISM OF THE MURAM SIMULATIONS OF THE SOLAR ATMOSPHERE

Evidently, the validity of the TSI model is contingent on how realistic the MURaM simulations are, especially in terms of the intensity contrast of faculae. MURaM simulations of

the solar atmosphere have been demonstrated, in numerous studies, to reproduce solar observations, including the intensity contrast of faculae at multiple wavelengths and as apparent to various instruments [17–20]. Here, we investigate the realism of the MURaM simulations by comparing facular intensity contrast in the synthetic HMI observations generated with the MHD snapshots to that in actual HMI observations.

The study by [4] examined the intensity contrast of faculae in HMI continuum intensity images, defined as the relative difference in intensity to the quiet Sun level. The authors derived an empirical relationship describing the variation in continuum intensity contrast with $B_{\rm HMI}$ and μ.

Intensity contrast in the synthetic HMI continuum intensity images is similarly calculated by taking the mean level in the images of the hydrodynamic snapshots as the quiet Sun level. At each value of μ where we generated synthetic HMI observations, we binned the points in these data by $B_{\rm HMI}$ in intervals of 40 G. The bin-averaged $B_{\rm HMI}$ and continuum intensity contrast is depicted in Fig. 6 along with the empirical relationship from [4].

As evident from Fig. 6, the intensity contrast of faculae in the synthetic HMI observations, based on MURaM simulations, is in good agreement with that in actual HMI observations. This not only validates the MURaM simulations, but also the process through which we generated the synthetic HMI observations from the snapshots.

TEST OF WHETHER THE 10 HYDRODYNAMIC AND 30 MHD SNAPSHOTS PROVIDE SUFFICIENT STATISTICS TO DETERMINE THE BOLOMETRIC INTENSITY OF THE QUIET SUN AND FACULAE

To ascertain if the 10 hydrodynamic and 30 MHD snapshots considered provide sufficient statistics to determine the bolometric intensity of the quiet Sun and faculae, we examined how the agreement between the TSI reconstruction and the TIM record varies with the number of snapshots employed.

First, we determined the bolometric intensity of faculae with just one of the 30 MHD snapshots, performed the TSI reconstruction and compared the result to the TIM record. We repeated this, adding one MHD snapshot chosen at random each time, till we are back at 30. This entire process is iterated 30 times, with each of the 30 MHD snapshots as the starting snapshot in turn. The agreement between the TSI reconstruction and the TIM

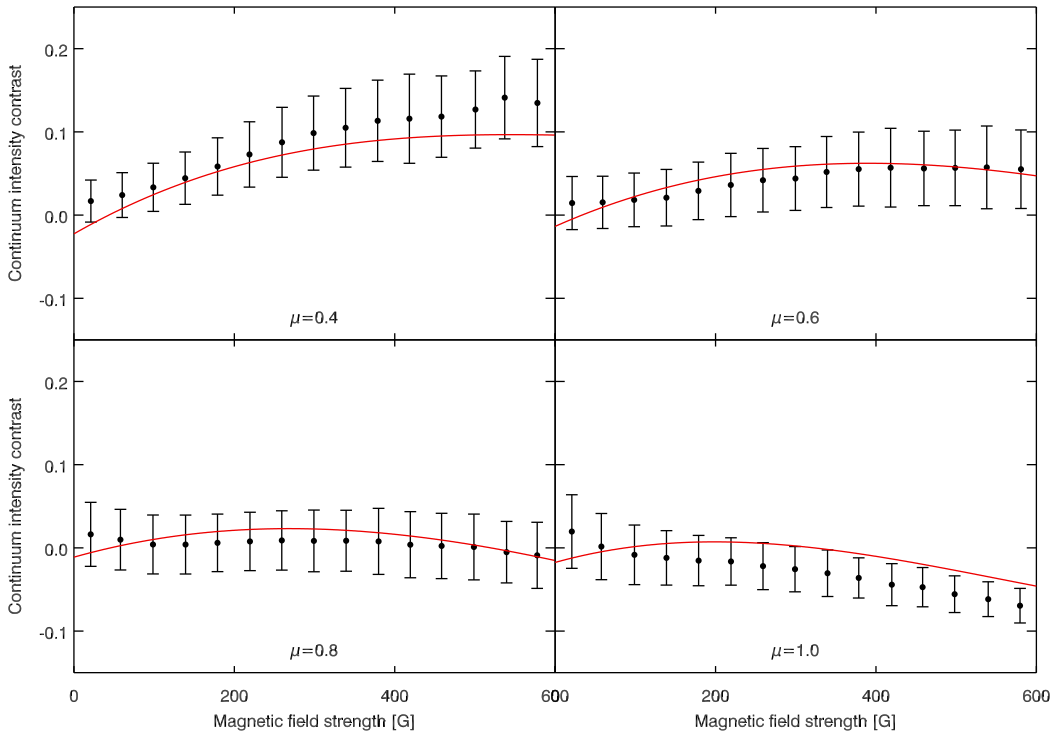


FIG. 6. Intensity contrast of faculae at the continuum of the Fe I 6173 Å line. The black circles denote the mean value in the synthetic HMI continuum intensity images, within successive intervals of 40 G, at the annotated values of μ. The error bars represent the corresponding standard deviation. The red curves follow the empirical relationship relating intensity contrast to magnetic field strength and μ based on actual HMI observations, taken from [4].

record increases with the number of MHD snapshots considered, saturating or coming close to the level of agreement we see with the full set after about 15 to 20 snapshots (Fig. 7A).

We then examined, by a similar procedure, how the agreement between the TSI reconstruction and the TIM record varies with the number of hydrodynamic snapshots considered. As evident from Fig. 7B, varying the number of hydrodynamic snapshots has minimal effect on the agreement between model and measurement (compare the vertical scale of Figs. 7A and 7B), especially after about 5 snapshots.

The above analysis indicates that there is hardly any gain in the accuracy of the reconstruction from including more than about 5 hydrodynamic and 15 to 20 MHD snapshots. We conclude then that the 10 hydrodynamic and 30 MHD snapshots considered provide

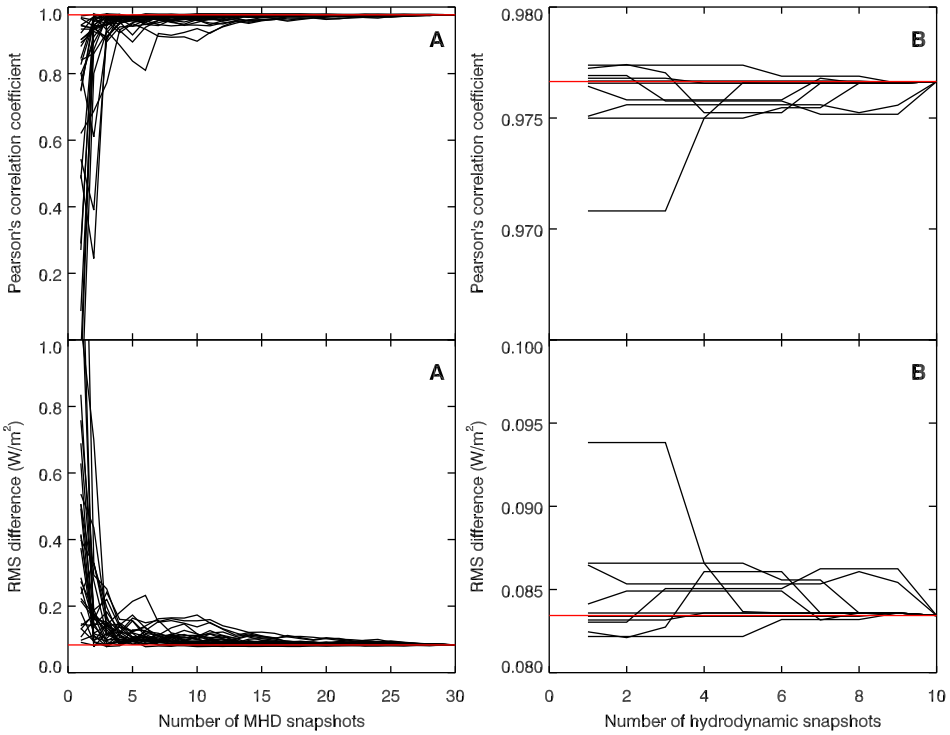


FIG. 7. A) The Pearson's correlation coefficient (top) and RMS difference (bottom) between the TSI reconstruction and the observational record from TIM as a function of the number of MHD snapshots taken to calculate the bolometric intensity of faculae (black). The analysis was iterated, each time with a different starting snapshot and the remaining snapshots added in random order, giving the multiple lines. The red lines follow the values from considering the full set of 30 MHD snapshots (see Table 1). B) The same, except as a function of the number of hydrodynamic snapshots taken to calculate the bolometric intensity of the quiet Sun.

more than sufficient statistics to determine the bolometric intensity of the quiet Sun and faculae.

THE LTE ASSUMPTION

Both SPINOR and ATLAS9 assume LTE. In the case of SPINOR, this does not present any issues. We used the code to calculate the Stokes parameters of the Fe I 6173 Å line, a line formed deep in the photosphere, where the LTE assumption remains reasonable [21, 22].

This is demonstrated in the agreement between the output of the code and observation (Fig 4A).

In the case of ATLAS9, as a result of the breakdown of the LTE assumption in the upper layers of the solar atmosphere, where strong lines in the UV are formed, the output intensity spectra are no longer accurate below 300 nm [23]. For the TSI model presented here and SATIRE-S, solar irradiance variability is modulated by the modelled intensity contrast of faculae and sunspots, that is, the difference between the calculated facular/sunspot and quiet Sun intensities. It has been demonstrated that the variability in the SATIRE-S reconstruction of spectral or wavelength-resolved solar irradiance, also based on ATLAS9 intensity spectra, is consistent with measurements down to 164 nm [2]. This is the case even though the overall level diverges from observations below 300 nm from the breakdown of the LTE assumption. This suggests that non-LTE effects influence the magnetized and unmagnetized solar atmosphere in such a way that the difference between facular/sunspot and quiet Sun intensities calculated assuming LTE remains reasonable below 300 nm even as absolute intensities goes awry.

In employing ATLAS9 here, we are assuming the effect of neglecting non-LTE effects on the modelled bolometric intensity contrast of faculae and sunspots, and hence on TSI variability, is negligible. In any case, any inaccuracy in the modelled bolometric intensity contrast of faculae and sunspots from assuming LTE would, in all possibility, degrade and not enhance the accuracy of the TSI model.

The assumption of LTE has therefore no bearing on the key result of this study, that the model of TSI variability presented reproduces 95% of observed variability over the period of the reconstruction without requiring any optimization to the latter.

---

* yeo@mps.mpg.de

† School of Space Research, Kyung Hee University, Yongjin, Gyeonggi 446-701, Korea.

[1] M. Fligge, S. K. Solanki, and Y. C. Unruh, Astron. Astrophys. **353**, 380 (2000).

[2] K. L. Yeo, N. A. Krivova, S. K. Solanki, and K. H. Glassmeier, Astron. Astrophys. **570**, A85 (2014).

[3] A. Vögler, S. Shelyag, M. Schüssler, F. Cattaneo, T. Emonet, and T. Linde, Astron. Astro-

phys. **429**, 335 (2005).

[4] K. L. Yeo, S. K. Solanki, and N. A. Krivova, Astron. Astrophys. **550**, A95 (2013).

[5] V. Martínez Pillet, B. W. Lites, and A. Skumanich, Astrophys. J. **474**, 810 (1997).

[6] D. Buehler, A. Lagg, S. K. Solanki, and M. van Noort, Astron. Astrophys. **576**, A27 (2015).

[7] F. J. Rogers, F. J. Swenson, and C. A. Iglesias, Astrophys. J. **456**, 902 (1996).

[8] E. Anders and N. Grevesse, Geochim. Cosmochim. Acta. **53**, 197 (1989).

[9] A. Vögler, J. H. M. J. Bruls, and M. Schüssler, Astron. Astrophys. **421**, 741 (2004).

[10] B. Beeck, R. H. Cameron, A. Reiners, and M. Schüssler, Astron. Astrophys. **558**, A48 (2013).

[11] R. L. Kurucz, Rev. Mex. Astron. Astrofis. **23** (1992).

[12] S. Couvidat, S. P. Rajaguru, R. Wachter, K. Sankarasubramanian, J. Schou, and P. H. Scherrer, Sol. Phys. **278**, 217 (2012).

[13] C. Frutiger, S. K. Solanki, M. Fligge, and J. H. M. J. Bruls, Astron. Astrophys. **358**, 1109 (2000).

[14] N. E. Piskunov, F. Kupka, T. A. Ryabchikova, W. W. Weiss, and C. S. Jeffery, Astron. Astrophys. Suppl. Ser. **112**, 525 (1995).

[15] L. R. Bellot Rubio and J. M. Borrero, Astron. Astrophys. **391**, 331 (2002).

[16] K. L. Yeo, A. Feller, S. K. Solanki, S. Couvidat, S. Danilovic, and N. A. Krivova, Astron. Astrophys. **561**, A22 (2014).

[17] S. Shelyag, M. Schüssler, S. K. Solanki, S. V. Berdyugina, and A. Vögler, Astron. Astrophys. **427**, 335 (2004).

[18] N. Afram, Y. C. Unruh, S. K. Solanki, M. Schüssler, A. Lagg, and A. Vögler, Astron. Astrophys. **526**, A120 (2011).

[19] S. Danilovic, D. Röhrbein, R. H. Cameron, and M. Schüssler, Astron. Astrophys. **550**, A118 (2013).

[20] T. L. Riethmüller, S. K. Solanki, S. V. Berdyugina, M. Schüssler, V. Martínez Pillet, A. Feller, A. Gandorfer, and J. Hirzberger, Astron. Astrophys. **568**, A13 (2014).

[21] R. J. Rutten and R. I. Kostik, Astron. Astrophys. **115**, 104 (1982).

[22] N. Shchukina and J. Trujillo Bueno, Astrophys. J. **550**, 970 (2001).

[23] N. A. Krivova, S. K. Solanki, and L. Floyd, Astron. Astrophys. **452**, 631 (2006).

Appendix E

Permissions

The following section contains permission obtained from Astronomy & Astrophysics for using figures from Oshagh et al. (2014) and Norris et al. (2017), and from AAS journals to use Fig 1.3 from Keller et al. (2004) and figures from Basri et al. (2011) and Duncan et al. (1991). APS do not require permission to be sought for an article of an author to be used in their thesis. This allows for use of Fig. 6.1 from Yeo et al. (2017), and the paper itself to be attached, as long as the APS copyright credit line is included. Additionally, permission was granted by Kopp (2016) for use of their TSI figures; Permission from the JSWSC is not required. Contact was unable to be made with Baliunas et al. (1998) or the conference in which the figure used was presented.

Astronomy and Astrophysics
Editor in Chief: T. Forveille

T. Forveille
Astronomy & Astrophysics
Observatoire de Paris
61, avenue de l'Observatoire
75014 Paris, France

Tel.: 33 0(1) 43 29 05 41
Fax: 33 0(1) 43 29 05 57
e-mail: aanda.paris@obspm.fr
Web: http://www.aanda.org

merging
Annales d'Astrophysique
Arkiv for Astronomi
Bulletin of the Astronomical Institutes of the Netherlands
Bulletin Astronomique
Journal des Observateurs
Zeitschrift fur Astrophysik
Bulletin of the Astronomical Institutes of Czechoslovakia

Paris, October 16, 2018

Reprint Permission

Material:
Figs. 2&3 in Oshagh et al. 2014, A&A, 568, A99

To be used in:
PhD thesis entitled "Spectral variability in cool main-sequence stars due to small-scale magnetic features", Imperial College London

Permission granted to:
Charlotte Norris
c.norris14@imperial.ac.uk

I hold copyright on the material referred to above, and hereby grant permission for its use as requested herewith. Credit should be given as follows:
Credit: Author, A&A, vol, page, year, reproduced with permission © ESO.



Thierry Forveille
A&A Editor-in-Chief

Sponsored by Argentina, Armenia, Austria, Belgium, Bulgaria, Chile, Croatia, Czech Republic, Denmark, Estonia, Finland, France, Germany, Greece, Hungary, Italy, Lithuania, Netherlands, Norway, Poland, Portugal, Slovak Republic, Spain, Sweden, and Switzerland.
Produced and distributed by EDP Sciences for ESO.

Astronomy and Astrophysics
Editor in Chief: T. Forveille

T. Forveille
Astronomy & Astrophysics
Observatoire de Paris
61, avenue de l'Observatoire
75014 Paris, France

Tel.: 33 0(1) 43 29 05 41
Fax: 33 0(1) 43 29 05 57
e-mail: aanda.paris@obspm.fr
Web: http://www.aanda.org

merging
Annales d'Astrophysique
Arkiv for Astronomi
Bulletin of the Astronomical Institutes of the Netherlands
Bulletin Astronomique
Journal des Observateurs
Zeitschrift fur Astrophysik
Bulletin of the Astronomical Institutes of Czechoslovakia

Paris, June 8, 2018

Reprint Permission

Material:
Figs. 1-5, 8, 9, A.1, A.2 in Norris et al. 2017, A&A, 605, A45

To be used in:
PhD thesis entitled "'Spectral variability in cool main-sequence stars due to small-scale magnetic features", Imperial College, London

Permission granted to:
Charlotte Norris
c.norris14@imperial.ac.uk

I hold copyright on the material referred to above, and hereby grant permission for its use as requested herewith. The credit should be given as follows:
Credit: Author, A&A, vol, page, year, reproduced with permission © ESO.



Thierry Forveille
A&A Editor-in-Chief

Sponsored by Argentina, Austria, Belgium, Brazil, Chile, Czech Republic, Denmark, Estonia, Finland, France, Germany, Greece, Hungary, Italy, Netherlands, Poland, Portugal, Slovak Republic, Spain, Sweden, and Switzerland.
Produced and distributed by EDP Sciences for ESO.

From: **Permissions** permissions@iop.org
Subject: Re: Figure reproduction permission
Date: 16 October 2018 13:45
To: Norris, Charlotte c.norris14@imperial.ac.uk

Dear Charlotte Norris,

Thank you for providing confirmation that you have received the consent of the authors to reproduce content from AAS journals ***in your thesis entitled "Spectral variability in cool main-sequence stars due to small-scale magnetic features"***

Regarding:

Figure 5 of the paper: Basri et al. 2011 The Astronomical Journal 141:20, "Photometric Variability in Kepler Target Stars. II. An Overview of Amplitude, Periodicity, and Rotation in First Quarter Data"

I am happy to confirm that permission is granted and you need take no further action.

Please include the following alongside the material:

- the source of the material, including author, article title, title of journal, volume number, issue number (if relevant), page range (or first page if this is the only information available) and date of first publication. This material can be contained in a footnote or reference.
- for material being published electronically, a link back to the article (via DOI)
- if practical and IN ALL CASES for works published under any of the Creative Commons licences the words "© AAS. Reproduced with permission".

This permission does not apply to any material/figure which is credited to another source in the AAS publication or has been obtained from a third party. Express permission for such materials/figures must be obtained from the copyright owner.

Kind regards,
Christina

Copyright & Permissions Team
Gemma Alaway – Senior Rights & Permissions Adviser
Christina Colwell - Rights & Permissions Assistant

Contact Details
E-mail: permissions@iop.org
For further information about copyright and how to request permission:
https://publishingsupport.iopscience.iop.org/copyright-journals/

See also: https://publishingsupport.iopscience.iop.org/

Please see our Author Rights Policy
https://publishingsupport.iopscience.iop.org/author-rights-policies/
Please note: We do not provide signed permission forms as a separate attachment. Please print this email and provide it to your publisher as proof of permission.

Please note: Any statements made by IOP Publishing to the effect that authors do not need to get permission to use any content where IOP Publishing is not the publisher is not intended to constitute any sort of legal advice. Authors must make their own decisions as to the suitability of the content they are using and whether they

From: **Permissions** permissions@iop.org
Subject: Re: Paper figure
Date: 16 October 2018 11:02
To: Norris, Charlotte c.norris14@imperial.ac.uk

Dear Charlotte Norris,

Thank you for providing confirmation that you have received the consent of the authors to reproduce content from AAS journals ***in your thesis entitled "Spectral variability in cool main-sequence stars due to small-scale magnetic features"***

Regarding:

figure 2 of the paper: Duncan et al. 1991 ApJS 76:383 "Ca II H and K measurements made at Mount Wilson Observatory, 1966-1983

I am happy to confirm that permission is granted and you need take no further action.

Please include the following alongside the material:

- the source of the material, including author, article title, title of journal, volume number, issue number (if relevant), page range (or first page if this is the only information available) and date of first publication. This material can be contained in a footnote or reference.
- for material being published electronically, a link back to the article (via DOI)
- if practical and IN ALL CASES for works published under any of the Creative Commons licences the words "© AAS. Reproduced with permission".

This permission does not apply to any material/figure which is credited to another source in the AAS publication or has been obtained from a third party. Express permission for such materials/figures must be obtained from the copyright owner.

Kind regards,
Christina

Copyright & Permissions Team
Gemma Alaway – Senior Rights & Permissions Adviser
Christina Colwell - Rights & Permissions Assistant

Contact Details
E-mail: permissions@iop.org
For further information about copyright and how to request permission:
https://publishingsupport.iopscience.iop.org/copyright-journals/

See also: https://publishingsupport.iopscience.iop.org/

Please see our Author Rights Policy
https://publishingsupport.iopscience.iop.org/author-rights-policies/
Please note: We do not provide signed permission forms as a separate attachment. Please print this email and provide it to your publisher as proof of permission.

Please note: Any statements made by IOP Publishing to the effect that authors do not need to get permission to use any content where IOP Publishing is not the publisher is not intended to constitute any sort of legal advice. Authors must make their own decisions as to the suitability of the content they are using and whether they

From: **Permissions** permissions@iop.org
Subject: Re: Permission for figure
Date: 12 June 2018 10:45
To: Norris, Charlotte c.norris14@imperial.ac.uk

Dear Charlotte Norris,

Thank you for providing confirmation that you have received the consent of the authors to reproduce content from AAS journals ***in your thesis***

Regarding:

figure 4 from the paper (Keller et al., 2004, ApJL, 607, L59)

I am happy to confirm that permission is granted and you need take no further action.

Please include the following alongside the material:

- the source of the material, including author, article title, title of journal, volume number, issue number (if relevant), page range (or first page if this is the only information available) and date of first publication. This material can be contained in a footnote or reference.
- for material being published electronically, a link back to the article (via DOI)
- if practical and IN ALL CASES for works published under any of the Creative Commons licences the words "© AAS. Reproduced with permission".

This permission does not apply to any material/figure which is credited to another source in the AAS publication or has been obtained from a third party. Express permission for such materials/figures must be obtained from the copyright owner.

Kind regards,
Christina

Copyright & Permissions Team
Gemma Alaway – Senior Rights & Permissions Adviser
Christina Colwell - Rights & Permissions Assistant

Contact Details
E-mail: permissions@iop.org
For further information about copyright and how to request permission:
https://publishingsupport.iopscience.iop.org/copyright-journals/

See also: https://publishingsupport.iopscience.iop.org/

Please see our Author Rights Policy
https://publishingsupport.iopscience.iop.org/author-rights-policies/
Please note: We do not provide signed permission forms as a separate attachment. Please print this email and provide it to your publisher as proof of permission.

Please note: Any statements made by IOP Publishing to the effect that authors do not need to get permission to use any content where IOP Publishing is not the publisher is not intended to constitute any sort of legal advice. Authors must make their own decisions as to the suitability of the content they are using and whether they require permission for it to be published within their article.

This email (and attachments) are confidential and intended for the addressee(s) only. If you are not the intended recipient please immediately notify the sender, permanently and securely delete any copies and do not take action with it or in reliance on it. Any views